

ESTIMATING VALENCE STATES OF TRANSITION METAL DOPANTS  
IN POLYCRYSTALLINE STRONTIUM TITANATE AND  
BARIUM ZIRCONATE WITH MAGNETOMETRY

by

Michael Robert Knight

© Copyright by Michael Robert Knight, 2022

All Rights Reserved

A thesis submitted to the Faculty and the Board of Trustees of the Colorado School of Mines in partial fulfillment of the requirements for the degree of Doctor of Philosophy (Materials Science).

Golden, Colorado

Date \_\_\_\_\_

Signed: \_\_\_\_\_

Michael Robert Knight

Signed: \_\_\_\_\_

Dr. Ivar Reimanis  
Thesis Advisor

Golden, Colorado

Date \_\_\_\_\_

Signed: \_\_\_\_\_

Dr. Ivar Reimanis  
Professor & Department Head  
Department of Metallurgical and Materials Engineering

## ABSTRACT

Doping with transition metal cations is known to impact processing and performance of polycrystalline strontium titanate (STO) and yttrium-doped barium zirconate (BZY). Lightly Fe-doped STO is commonly used as a model representative for acceptor-doped large band gap electroceramics. BZY is a promising proton conductor for applications in protonic ceramic fuel cells (PCFCs) operating on methane or other hydrocarbon fuels. BZY is difficult to sinter below 1700 °C, however, when small amounts of Ni are incorporated, sintering temperatures are significantly reduced. In both systems, the valence state of the dopant may affect transport properties and redox reactions in electrochemical applications. Valence states can be estimated from their magnetic properties because the only major species having unpaired valence electrons are the dopants, which manifests an electronic magnetic moment. In particular, superconducting quantum interference device (SQUID) magnetometry is demonstrated to provide new information about these two technologically relevant material systems. In STO, the ratio  $\text{Fe}^{4+}/\text{Fe}^{3+}$  increases with  $P_{\text{O}_2}$  of the sintering atmosphere and with increasing Fe-doping from 0.2 mol% to 1.2 mol%. In BZY,  $\text{Ni}^{3+}$  is shown to exist in a low-spin state and anisotropic coordination environment. Dopant segregation near grain boundaries is suggested by the presence of superexchange interactions in both systems, and experimentally observed by STEM-EDS mapping in 4 mol% Ni-doped BZY. Additionally, this work reveals that greater concentrations of the secondary active-sintering  $\text{BaY}_2\text{NiO}_5$  phase remain in the BZY microstructure upon completion of solid-state reactive sintering when NiO is added as a sintering aid versus when Ni is substituted for Zr.

## TABLE OF CONTENTS

ABSTRACT . . . . .	iii
LIST OF FIGURES . . . . .	viii
LIST OF TABLES . . . . .	xii
LIST OF SYMBOLS . . . . .	xiii
LIST OF ABBREVIATIONS . . . . .	xv
ACKNOWLEDGMENTS . . . . .	xvii
DEDICATION . . . . .	xviii
CHAPTER 1 INTRODUCTION . . . . .	1
1.1 Hydrogen Fuel Production . . . . .	1
1.2 Hydrogen Fuel Use . . . . .	3
1.2.1 Solid Oxide Fuel Cells . . . . .	5
1.2.2 Protonic Ceramic Fuel Cells . . . . .	8
CHAPTER 2 BACKGROUND . . . . .	11
2.1 Materials . . . . .	11
2.1.1 Strontium Titanate . . . . .	14
2.1.2 Barium Zirconate . . . . .	19
2.2 Electronic Magnetism . . . . .	24
2.2.1 Diamagnetism . . . . .	28
2.2.2 Paramagnetism . . . . .	28
2.2.3 Ferromagnetism . . . . .	32

2.2.4	Antiferromagnetism . . . . .	33
2.3	Magnetometry Applications . . . . .	35
2.3.1	Historical Examples . . . . .	35
2.4	Electron Paramagnetic Resonance . . . . .	39
2.4.1	Zeeman Interaction . . . . .	40
2.4.2	Hyperfine Interaction . . . . .	41
2.4.3	Zero Field Splitting . . . . .	43
2.4.4	Relaxation Processes . . . . .	43
CHAPTER 3	EXPERIMENTAL . . . . .	45
3.1	Preparation of Iron-doped Strontium Titanate . . . . .	45
3.2	Preparation of Nickel- and Yttrium-doped Barium Zirconate . . . . .	46
3.3	Magnetometry . . . . .	47
3.3.1	Instrumentation . . . . .	48
3.3.2	Measurements . . . . .	49
3.4	Electron Paramagnetic Resonance . . . . .	53
3.5	Electron Microscopy . . . . .	55
3.6	X-ray Diffraction . . . . .	56
CHAPTER 4	DILUTE IRON-DOPED POLYCRYSTALLINE STRONTIUM TITATATE: TRACKING IRON VALENCE STATES AND LOCAL INTERACTIONS . . . . .	57
4.1	Abstract . . . . .	57
4.2	Introduction . . . . .	58
4.3	Experimental . . . . .	60
4.4	Results . . . . .	63

4.5	Discussion . . . . .	72
4.6	Conclusions . . . . .	74
4.7	Acknowledgments . . . . .	75
4.8	Supplemental Information . . . . .	75
CHAPTER 5 ESTIMATING NICKEL VALENCE WITH MAGNETOMETRY IN SOLID-STATE REACTIVE SINTERED YTTRIUM DOPED BARIUM ZIRCONATE . . . . .		
		84
5.1	Abstract . . . . .	84
5.2	Introduction . . . . .	85
5.3	Experimental . . . . .	86
5.4	Results . . . . .	90
5.5	Discussion . . . . .	101
5.6	Conclusions . . . . .	105
5.7	Acknowledgements . . . . .	105
5.8	Supplemental Information . . . . .	106
	5.8.1 Magnetic Characterization . . . . .	106
	5.8.2 Powder X-ray Diffraction . . . . .	113
	5.8.3 Electron Microscopy . . . . .	115
CHAPTER 6 MINIMIZING RESIDUAL BYN PHASE IN SSRS YTTRIUM DOPED BARIUM ZIRCONATE: NICKEL ADDITION VS. NICKEL SUBSTITUTION . . . . .		
		118
6.1	Abstract . . . . .	118
6.2	Characterization of SSRS BZY with NiO additive . . . . .	119
	6.2.1 Powder X-ray Diffraction Results . . . . .	120
	6.2.2 Magnetometry Results . . . . .	122

6.3	Characterization of Ni-doped BZY Quenched after SSRS . . . . .	127
6.3.1	Magnetometry Results . . . . .	128
6.3.2	BYN Phase Analysis . . . . .	132
6.4	Conclusions . . . . .	135
CHAPTER 7 CONCLUSIONS . . . . .		137
7.1	Strontium Titanate . . . . .	137
7.2	Yttrium-doped Barium Zirconate . . . . .	139
7.3	Recommendations for Future Work . . . . .	140
REFERENCES . . . . .		142
APPENDIX A ADDITIONAL RESULTS AND FIGURES . . . . .		160
A.1	Cu-doped BZY15 Prepared by Wet Chemical Methods . . . . .	160
A.2	Additional Figures . . . . .	163
APPENDIX B MAGNETOMETRY SEQUENCES AND DATA FITTING SCRIPTS		169
B.1	Example ZFC-FC M(T) MultiVu Sequence . . . . .	169
B.2	Example M(H) MultiVu Sequence . . . . .	170
B.3	Example Code for Magnetometry Data Analysis . . . . .	170
B.3.1	Importing and Converting Data to SI Units . . . . .	170
B.3.2	Correcting Data for Diamagnetic Background . . . . .	173
B.3.3	Curie-Weiss Analysis of Paramagnetic M(T) Data . . . . .	174
B.3.4	Brillouin Analysis of Paramagnetic M(H) Data . . . . .	176

## LIST OF FIGURES

Figure 1.1	Schematic of SOFC and PCFC . . . . .	5
Figure 2.1	Cubic $\text{ABO}_3$ perovskite structure . . . . .	12
Figure 2.2	Grain boundary and space charge schematic . . . . .	13
Figure 2.3	Jahn-Teller distortion of oxygen octahedra around $\text{Fe}^{4+}$ . . . . .	18
Figure 2.4	Schematic of GB and SC region . . . . .	21
Figure 2.5	Protonic defect trapping and repulsion . . . . .	23
Figure 2.6	Zeeman splitting diagram. . . . .	40
Figure 2.7	Hyperfine splitting diagram. . . . .	42
Figure 3.1	Schematic of a SQUID magnetometer. . . . .	49
Figure 4.1	Powder X-ray diffraction of Fe-doped STO . . . . .	64
Figure 4.2	Fe-doped STO microstructures . . . . .	65
Figure 4.3	Raman spectra of Fe-doped STO . . . . .	66
Figure 4.4	1.2 mol% Fe-doped STO EPR spectra . . . . .	68
Figure 4.5	$\mu_{\text{eff}}/\text{Fe}$ changes at low-temperature . . . . .	70
Figure 4.6	Estimated $\text{Fe}^{4+/3+}$ concentrations and $\Delta H_f$ . . . . .	71
Figure 4.7	SEM micrographs of STO sintered in pure $\text{O}_2$ . . . . .	76
Figure 4.8	SEM micrographs of STO sintered in air . . . . .	77
Figure 4.9	Raman spectra of Fe-doped STO . . . . .	78
Figure 4.10	1.2 mol% Fe-doped STO Mössbauer spectra . . . . .	79
Figure 4.11	ZFC-FC curves of 1.2 mol% Fe-doped STO . . . . .	81

Figure 4.12	Fitted $M(H)$ curves for Fe-doped STO sintered in air . . . . .	82
Figure 4.13	Fitted $M(H)$ curves with two Brillouin functions . . . . .	83
Figure 5.1	Powder X-ray diffraction patterns of Ni-doped BZY20 . . . . .	90
Figure 5.2	SEM micrographs of SSRS Ni-doped BZY20 . . . . .	92
Figure 5.3	SEM micrographs of SSRS quenched Ni-doped BZY20 . . . . .	93
Figure 5.4	STEM-EDS map of SSRS 4NiBZY20 grain boundary region . . . . .	94
Figure 5.5	STEM-EDS map of adjacent BZY and BYN grains . . . . .	95
Figure 5.6	$\chi^{-1}(T)$ of SSRS Ni-doped BZY20 . . . . .	97
Figure 5.7	Product function $\chi T(T)$ of SSRS Ni-doped BZY20 . . . . .	98
Figure 5.8	$\mu_{\text{eff}}/\text{Ni}$ of SSRS Ni-doped BZY20 . . . . .	100
Figure 5.9	$\chi(T)$ of SSRS Ni-doped BZY20 . . . . .	106
Figure 5.10	EPR spectra of 4NiBZY20 at 3 K and 100 K . . . . .	107
Figure 5.11	$M(H)$ of SSRS xNiBZY20 at 3 K and 100 K . . . . .	108
Figure 5.12	$M(H)$ fit results for Ni-doped BZY20 . . . . .	109
Figure 5.13	Magnetometry data for undoped BZY20 . . . . .	110
Figure 5.14	Demonstration of diamagnetic background correction . . . . .	111
Figure 5.15	Demonstration of fitting MH data . . . . .	112
Figure 5.16	Lattice parameters of Ni-doped BZY20 . . . . .	113
Figure 5.17	Magnified XRD patterns showing absense of BYN phase . . . . .	114
Figure 5.18	STEM-EDS map of $\text{Y}_2\text{O}_3$ precipitate in 4NiBZY20 . . . . .	115
Figure 5.19	STEM-EDS line scan across grain boundary . . . . .	116
Figure 5.20	STEM-EDS map of BZY grains in quenched 4NiBZY20 . . . . .	117
Figure 5.21	STEM-EDS quantification of BYN and BZY phases . . . . .	117

Figure 6.1	XRD of SSRS BZY with NiO additive . . . . .	121
Figure 6.2	Lattice parameters of SSRS BZY with NiO additive . . . . .	122
Figure 6.3	ZFC FC $\chi(T)$ of SSRS BZY with NiO additive . . . . .	123
Figure 6.4	$\chi^{-1}(T)$ and $M(H)$ of SSRS BZY with NiO additive . . . . .	124
Figure 6.5	Product function $\chi T(T)$ of SSRS BZY with NiO additive . . . . .	125
Figure 6.6	$\mu_{\text{eff}}/\text{Ni}$ of SSRS BZY with NiO additive . . . . .	126
Figure 6.7	Lattice parameters of all three BZY sample sets . . . . .	127
Figure 6.8	$\chi^{-1}(T)$ and $M(H)$ of quenched Ni-doped SSRS BZY . . . . .	129
Figure 6.9	Product function $\chi T(T)$ of quenched Ni-doped SSRS BZY . . . . .	130
Figure 6.10	$\mu_{\text{eff}}/\text{Ni}$ of quenched Ni-doped SSRS BZY . . . . .	131
Figure 6.11	Crystal structure of $\text{BaY}_2\text{NiO}_5$ . . . . .	132
Figure 6.12	XRD pattern of $\text{BaY}_2\text{NiO}_5$ . . . . .	133
Figure 6.13	ZFC FC $\chi(T)$ of polycrystalline $\text{BaY}_2\text{NiO}_5$ . . . . .	134
Figure 6.14	$M(H)$ of polycrystalline $\text{BaY}_2\text{NiO}_5$ . . . . .	135
Figure 7.1	Diagram showing overall Fe-doped STO conclusions . . . . .	138
Figure 7.2	Proposed superexchange interaction between segregated Ni . . . . .	140
Figure A.1	XRD patterns of Cu-doped BZY15 . . . . .	161
Figure A.2	$\chi^{-1}(T)$ and $\mu_{\text{eff}}/\text{Cu}$ of Cu-doped BZY15 . . . . .	162
Figure A.3	Powder X-ray diffraction of slow-cooled $\text{BaZr}_{0.8}\text{Y}_{0.2}\text{O}_{3-\delta}$ . . . . .	163
Figure A.4	Powder X-ray diffraction of slow-cooled $\text{BaZr}_{0.795}\text{Y}_{0.2}\text{Ni}_{0.005}\text{O}_{3-\delta}$ . . . . .	164
Figure A.5	Powder X-ray diffraction of slow-cooled $\text{BaZr}_{0.79}\text{Y}_{0.2}\text{Ni}_{0.01}\text{O}_{3-\delta}$ . . . . .	164
Figure A.6	Powder X-ray diffraction of slow-cooled $\text{BaZr}_{0.78}\text{Y}_{0.2}\text{Ni}_{0.02}\text{O}_{3-\delta}$ . . . . .	165
Figure A.7	Powder X-ray diffraction of slow-cooled $\text{BaZr}_{0.77}\text{Y}_{0.2}\text{Ni}_{0.03}\text{O}_{3-\delta}$ . . . . .	165

Figure A.8	Powder X-ray diffraction of slow-cooled $\text{BaZr}_{0.76}\text{Y}_{0.2}\text{Ni}_{0.04}\text{O}_{3-\delta}$ . . . . .	166
Figure A.9	Powder X-ray diffraction of quenched $\text{BaZr}_{0.795}\text{Y}_{0.2}\text{Ni}_{0.005}\text{O}_{3-\delta}$ . . . . .	166
Figure A.10	Powder X-ray diffraction of quenched $\text{BaZr}_{0.79}\text{Y}_{0.2}\text{Ni}_{0.01}\text{O}_{3-\delta}$ . . . . .	167
Figure A.11	Powder X-ray diffraction of quenched $\text{BaZr}_{0.78}\text{Y}_{0.2}\text{Ni}_{0.02}\text{O}_{3-\delta}$ . . . . .	167
Figure A.12	Powder X-ray diffraction of quenched $\text{BaZr}_{0.77}\text{Y}_{0.2}\text{Ni}_{0.03}\text{O}_{3-\delta}$ . . . . .	168
Figure A.13	Powder X-ray diffraction of quenched $\text{BaZr}_{0.76}\text{Y}_{0.2}\text{Ni}_{0.04}\text{O}_{3-\delta}$ . . . . .	168

## LIST OF TABLES

Table 2.1	Theoretical effective moments of selected $3d$ cations . . . . .	26
Table 2.2	Number of unpaired electrons for selected $3d$ cations . . . . .	27
Table 2.3	Diamagnetic susceptibilities of selected ions . . . . .	28
Table 4.1	Lattice parameters of Fe-doped STO . . . . .	63
Table 4.2	1.2 mol% Fe-doped STO Mössbauer results . . . . .	80
Table 5.1	X-ray diffractometer instrument settings . . . . .	114

## LIST OF SYMBOLS

Absolute temperature . . . . .	$T$
Bohr magneton . . . . .	$\mu_B$
Boltzmann constant . . . . .	$k_B$
Brillouin function . . . . .	$\mathcal{B}(x)$
Effective magnetic moment . . . . .	$\mu_{\text{eff}}$
Electron volt . . . . .	eV
Energy penalty of doubly occupied orbital . . . . .	$U$
Enthalpy change . . . . .	$\Delta H$
Gibbs free energy . . . . .	$\Delta G^\circ$
Landé $g$ -factor . . . . .	$g$
Langevin function . . . . .	$\mathcal{L}(x)$
Magnetic field strength . . . . .	$H$
Magnetic flux density . . . . .	$B$
Magnetic moment . . . . .	$\mu$
Magnetic susceptibility . . . . .	$\chi$
Magnetization . . . . .	$M$
Multielectron orbital angular momentum number . . . . .	$L$
Multielectron spin angular momentum number . . . . .	$S$
Multielectron total angular momentum number . . . . .	$J$
Néel temperature . . . . .	$T_N$

Number of moments per unit mass . . . . .	$N$
Number of moments per unit volume . . . . .	$n$
Partial pressure of oxygen . . . . .	$P_{O_2}$
Reduced Planck constant . . . . .	$\hbar$
Vacuum permeability . . . . .	$\mu_0$
Weiss coefficient . . . . .	$n_W$
Weiss temperature . . . . .	$\theta$
Zeeman energy . . . . .	$\varepsilon$

**General Nomenclature**

Electron hole . . . . .	$h^\bullet$
Electron . . . . .	$e'$
Oxygen vacancy . . . . .	$V_O^{\bullet\bullet}$
Protonic defect . . . . .	$OH_O^\bullet$
Singly charged acceptor . . . . .	$A'_M$

## LIST OF ABBREVIATIONS

Alternating current . . . . .	AC
Antiferromagnetic . . . . .	AF
Barium cerate . . . . .	BC
Barium zirconate . . . . .	BZ
Coefficient of thermal expansion . . . . .	CTE
Colorado School of Mines . . . . .	CSM
Direct current . . . . .	DC
Electron paramagnetic resonance . . . . .	EPR
Ferromagnetic . . . . .	FM
Grain boundary . . . . .	GB
Hydrogen evolution reaction . . . . .	HER
Intergranular film . . . . .	IGF
Lanthanum strontium manganite . . . . .	LSM
Membrane electrode assembly . . . . .	MEA
Mixed ionic and electronic conductor . . . . .	MIEC
Nuclear magnetic resonance . . . . .	NMR
Oxygen evolution reaction . . . . .	OER
Protonic ceramic fuel cell . . . . .	PCFC
Scanning electron microscopy . . . . .	SEM
Scanning transmission electron microscopy . . . . .	STEM

Solid oxide fuel cell . . . . .	SOFC
Solid state reactive sintering . . . . .	SSRS
Space charge . . . . .	SC
Strontium titanate . . . . .	STO
Thermogravimetric analysis . . . . .	TGA
Transition metal . . . . .	TM
Transmission electron microscopy . . . . .	TEM
Triple point boundary . . . . .	TPB
X-ray diffraction . . . . .	XRD
Yttria stabilized zirconia . . . . .	YSZ
Yttrium-doped barium zirconate . . . . .	BZY

## ACKNOWLEDGMENTS

I would like to thank and acknowledge the National Science Foundation Graduate Research Fellowship Program and everyone who has supported me in this endeavor. None of this research would have been possible without my advisor and mentor Ivar Reimanis, who always supported a healthy work-life balance, guided me through difficult research questions, and challenged me to learn new skills. Interactions with Ron Goldfarb, at the National Institute of Standards and Technology, provided a critical introduction to the art of magnetometry experiments. My undergraduate research advisor Ram Seshadri, at the University of California Santa Barbara, motivated me to pursue a Ph.D. and prepared me through invaluable lessons on effective research habits. Most importantly, I am eternally grateful to my partner Kristina, who provided nearly everything our family needed to survive during my ten years of educational pursuits.

For my son, Henri.

# CHAPTER 1

## INTRODUCTION

Energy production from coal, natural gas, and oil has powered the modern world since the industrial revolution. Continuing use of these fossil fuels strains the environment and eventually such energy supply will diminish. Clean energy conversion technologies are critical to transitioning off these energy sources. This transition will be made possible through development of viable technologies that fundamentally rely on materials research.

A significant concern associated with renewable energy sources such as wind, geothermal, solar or hydro is matching power supply with power demand. Energy storage in batteries has been extensively pursued due to their widespread utility in modern technologies, however, high costs for large requirements and loss of capacity over time limit widespread application in grid scale energy storage.[1] An alternative approach is through conversion of solar energy into chemical energy, then conversion of chemical energy into electrical energy, and vice versa.

Hydrogen is a promising alternative to fossil fuels since the only byproduct is water when used in fuel cells or heat engines. One major setback lies in the fact that hydrogen is not found in nature as  $H_2$ . Instead, it is tied up in other compounds like water and hydrocarbons. Hydrogen production is therefore the first step in the transition process. The next step is developing infrastructure for storage and transportation of the resource, and the final step is developing the technology necessary to use the resource as an energy source in a commercially viable manner. Only the first and last steps are relevant to the materials studied in this thesis, so they will be briefly introduced in the following sections.

### 1.1 Hydrogen Fuel Production

Currently, the primary method to produce hydrogen fuel is steam methane reforming of natural gas, which unfortunately has  $CO_2$  as a byproduct.[2] This method just shifts the

use of fossil fuel to an earlier step in the energy production process, and since the ultimate goal is energy production free of fossil fuels, producing hydrogen with a renewable energy source is ideal. Harnessing solar energy from the sun to split water (equation 1.1) is an attractive approach to produce hydrogen fuel.



This uphill chemical reaction has an associated increase in the Gibbs free energy of  $\Delta G^\circ = 237 \text{ kJ/mol}$ , making the reaction thermodynamically unfavorable.[3] Various approaches to drive this reaction using solar energy have been validated, however, only solar thermal water splitting and photocatalytic water splitting over semiconductors will be introduced here as examples.

Solar thermal water splitting is the process of concentrating solar energy onto a reactor using mirrors to produce heat which drives the endothermic decomposition of  $\text{H}_2\text{O}$  into  $\text{H}_2$  and  $\text{O}_2$ . This single-step process requires reaction temperatures  $> 2200^\circ\text{C}$  to achieve minimal extents of reaction.[4] Additionally, simultaneous production of  $\text{H}_2$  and  $\text{O}_2$  requires additional high-temperature steps to separate the two in order to prevent recombination. An alternative approach is to divide the water splitting process into multiple steps, with a two-step process being the most likely to achieve high efficiencies.[5]

The two-step process starts with applying the solar-generated heat to a metal oxide under low  $P_{\text{O}_2}$ . The metal oxide undergoes reduction and generates  $\text{O}_2$ . In the second step, the reduced metal oxide is reoxidized by exposure to water vapor, in turn generating  $\text{H}_2$ . This conceptually simple process requires finding an optimal metal oxide for the reduction and oxidation steps, as well as, overall reactor system design that operates under conditions maximizing efficiency. The optimal metal oxide must have a high capacity for  $\text{H}_2$  production, low reduction temperature, fast kinetics, long lifetime, compatibility with containment materials in the reactor, and economically viable cost.[6]

Another approach is to split water over semiconducting photocatalysts. This is accomplished by the semiconductor first absorbing photons with energies greater than its

bandgap, then electrons are excited from the valence band to the conduction band, generating holes and excited electrons that diffuse to the surface of the semiconductor.[7] The holes and excited electrons at the surface can then participate in the oxygen evolution reaction (OER) and hydrogen evolution reaction (HER), respectively:



The water splitting efficiency of the overall process is dependent on the efficiencies of the light absorption, charge transfer, and surface reactions.[8] One effective way to improve absorption efficiency is to extend the usable wavelengths of incident photons. The usable wavelengths are dependant on the optical absorption properties of the photocatalyst material and development necessitates optimizing electronic structures. Another critical requirement is optimizing quantum efficiency at the wavelengths used in conversion. In general, it is believed the most detrimental factor to quantum efficiency is the recombination of excited electrons and holes at recombination centers such as lattice defects.[9–11] However, the direct observation and relation of specific defects to recombination is experimentally difficult.

Some notable semiconductors demonstrating active photocatalysis are perovskites such as  $\text{SrTiO}_3$  and  $\text{NaTaO}_3$ , however, large band gaps restrict their practical application to the ultraviolet range.[12–14] One approach to extend photocatalytic activity of semiconductors with wide band gaps into the visible region is to dope with aliovalent cations. In the case of  $\text{SrTiO}_3$ , substitution of Ti with Fe introduces some Fe  $3d$  states above the top of the valence band. This decreases the band gap relative to pure  $\text{SrTiO}_3$  (3.2 eV) and visible light absorption is observed.[15]

## 1.2 Hydrogen Fuel Use

Hydrogen can be utilized as a fuel in electrochemical devices, e.g., fuel cells, to provide power in stationary and portable applications, as well as, to replace the internal

combustion engine in motor vehicles. Fuel cells convert energy from the chemical reaction of fuels to electrical energy with water as a byproduct.[16] Historically, fuel cells are a relatively old technology. In 1802 Sir Humphrey Davy created a simple fuel cell that produced a small electric shock, but in 1839 Sir William Grove created the first fuel cell based on reversing electrolysis of water.[17]

Fuel cells are structured similar to a battery, having an ion conducting electrolyte layer sandwiched between anode and cathode electrodes on either side. The classification of a fuel cell is based on the type of electrolyte and fuel used, which in turn dictates the operating temperature. The types relevant to this thesis are the solid oxide fuel cell (SOFC) and the protonic ceramic fuel cell (PCFC). Many advances in operating devices with various fuels have been made,[18] but for the sake of simplicity, operation with hydrogen fuel will only be discussed.

The hydrogen fuel is introduced at the anode and the oxidant is introduced at the cathode. There exists a chemical driving force to produce water from the reaction of the hydrogen and oxygen, however, this direct reaction is prevented by the electrolyte physically separating the fuel and oxidant. The electrolyte allows ions to conduct between the electrodes while preventing gas diffusion. The overall chemical reaction is:



Both electrodes are connected externally through a load and appropriate half reactions occur at each electrode, which depend on the ions being conducted. If the electrolyte conducts  $\text{O}^{2-}$ , then those ions are produced by electro-reduction of  $\text{O}_2$  at the cathode, which consumes electrons. The  $\text{O}^{2-}$  then migrates through the electrolyte and reacts with  $\text{H}_2$ , releasing electrons and producing water. Alternatively, if the electrolyte conducts  $\text{H}^+$ , then those ions are produced by catalytic oxidation of  $\text{H}_2$  at the anode and electrons are released. The  $\text{H}^+$  then migrates across the electrolyte and reacts with  $\text{O}_2$ , consuming electrons and producing  $\text{H}_2\text{O}$ . In both cases, the flow of ionic charge through the electrolyte is balanced by electrical current flowing through an external circuit. Figure 1.1

shows schematics of both examples, an  $O^{2-}$  conducting SOFC (a) and a  $H^+$  conducting PCFC (b). The respective half cell reactions are displayed at each anode and cathode.

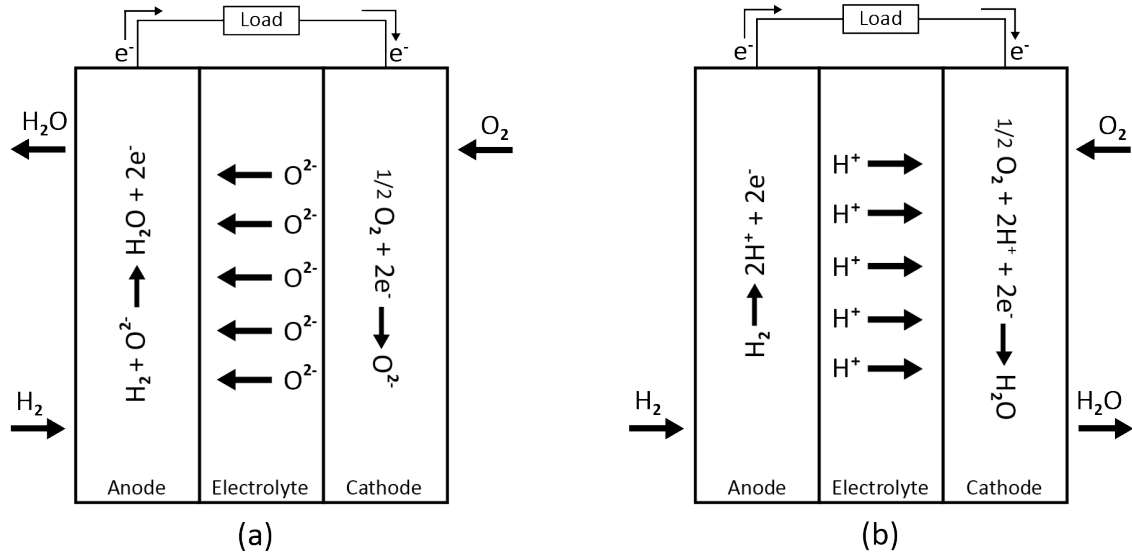


Figure 1.1 Fuel cell schematic showing differences between (a) oxygen ion and (b) proton conducting situations.

### 1.2.1 Solid Oxide Fuel Cells

The electrical current obtained from an SOFC necessitates conduction of  $O^{2-}$  through the electrolyte. In order to obtain useful ionic conductivity it is imperative to operate the system at temperatures above  $800^\circ\text{C}$ . [19] Such high temperatures produce a number of complicating material factors, such as electrode sintering, interfacial diffusion between electrolyte and electrodes, catalyst poisoning, and mechanical stresses caused by mismatched coefficients of thermal expansion (CTE) of the components. [20] Therefore, a main objective of SOFC research has been to lower the operating temperatures.

To maintain sufficient ionic conduction the electrolyte is consequently made as thin as possible without allowing an electrical short circuit to form across it. Additionally, the electrolyte must show excellent phase stability in the reducing and oxidizing atmospheres present at the anode and cathode, respectively. The most commonly used  $O^{2-}$  conducting electrolyte is yttria-stabilized zirconia (YSZ), which demonstrates sufficient conductivity

above 800 °C with chemical stability. The addition of  $Y_2O_3$  to  $ZrO_2$  stabilizes the cubic phase at room temperature and introduces oxygen vacancies due to the charge mismatch between the metal cations. Represented in Kröger-Vink notation this is:



where the  $Y^{3+}$  substituting for  $Zr^{4+}$  leads to the generation of  $V_{\text{O}}^{\bullet\bullet}$  required to maintain charge neutrality. Overall charge neutrality can then be described by

$$[Y'_{Zr}] = 2[V_{\text{O}}^{\bullet\bullet}] \quad (1.6)$$

where the square brackets indicate concentrations. For every two acceptor ions only one oxygen vacancy is formed, showing that high solubility is required to get significant oxygen vacancy concentration. These vacant oxygen sites provide positions in the lattice for  $O^{2-}$  to move through the YSZ electrolyte during SOFC operation. Furthermore, with high defect densities the formation of defect associates appear and can reduce ionic conductivity.[21]

The electrolyte should have high ionic conductivity, resistant to electronic conductivity, chemically/mechanically stable under operating conditions, and impermeable to gases.[19] An ideal electrolyte would be single crystalline, however, in reality the production cost would be far too expensive to make the technology competitive in the market, and dense polycrystalline materials are used instead. The interfaces between crystallites, i.e., grain boundaries (GB), often block transport of ions between grains and reduce overall ionic conductivity.[21]

At the GB, lattice periodicity is disrupted and is accommodated by missing bonds or mechanical strain.[21] Additionally, the GB acts as a sink or source for point defects and relative to the grain interior, the GB takes on a net positive or negative charge, depending on the defects. Consequently a volume adjacent to the GB is oppositely charged to maintain overall charge neutrality. This volume is usually referred to as the space charge (SC) region.[21, 22]

SOFC electrodes should be compatible with the electrolyte to avoid detrimental interactions while operating at high temperatures, like large CTE mismatches that induce mechanical stresses or chemical reactions that form unwanted phases.[19] Additionally, an ideal electrode must conduct electrons and  $O^{2-}$ , as well as, allow transport of gases to the points where all three species meet, i.e., the triple-point boundaries (TPB).[19] At the anode TPBs is where electro-oxidation occurs, and at the cathode TPBs is where electro-reduction occurs. Therefore, the electrodes must be mixed conductors, have high surface area, enough porosity for gas transport, and be electrochemically active.

Finding such a material that satisfies all of these requirements is difficult, and consequently composite materials are typically used for the electrodes.[19] The most commonly used SOFC anode has been a composite of metallic Ni and YSZ. This composite is prepared by mixing a ratio of NiO:YSZ in an approximately 50:50 ratio, and the NiO is reduced to metallic Ni in situ due to the reducing atmosphere at the anode. This produces a fine distribution of Ni catalyst particles supported on a porous YSZ matrix. A historically popular SOFC cathode composite material is  $La_{1-x}Sr_xMnO_{3-\delta}$  (LSM) mixed with YSZ. The properties of LSM provide necessary electro-reduction activity and electronic conductivity, while the YSZ component provides  $O^{2-}$  conduction.[19]

Oxygen incorporation and transport through the SOFC is critical to performance. Therefore, fundamental understanding of defect segregation and blocking effects at GBs in ion conducting materials are necessary to explore. These phenomena have been heavily researched in  $Fe^{3+}$  doped  $SrTiO_3$  (STO), a model material representative of acceptor-doped wide bandgap oxides.[22–41] One important factor to consider is that Fe can adopt mixed valences in  $SrTiO_3$  when substitution is low enough to be considered dilute, i.e., no ordering of Fe in the lattice occurs.[33, 42–44] Therefore, experimental methods to estimate dilute Fe valences, and potential interactions between them upon accumulation, would be useful.

### 1.2.2 Protonic Ceramic Fuel Cells

As mentioned in the previous section, lower fuel cell operating temperatures opens up more cost effective routes to achieve wide adoption of the technology. The most promising route is through development of fuel cells that rely on  $H^+$  conduction rather than  $O^{2-}$  conduction.  $O^{2-}$  conducting materials typically have high activation enthalpies and require high temperatures ( $> 800^\circ\text{C}$ ) for sufficient ionic conduction, whereas  $H^+$  conducting materials can achieve high conductivity at lower temperatures ( $350\text{--}600^\circ\text{C}$ ).<sup>[45, 46]</sup> These materials are typically referred to as protonic ceramics, and are emerging as a favorable alternative to conventional SOFCs in electrochemical energy conversion and storage. This section will only introduce the application of this class of ion conducting materials as used in hydrogen fuel cells. For an extensive review of all the potential use cases and history of development, the reader is directed to the recent article by Duan et al.<sup>[46]</sup>

In a PCFC, the protonic defects are described as  $\text{OH}_\text{O}^\bullet$ , which are generated by dissociative incorporation of water into oxygen vacancies:



Since protons are not intrinsic to the material, they must be added through this hydration reaction. Therefore, significant concentrations of oxygen vacancies are required to achieve the requisite amount of hydration. This is typically done by doping with an acceptor (substitution with a cation having lower oxidation state than the host), which generates extrinsic oxygen vacancies to satisfy electroneutrality in the lattice. The protonic defects are mobile via phonon assisted proton hopping, in other words, detachment and transfer between oxygen ions in the lattice.<sup>[47]</sup>

The  $\text{ABO}_3$  cubic perovskites have a large unit cell volume, which benefits hydration (formation of protons) and high proton mobility.<sup>[48]</sup> Iwahara et al. first reported proton conduction in  $\text{ABO}_3$  perovskite compounds of acceptor-doped  $\text{SrCeO}_3$  and  $\text{BaCeO}_3$  (BC) over 30 years ago.<sup>[49, 50]</sup> A few years later, acceptor doped  $\text{BaZrO}_3$  (BZ) was found to

have lower proton conductivity than BC, but demonstrated better mechanical and chemical stability.[51] Ryu and Haile then showed that increasing Zr content in the BC-BZ solid solution system leads to a monotonic decrease in unit cell volume, a monotonic increase of chemical stability in CO<sub>2</sub>, and the ionic conductivity in both wet and dry atmospheres monotonically decreases.[52] Shortly after, Kreuer et al. found that proton conductivity in this system is very sensitive towards the acceptor dopant species, and Y<sup>3+</sup> is an excellent match for BZ, i.e., the enthalpy of formation and mobility of protonic defects are unchanged by the presence of the dopant.[53] Subsequently, yttrium-doped BZ (BZY) has become one of the most widely used electrolytes in PCFC devices.[46]

Studies have shown that the grain interior conductivity of BZY is substantial, however, highly resistive GBs lead to low overall conductivity and methods to enhance densification and grain growth are necessary.[53, 54] The highly refractory nature of BZY requires high sintering temperatures and long sintering times to achieve a large-grained dense electrolyte. This introduces unwanted Ba evaporation and incompatibilities with electrode materials that need to be co-sintered together with the electrolyte.[52, 55, 56] Various approaches have been used to enhance densification at lower temperatures, and the incorporation of a sintering aid or additive has shown great efficacy.[57–60]

Babilo and Haile pioneered this approach by adding 4 wt% ZnO to BZY powders before sintering and achieved enhanced sinterability.[57] Building upon this result, Tong et al., Nikodemski et al., and Duan et al. introduced sintering additives to the precursor powders, effectively combining phase formation, densification, and grain growth in one step.[58, 61, 62] This simplified process has become known as solid-state reactive sintering (SSRS) and is widely used in preparation of BZY based electrolyte materials for PCFCs.[46] The most effective sintering additive for BZY was found to be NiO, which reduced the sintering temperature to 1400 °C and is the most compatible with NiO-BZY composite anodes.[62]

Over a decade ago, Tong et al. proposed the mechanism of enhanced BZY sinterability with NiO involves the formation of a secondary phase with composition  $\text{BaY}_2\text{NiO}_5$  (BYN) that accelerates grain growth at high-temperature and dissolves back into the BZY lattice upon completion of SSRS.[59] During PCFC anode operating conditions (reducing environment), this BYN phase will decompose into Ba-phases, a yttria phase, and metallic Ni, which will degrade performance.[63, 64] Therefore, formation of excess BYN phase in the sintered electrolyte is undesirable. Previous researchers compared NiO additions with Ni-substitution for Zr and found that proton uptake was improved with Ni-substitution.[65] Details about the role of Ni in BZY phase evolution and final microstructure remain somewhat mysterious, therefore it is desirable to establish methods to track Ni distribution and valence state. Knowledge of this information would inform researchers preparing BZY electrolytes by the SSRS method about the optimal approach to incorporate Ni.

## CHAPTER 2

### BACKGROUND

A key issue for commercialization of electrochemical energy conversion technologies is finding stable, environmentally sustainable, and low-cost materials that perform with high-efficiency. In addition, the device must be economically competitive with current technologies for widespread adoption. These technologies rely on different energy conversion processes and therefore require different functional material properties. Due to their extreme compositional and structural flexibility, complex perovskite-structured oxides and their many derivatives, are promising candidates for electrochemical energy conversion applications.[66]

#### 2.1 Materials

A wide variety of compositions that fall into the category of perovskite-structured oxides can display many useful properties, e.g., ionic and/or electronic conductivity, colossal magnetoresistance, superconductivity, ferroelectricity, thermoelectricity, or even catalytic activity. The compositions of interest to this work have the chemical formula of  $A^{2+}B^{4+}O^{6-}$  and crystallize in the ideal cubic perovskite  $Pm\bar{3}m$  space group at room temperature. Here, the A- and B-site cations form mainly ionic bonds with the oxygen anions. The smaller B-site cations occupy the corners of a cube in 6-fold oxygen coordination and the larger A-site cations are situated at the center of the cube with 12-fold oxygen coordination (Figure 2.1).

The deviation from ideal stoichiometry is a critical parameter for conduction properties, where oxygen non-stoichiometry may determine whether the oxide is ionically or electronically conducting, an n- or p-type semiconductor, or superconducting.[67] Therefore, variations in oxygen partial pressure or substitution of host cations with aliovalent cations can act as useful knobs to tune conduction properties. Subsequently,

perovskite oxides with significant oxygen understoichiometry, induced from acceptor doping, are often used as solid electrolytes in gas sensors or fuel cells.[38]

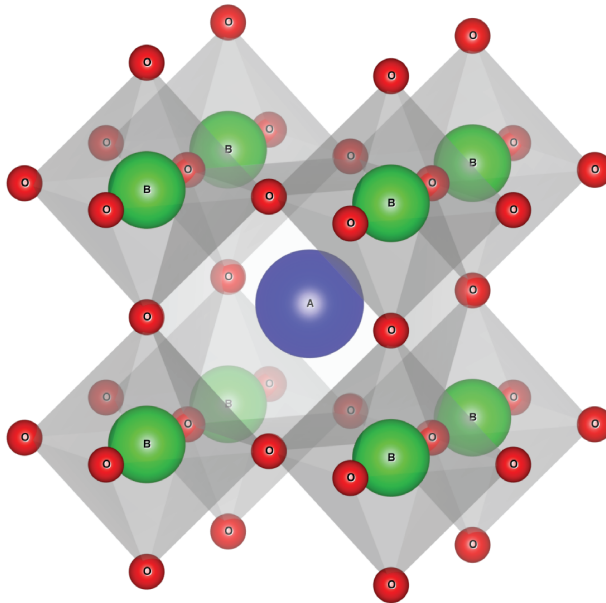


Figure 2.1 Cubic  $ABO_3$  perovskite structure. For the materials in this work, A is a 2+ cation 12-coordinate with oxygen and B is a 4+ cation 6-coordinate with oxygen.

A high-performing solid electrolyte usually demonstrates excellent bulk conductivity through the lattice, however, the presence of GBs in a polycrystalline solid has an impact on the macroscopic conductivity. These interfaces can serve as pathways for high-conductivity or, more commonly, as barriers with high-resistivity, which can be several orders of magnitude higher than in the bulk.[68] Two important phenomena can occur at such interfaces, the formation of SC regions and two-dimensional interfacial phases, which can both significantly modify the conductivity across or along the interface.[68]

The origin of the SC region is similar to the electrical double layers at interfaces between electrodes and aqueous electrolytes or at p-n junctions in semiconductors. In high-purity solid electrolytes, SC blocking effects on conductivity have become accepted as the primary cause of high GB resistivity.[22, 38, 69] Frenkel was historically the first to propose that the presence of a SC region near free surfaces in ionic conductors was a result



phases can significantly alter the adjacent space charge regions by changing the net charge accumulation at the core, and alter the ion mobility along the interface by modifying the interfacial structure or cause chemical disorder.[68] The most commonly observed IGFs are silicate-based and amorphous, which are presumably resistive and reduce GB conductivity.[68] The formation of IGFs is usually caused by the unintentional contamination of siliceous impurities and two strategies can be used to alleviate the effects. First, annealing at a lower temperature after sintering the polycrystalline solid can be used to 'dewet' the phase, where a temperature-induced GB phase-like transition results in a clean GB and improves interfacial conductivity. Secondly, scavengers that form solid solutions with the electrolyte or precipitated secondary phases can be used. These scavengers reduce the chemical potential of  $\text{SiO}_2$  and destabilize formation of the IGF.[73]

### 2.1.1 Strontium Titanate

STO is a model cubic perovskite oxide at room temperature with a wide indirect bandgap and high dielectric constant.[74, 75] This material is useful for a wide range of commercial applications, e.g., capacitors, substrates for thin film growth, fuel cells, sensors, varistors, and memristors.[76–81] Many recent articles have been published that explore the roles of impurities (or dopants) and processing environments on the properties of single crystal STO.[82–86] In ideal bulk STO crystals, Ti and Sr donate electrons to O, becoming positively and negatively charged ions, respectively. The electronic structure consists of Sr 5s states lying far above the conduction band minimum, Ti 3d states forming the conduction band, and the now filled O 2p states comprising the valence band.[87]

However, many applications use polycrystalline STO for practical reasons, and it becomes important to consider microstructural effects when attempting to understand the roles of impurities on the electronic structure. Review of the literature suggests the {100} surfaces are the most predominant GB termination and typically exhibit excess cation concentrations with respect to the bulk.[88–91] Observation of excess cations at these GBs are likely associated with the accumulation of  $\text{V}_{\text{O}}^{\bullet\bullet}$  at the core. In this case, there will be

electronic states associated with the excess cation dangling bonds that would normally transfer to the valence band oxygen states. However, with an oxygen deficient GB core these instead fill states near the conduction band, in other words, donor states.[87] These dangling electrons would remain spatially located in the GB core if there were no other defect states lower in the gap to transfer to. In reality, there are always point defects present as impurities or cation vacancies. The impurities are typically acceptors, which provide a route to lower the electronic free energy via transfer of the GB dangling bond electrons to the acceptor. This leaves behind a positively charged GB core, and those acceptors closest to the GB core form the negatively charged SC region (satisfaction of Poisson’s equation for the electrostatic potential).[87]

The GBs in acceptor-doped STO have been shown to consistently hinder transport of positively charged carriers, as evident by the appearance of a low-frequency semicircle in impedance spectroscopy.[38] The effective thickness of the blocking layer in STO is typically 5-50nm, depending on the GB core charge and acceptor concentration.[38] Due to the large dielectric constant of this material, the SC region is broad, especially when acceptor concentration is low.[38] Klie and Browning investigated nanocrystalline STO with residual acceptor concentration on the order of 100ppm and revealed the absence of separated bulk and GB semicircles in impedance spectra when the SC region extends across the entire grain.[27] Therefore, it is important to consider defect concentrations when discussing the extent of the SC region.

In order to calculate defect concentrations as a function of thermodynamic variables, a brief summary of the relevant bulk defect chemistry is given below. Experimental and theoretical results have shown the most favorable intrinsic defect reaction in pure STO is the partial Schottky disorder reaction[92, 93]:



where strontium vacancies act as acceptors. The other important intrinsic defect reaction is generation of holes and electrons by thermal excitation across the bandgap[94]:



Defect concentrations are rarely dictated by these intrinsic reactions because impurities will be present in concentrations on the order of hundreds ppm under most conditions.[95] The predominant acceptor impurity (or intentional dopant) found in STO is  $\text{Fe}^{3+}$ . This acceptor is incorporated in STO according to the following reaction:



Additional complications to the defect chemistry arise because Fe can easily adopt various valence states.[96, 97] Therefore, the ionization reaction of the Fe-dopant needs to be considered:



Additionally, the equilibrium reactions with gaseous oxygen or water vapor can be taken into account



respectively. The charge neutrality condition for Fe-doped STO then becomes:

$$[e'] + [\text{Fe}'_{\text{Ti}}] + 2[\text{V}''_{\text{Sr}}] = [h^\bullet] + 2[\text{V}_\text{O}^{\bullet\bullet}] + [\text{OH}_\text{O}^\bullet]. \quad (2.7)$$

If strontium vacancies are omitted (generally much lower concentration than Fe), the atmosphere is dry, and temperature is not too high ( $< 700^\circ\text{C}$ ), then the acceptor concentration is[98]:

$$[\text{Fe}'_{\text{Ti}}] \approx 2[\text{V}_\text{O}^{\bullet\bullet}] > [h^\bullet] \gg [e']. \quad (2.8)$$

At typical transport characterization temperatures ( $< 1000^\circ\text{C}$ ), the bulk conductivity in STO is comprised of contributions from only  $\text{V}_\text{O}^{\bullet\bullet}$ ,  $e'$ , and  $h^\bullet$  since the cations may be

considered immobile.[99] Although  $V_{\text{O}}^{\bullet\bullet}$  are in greater concentration, the dominant contribution to conductivity comes from  $h^{\bullet}$ , which have greater defect mobility.[92, 97]

Hopefully it has been made clear that the interaction of point defects with GBs is critically important in polycrystalline STO. The most common impurity (or dopant) cation, Fe, fortunately, has unpaired electrons that produce a magnetic moment. This makes Fe cations readily distinguishable from all the other nominally diamagnetic STO constituents through magnetic characterization, e.g., magnetic susceptibility and electron paramagnetic resonance (EPR) spectroscopy. Leveraging this knowledge has led to many studies over the decades estimating the valences of Fe in the  $\text{Sr}(\text{Ti},\text{Fe})\text{O}_3$  system.[31, 33, 44, 100–109]

The  $\text{SrTi}_{1-x}\text{Fe}_x\text{O}_{3-\delta}$  (STFO) system forms a solid-solution for all values of  $x$  and is a mixed ionic and electronic conductor (MIEC), especially for Fe-rich compositions ( $x > 0.1$ ).[33] Zhou and Goodenough reported on the mixed valence character of Fe, which showed a general trend of the  $\text{Fe}^{3+/4+}$  ratio increasing as  $x$  increases from 0.1 to 0.95.[103] Furthermore, they concluded that the transport and magnetic properties in this system are strongly influenced by interactions between Fe cations. Such interactions in the lattice indicate that extending the properties of the STFO system to the dilute Fe-doped STO model system is inappropriate. It has been suggested that only Fe doping concentrations less than 1-2mol% can be considered dilute, because at higher concentrations there are significant Fe electronic states that overlap with one another and admix with O  $2p$  valence states.[33, 103, 110]

The focus of the current work is on the dilute Fe-doped STO model system, where the defect chemistry has been extensively studied. As discussed earlier, the existence of excess  $V_{\text{O}}^{\bullet\bullet}$  at GB cores and subsequent accumulation of  $\text{Fe}'_{\text{Ti}}$  acceptors in the adjacent space charge region is well understood theoretically, and is frequently correlated with conductivity results. However, observing this phenomenon directly is experimentally difficult due to such low Fe concentrations in the dilute limit.

Evarestov et al. performed first-principles calculations on a single (isolated)  $\text{Fe}^{4+}$  impurity substituted for Ti in STO and predicted the high-spin state ( $S = 2$ ), having four unpaired electrons, lies lower in energy (by 5.4 eV after lattice relaxation) than the low-spin state ( $S = 0$ ), having zero unpaired electrons.[110] The octahedral crystal field at the B-site stabilizes the structure by splitting the five degenerate  $d$  energy levels into three lower energy degenerate  $t_{2g}$  levels and two higher energy degenerate  $e_g$  levels. For high-spin  $\text{Fe}^{4+}$ , three electrons singly occupy the  $t_{2g}$  levels and one electron singly occupies an  $e_g$  level. A  $d^4$  cation in octahedral symmetry, such as  $\text{Fe}^{4+}$ , will distort the octahedra by tetragonal extension to further stabilize the structure. This distortion was shown theoretically and experimentally to occur for isolated  $\text{Fe}^{4+}$  in STO.[110–115] A visual adaptation of the computational results[111] are shown in Figure 2.3.

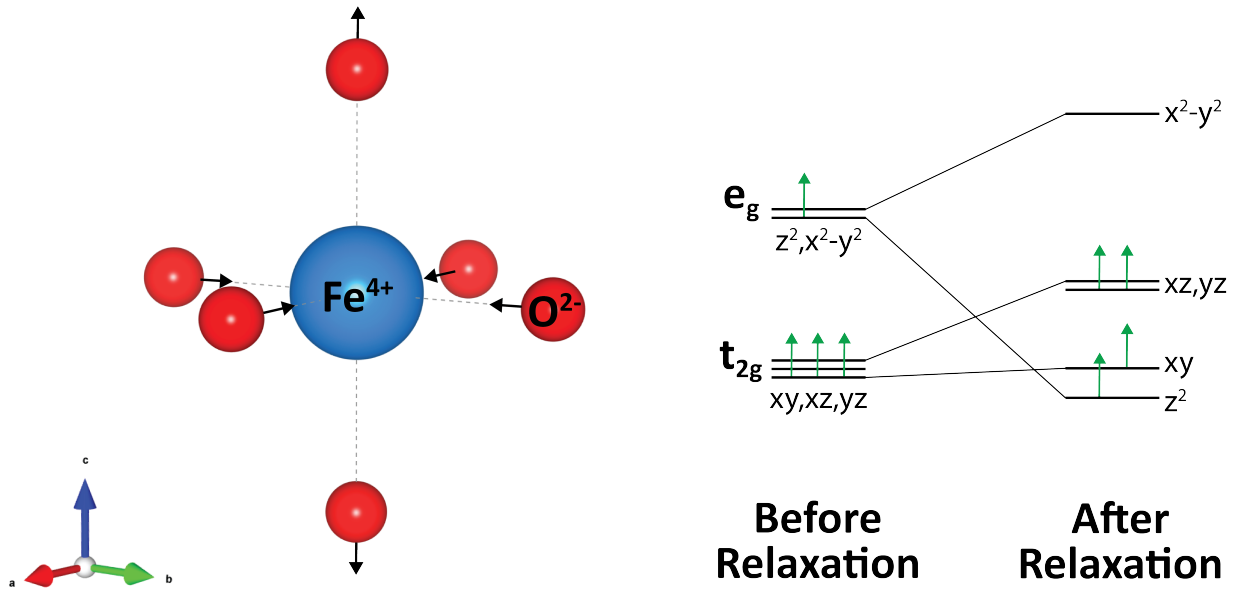


Figure 2.3 Tetragonal distortion around isolated  $\text{Fe}^{4+}$  defects in  $\text{SrTiO}_3$  and subsequent splitting of the  $d$  electron energy levels, adapted from [111].

Isovalent substitutional  $\text{Fe}^{4+}$  will not interact with the positively charged GB in STO, but aliovalent  $\text{Fe}^{3+}$  has a negative effective charge when substituting for titanium and would be attracted.  $\text{Fe}^{3+}$  in STO exists in a high-spin state, having five unpaired

electrons.[103] This  $d^5$  cation does not exhibit any crystal field stabilization energy like  $\text{Fe}^{4+}$ , because it has all five  $d$ -orbitals singly occupied.[116] The typical precursor used to intentionally dope Fe in STO is  $\text{Fe}_2\text{O}_3$ , which is antiferromagnetically ordered. When the Fe cations are dilute and isolated from each other in the STO lattice, they would not be magnetically ordered and display paramagnetism. This makes estimations of the valence possible through magnetic susceptibility measurements.

In the dilute limit, the Fe dopants are expected to be well separated and non interacting. However, for high concentrations of  $x$  in STFO, multiple exchange interactions between Fe cations are present and produce different magnetic behaviors. The main three interactions are: (1) antiferromagnetic  $\text{Fe}^{3+}\text{-O-Fe}^{3+}$ , (2) ferromagnetic  $\text{Fe}^{4+}\text{-O-Fe}^{3+}$ , and (3) ferromagnetic  $\text{Fe}^{4+}\text{-O-Fe}^{4+}$ . [103] In the presence of positively charged GB cores,  $\text{Fe}'_{\text{Ti}}$  acceptors would accumulate in the SC region and could exist as next-nearest neighbors. Therefore, the acceptors are no longer locally dilute and interaction (1) could occur. Additional background on electronic magnetism will be discussed later in this chapter.

The positively charged GB core in STO would lead to electrostatic repulsion of  $\text{V}_\text{O}^{\bullet\bullet}$  and concentration of these defects would be decreased in the adjacent SC region. For  $\text{Fe}'_{\text{Ti}}$  acceptors in the bulk, charge compensation would occur by the formation of  $\text{V}_\text{O}^{\bullet\bullet}$  in a 2:1 ratio, i.e.,  $[\text{Fe}'_{\text{Ti}}] \approx 2[\text{V}_\text{O}^{\bullet\bullet}]$ . Indeed, the presence of  $\text{V}_\text{O}^{\bullet\bullet}$  in the first coordination shell of  $\text{Fe}'_{\text{Ti}}$  forms a defect complex and has been observed experimentally.[31, 106, 112] The acceptor effectively traps the  $\text{V}_\text{O}^{\bullet\bullet}$  and forms a positively charged defect complex  $(\text{Fe}'_{\text{Ti}} - \text{V}_\text{O}^{\bullet\bullet})^\bullet$ . These defect complexes may then trap negatively charged carriers and repel positively charged carriers, e.g., trap  $e'$  and repel  $h^\bullet$  or  $\text{V}_\text{O}^{\bullet\bullet}$ . This phenomenon in Fe-doped STO would then affect MIEC behavior in practice.

### 2.1.2 Barium Zirconate

As introduced in the previous chapter, lowering operating temperatures of SOFCs has led to the development of PCFCs, where the mobile charge carriers are protons. One of the most studied systems in proton conducting solid electrolytes for PCFCs are the

acceptor-doped barium zirconates. These electrolytes offer improved chemical stability in H<sub>2</sub>O and CO<sub>2</sub> environments over acceptor doped barium cerates.

The main requirement to enable proton transport is to have appreciable V<sub>O</sub><sup>••</sup> content. The most common acceptor dopant used in this system is Y<sup>3+</sup>, which substitutes for Zr<sup>4+</sup> and generates oxygen vacancies according to the following defect reaction:



Between 5 mol% and 10 mol% yttrium is incorporated to achieve the requisite V<sub>O</sub><sup>••</sup> content and upon hydration the BZY achieves bulk proton conductivities around 0.001–0.03 Ω<sup>-1</sup> cm<sup>-1</sup> in the temperature range of 200–500 °C.[45, 51, 117] Conductivity is significantly decreased by the blocking effect of GBs, which are significant in number due to the relatively small grain sizes.[45, 55, 57, 118]

Multiple reasons for conductivity blocking grain boundaries may be considered. Insulating grain boundary phases or constriction of current at grain to grain contact are possibilities, however, these phases are rarely observed in perovskite protonic electrolytes, and much higher GB conduction activation energy compared to bulk makes constriction unlikely.[119] Specifically for BZY, barium loss due to high BaO vapor pressure at high sintering temperatures of BZY could lead to cross substitution of Y<sup>3+</sup> to the A-site and act as a donor, or formation of a secondary zirconia phase.[119] The observed higher GB conduction activation energy in BZY could be caused by segregated impurities or dopants at GBs, which would cause local distortions or electrostatic interactions to occur.

Size mismatch between dopant and host, or electrostatic attraction to the GB due to preexisting GB charge would lead to inhomogeneous dopant distribution.[119] An excess positive charge in the GB core could result from different defect formation energies of positively charged defects at the structurally different GB.[120] Studies have correlated sintering and annealing conditions with modification of GB properties in the absence of secondary GB phases, suggesting the blocking origin of GBs stems from intrinsic properties.[121, 122]

Multiple studies have provided evidence that the presence of an excess positive charge at the GB core and adjacent negatively charged SC region that depresses protonic defect concentrations and results in an overall increase of local resistivity.[123–127] This is in general agreement with the situation discussed above for Fe-doped STO, and is shown schematically in Figure 2.4. However, it is important to mention computational studies revealed that in BZY both oxygen vacancies and protonic defects tend to segregate to the GB core.[128, 129]

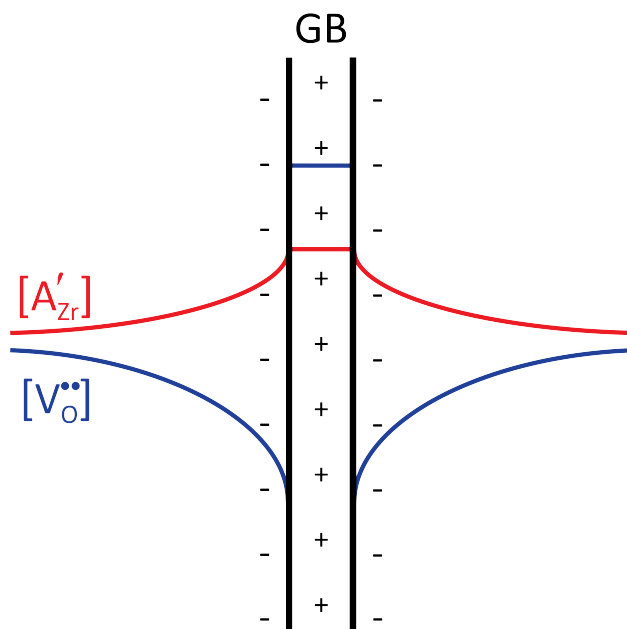


Figure 2.4 Schematic showing  $A'_{Zr}$  segregation and  $V_{O}^{••}$  depletion in the SC region adjacent to a GB having excess  $V_{O}^{••}$ . Here A is a cation with a 3+ charge.

The blocking effect is strongest for low acceptor doping concentrations, because increasing acceptor concentration decreases the space charge potential.[38] Impedance spectroscopy results show the capacitance extracted from the GB semicircle suggests the blocking layer far exceeds the width of the GB core and the width decreases with increasing dopant concentration.[123, 124, 127] For comparable acceptor dopant concentrations, the space charge potentials in BZY are larger than those in acceptor-doped STO.[38] Impedance spectroscopy measurements over a large  $P_{O_2}$  range revealed the bulk

remains ionic over the whole range, while a slight increase in n-type conductivity for low  $P_{O_2}$  suggests electron accumulation in the SC region that decreases proton blocking.[123]

Accumulation of acceptor dopants in the GB region occurs during high-temperature treatments, where mobility of the cations is sufficient. Acceptor segregation in such samples provides evidence for SC depletion of positively charged defects.[56, 122, 130] Fortunately, this accumulation results in less blocking and the amount of accumulation does not seem to depend on the acceptor radius.[119] Additionally, high-resolution energy dispersive X-ray spectroscopy investigations of Sc-doped BZ revealed the dopants actually enter the GB core and more effectively compensate the positive charge, rather than just accumulate in the SC region.[131]

More evidence confirming the existence of a positive GB core potential, acceptor accumulation in the GB region, and depletion of oxygen in the GB region, was provided by laser assisted atom probe tomography of a  $BaZr_{0.9}Y_{0.1}O_{3-\delta}$  GB.[132] These results also revealed that the elemental distribution and electrical properties along a single GB exhibit lateral inhomogeneities, demonstrating the complicated nature of curved GBs and resulting defect chemistry.

Another important concern exists regarding the local environment of the acceptor dopant. Just like the situation for Fe-doped STO, there could exist associations between oxygen vacancies and acceptors. Oikawa and Takamura explored the room temperature distribution of protons and oxygen vacancies under different levels of hydration in  $BaZr_{0.9}Sc_{0.1}O_{3-\delta}$  using nuclear magnetic resonance (NMR) spectroscopy and thermogravimetric analysis (TGA).[133] Their results suggested protonic defects avoided the positively charged defect associate,  $(Sc'_{Zr}-V_{O}^{\bullet\bullet})^{\bullet}$ , under partially hydrated situations. The overall effect of such repulsion is less proton trapping near isolated acceptors having a negative charge, positively effecting long range transport of protons. This phenomenon is shown graphically in Figure 2.5.

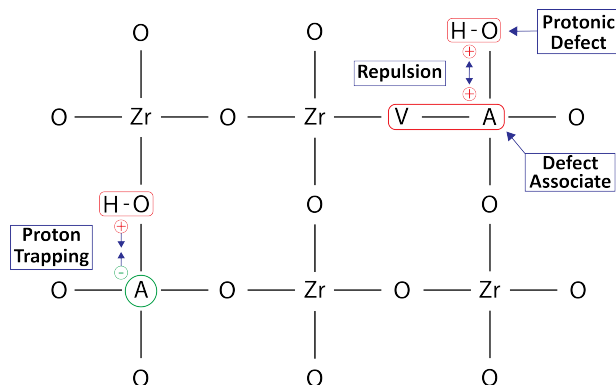


Figure 2.5 Schematic showing  $\text{OH}_\text{O}^\bullet$  trapping near isolated acceptors and  $\text{OH}_\text{O}^\bullet$  repulsion by defect associates.

The use of transition metal (TM) sintering aids to lower sintering temperature introduces additional acceptors, of which Ni has been shown to be very effective in BZY when combined with SSRS. Ni is incorporated by superstoichiometric<sup>1</sup> NiO additions to, or stoichiometric Ni substitution with, the other precursors before SSRS. In NiO, the Ni exists in a 2+ oxidation state and has two unpaired electrons. This useful property makes estimations of the valence state of this TM sintering aid possible with magnetic susceptibility measurements because all other BZY constituents are diamagnetic, i.e., no unpaired electrons.

NiO is a strongly antiferromagnetic material, however, isolated  $\text{Ni}^{2+}$  in the BZY lattice would just be paramagnetic. Similarly, isolated  $\text{Ni}^{3+}$  in the BZY lattice would also display paramagnetism. Most studies including Ni sintering aids with BZY processing take the assumption that it remains in the ideal 2+ oxidation state, however, one could postulate that the 3+ oxidation state may be more favorable if substituting for  $\text{Zr}^{4+}$  in the perovskite lattice. To the authors best knowledge, only one study experimentally determined the effective oxidation state of Ni when NiO is added superstoichiometrically to BZY during processing.[134] They used synchrotron X-ray absorption fine structure of the Ni *K*-edge to estimate an oxidation state of 2.80–2.89, dependant on sintering temperature

<sup>1</sup>Superstoichiometric refers to having a greater than stoichiometric ratio in the chemical formula, i.e., the BZY elements exist in a stoichiometric ratio and NiO elements are present in excess.

for 1 wt% NiO additions (the typical concentration used in BZY). Furthermore, the authors determined Ba-deficiency around the Ni cations, indicating that Ba cations were driven to the grain boundary due to Ni residing in the  $(1/2, 0, 0)$  octahedral interstice.

Extensive studies aimed at determining the influence of sintering aids on BZY-based PCFC performance have been performed, summarized in multiple recent review articles.[46, 135–139] Many sintering aids have been explored, some of which enhanced sinterability, resulting in improved total conductivity by the existence of larger grains (less blocking GBs). However, for comparable BZY grain sizes, the use of a sintering aid, in general, has a deleterious effect on electrochemical performance.[139] The most promising method to mitigate the negative effects of the Ni sintering aid specifically, is through the SSRS method, which not only produces large-grain BZY, but increases the total conductivity (suggesting partial change of charge carriers).[59] Huang et al. intentionally compared NiO additions with Ni substitution for Zr in BZY.[65] They found that substitution results in significantly higher proton uptake than the addition approach, however, the amount of Ni should be minimized because it may decrease effective  $Y'_{Zr}$  concentration in the bulk if a residual BYN phase is formed during sintering. Unfortunately, the authors observed more negative enthalpies and entropies of hydration when Ni is substituted, which can be explained by trapping of protons (Figure 2.5).

## 2.2 Electronic Magnetism

Magnetism originates from angular momentum of elementary particles, therefore the quantum theory of magnetism is connected to quantization of such angular momentum. Electrons, protons, and neutrons possess intrinsic angular momentum  $\frac{1}{2}\hbar$  called spin. Nuclear spin creates significantly smaller magnetic moments than electron spin due to a much greater nucleon mass ( $\approx 1.67 \times 10^{-27}$  kg) and in practice can be neglected, leaving electrons as the particles of interest when studying magnetism in solids.[116]

Briefly, the quantum mechanics of a single electron in a potential, leads to electronic states being classified in terms of four quantum numbers:  $n, l, m_l, M_s$ . A single electron

has intrinsic spin angular momentum with quantum number  $M_S = \frac{1}{2}$ . Conventionally, the lower-case letters  $l$ ,  $s$ , and  $j$  denote quantum numbers of a single electron, while the upper-case letters  $S$ ,  $L$ , and  $J$  are used for multielectron atoms. The effective spin and orbital angular momenta in an isolated many electron ion are coupled to give total spin and orbital quantum numbers  $S$  and  $L$ . The energy levels are split by spin orbit coupling into a series of  $J$ -multiplets ( $|L - S| \leq J \leq L + S$ ), of which the ground state is specified by Hund's rules. When placed in a solid, the ion experiences an electrostatic potential called the crystal field, where this potential surrounding the ion disturbs the spin-orbit coupling, leaving either  $S$  or  $J$  as the appropriate quantum number. The crystal field modifies the structure of the lowest magnetic sub levels which are split by the Zeeman interaction and introduces single-ion anisotropy (more on this in the last section of this chapter).[116]

Many transition metal ions and rare-earth ions will have incomplete  $3d$ - and  $4f$ -shells respectively, therefore a net magnetic moment due to non-cancellation of the spin and orbital components of angular momentum is observed. From quantum mechanics, the effective magnetic moment  $\mu$  of an ion with such incomplete shells is calculated from  $J$ , the total angular momentum quantum number:

$$\mu = g\mu_B\sqrt{J(J+1)} \quad (2.10)$$

where the Bohr magneton  $\mu_B = 9.274 \times 10^{-24} \text{ A m}^2$  is the magnetic moment of a single isolated electron and the dimensionless Landé  $g$ -factor is:

$$g = \frac{3}{2} + \frac{(S(S+1) - L(L+1))}{2J(J+1)} \quad (2.11)$$

For  $3d$ -ions, the orbital contribution to the effective moment appears to be quenched by the crystal field and the magnetism for this series of ions appears entirely due to the spin contribution.[116] This is not the case for  $4f$ -ions, where the electrons are partially shielded from the crystal field by an outer shell and contributions to the magnetic moment arise from both  $S$  and  $L$ . Table 2.1 compares effective magnetic moments of  $3d$ -ions calculated using  $J$  and  $S$ , then compares them to experimental values. Generally,  $3d$ -electrons are

delocalized in metals, but usually localized in oxides and other ionic compounds, where the most common coordinations are six-fold (octahedral), or four-fold (tetrahedral).

Table 2.1 Selected  $3d$  transition metal cations and corresponding  $S, L, J$ , and  $g$  values, as well as, the theoretical moments  $\mu(J)$  and  $\mu(S)$  calculated from total or spin-only angular momentum numbers, respectively. Experimental values measured on dilute magnetic salts show the orbital contribution of the moment is quenched by the crystal field, and the measured moment mostly comes from spin contributions.[116]

$3d^n$	Ion	$S$	$L$	$J$	$g$	$\mu(J)$	$\mu(S)$	Expt.
1	Ti <sup>3+</sup> V <sup>4+</sup>	$\frac{1}{2}$	2	$\frac{3}{2}$	$\frac{4}{5}$	1.55	1.73	1.7
2	Ti <sup>2+</sup> V <sup>3+</sup>	1	3	2	$\frac{2}{3}$	1.63	2.83	2.8
3	V <sup>2+</sup> Cr <sup>3+</sup>	$\frac{3}{2}$	3	$\frac{3}{2}$	$\frac{2}{5}$	0.78	3.87	3.8
4	Cr <sup>2+</sup> Mn <sup>3+</sup>	2	2	0	—	—	4.90	4.9
5	Mn <sup>2+</sup> Fe <sup>3+</sup>	$\frac{5}{2}$	0	$\frac{5}{2}$	2	5.92	5.92	5.9
6	Fe <sup>2+</sup> Co <sup>3+</sup>	2	2	4	$\frac{3}{2}$	6.71	4.90	5.4
7	Co <sup>2+</sup> Ni <sup>3+</sup>	$\frac{3}{2}$	3	$\frac{9}{2}$	$\frac{4}{3}$	6.63	3.87	4.8
8	Ni <sup>2+</sup>	1	3	4	$\frac{5}{4}$	5.59	2.83	3.2
9	Cu <sup>2+</sup>	$\frac{1}{2}$	2	$\frac{5}{2}$	$\frac{6}{5}$	3.55	1.73	1.9

A  $3d$ -ion in octahedral oxygen coordination has  $3d$ -orbitals that overlap with the oxygen  $2p$ -orbitals and form a partially covalent bond. Because of their orientation, the overlap is greater for  $e_g$ -orbitals (2-fold degenerate with symmetric wave function) than  $t_{2g}$ -orbitals (3-fold degenerate with symmetric wave function and diagonal mirror planes). This overlap leads to mixed wavefunctions, producing bonding and antibonding orbitals, whose splitting increases with overlap. The  $3d$ -states usually lie higher in energy than the  $2p$ -states in oxides, so the hybridized orbitals with mainly  $2p$  character are bonding and those with mainly  $3d$  character are antibonding.

In some cases, the ligands create such intense crystal fields that the ion can be driven into a low spin state. The on-site Coulomb interaction raises the energy of doubly occupied orbitals by  $U$ , compared to singly occupied orbitals (an electrostatic penalty). When  $U$  exceeds the crystal field splitting of the one electron levels, Hund's first rule applies (maximize  $S$ ), but when  $U$  is less than the splitting, the  $t_{2g}$ -orbitals for an octahedral site will be doubly occupied. Table 2.2 shows the number of unpaired electrons for  $3d$ -ions in an octahedral coordination with high-spin and low-spin values for relevant species.

Table 2.2 Number of unpaired electrons is listed for  $3d$ -ions in octahedral coordination. Two values are given for typical high-spin and low-spin configurations.[116]

$3d^n$	Ion	Unpaired Electrons
1	Ti <sup>3+</sup> V <sup>4+</sup>	1
2	Ti <sup>2+</sup> V <sup>3+</sup>	2
3	V <sup>2+</sup> Cr <sup>3+</sup>	3
4	Cr <sup>2+</sup> Mn <sup>3+</sup>	4(high), 2(low)
5	Mn <sup>2+</sup> Fe <sup>3+</sup>	5(high), 1(low)
6	Fe <sup>2+</sup> Co <sup>3+</sup>	4(high), 0(low)
7	Co <sup>2+</sup> Ni <sup>3+</sup>	3(high), 1(low)
8	Ni <sup>2+</sup>	2
9	Cu <sup>2+</sup>	1

The categories of magnetic materials relative to this thesis are diamagnetic, paramagnetic, antiferromagnetic, and ferromagnetic. Other classifications of magnetic materials exist, however, those won't be discussed in this work. Studying magnetic properties in the solid-state implies perusal of substance specific interactions between electrons associated with neighboring species, and consequently magnetization of different material classes under applied magnetic fields and temperature regimes differs significantly. Familiarity with such differences instills intuition that can aid interpretation of magnetometry data. This is particularly useful when characterizing a new material.

### 2.2.1 Diamagnetism

The weakest phenomenon, diamagnetism, is present in all materials and magnetic response opposes the direction of applied magnetic field. This occurs when electrons making up closed shells have spin and orbital moments oriented so there is no net moment. The process of bonding in ionic solids involves transfer of electrons from a cation to an anion, and in many cases, produces closed shells that are diamagnetic. Covalent bonding through sharing of electrons can also lead to closed shells and diamagnetism.

Diamagnetic response to an applied magnetic field is very weak and only requires consideration when quantitative analysis of a weak magnetization of similar magnitude is necessary. This is relevant when a diamagnetic material contains dilute concentrations of magnetic species, a small fraction of magnetic secondary phase, or a very small volume of magnetic material is deposited on a diamagnetic substrate. The first point qualifies much of the work in this thesis to undergo such consideration because of small concentrations of magnetic cations doped into diamagnetic lattices. Diamagnetic mass susceptibilities of cations relative to this work are shown in Table 2.3.

Table 2.3 Diamagnetic mass susceptibilities ( $\chi$ ) of ions relative to this thesis.[116]

Ion	$\chi(10^{-9} \text{ m}^3 \text{ kg}^{-1})$
Ba <sup>2+</sup>	2.9
Sr <sup>2+</sup>	2.1
Zr <sup>4+</sup>	1.4
Ti <sup>4+</sup>	1.3
Y <sup>3+</sup>	1.8
O <sup>2-</sup>	9.4

### 2.2.2 Paramagnetism

This section begins with the classical Curie description of paramagnetism for a single unpaired electron system. Next, the Langevin classical theory of paramagnetism for multielectron systems is introduced, and then concludes with the Brillouin quantum theory

of paramagnetism for multielectron systems. Unpaired electron spins in a partially filled orbital produce paramagnetism, of which two extremes exist: localized electrons and delocalized electrons. The former is the subject of interest in this thesis due to the electronically insulating nature of the materials studied, therefore the latter is omitted.

The classical Curie description of paramagnetism begins with an ensemble of single localized electron spins placed in a magnetic field along the positive z-direction. The spin up  $|\uparrow\rangle$  and spin down  $|\downarrow\rangle$  states are split by  $\approx 2\mu_B B$ , where  $B$  is the scalar magnetic field. The Boltzmann population of the  $|\uparrow\rangle$  state relative to the  $|\downarrow\rangle$  state increases with increasing field. These populations are  $n^\uparrow$  and  $n^\downarrow$  respectively, and the concentration of electrons per unit volume is then  $n = (n^\uparrow + n^\downarrow)$ . These populations are proportional to

$$\exp\left(\frac{\pm\mu_B B}{k_B T}\right) \quad (2.12)$$

and the induced magnetization along the z-axis is  $(n^\uparrow - n^\downarrow)\mu_B$ . The average z-component of the moment per atom  $\langle\mu_z\rangle = (n^\uparrow - n^\downarrow)\mu_B/(n^\uparrow + n^\downarrow)$  is then

$$\langle\mu_z\rangle = \frac{[\exp(x) - \exp(-x)]\mu_B}{\exp(x) + \exp(-x)} \quad (2.13)$$

where  $x = \mu_B B/k_B T$ , and the resulting magnetic moment  $\mu$  is

$$\mu = n\mu_B \tanh(x). \quad (2.14)$$

At room temperature,  $x$  is small because  $\mu_B B \ll k_B T$ , giving the approximation  $\tanh(x) \approx x$ . This produces the classical Curie-law expression for paramagnetic susceptibility  $\chi = \mu_0 M/B$ :

$$\chi = \frac{n\mu_0\mu_B^2}{k_B T}. \quad (2.15)$$

The classical Langevin description of paramagnetism in the general multielectron atom case was worked out by Paul Langevin in 1905.[116] Non-interacting species with a magnetic moment  $\mu$  can take any orientation  $\theta$  relative to a magnetic field  $H = \mathbf{B}/\mu_0$

applied in the z-direction. The Zeeman energy  $\varepsilon$  is then

$$\varepsilon(\theta) = -\boldsymbol{\mu} \cdot \mathbf{B} = -\mu_0 \mu H \cos \theta \quad (2.16)$$

and the probability  $P(\theta)$  of the moment taking an angle  $\theta$  with the applied field is the product of a Boltzmann factor and the geometric factor  $2\pi \sin \theta$ :

$$P(\theta) = C 2\pi \sin \theta \exp\left(\frac{\varepsilon(\theta)}{k_B T}\right). \quad (2.17)$$

The number of atoms in the system  $N$  determines the constant  $C$  through the normalization condition  $\int_0^\pi P(\theta) d\theta = N$ . The resulting average z-component of the moment per atom is  $\langle \mu_z \rangle = \mu \mathcal{L}(x)$ , where

$$\mathcal{L}(x) = (\coth(x) - 1/x) \quad (2.18)$$

is the Langevin function and  $x$  is the dimensionless ratio of magnetic energy to thermal energy  $\mu_0 \mu H / k_B T$ . At low fields or high temperatures,  $x$  is small and  $\mathcal{L} \approx x/3$ . Then the susceptibility of an ensemble of  $n$  moments per cubic meter is

$$\chi = \frac{\mu_0 n \mu^2}{3 k_B T}. \quad (2.19)$$

At high fields,  $x \gg 1$ , the magnetization saturates and all of the moments align. In this high field limit, the Langevin function is  $\mathcal{L} \approx 1 - 1/x$ .

The quantum description of paramagnetism for multielectron atoms was formalized by the French physicist Leon Brillouin. The theory begins with the thermodynamic average  $\langle \mu_z \rangle$  of i-magnetic states, weighted by their Boltzmann populations:

$$\langle \mu_z \rangle = \frac{\sum_i \mu_i \exp(-\varepsilon_i / k_B T)}{\sum_i \exp(-\varepsilon_i / k_B T)} \quad (2.20)$$

Now there are  $2J + 1$  energy levels  $\varepsilon_i = +\mu_0 g \mu_B M_J H$ , with moments  $\mu_i = -g \mu_B M_J$ , where  $M_J = J, J - 1, J - 2, \dots, -J$ . To calculate the susceptibility (the initial slope of the magnetization curve), take the limit  $x \ll 1$  and expand the exponential as

$\exp(x) \approx 1 + x + \dots$  to get

$$\langle \mu_z \rangle = \frac{\sum_{-J}^J -g\mu_B M_J (1 - \mu_0 g\mu_B M_J H/k_B T)}{\sum_{-J}^J (1 - \mu_0 g\mu_B M_J H/k_B T)}. \quad (2.21)$$

Using summation identities, this reduces to

$$\langle \mu_z \rangle = \frac{\mu_0 g^2 \mu_B^2 J(J+1)H}{3k_B T}. \quad (2.22)$$

The quantity  $g\mu_B \sqrt{J(J+1)}$  can be considered the effective moment,  $\mu_{\text{eff}}$ , and now the susceptibility  $\chi = M/H$  resembles the Curie law:

$$\chi = \frac{\mu_0 n \mu_{\text{eff}}^2}{3k_B T} \quad (2.23)$$

To calculate the complete magnetization curve we write the thermodynamic average

$\langle \mu_z \rangle = \langle -g\mu_B M_J \rangle$  as

$$\langle \mu_z \rangle = g\mu_B \frac{\partial}{\partial y} \left[ \ln \sum_{-J}^J \exp(-M_J y) \right], \quad (2.24)$$

where  $y = \mu_0 g\mu_B H/k_B T$ . After evaluating the sum over the energy levels and setting  $x = Jy$  we get

$$\langle \mu_z \rangle = M_0 \left[ \frac{2J+1}{2J} \coth \frac{2J+1}{2J} x - \frac{1}{2J} \coth \frac{x}{2J} \right], \quad (2.25)$$

where  $M_0 = ng\mu_B J$  is the maximum magnitude of the moment and the quantity inside the brackets is the Brillouin function  $\mathcal{B}(x)$ . The magnetization is now written as

$$M = M_0 \mathcal{B}(x), \quad (2.26)$$

and when  $x$  is small the Brillouin function reduces to

$$\mathcal{B}(x) \approx \frac{(J+1)}{3J} x - \frac{[(J+1)^2 + J^2](J+1)}{90J^2} x^3 + \dots \quad (2.27)$$

Taking the leading term from this approximation reproduces the susceptibility in the general form of the Curie law.

This theory of localized magnetism is applicable to systems where the individual magnetic moments do not interact with each other. The magnetization response to an

applied field,  $M(H)$ , is linear except at very low temperatures or under applied fields of significant magnitude. Under such conditions the magnetic energy overcomes the thermal energy and the moments saturate with the field. The accuracy of this theory is illustrated by the fact that magnetization data (for a homogeneous spin system) taken at different temperatures superimpose on a single Brillouin curve if plotted as a function of  $H/T$ . [116]

### 2.2.3 Ferromagnetism

Ferromagnetism in a solid is described by spontaneous cooperative magnetization, which is caused by the alignment of individual magnetic moments in a periodic atomic lattice. Pierre Weiss proposed the first modern theory of ferromagnetism in 1906 based on the classical paramagnetism described by Langevin. [116] He extended the concept to the general Brillouin theory of localized moments and conceptualized an internal 'molecular field'  $H^i$  that is proportional to the magnetization of the ferromagnet:

$$H^i = n_W M + H \quad (2.28)$$

Here,  $M$  is the magnetization,  $H$  is the applied magnetic field, and the Weiss coefficient is  $n_W$ . The magnetization is given by the same function as 2.17, but now

$$x = \mu_0 g \mu_B J (n_W M + H) / k_B T:$$

$$M = M_0 \mathcal{B}(x) \quad (2.29)$$

Under zero applied field,  $M$  is just the spontaneous magnetization  $M_s$  and we have

$$\frac{M_s}{M_0} = \mathcal{B}(x_0), \quad (2.30)$$

where  $x_0 = \mu_0 g \mu_B J n_W M_s / k_B T$ . Then  $x_0$  can be combined with  $M_0$  to get

$$\frac{M_s}{M_0} = x_0 \left( \frac{n k_B T}{\mu_0 M_0^2 n_W} \right). \quad (2.31)$$

The simultaneous solution of the two previous equations can be solved graphically or numerically and the collapse of the spontaneous magnetization occurs when the material is heated above a critical temperature,  $T_C$ , known as the Curie temperature. At and above

$T_C$ , the moments are completely disordered and the  $2J + 1$  energetically degenerate  $M_J$  levels are equally populated. The susceptibility is now paramagnetic, and in the small  $x$  limit, results in the Curie-Weiss law:

$$\chi = \frac{\mu_0 n \mu_{\text{eff}}^2}{3k_B(T - \theta)}. \quad (2.32)$$

In Weiss molecular field theory,  $\theta$  is equal to  $T_C$ , however, this equation is often extended to paramagnetic systems where  $\theta$  is used as a measure of the effective interaction between paramagnetic moments. Here, a positive  $\theta$  corresponds to ferromagnetic alignment (parallel), and a negative  $\theta$  corresponds to antiferromagnetic alignment (antiparallel). More complex and accurate theories on ferromagnetism exist, however, going into such detail is unnecessary for this thesis and the interested reader is suggested to explore chapter five of Coey's magnetic materials textbook.[116]

#### 2.2.4 Antiferromagnetism

Antiferromagnetic materials have structures with two or more equal but oppositely oriented magnetic sublattices such that the net magnetization is zero. In 1936 a student of Pierre Weiss named Louis Néel first proposed this mechanism and adopted Weiss molecular field theory as the framework.[116] Néel antiferromagnets with two oppositely oriented magnetic sublattices:  $M_A = -M_B$ . There is a Weiss coefficient  $n_{AB}$  representing intersublattice molecular field coupling and is negative. Another coefficient  $n_{AA}$  is included for intrasublattice molecular field interactions. Similar to Weiss molecular field theory discussed previously, there are molecular fields  $H_\alpha^i$  acting on each sublattice:

$$\begin{aligned} H_A^i &= n_{AA}M_A + n_{AB}M_B + H \\ H_B^i &= n_{BA}M_A + n_{BB}M_B + H \end{aligned} \quad (2.33)$$

Here,  $H$  is the external applied field,  $n_{AA} = n_{BB}$ , and  $n_{BA} = n_{AB}$ . When  $H = 0$ , the net magnetization  $M = M_A + M_B$  also equals zero. Each sublattice spontaneous magnetization

is represented by a Brillouin function:

$$M_\alpha = M_{\alpha,0}\mathcal{B}(x_\alpha). \quad (2.34)$$

Here,  $\alpha = A$  or  $B$ ,  $x_\alpha = \mu_0\mu|H_\alpha^i|/k_B T$ , and  $M_{A,0} = -M_{B,0} = (n/2)g\mu_B J = (n/2)\mu$ . There are  $n/2$  magnetic ions on each sublattice, with a total of  $n$  magnetic ions per unit volume.

Similar to the Curie transition temperature for ferromagnets, there is a transition temperature,  $T_N$ , called the Néel temperature. Above  $T_N$  the system becomes paramagnetic and the susceptibility of each sublattice is

$$\chi = M_\alpha/H_{\alpha}^i = \frac{\mu_0(n/2)\mu_{\text{eff}}^2}{3k_B T}. \quad (2.35)$$

Using the susceptibility, we can rewrite the equations for magnetization of each sublattice:

$$\begin{aligned} M_A &= \frac{\mu_0(n/2)\mu_{\text{eff}}^2}{3k_B T}(n_{AA}M_A + n_{AB}M_B + H) \\ M_B &= \frac{\mu_0(n/2)\mu_{\text{eff}}^2}{3k_B T}(n_{BA}M_A + n_{BB}M_B + H) \end{aligned} \quad (2.36)$$

These equations have a nonzero solution in zero applied field, providing the conditions for spontaneous magnetization. The determinant of the coefficients of  $M_A$  and  $M_B$  must equal zero:

$$\left[ \frac{\mu_0(n/2)\mu_{\text{eff}}^2}{3k_B T}n_{AA} - 1 \right]^2 - \left[ \frac{\mu_0(n/2)\mu_{\text{eff}}^2}{3k_B T}n_{AB} \right]^2 = 0 \quad (2.37)$$

This requirement yields the Néel temperature

$$T_N = \frac{\mu_0(n/2)\mu_{\text{eff}}^2}{3k_B}(n_{AA} - n_{AB}), \quad (2.38)$$

where  $T_N$  is positive and  $n_{AB}$  is negative. The overall susceptibility above  $T_N$  uses the addition of the magnetization of both sublattices and produces the Curie-Weiss law:

$$\chi = \frac{(M_A + M_B)}{H} = \frac{\mu_0 n \mu_{\text{eff}}^2}{3k_B(T - \theta)}. \quad (2.39)$$

For antiferromagnets, the reciprocal susceptibility above  $T_N$  is plotted, then  $\theta$  is determined by linear extrapolation to the temperature axis intercept, and  $\mu_{\text{eff}}$  is obtained

from the slope. With knowledge of  $T_N$  and  $\theta$ , both  $n_{AA}$  and  $n_{AB}$  can be evaluated.

## 2.3 Magnetometry Applications

“The electromagnetic forces arising from electron spin are far too weak to be responsible for chemical bonding... yet electron spin lies at the heart of chemistry” – J. H. Van Vleck.

### 2.3.1 Historical Examples

Electron spin has been used as the indicator of valence behavior for over a century, and magnetic measurements have found utility in a very diverse range of disciplines. As early as the 1930's, magnetic measurements were used in biology to study ferro-haemoglobin that exhibits high- or low-spin states in the presence of  $H_2O$  and  $O_2$ , respectively.[140] Since the 1950's, magnetic methods have been used to estimate particle sizes of ferromagnetic and antiferromagnetic catalyst particles, as well as, determination of the nature and number of active paramagnetic sites in the study of chemisorption.[141] In the 1990's, some authors relied upon magnetic characterization to track percolation threshold and particle sizes of Ni composited with  $Al_2O_3$  to optimize mechanical properties.[142, 143] There has been, and still is, extensive use of magnetic characterization to study materials displaying bulk ordered magnetism, superconductivity, or other exotic magnetic phenomena. However, the focus of the current work is to study TM-dopants in solid electrolytes, so particular emphasis of this background section will be given to notable examples in the field of electrochemistry.

In the 1950's Selwood and coworkers measured magnetization of supported Ni catalysts and found that highly dispersed Ni particles show a change in magnetization upon exposure to gases adsorbed on surfaces.[144, 145] Shortly after in 1961, Rymer et al. characterized NiO catalysts supported on alumina and silica, showing that Ni is present in the 2+ oxidation state.[146] Then in 1966 Carter et al. used magnetization measurements to estimate crystallite sizes of supported Ni catalysts, and found that the catalytic activity per unit surface area of the Ni decreased with increased crystallite size.[147]

Voorhoeve reviewed relationships between TM catalysts and magnetism in 1974, and discussed the possibility of magnetic ordering and spin waves playing a role in the elementary steps of chemical reactions.[141] A few years later, Richardson reviewed characterization of TM catalysts with magnetic measurements. The overall emphasis was on measurements of crystallite size distributions and identification of chemisorption bond type, and concluded that unpaired electrons not only makes magnetic characterization possible, but enables the TM to form chemisorption bonds and exchange electrons in redox reactions.[148]

Banerjee and Sen used magnetic measurements to characterize impregnated Ni/Al<sub>2</sub>O<sub>3</sub> catalyst system with varying Ni content.[149] At low nickel concentration, NiO ensembles appeared to be bound to alumina by orbital angular moments. The unpaired 3*d*-electrons of Ni<sup>2+</sup> are stabilized by vacant *p*-orbitals of Al<sup>3+</sup>. As the Ni content increased, antiferromagnetism developed with the appearance of a Néel point ( $T_N$ ), negative Weiss constant ( $\theta$ ), and spin compensation. At higher Ni concentrations, magnetic moments increased slightly due to overcoming of the influence of the support and suggests the formation of NiO multilayers. Changes in magnetic susceptibility were measured over time during reduction above the Curie temperature of Ni. The susceptibility rose continuously for ten minutes, then decreased for approximately two minutes. The authors concluded that the increase was caused by formation of Ni nuclei, and the subsequent decrease happened when the unpaired electrons began to delocalize in the conduction band of aggregated nuclei.

Catalytic activity depends on the valence, location, dispersion, and concentration of the catalyst, but such information is hard to obtain when concentrations are low. Dutta et al. doped 0.2 wt% and 1.75 wt% Ni in silicoaluminophosphate and leveraged the sensitivity of modern magnetometers to provide insight on the dilute catalyst.[150] They estimated Ni metal particle sizes based on blocking temperature of superparamagnetic behavior and observed positive Weiss constants ( $\theta$ ), which indicated slight ferromagnetic exchange

between the remaining paramagnetic Ni cations.

Señarís-Rodríguez et al. prepared polycrystalline  $\text{LiNi}_{1-y}\text{Co}_y\text{O}_2$  battery cathode materials with nanometer scale particles using low-temperature sol-gel method.[151] XRD indicated single phase for  $0.2 < y < 1$  with ordered distribution of Li and Ni/Co in the layered structure, however, this technique only provides averaged structural information and the possibility of local disorder still exists, which could effect electrochemical behavior. Fourier transform infrared spectroscopy revealed a slight deviation from linear behavior for the Li-O band with high Ni content. Magnetic susceptibility and magnetization measurements revealed the presence of some  $\text{Ni}^{2+}$  occupying  $\text{Li}^+$  places, leading the formation of small ferromagnetic islands. Additionally, magnetization results estimated that the size of the nanoscale magnetic inhomogeneities decreases upon Co-doping, confirming the addition of  $\text{Co}^{3+}$  inhibits the presence of interlayer  $\text{Ni}^{2+}$ .

Schaniel et al. doped strontium barium niobate with small amounts of Ce and Cr, then studied valence and concentration of the dopants with magnetometry.[152] Doping with rare-earths enhances photorefractive properties and is used to tune the crystals for optical applications. The magnetic properties were investigated to determine the concentration of  $\text{Ce}^{3+}$  and  $\text{Cr}^{3+}$  because knowledge of the concentration of charge carriers is of importance for phenomena dependent on photoinduced charge transport. In SBN the dopants act as photorefractive centers so that the valence state is changed from 3+ to 4+ by light-induced excitation of free electrons, or from 4+ to 3+ by trapping electrons. Knowledge of the respective concentration of each oxidation state enables understanding of the kinetics and steady state properties of the resulting space charge fields, which modulate the refractive index via the electro-optic effect. Fits of magnetization data to Brillouin functions were used to determine the  $g$ -values and concentration of the dopant cations. These fits were done at multiple temperatures to ensure the values were extracted independently. The concentrations were compared to X-ray fluorescence and instrumental neutron activation analysis where the total number density of dopants was previously obtained, enabling the

additional concentration of dopants in states other than 3+. Analysis of the dynamic susceptibility (AC) indicated a distribution of spin-lattice relaxation times is involved in the spin-lattice relaxation process. This is explained by the fact that the Ce occupies the off-center Sr position in the lattice. Therefore every Ce exists in a slightly different environment, leading to different level splitting and influences relaxation time distributions. Cr occupies the Nb position and does not exhibit a frequency dependence due to much less disorder at this octahedral site in the SBN lattice.

Magnetometry was used to track the size distribution of pulsed laser deposited Ni nanoparticles in layered YSZ by Abiade et al.[153] As the laser ablation time increased, the size of the nanoparticles grew, and a corresponding transition from superparamagnetic response to ferromagnetic response was observed. A few years later, magnetometry experiments on Ni-doped YSZ were performed by White et al. .[154] The authors leveraged the high-vacuum environment of a magnetometer sample chamber, combined with a heated sample stage, to perform *in situ* reduction of Ni-doped YSZ up to 1100 K. Above the Ni solubility limit (1.5–2 mol%), NiO was easily reduced and detected by the ferromagnetic to paramagnetic Curie transition temperature. However, when doping was below the solubility limit, reduction of the substitutional Ni<sup>2+</sup> to Ni<sup>0</sup> could not be achieved in high-vacuum atmosphere and an *ex situ* H<sub>2</sub> reducing atmosphere was required during heating. After heat treating in the reducing environment, Ni<sup>0</sup> nanoparticles were observed at GBs in the YSZ microstructure, which indicated the GBs serve as the preferential location for internal reduction of the Ni dopant to occur.

Morrisey et al. used magnetometry to study the solubility of Ni in YSZ with different grain sizes.[155] The solubility of Ni in YSZ increases dramatically when the YSZ grain size is on the order of several nanometers.[154, 156] It was determined through magnetometry that a large amount of Ni<sup>2+</sup> may be segregated at surfaces and GBs in nanometer sized YSZ, but upon grain growth, precipitation of NiO phase occurs for the same concentration. Morrisey et al. also used magnetometry to track redox cycling of Ni<sup>2+</sup> in YSZ.[157] For

0.5 mol% Ni-doping, the  $\text{Ni}^{2+}$  was in solution or segregated at surfaces and GBs, then precipitated as  $\text{Ni}^0$  at pores, GBs, and grain interiors after heat treatment in a reducing environment. Upon heat treatment in an oxidizing atmosphere,  $\text{Ni}^{2+}$  forms, but the distribution of ions is not the same as the original microstructure, i.e., NiO formed and then after an additional reduction treatment, a different distribution of  $\text{Ni}^0$  formed. This demonstrated that particular nanoscale composites of Ni-YSZ can be selectively engineered by redox cycles, as well as, the utility of magnetometry to track the state of the Ni dopant.

## 2.4 Electron Paramagnetic Resonance

This section will introduce electron paramagnetic resonance (EPR), which may also be referred to as electron spin resonance (ESR). This spectroscopic technique can be used to study paramagnetic centers in various oxide systems. These centers can include surface defects, organic or inorganic radicals, metal cations or supported metal complexes and clusters. Each paramagnetic center will produce a characteristic spectrum that can be described by well-defined spin Hamiltonian parameters, and reveal perturbations caused by interactions with its local environment. Therefore, the experimental spectrum must be interpreted with careful consideration of possible variables and if possible, measure the spectra under a variety of conditions. For the most accurate analysis of spin Hamiltonian parameters, those determined from an experimental spectrum should be compared to those obtained from a simulated spectrum by theoretical treatment, ideally resulting in a complete description of the electronic structure of the paramagnetic species.

A complete description of the theoretical background is beyond the scope of this writing, so the interested reader is referred to the monumental text by Abragam and Bleaney.[158] Additionally, various authors have summarized EPR applications in electrochemistry and TM oxides over the decades.[159–162] This background section will only describe the resonance phenomenon at an introductory level, which provides sufficient information for interpretation of the experimental results shown.

### 2.4.1 Zeeman Interaction

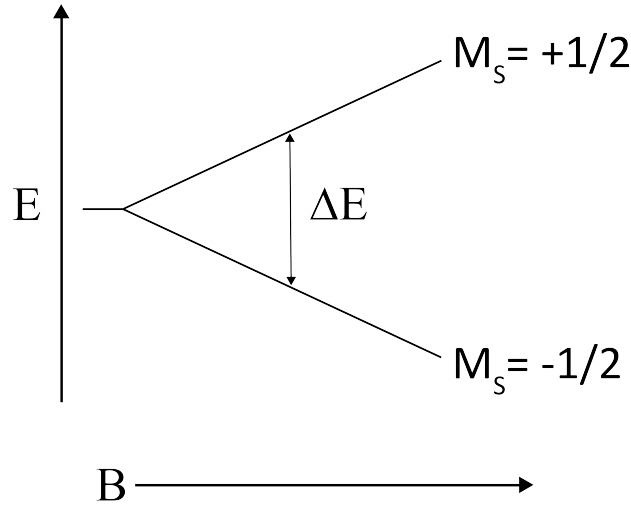


Figure 2.6 Zeeman split energy levels for a single, free electron in an applied magnetic field  $B$ .

Consider a free electron in an external magnetic field,  $\mathbf{B}$ , applied along the  $z$ -direction. The Hamiltonian describing this Zeeman interaction of the electron with the field is:

$$\hat{H}_Z = g_e \mu_B \mathbf{S}_z \cdot \mathbf{B}. \quad (2.40)$$

Here  $g_e$  is the free electron  $g$ -factor ( $g_e = 2.0023$ )[116],  $\mu_B$  is the usual Bohr magneton value, and  $\mathbf{S}_z$  is the spin operator.  $\mathbf{S}_z$  in the above equation can be replaced by the spin quantum number,  $M_S = \pm \frac{1}{2}$ , which only has two possible states for a single electron. Then the energy of each level is:

$$E = \pm \frac{1}{2} g_e \mu_B B. \quad (2.41)$$

In the absence of a magnetic field these two levels are degenerate, however, as the magnitude of  $B$  increases from zero, degeneracy between the levels is lifted linearly.[116] This is schematically shown in Figure 2.6. Separation of the two levels can be quantified through the Bohr frequency relation:

$$\Delta E = h\nu = g_e \mu_B B. \quad (2.42)$$

Transitions from the lower level to the higher level are made possible based on the above relation. The experiment is most typically done by applying a constant frequency ( $\nu$ ) and sweeping the applied magnetic field. For transitions occurring around the free electron value  $g \approx 2$ , the magnetic field is swept around 340 mT, while a constant frequency in the microwave region is applied ( $\nu \approx 9\text{--}10$  GHz). These experimental conditions are known as X-band, and are the most common due to the relative ease to obtain magnetic fields of hundreds of mT with laboratory scale electromagnets.

The population difference between each  $M_S = \pm\frac{1}{2}$  energy level at equilibrium is determined by the Maxwell-Boltzman relation:

$$\frac{n_+}{n_-} = \exp\left(\frac{-\Delta E}{k_B T}\right). \quad (2.43)$$

Here  $k_B$  is the usual Boltzmann constant,  $T$  is absolute temperature,  $n_+$  is the population of the upper level, and  $n_-$  is the population of the lower level. For applied fields in the 300 mT range and temperature at 298 K, a slight excess in the lower level ( $n_+/n_- = 0.9986$ ) allows net absorption to occur.

## 2.4.2 Hyperfine Interaction

The interaction of an electron with the applied field is just the foundation of EPR. Nuclei with an uneven number of neutrons and protons have a spin angular momentum. The nucleus spin also interacts with the external magnetic field and an analogous Zeeman splitting occurs. An additional interaction between the electron spin and nuclear spin is now present and is known as the hyperfine interaction. Extending the simple model system of the free electron above, consider the addition of a single nuclear spin ( $I = \frac{1}{2}$ ). In an applied magnetic field the simplified Hamiltonian for the two-spin system now has three terms:

$$H = H_{SZ} - H_{IZ} - H_{HF} \quad (2.44)$$

where SZ indicate the electron spin Zeeman interaction, IZ indicates the nuclear spin Zeeman interaction, and HF indicates the hyperfine interaction. Assuming the field is in

the z-direction, the  $g$  and  $a$  values (hyperfine coupling factor) are isotropic, this hamiltonian takes the form:

$$\hat{H} = g\mu_B B S_Z - g_N \mu_N B I_Z + haSI \quad (2.45)$$

where  $a$  is the isotropic hyperfine coupling in units of Hz. Only considering first order terms and the high field approximation, the SZ interaction will dominate, and the energy levels for this two-spin system are described by:

$$E(M_S, M_I) = g\mu_B B M_S - g_N \mu_N B M_I + haM_S M_I \quad (2.46)$$

Now there are four energy levels, with different possible transitions determined by the selection rules:  $\Delta M_I = 0$  and  $\Delta M_S = \pm 1$ . This is shown schematically in Figure 2.7, where the transitions induced under EPR and NMR conditions are labelled. The nuclei carry much smaller moments and resonate at relatively low frequencies compared to electrons.

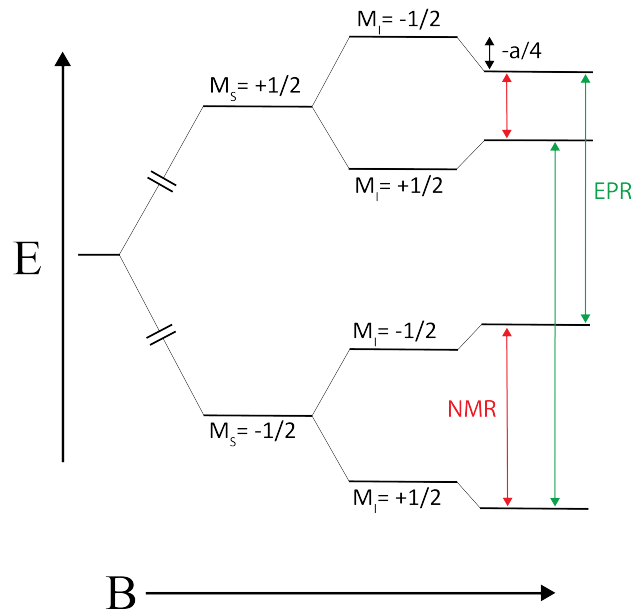


Figure 2.7 Energy level diagram for a system having one electron spin and one nuclear spin, in the high-field approximation, showing the electron Zeeman, nuclear Zeeman, and hyperfine splittings.

### 2.4.3 Zero Field Splitting

Up until now the basic theory assumed a single electron in an isotropic environment. In solid-state systems the  $g$  value is actually a tensor and represented by a  $3 \times 3$  matrix that is symmetric and has a trace of zero. When there are multiple unpaired electrons at a site in the lattice, there are also electron-electron interactions that gives rise to zero field splitting (ZFS). The electrons mutually interact to add two or more additional energy states. ZFS refers to lifting the electron energy states degeneracy, even in the absence of a magnetic field. The example for two unpaired electrons is the simplest case and will be briefly introduced.

The multiplicity of states for two unpaired electrons results in either  $S = 0$ , or  $S = 1$  state, i.e., the values of spin quantum numbers are  $M_S = 0$  or  $M_S \pm 1$ . In the absence of a magnetic field, the three levels are degenerate to first order, however, when inter-electron repulsion is considered, the three levels separate. This interaction is represented by an additional term in the Hamiltonian:

$$\hat{H}_{\text{ZFS}} = D \left( S_z^2 - \frac{1}{3} S(S+1) \right) + E (S_x^2 - S_y^2) \quad (2.47)$$

This ZFS term would be included with the electron Zeeman term introduced above when constructing the overall spin Hamiltonian. Depending on the symmetry of the crystal field at the lattice site, this ZFS term will reduce to only containing the required parameters.

For uniaxial, orthorhombic, or cubic symmetries it becomes:  $DS_z^2$ ,  $E(S_x^2 - S_y^2)$ , or  $D(S_x^4 + S_y^4 + S_z^4)$ , respectively.[116] Here, the  $D$  parameter describes the axial component of the magnetic dipole interactions between the electrons, and  $E$  the transverse component.

### 2.4.4 Relaxation Processes

Absorption of the microwave radiation is a dynamic process that equalizes the levels, however, the spin system desires to regain thermal equilibrium. In a real system, e.g., an unpaired electron on an ion in a crystal lattice, an exchange of energy between the spins and the lattice occurs. This process is known as spin-lattice relaxation, which influences

specific features of the resonance spectrum and the level of detail that can be obtained under experimental conditions of the measurement, i.e., temperature or microwave frequency.

To maintain excess populations in the lower Zeeman split energy level, the odd electrons in the upper level release a quanta of energy,  $h\nu$ , to satisfy the Maxwell-Boltzman relation and return to the lower energy level. There are two types of processes by which this can occur. The first is known as spin-lattice relaxation. The released energy is dissipated into the lattice as vibrational, translational, and rotational energy, i.e., phonons. This process is characterized by exponential decay of energy over time,  $T_{e1}$ . The second process involves an exchange of energy solely between individual spins and is known as spin-spin relaxation. This process is characterized by the time constant  $T_{e2}$ . When both processes contribute to the resonance phenomenon the resonance line width can be written as:

$$\Delta B \propto \frac{1}{T_{e1}} + \frac{1}{T_{e2}} \quad (2.48)$$

Generally  $T_{e1}$  is greater than  $T_{e2}$ , meaning  $\Delta B$  mostly depends on spin-spin relaxation processes. As spin concentration in the system decreases,  $T_{e2}$  increases, in other words, the physical distance between spins increases. Alternatively, when  $T_{e1}$  becomes very short, it can start to make more contributions to  $\Delta B$ . In some situations,  $\Delta B$  may be so large that no signal is detected. In this case, cooling the sample can increase  $T_{e1}$  because it is inversely proportional to absolute temperature. In the opposite situation when  $T_{e1}$  is too long, the electrons don't have enough time to return to the lower level and the populations tend to equalize. This decreases the resonance signal intensity and is known as saturation.

## CHAPTER 3

### EXPERIMENTAL

This chapter details the solid-state preparation of polycrystalline Fe-doped STO and Ni-doped BZY, as well as, the main characterization methods employed. STO was prepared by solid-state reaction and BZY was prepared by solid-state reactive sintering.

#### 3.1 Preparation of Iron-doped Strontium Titanate

$\text{Sr}(\text{Ti}_{1-x}\text{Fe}_x)\text{O}_{3-\delta}$  powders ( $x = 0.002, 0.005, 0.012$ ) were prepared by solid-state reaction using  $\text{SrCO}_3$  (99.9+%, Sigma Aldrich Chemie GmbH, Taufkirchen, Germany),  $\text{TiO}_2$  (99.9+%, Sigma Aldrich Chemie GmbH, Taufkirchen, Germany) and  $\text{Fe}_2\text{O}_3$  (99+%, Merck, Darmstadt, Germany) precursors. A- to B-site molar ratio was kept equal for all compositions. Zirconia milling balls with a diameter of 2 mm and 2-propanol were combined with the precursor mixtures in polyamide jars and subsequently attrition milled for 4 h at  $1000 \text{ rev min}^{-1}$ . After milling, the powders were calcined at  $975^\circ\text{C}$  for 6 h in an air furnace to remove  $\text{CO}_2$  and form  $\text{Sr}(\text{Ti}_{1-x}\text{Fe}_x)\text{O}_{3-\delta}$ . After calcination, the powders were milled again in a planetary mill with zirconia milling balls of 10 mm diameter for 16 h at  $300 \text{ rev min}^{-1}$  to break up agglomerates.

Bulk polycrystalline pellets of all three compositions were prepared by uniaxial pressing the powders into 13 mm cylindrical green bodies under 110 MPa pressure. No additives to optimize green body density were used in order to avoid introducing unnecessary impurities. Multiple pellets of each composition were prepared by placement on sacrificial powders of respective compositions on alumina plates, covered with alumina boats, and sintered in static air at  $1500^\circ\text{C}$  or  $1300^\circ\text{C}$  for approximately 20 h. Additional sample sets were prepared under flowing pure  $\text{O}_2$  at a rate of 30–50 sccm, with all other parameters the same as the air-sintered sample sets. The heating and cooling rates of all heat treatments were  $5^\circ\text{C}/\text{min}$ .

The surfaces of pellets selected for microscopy were prepared by grinding, polishing, and thermal etching at 1200 °C for 2 h. Additional pellets were ground with an agate mortar and pestle into powders for additional characterization. The remainder of the text uses shorthand notation of XFeSTO, where X is mol% of Fe in  $\text{Sr}(\text{Ti}_{1-x}\text{Fe}_x)\text{O}_{3-\delta}$ .

### 3.2 Preparation of Nickel- and Yttrium-doped Barium Zirconate

Bulk polycrystalline samples of  $\text{BaZr}_{0.8-x}\text{Y}_{0.2}\text{Ni}_x\text{O}_{3-\delta}$  (BZY20) were prepared similarly to the single step SSRS process utilized in producing the PCFCs of Duan et al., as described below.[18] The compositions of precursors were chosen such that Ni replaced Zr (i.e., Ni-substitution). The highest concentration  $x = 0.04$  (0.8 wt%) is less than the 1 wt% concentration added in the SSRS method employed by Tong et al.[59] This upper limit was chosen in an attempt to maintain single phase BZY due to the BYN phase having been previously identified via X-ray diffraction when 1 wt% or more NiO was added.[163, 164] Shorthand notation for sample referencing of XNiBZY20 is used throughout the rest of the text, where X is Ni-doping expressed as mol%.

Stoichiometric quantities of the precursor powders  $\text{BaCO}_3$  (Alfa Aesar, 99%),  $\text{ZrO}_2$  (Alfa Aesar, 99.978%),  $\text{Y}_2\text{O}_3$  (CoorsTek, 99.999%), and NiO (Alfa Aesar, 99.998%) were massed and combined with 5 mm  $\text{ZrO}_2$  media (in a 2:1 media to powder mass ratio) and ethyl alcohol (in a 1:1 ml to g ratio), then ball-milled for 48 h in polyethylene bottles. The slurry was dried in an oven for 24 h at 130 °C. The dried precursor powders were ball-milled an additional 48 h without solvent to break up agglomerated particles. The final precursor powders were uniaxially pressed into 25 mm diameter cylindrical pellets at 375 MPa. All pellets were buried in sacrificial precursor powders of the respective compositions and heated at 1500 °C for 20 h using a covered high-purity alumina boat inside a box furnace. Additionally, air-quenched XNiBZY20 pellets were prepared by replacing the final 5 °C/min cooling step with air quenching to room temperature by removing the boat from a bottom loading box furnace after 20 h at 1500 °C. Sample purity and structure was verified with powder X-ray diffraction (XRD), and investigation of

microstructural features (indicative of secondary phases not detected with XRD) with electron microscopy, as detailed at the end of this chapter.

### 3.3 Magnetometry

Magnetic properties of materials can be measured by a variety of methods depending on the size or state of the material, and the required sensitivity for detection of the magnetization response. Instruments can utilize sensing methods based on flux gate magnetometers, optically pumped magnetometers, induction coils, Hall effect and magnetoresistive magnetometers, or magneto-optical magnetometers; with sensitivities ranging from micro Tesla to pico Tesla level of resolution.[165] The most sensitive instruments utilize a superconducting quantum interference device (SQUID) to detect changes in magnetic flux.

The coexistence of two different unit systems is a common source of confusion in the realm of magnetics. The International System of Units (SI) has been generally accepted as the standard for most fields, however, magnetics has an additional commonly used system: the centimeter-gram-second (CGS) system of electromagnetic units (EMU). The EMU system introduces ambiguities and with the SI revision of 2019 the two systems are now incompatible.[166]

The CGS system has separate descriptions for magnetic and electrical units, EMU and electrostatic units (ESU) respectively. The unification of magnetic and electrical units is a major advantage for the SI formalism. The relation between magnetic flux density and magnetization in SI is  $B = \mu_0(H + M)$ , and in CGS is  $B = H + 4\pi M$ . Here  $B$  is magnetic flux density,  $\mu_0$  is the permeability of vacuum,  $H$  is applied magnetic field, and  $M$  is magnetization.

One mistake researchers often make with SI is reporting  $H$  in units of Tesla. The Tesla unit is appropriate if the applied magnetic field is instead labelled as  $\mu_0 H$ . The units for  $H$  are A/m in SI and are  $4\pi\text{Oe}$  in CGS, where A is amperes, m is meters, and Oe is oersteds. Another mistake would be to refer to the applied magnetic field as  $B$ .

When not using SI, magnetic moments are frequently expressed in units of emu. This is inappropriate because emu is not an actual unit, and the real units in the CGS system for magnetic moment are erg/G or erg/Oe. The magnetic moment in SI is reported in fundamental units of A/m<sup>2</sup>. Additionally  $M$  is often expressed with CGS units as emu/cm<sup>3</sup>, while in SI the units are A/m.

The SI revision of 2019 assigns fixed values to the Planck constant  $h$  and the elementary charge  $e$ . The speed of light  $c$ ,  $h$ ,  $e$  and the experimentally determined fine structure constant  $\alpha$  are now used to derive  $\mu_0$ :

$$\mu_0 = \frac{2h}{ce^2}\alpha \quad (3.1)$$

In CGS  $\mu_0$  remains fixed at unity, and in SI the value of  $4\pi \times 10^{-7}$  H/m to nine significant figures will change as measurements of  $\alpha$  are improved.[166] It is recommended for researchers publishing magnetometry results to utilize SI units in order to avoid incompatibility with the outdated EMU formalism.

### 3.3.1 Instrumentation

The SQUID magnetometer is based on a superconducting loop where electrons tunnel through two small insulating gaps called a Josephson junctions. A changing magnetic flux through the circuit generates a current and voltage according to Faraday's Law, where a change in the voltage is how the change in flux is monitored.[116] The magnetic flux is inductively coupled to the SQUID circuit through a superconducting input coil with additional coils above and below forming a second derivative gradiometer.[165]

The entire superconducting circuit and magnet sit inside a liquid He (4.2 K) bath in order to keep the materials below the critical superconducting temperature. This feature also allows the sample chamber to be cooled down to 1.8 K by pumping on the liquid He through a small pipe at the bottom of the chamber. Combined with heaters, the temperature can be controlled up to 400 K. The detection coils surround the sample measurement region and sit at the center of the magnet that applies a uniform magnetic

field. The magnetic moment of the sample is directly proportional to the change in detected magnetization as the sample is moved vertically through the detection circuit. A basic schematic of the magnetometer is shown in Figure 3.1.

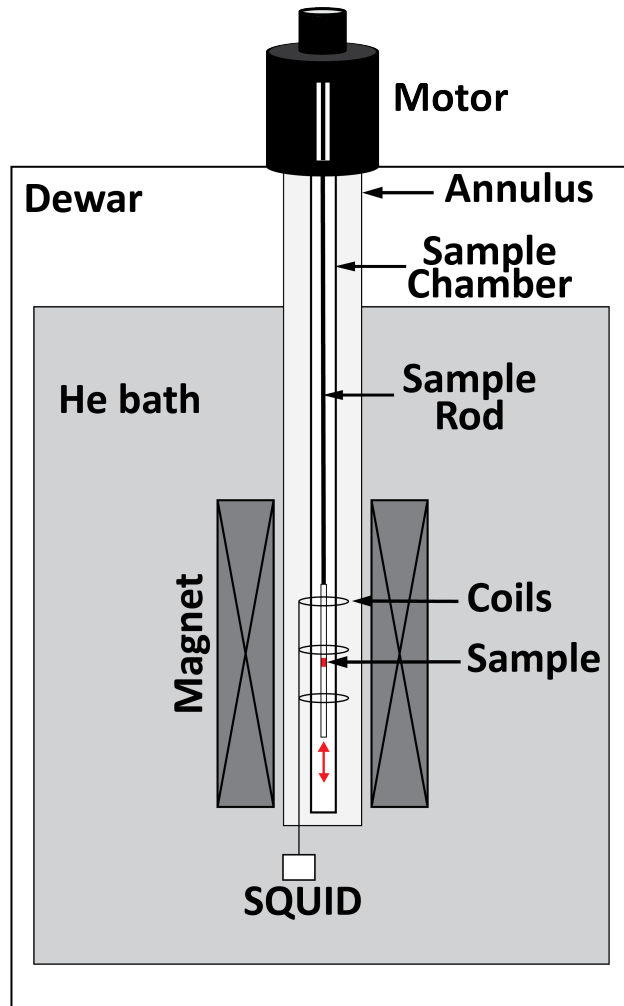


Figure 3.1 Schematic showing the general layout of a modern SQUID magnetometer. The sample is attached to the end of a long sample rod that moves through the detection coils attached to the SQUID circuitry.

### 3.3.2 Measurements

All magnetic measurements were performed in a Magnetic Property Measurement System 3 (MPMS3) (Quantum Design Inc.) SQUID magnetometer. Example sequences and data analysis scripts are available in Appendix B. The instrument was operated in DC

scan mode. All samples were finely ground into powders using a clean agate mortar and pestle, then 0.5–1 g of each were packed into gelatin capsules, inserted into clear drinking straws and attached to the end of the instrument sample rod.

For paramagnetic moments, the magnetization as a function of applied magnetic field,  $M(H)$  can be well described with the quantum theory of isolated, non-interacting moments.[116] The complete mass magnetization curve is modeled by  $M(H) = M_0\mathcal{B}(x)$ , as detailed in Chapter 2.  $M(H)$  curves up to 7 T were collected for all samples at multiple temperatures. Measurements of magnetic moment as a function of temperature were performed from 1.8 K to 300 K under 0.2 T applied magnetic field for Ni-doped BZY samples and under 1 T for Fe-doped STO samples. The effective magnetic moment per Ni,  $\mu_{\text{eff}}/\text{Ni}$ , can be estimated using the Curie-Weiss relation describing paramagnetic mass susceptibility (equation 2.15) The effective magnetic moment per magnetic ion can then be determined by linear fit to the reciprocal susceptibility data, where the slope is equal to  $1/C$  after correcting for the background diamagnetic susceptibility of the diamagnetic cations and sample holder.

The magnetization of each powder sample was normalized by sample mass. Mass was used instead of volume or molar quantities because the volume of the sample or number of magnetic species per mol were not accurately known. Magnetization per kg of sample (mass magnetization) is related to the raw magnetic moment  $\mu$  simply as  $M = \mu/\text{kg}$ . The MPMS3 outputs the magnetic moment in units of emu, which needs to be converted to SI units of  $\text{A m}^2$ . Fortunately, this is simply done during the process of converting to magnetization because  $\text{emu/g} = \text{A m}^2/\text{kg}$ , in other words, simply divide the moment in units of emu by the sample mass in grams to obtain the magnetization in SI units. Magnetization measured as a function of applied magnetic field,  $M(H)$ , is one of the standard measurement types. The MPMS3 provides the magnetic field  $H$  in units of Oe, rather than the somewhat obscure SI unit  $\text{A/m}$ . Typically, the applied field is converted to the common unit T (Tesla). The values are denoted as  $\mu_0 H$  to indicate the value refers to

the magnetic field strength outside the specimen, where  $H$  is approximately identical to  $B$ .

$M(H)$  measurements are performed at a fixed temperature of interest. The prototypical example of an  $M(H)$  measurement would be for the case of a ferromagnetic sample, which will show irreversibility (hysteresis) as the field is varied between equivalent positive and negative values. The irreversibility manifests in the zero field crossing, where a remnant magnetization exists in the absence of applied field. This leads to these types of materials being labelled permanent magnets. As the field increases (in positive or negative value) the magnetization will saturate at some field value and is called the magnetic saturation, i.e., all the individual moments are aligned. At low enough temperatures, paramagnetic materials will also saturate with applied field as long as the field is strong enough to align all the individual moments in the same direction. However, purely paramagnetic materials have moments that do not interact with each other, are reversible (no remnant magnetization), and  $M(H)$  will be linear in the absence of saturation.

Irreversibility in  $M(H)$  curves is part of a larger phenomenon often referred to history dependent behavior, meaning the value of magnetic moment observed depends on the sequence of magnetic field and temperature changes involved in the conditions of the measurement. Magnetization as a function of temperature,  $M(T)$  can also show dependence on the field history if saturation is not achieved. The common approach to determining such irreversibility is to do a set of zero-field-cooled/field-cooled (ZFC/FC) measurements. These measurements are performed by cooling the sample to the lowest measurement temperature under zero applied field, then applying the field at the lowest temperature and measuring  $M(T)$  upon heating to the highest temperature desired. The ZFC portion of the set is then followed by leaving the applied field on and cooling back down to the same lowest temperature and repeating the  $M(T)$  measurement. The ZFC/FC measurement set will show the temperature range in which the system is irreversible because there will be a bifurcation in the data as temperature decreases, which is where interaction of the individual moments begins to occur. Subsequently, the  $M(H)$  behavior

will differ above and below that bifurcation temperature. Purely paramagnetic systems will display the same  $M(T)$  behavior for ZFC and FC measurements.

$M(H)$  response of antiferromagnetic systems will resemble that of a paramagnet due to the antiparallel alignment of individual moments in a periodic manner. The magnetization will not saturate under fields produced in the typical laboratory magnetometer, because there will always be some moments opposing the direction of the field and negate the magnetization. The temperature dependence of an antiferromagnet will resemble a paramagnet above the Néel temperature, where thermal energy disrupts the long range antiparallel ordering of moments. Below this temperature, the system will display a decreasing magnetic moment with decreasing temperature as the effects of antiparallel ordering become stronger. A perfect antiferromagnetic material would then be expected to have zero magnetic moment at absolute zero temperature, however, this is type of ideal material could not exist in reality since there are always going to be some individual moments that are uncompensated in the presence of defects, surfaces, interfaces, etc.

When initiating magnetic characterization of a new material, it is advisable to first determine the temperature dependence as discussed above. First, a ZFC  $M(T)$  curve should be measured under a low magnetic field ( $\approx 0.01$  T) to avoid saturation across the entire temperature range available in the magnetometer. Additional ZFC curves under subsequently higher magnetic fields can be measured across the same temperature range, and saturation effects will be distinguishable if the curves get closer together below the temperature that saturation is occurring. In other words, if an  $M(H)$  curve is linear at a given temperature, then the  $M(T)$  curves will be evenly spaced at that temperature; if an  $M(H)$  curve saturates at a given temperature, then then  $M(T)$  curves will get closer together at that temperature. After temperature dependence is determined, then additional detailed measurements of history dependence with ZFC/FC sets, as well as, field dependence at specific temperatures, can be efficiently explored.

### 3.4 Electron Paramagnetic Resonance

X-band EPR spectroscopy was performed in a Bruker ELEXSYS E-500 continuous wave spectrometer on all 1.2FeSTO samples and just one 4NiBZY20 sample. All samples measured by EPR were finely ground into powders and loaded into 4 mm quartz tubes. Measurements of 1.2FeSTO samples were field swept from 50 mT to 450 mT, while the 4NiBZY20 sample was field swept from 235 mT to 435 mT. EPR standards were not added for field or spin concentration calibrations for any measurements, so the absolute resonance fields reported are only close estimates, and spectra were qualitatively used to identify resonant species. Measurements were performed at 100 K and 3 K for the 4NiBZY20 sample, while xFeSTO samples were measured only at 298 K. All measurements were performed with a microwave attenuation setting of 25 decibel.

Powder EPR measurements are inherently more complicated than single crystal or liquid measurements. The powder consists of many randomly oriented crystallites, and spectra often reveal multiple active species, distributions in  $g$ -factors, and large linewidths. This random orientation leads to only the principle values of the  $\mathbf{g}$ -tensor being extracted, not the principle directions with respect to the local structure because this is not explicitly known. Therefore, the observed values of  $\mathbf{g}$  will be labelled  $g_1$ ,  $g_2$ , and  $g_3$  rather than  $g_{xx}$ ,  $g_{yy}$ , and  $g_{zz}$  in a powder spectrum. For the simplest case of equivalent principle axes at each paramagnetic center, no hyperfine or ZFS interactions, the three values would be equivalent ( $g_1 = g_2 = g_3$ ) and a single resonance line would be observed. This situation is rarely observed in real powders and more commonly are axial or rhombic symmetries of the principle axes.

In the axial case there will be two principle values of  $\mathbf{g}$ ,  $g_{\perp}$  and  $g_{\parallel}$ . This situation could correspond to the case where  $g_{xx} = g_{yy} \neq g_{zz}$  (still assuming no hyperfine or ZFS interactions). The values  $g_{\perp}$  and  $g_{\parallel}$  determine the range of magnetic field over which absorption occurs. When the field is aligned along the unique axes,  $g_{\parallel}$ , absorption occurs, and as the field increases to where  $g_{\perp}$  is located, the signal intensity increases and a

maximum intensity is reached at  $g_{\perp}$ , where a large number of orientations perpendicular to the field are able to resonate. For a rhombic spectrum, there are three unique axes  $g_1$ ,  $g_2$ , and  $g_3$ . This situation would correspond the  $g_{xx} \neq g_{yy} \neq g_{zz}$  symmetry example. This powder spectrum will have a relatively small number of centers orientated with the field at the two limits of  $g_1$  and  $g_3$ , while a large number of orientations between those two limits will contribute to the  $g_2$  absorption, in other words, maximum absorption will occur at the  $g_2$  value.

Analysis of powder EPR spectra can be riddled with complicating factors, as mentioned above. Many experimental conditions can be varied to aid interpretation, such as, variation of microwave power, changing temperature, using higher microwave frequencies, or even preparing materials with different isotopes to control hyperfine interaction. A common quantitative analysis of EPR spectra is to estimate the number of paramagnetic species in a sample from the signal intensity. Accurate determination of such concentrations is an inherently difficult task. The relationship between concentration and signal intensity is [167]

$$c = \frac{KI}{GP} \quad (3.2)$$

where  $K$  is a proportionality constant dependent on cavity properties with the sample in it, the incident microwave power, and the modulation amplitude.  $I$  is the signal intensity,  $G$  is receiver gain of the spectrometer, and  $P$  is the EPR transition probability. For the signal intensity to be used in this calculation, the spectra must not be collected under saturation conditions. The spectra is typically output as the first derivative of the absorption, which needs to have the baseline carefully adjusted and then the signal doubly integrated to accurately know the intensity. This baseline correction is often the largest source of error in the process.[167] Additionally, a standard reference material with known paramagnetic concentration needs to be measured for quantitative determination of paramagnetic centers. The standard and sample must have the same  $K$  and  $P$  values, i.e., the same EPR properties and measurement conditions, which is difficult to achieve. No

standards appropriate for the materials studied in this thesis were available, so EPR was only utilized here to identify  $g$ -factors, not for quantitative analysis.

Measurement at different microwave frequencies can significantly aid interpretation of complicated spectra. Going to higher frequency will improve  $g$  resolution, sensitivity, and simplify spectra of species having large ZFS.[167] One consideration when going to higher frequencies is the requisite higher magnetic fields. For X-band (10 GHz), the resonance field around  $g = 2$  is around 340 mT, and for K- and Q-band (24 GHz and 35 GHz), the fields are 860 mT and 1250 mT. These fields can be reliably generated by laboratory scale electromagnets, but going to even higher frequencies requires superconducting magnets and specialized microwave components.

Measurements above Q-band frequencies offers many advantages:  $g$  resolution improves, high fields reduce second order effects, systems with large ZFS are more accessible due to larger microwave quantum energy, and decreased cross-relaxation between paramagnetic centers. The most common reason to use higher frequencies is to determine  $g$  values that have small anisotropies, in other words, the distance between the individual  $g$  values will have less overlap.

Varying microwave power and measurement temperature are also important considerations. At low microwave powers, the EPR signal amplitude will increase proportionally to the square root of the power. This proportionality will no longer be true above a certain power level and the signal amplitude will increase at a rate less than the square root of the power (saturation). Very few transition metal ions will saturate at room temperature, but low temperatures can lead to saturation.[167] For quantitative analysis of concentrations of paramagnetic centers, these effects are critical to watch out for.

### 3.5 Electron Microscopy

Scanning electron microscopy was performed on xFeSTO and xNiBZY pellets using secondary electron detectors in two different field emission microscopes (Tescan S8252G or JEOL 7000). The typical voltages and currents used during imaging were between 3–5 kV

and 30–100 pA, respectively. Surfaces were typically coated with a thin layer of Au to reduced charging effects. A focused ion beam (FIB) (FEI Helios Nanolab 600i or Tescan S8252G) was used to prepare lift-outs for transmission electron microscopy (TEM) and scanning TEM (STEM) energy dispersive x-ray spectroscopy (EDS) (FEI Talos F200x). The region of interest for the lift-out procedure had a protective layer of Pt or W deposited before etching with the ion beam.

### 3.6 X-ray Diffraction

Powder X-ray diffraction (XRD) using Cu  $K\alpha$  ( $\lambda = 1.540598$ , 40 mA, 45 kV) were collected (Malvern PANalytical Empyrean) at room temperature in Bragg-Brentano geometry from  $2\theta = 20$  to  $2\theta = 100^\circ$  with a step size of  $2\theta = 0.007^\circ$  and step time of 25 s for all samples. Lattice parameters were estimated using Rietveld refinement, as implemented in HighScore Plus XRD analysis software (Malvern PANalytical). All measurements were performed by loading powders into a zero-background holder and using appropriate incident beam slits to ensure precise interaction of the incident X-rays on the samples.

CHAPTER 4  
DILUTE IRON-DOPED POLYCRYSTALLINE STRONTIUM  
TITATATE: TRACKING IRON VALENCE STATES  
AND LOCAL INTERACTIONS

This chapter is a reproduction of an article submitted to the Journal of the American Ceramic Society. Michael Knight<sup>2</sup> prepared the manuscript, the bulk samples, performed data analysis, electron microscopy, X-ray diffraction, Raman spectroscopy, and magnetometry. Ivar Reimanis<sup>2</sup> assisted in design of experiments, manuscript editing, and provided funding for the project. Abigail Meyer<sup>3</sup> performed electron paramagnetic resonance measurements and assisted in manuscript editing. Jan-Helmut Preusker<sup>4</sup> prepared the STO powders and assisted in manuscript editing, and Wolfgang Rheinheimer<sup>5</sup> assisted in design of experiments and manuscript editing.

#### 4.1 Abstract

In this work, the mixed-valence states of dilute Fe (0.2 mol%, 0.5 mol%, and 1.2 mol%) in bulk polycrystalline strontium titanate are determined. Results from Mössbauer spectroscopy, electron paramagnetic resonance spectroscopy, and magnetometry are combined to track changes in Fe valence states; while Raman spectroscopy and X-ray diffraction results correlate structural changes. Small concentrations of  $(\text{Fe}'_{\text{Ti}} - \text{V}^{\bullet\bullet}_{\text{O}})^{\bullet}$  defect associates are detected, but the majority of  $\text{Fe}'_{\text{Ti}}$  acceptors are isolated from oxygen vacancies. As doping increases, negative exchange interactions increase, suggesting

---

<sup>2</sup>Colorado Center for Advanced Ceramics, Metallurgical and Materials Engineering Department, Colorado School of Mines, Golden, Colorado

<sup>3</sup>Chemical and Biological Engineering Department, Colorado School of Mines, Golden, Colorado, United States of America

<sup>4</sup>Institute for Applied Materials: Ceramic Materials and Technologies, Karlsruhe Institute of Technology, Karlsruhe, Germany

<sup>5</sup>Institute of Energy and Climate Research: Materials Synthesis and Processing, Forschungszentrum Jülich, Jülich, Germany

concentration of  $\text{Fe}'_{\text{Ti}} - \text{O}^{\times} - \text{Fe}'_{\text{Ti}}$  configurations increase, as expected for acceptor segregation in grain boundary regions. Additionally, the fraction of dopants existing as isovalent  $\text{Fe}^{\times}_{\text{Ti}}$  increased with  $P_{\text{O}_2}$  of the sintering atmosphere and with total Fe content.

## 4.2 Introduction

Strontium titanate ( $\text{SrTiO}_3$ ) (STO) has undergone extensive investigation for applications such as solid-state ionic conduction, memristors, thermoelectricity, superconductivity, and photocatalytic water splitting.[168–172] Lightly Fe-doped STO is commonly used as a model representative for acceptor-doped large band gap electroceramics. It is generally accepted that low concentrations of Fe-dopants in STO substitute for  $\text{Ti}^{4+}$  and can exist in 4+, 3+, or 2+ oxidation states depending on  $P_{\text{O}_2}$  and temperature.[82, 112, 173] When treated or prepared in oxidizing conditions  $\text{Fe}^{3+}$  and  $\text{Fe}^{4+}$  are expected to be preferred if substituted for  $\text{Ti}^{4+}$ .

The  $\text{SrTi}_{1-x}\text{Fe}_x\text{O}_{3-\delta}$  (STFO) system forms a solid-solution for all values of  $x$  and is a mixed ionic and electronic conductor (MIEC), especially for Fe-rich compositions ( $x > 0.1$ ).[33] Zhou and Goodenough reported on the mixed valence character of Fe, which showed a general trend of the  $\text{Fe}^{3+/4+}$  ratio increasing as Fe content increases from 10 mol% to 95 mol%.[103] Furthermore, they concluded that the transport and magnetic properties in this system are strongly influenced by interactions between Fe cations. Such interactions in the lattice indicate that extending the properties of the STFO system to the dilute Fe-doped STO model system is inappropriate. It has been suggested that only Fe doping concentrations less than 1–2 mol% can be considered dilute, because at higher concentrations there are significant Fe electronic states that overlap with one another and admix with O  $2p$  valence states.[33, 103, 110]

It is generally accepted that grain boundaries (GBs) in polycrystalline acceptor-doped STO hinder the transport of holes ( $h^{\bullet}$ ) and oxygen vacancies ( $\text{V}^{\bullet\bullet}_{\text{O}}$ ), while favoring electron transport.[38] This has been attributed to the increased concentration of  $\text{V}^{\bullet\bullet}_{\text{O}}$  at the GB cores, necessary for the structural accomodation of grains with different orientations. In

this case, there will be electronic states associated with excess cation dangling bonds that would normally transfer to the valence band oxygen states. However, with an oxygen deficient GB core, these instead fill states near the conduction band, in other words, donor states.[87] These dangling bond electrons would remain spatially located in the GB core if there were no other defect states lower in the gap to which electrons could transfer. In reality, there are always point defects present as impurities or cation vacancies. The impurities are typically acceptors, thereby providing a route to lower the electronic free energy via transfer of the GB dangling bond electrons to the acceptor. This leaves behind a positively charged GB core, and those acceptors closest to the GB core form a negative space charge (SC) region that satisfies Poisson’s equation for electrostatic potential.[87] The net positive charge at the core leads to repulsion of positively charged carriers and subsequently lower GB conductivity compared to single-crystalline STO.

Charge compensation for  $\text{Fe}'_{\text{Ti}}$  acceptors occurs in the lattice by formation of  $\text{V}_{\text{O}}^{\bullet\bullet}$ . [34] Ideal electroneutrality requires that the compensating  $\text{V}_{\text{O}}^{\bullet\bullet}$  concentration be half the  $\text{Fe}^{3+}$  concentration.[112] Therefore, even if strong electrostatic attraction of the oppositely charged defects exists, only half of the dilute  $\text{Fe}'_{\text{Ti}}$  defects can have a  $\text{V}_{\text{O}}^{\bullet\bullet}$  in the first coordination shell. For Fe concentrations less than 0.3 mol%, electron paramagnetic resonance (EPR) measurements show that the tendency for a  $\text{V}_{\text{O}}^{\bullet\bullet}$  to be located in the first coordination shell of  $\text{Fe}'_{\text{Ti}}$  decreases with increasing Fe content.[31] EPR results of Drahus et al. suggested that, when prepared in air and Fe doping concentration is below 1 mol%, the majority of Fe cations are present as  $\text{Fe}^{3+}$ . [106] Additionally, the same authors also verified the presence of a small concentration of the  $(\text{Fe}'_{\text{Ti}} - \text{V}_{\text{O}}^{\bullet\bullet})^{\bullet}$  defect complex. It is common for acceptor defects in STO to segregate in GB regions.[174–176] However, the use of spatially resolved spectroscopic techniques to directly observe segregation is difficult when the acceptor concentration is very low. The present work combines Mössbauer spectroscopy, EPR spectroscopy, and magnetometry to characterize Fe valence states in bulk polycrystalline STO with 0.2 mol%, 0.5 mol%, and 1.2 mol% substituted for Ti.

Long-range magnetic ordering of Fe in the bulk lattice is avoided by doping at such low concentrations and paramagnetic behavior of the dopants is expected. Mössbauer spectroscopy is useful for identifying the number of unique Fe sites in the system. Magnetometry is useful for estimating overall effective valence of paramagnetic species, as well as detecting exchange interactions between them. In particular, superconducting quantum interference device (SQUID) magnetometers are highly sensitive and capable of detecting very low concentrations of magnetic moments. Additionally, EPR spectroscopy is highly sensitive and can identify specific valence states, but under common X-band microwave excitation, only Kramers ions are detectable, e.g.,  $\text{Fe}^{3+}$  but not  $\text{Fe}^{2+/4+}$ . [106, 158] Combining all three experimental techniques is demonstrated here to provide a comprehensive method for estimating valence states and detecting local interactions of dilute Fe in polycrystalline STO.

### 4.3 Experimental

$\text{Sr}(\text{Ti}_{1-x}\text{Fe}_x)\text{O}_{3-\delta}$  ( $x = 0.002, 0.005, 0.012$ ) powders were prepared by solid-state reaction using  $\text{SrCO}_3$  (99.9+%, Sigma Aldrich Chemie GmbH, Taufkirchen, Germany),  $\text{TiO}_2$  (99.9+%, Sigma Aldrich Chemie GmbH, Taufkirchen, Germany) and  $\text{Fe}_2\text{O}_3$  (99+%, Merck, Darmstadt, Germany) precursors. The A- to B-site molar ratio was kept equal for all compositions. Zirconia milling balls with a diameter of 2 mm and 2-propanol were combined with the precursor mixtures in polyamide jars and subsequently attrition milled for four hours at  $1000 \text{ rev min}^{-1}$ . After milling, the powders were calcined at  $975^\circ\text{C}$  for six hours in an air furnace to remove  $\text{CO}_2$  and form  $\text{Sr}(\text{Ti}_{1-x}\text{Fe}_x)\text{O}_{3-\delta}$ . After calcination, the powders were milled again in a planetary mill with zirconia milling balls of 10 mm diameter for 16 hours at  $300 \text{ rev min}^{-1}$  to break up agglomerates. The final particle sizes of the calcined powders were approximately 500 nm.

Bulk polycrystalline pellets of all three compositions were prepared by uniaxial pressing the calcined powders into 13 mm cylindrical green bodies under 110 MPa pressure. No additives to optimize green body density were used in order to avoid introducing

unnecessary impurities. Multiple pellets of each composition were prepared by placement on sacrificial powders of the respective compositions on alumina plates, covered with alumina boats, and sintered in static air ( $P_{\text{O}_2} = 2.1 \times 10^4 \text{ Pa}$ ) or flowing pure  $\text{O}_2$  ( $P_{\text{O}_2} = 10.1 \times 10^4 \text{ Pa}$ ) at  $1500^\circ\text{C}$  or  $1300^\circ\text{C}$  for 20 hours. The surfaces of pellets selected for microscopy were prepared by grinding, polishing, and thermal etching at  $1200^\circ\text{C}$  for two hours in the same respective atmospheres. Additional pellets were ground with an agate mortar and pestle into powders for additional characterization. The remainder of the text uses shorthand notation of  $x\text{Fe}$ , where  $x$  is mol% of Fe in STO.

Room temperature powder X-ray diffraction (XRD)(Malvern Panalytical) was performed on all samples. Lattice parameters were estimated from Rietveld refinement as implemented in the HighScore Plus software (Malvern Panalytical). An XRD standard was not incorporated for calibration, so the lattice parameters are only used for comparison between samples and not for absolute accuracy. Scanning electron microscopy (SEM) (Tescan S8252G) using simultaneous in-beam secondary electron and back scatter electron detectors, as well as, Raman spectroscopy (WiTec, 532 nm excitation) were performed at room temperature on polished surfaces of pellets. The Raman spectra were collected from the center of the grains. Room temperature, 298 K, X-band electron paramagnetic resonance (EPR) spectroscopy (Bruker ELEXSYS E-500 CW EPR) field swept from 80mT to 450 mT was performed on all 1.2Fe samples. An EPR standard was not available for field calibration, so the absolute resonance fields reported are only close estimates and spectra qualitatively used to identify resonant species.

Mössbauer spectra were acquired at 296 K with a  $^{57}\text{Co}$ -Rh source using a spectrometer operating in the triangular constant-acceleration mode. Each 1.2Fe sample was mounted on an 11mm collimator for all measurements. Due to the small expected resonance signal, samples were made with the maximum amount of powder allowed by the mass absorption of the  $\gamma$ -rays. A Kr-filled proportional counter and a WissEL (Wissenschaftliche Elektronik GmbH, Germany) data acquisition module (CMCA-550 USB) were used to collect and sort

the data into 1024 channels. Both the 1.8keV Kr escape peak and the 14.4keV  $\gamma$ -ray were counted using the two-window pulse-height analysis capability of the module. Samples were run for three to four days to obtain sufficient counting statistics (an off-resonance count of about  $3 \times 10^6$ ) to allow analysis of the very weak signal. Velocity calibration and the isomer shift zero value were established with a pure bcc ( $\alpha$ )-Fe foil. The counts for each channel (velocity) were normalized (with respect to the total baseline counts) and subspectra were fit to the normalized data using Lorentzian line shapes with WinNormos V3.0 coupled with the IGOR Pro V6.3 software package, also from WissEL.

Magnetometry was performed on all Fe-doped samples using a Magnetic Property Measurement System 3 (MPMS3) (Quantum Design Inc.) operated in DC scan mode. For each sample, approximately 0.5 g powder was loaded into a gelatin capsule and mounted inside a clear drinking straw, the typical method for powder measurements. Measurements of mass magnetization as a function of applied magnetic field ( $M(H)$ ) were performed at 1.8 K, 5 K, 10 K, 20 K, and 30 K, where the magnitude of magnetization is much greater than the opposing diamagnetic component. To be as accurate as possible, the data was still corrected for contributions from the small diamagnetic background signal arising from the non-magnetic constituents and sample mounting materials. The  $M(H)$  curves were fit for the spin magnetic quantum number for a multi-electron species,  $S$ , using the relation for magnetization of a paramagnetic species,  $M = M_0 B(y)$ , where  $M_0 = Ng\mu_B S$  is the maximum magnitude of the moment,  $B(y)$  is the Brillouin function, and  $y = S\mu_0 g\mu_B H/k_B T$ . [116] Here,  $N$  is the number of magnetic species per kg (allowed to vary during the fit),  $g$  is the  $g$ -factor (determined by EPR),  $\mu_B$  is the Bohr magneton value,  $H$  is the applied magnetic field,  $\mu_0$  is the permeability of vacuum,  $k_B$  is Boltzmann's constant, and  $T$  is absolute temperature. Measurements of mass susceptibility as a function of temperature were performed from 1.8 K to 300 K under 0.2 T applied magnetic field after cooling in zero field (ZFC), and repeated after cooling under field (FC). Overlaid ZFC/FC curves were used to verify Fe is paramagnetic, i.e., to check for transition

temperatures indicating long-range ordering of Fe cations. An additional fitting with the summation of two Brillouin functions was performed on  $M(H)$  curves collected at 30 K for the 1.2Fe samples to estimate the ratio  $\text{Fe}^{4+}/\text{Fe}^{3+}$  for comparison with EPR and Mössbauer results. For this additional analysis, the individual Brillouin functions were assigned a spin number of 5/2 or 2, for high-spin  $\text{Fe}^{3+}$  or  $\text{Fe}^{4+}$ , respectively, and the concentrations of each species allowed to vary during the fit. It should be noted that high-spin  $\text{Fe}^{2+}$  also has four unpaired electrons and is therefore difficult to distinguish from  $\text{Fe}^{4+}$ . However, the concentration of  $\text{Fe}^{2+}$  has been previously calculated to be orders of magnitude lower than concentration of  $\text{Fe}^{4+}$  in STO at 900 °C and  $P_{\text{O}_2} \approx 10^4$  Pa.[82]

#### 4.4 Results

Powder XRD patterns for the four sample sets are shown in Figure 4.1. All samples were refined to the cubic perovskite structure ( $Pm\bar{3}m$ ) and the patterns showed no detectable secondary phases. The refined lattice parameters for all samples are shown in Table 4.1. The lattice parameters slightly increased above the 0 mol% value as Fe-doping increased for all but the 1500 °C  $\text{O}_2$  sample set.

Table 4.1 Cubic lattice parameter (a) of Fe-doped STO samples sintered in air or  $\text{O}_2$  at 1500 °C or 1300 °C. The values were determined by Rietveld refinement of powder X-ray diffraction data shown in Figure 4.1. The uncertainties of the last digits are displayed in parenthesis.

	$a_{0\text{Fe}}(\text{Å})$	$a_{0.2\text{Fe}}(\text{Å})$	$a_{0.5\text{Fe}}(\text{Å})$	$a_{1.2\text{Fe}}(\text{Å})$
1300 °C Air	3.90799(1)	3.90822(1)	3.90860(1)	3.90874(1)
1500 °C Air	3.90812(1)	3.90818(1)	3.90863(1)	3.90872(1)
1300 °C $\text{O}_2$	3.90787(1)	3.90820(1)	3.90860(1)	3.90867(1)
1500 °C $\text{O}_2$	3.90799(1)	3.90631(2)	3.90698(1)	3.90684(1)

SEM micrographs of 1.2 mol% Fe-doped STO samples sintered in air are shown in Figure 4.2. Inspection of these representative micrographs reveals that sintering at 1500 °C produced slightly larger grain sizes than sintering at 1300 °C. Micrographs of all other samples are available in Supplemental Figure 4.7 and Figure 4.8.

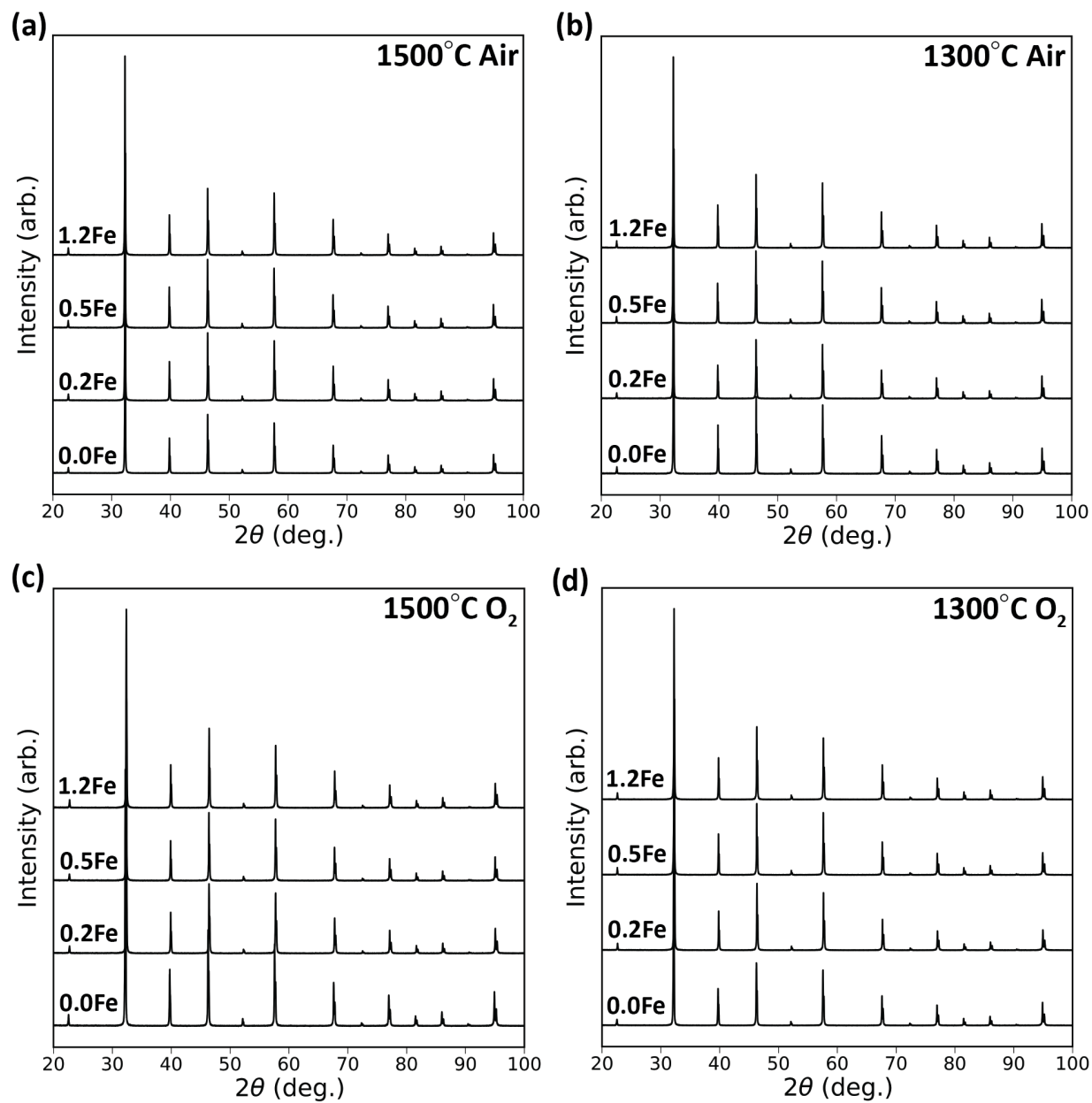


Figure 4.1 Room temperature powder X-ray diffraction patterns of the four sample sets: (a) air sintered at 1500 °C, (b) air sintered at 1300 °C, (c) O<sub>2</sub> sintered at 1500 °C, and (d) O<sub>2</sub> sintered at 1300 °C. All samples were refined to the cubic perovskite structure ( $Pm\bar{3}m$ ) and no detectable secondary phases were observed.

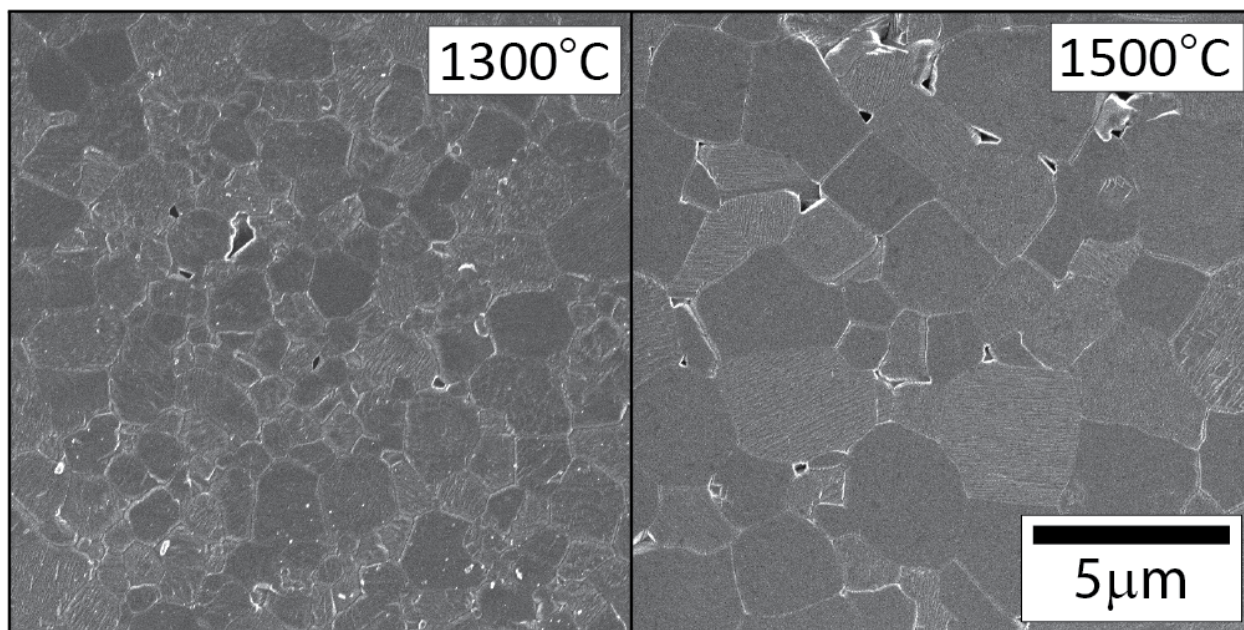


Figure 4.2 SEM micrographs of 1.2 mol% Fe-doped STO samples sintered in air. This representative example shows how sintering at 1500 °C produced slightly larger grains than sintering at 1300 °C. Micrographs of all samples are available in Supplemental Figure 4.7 and Supplemental Figure 4.8

No significant microstructural differences related to sintering atmosphere or Fe-doping were observed. Previous work has shown that sintering STO at higher temperatures (1500 °C) produces a bi-modal microstructure, which eventually becomes unimodal after enough time.[177] Furthermore, when higher Fe concentrations are present (5 mol%), Fe segregation at GBs was shown to induce solute drag effects that result in fine-grained unimodal microstructures.[178]

STO at room temperature is cubic with space group ( $Pm\bar{3}m$ ) having 5 atoms per unit cell, each located at a point of inversion symmetry, and no first-order Raman scattering is expected for an ideal crystal.[179] Broken central symmetry due to strain, impurities, and oxygen vacancies, have been shown to cause first-order scattering in cubic STO.[180, 181] Raman spectra of pellets sintered in air at 1300 °C are shown in Figure 4.3, and are representative of all samples, while all other spectra are shown in Supplemental Figure 4.9.

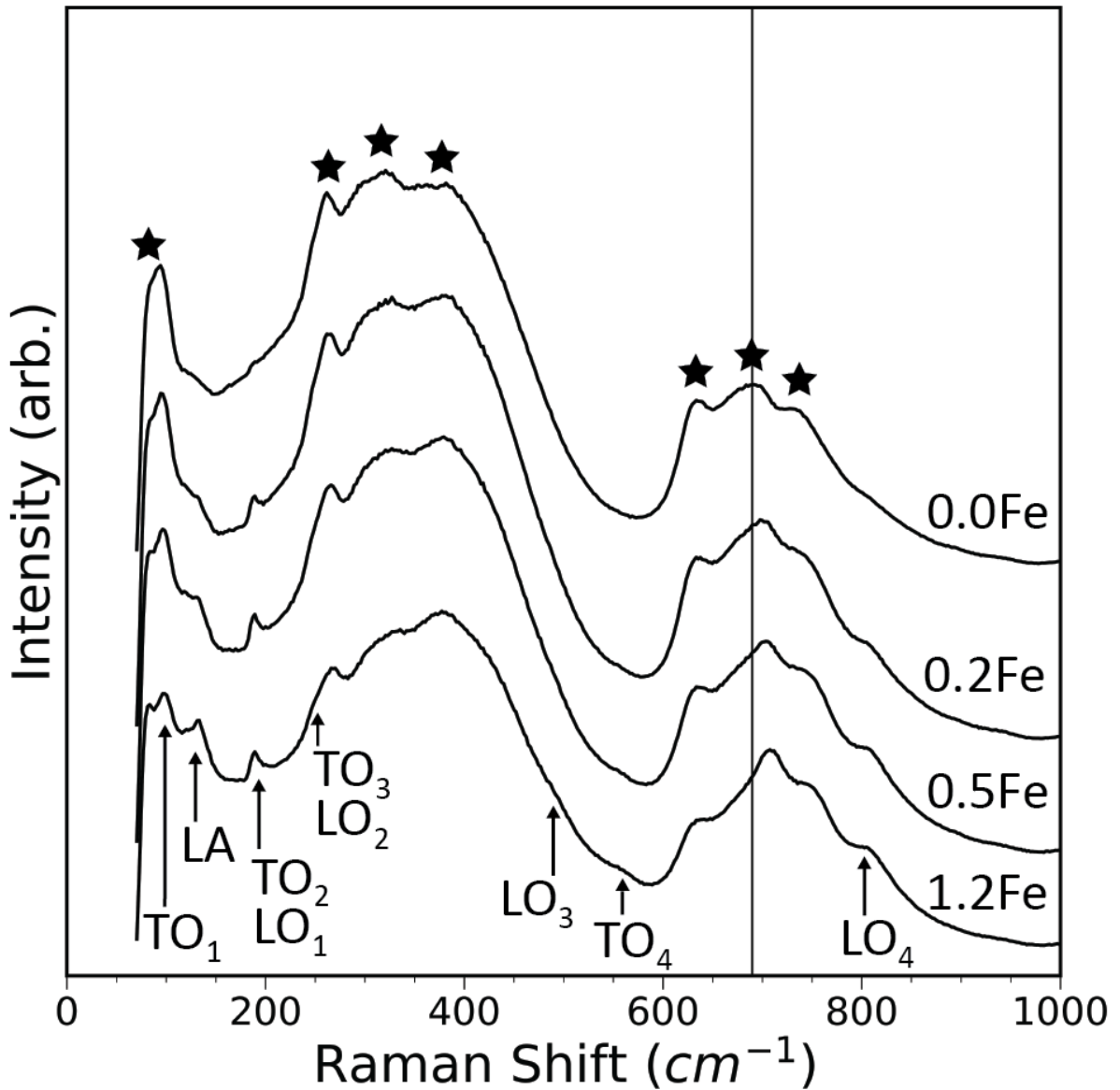


Figure 4.3 Raman spectra of pellets sintered in air at  $1300^\circ\text{C}$  as a representative example. Spectra were collected from grain interior regions of polished surfaces. The spectra are dominated by broad second-order modes (stars), however, the appearance of first order modes (labeled) is connected to slight disruption of ideal cubic symmetry by incorporation of Fe. The single vertical line at  $690 \text{ cm}^{-1}$  indicates the location of a peak previously connected to substitutional  $\text{Fe}^{4+}$ . [112]

All spectra are largely dominated by broad signals from second-order scattering (two-phonon processes). After a survey of many reported STO Raman spectra, first-order phonon modes have been labeled at their estimated locations, whereas second-order modes are marked with stars, in Figure 4.3. The single vertical line around  $690\text{ cm}^{-1}$  was observed to be the only peak that shifted to higher frequency with increased Fe-doping. This peak does not correspond to any possible first order modes and has been previously suggested to indicate the presence of  $\text{Fe}_{\text{Ti}}^{\times}$ . Doping with Fe appears to have disrupted the local B-site cubic symmetry enough to allow multiple first-order Raman modes to be observed.

Mössbauer spectra of all four 1.2Fe samples are shown in Supplemental Figure 4.10. The asymmetric doublet signals indicate at least two types of Fe sites are present. The solid blue line is the complete spectral fit, while the red line subspectrums were assigned to  $\text{Fe}^{4+}$  and the green line subspectrums assigned to  $\text{Fe}^{3+}$ , after comparison with reports in the literature.[182–186] The third site fitted with a single yellow line may be only half of the resonance since it is likely a quadrupole doublet with the other half unresolved at a lower velocity resonance. An average of the linewidths from the other two sites was assumed for the site 3 linewidth. There is significant scatter in the data due to large grain sizes, meaning that the samples are less uniform. The spectral parameters are listed in Supplemental Table 4.2. The linewidths are significantly larger than expected for a unique Fe site, implying there is a distribution of Fe sites centered at each position. This suggests a slight distribution of isomer shifts and quadrupole splittings caused by variations in near neighbor environments.

EPR spectra collected at 298 K for all four 1.2Fe samples are shown in Figure 4.4. The spectra are scaled to have approximately the same intensity at  $g = 2.0$  and a  $6\times$  magnification of the low-field regions are inset above each total spectra. Overall, the spectra are dominated by main resonances at the isotropic  $g = 2.0$  field ( 340 mT), with small satellites on either side owing to 4th-order fine structure interaction.[106] This isotropic signal is due to high-spin  $\text{Fe}^{3+}$ , as  $\text{Fe}^{4+}$  and  $\text{Fe}^{2+}$  are non-Kramers ions and their

resonances are not directly observable under the experimental conditions used here, however, their presence does contribute to line broadening.[158]

The very weak resonance, at  $g = 5.9$ , has been previously assigned to  $(\text{Fe}'_{\text{Ti}} - \text{V}^{\bullet\bullet}_{\text{O}})^{\bullet}$  defect associates.[31, 106] Comparing the intensities between the two regions, it can be concluded that the majority of  $\text{Fe}^{3+}$  species appear to exist as substitutional  $\text{Fe}'_{\text{Ti}}$  defects not associated with a nearest neighbor  $\text{V}^{\bullet\bullet}_{\text{O}}$ . Quantitative conclusions about the relative concentrations of EPR silent  $\text{Fe}^{4+/2+}$  and EPR active  $\text{Fe}^{3+}$  could not be made due to the lack of an appropriate standard that could be incorporated into the measurement process.

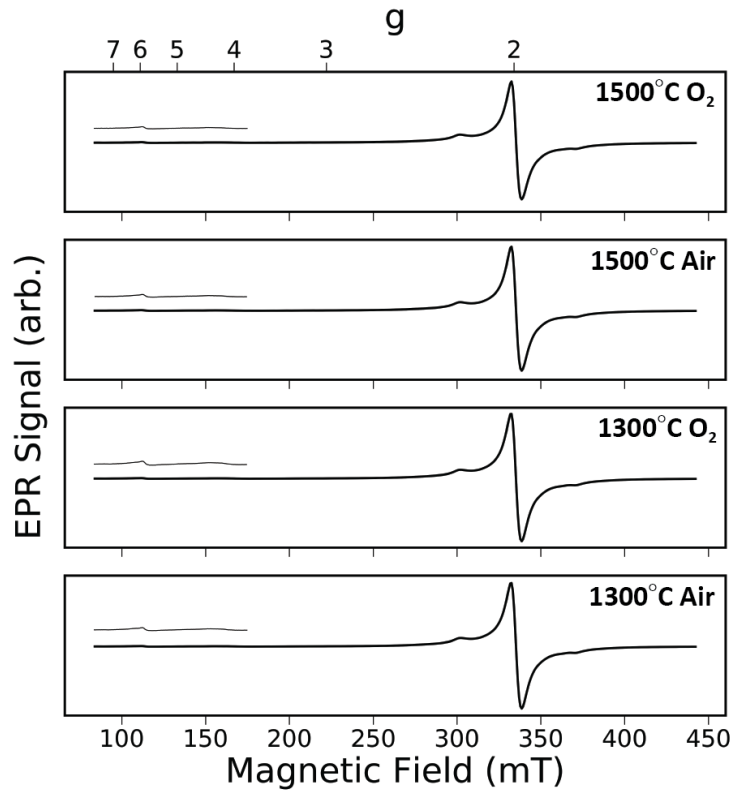


Figure 4.4 Room temperature X-band electron paramagnetic resonance spectra of all four 1.2 mol% Fe-doped STO samples. Nearly all the  $\text{Fe}^{3+}$  resonate at the isotropic  $g = 2$  field (340 mT), however, a low-intensity resonance around  $g = 5.9$  was also observed. This region is magnified by  $6\times$  and inset above each total spectra. This has been previously shown to be a signature of  $(\text{Fe}'_{\text{Ti}} - \text{V}^{\bullet\bullet}_{\text{O}})^{\bullet}$  defect associates.[31, 106]

Measurements of zero-field-cooled (ZFC) and field-cooled (FC) mass magnetic susceptibility *versus* temperature of the 1.2Fe sample sintered at 1500 °C in  $\text{O}_2$  are

superimposed in Supplemental Figure 4.11. This representative example shows the majority of the Fe dopants are paramagnetic centers and long-range magnetic ordering is absent, in other words, no magnetic transition temperatures could be detected, unlike previous results that studied higher Fe concentrations.[103] Examples of possible secondary Fe-containing phases having magnetic ordering could be antiferromagnetic FeTiO<sub>3</sub> with  $T_N = 52$  K,[187] antiferromagnetic SrFeO<sub>3</sub> with  $T_N = 134$  K,[188] or one of the many iron oxide phases that are all magnetically ordered. The magnetometry results reported here were not significantly influenced by minority magnetically ordered phases that may have formed under non-equilibrium conditions because all samples displayed only paramagnetic behavior.

Figure 4.5 shows  $\mu_{\text{eff}}/\text{Fe}$  values determined from Brillouin fits of  $M(H)$  curves measured at 1.8 K, 5 K, 10 K, 20 K and 30 K. As temperature decreases to 1.8 K,  $\mu_{\text{eff}}/\text{Fe}$  decreases for all samples, with the 1.2Fe samples showing the greatest decreases. These observations suggest the presence of negative exchange interactions between paramagnetic species.[189] Decreases in  $\mu_{\text{eff}}/\text{Fe}$  at low temperature could also be caused by zero field splitting, however, the EPR spectra for all 1.2Fe samples revealed isotropic  $g$ -factors for the Fe<sup>3+</sup> species. Comparison between the different Fe concentrations reveals a general trend of slightly decreasing  $\mu_{\text{eff}}/\text{Fe}$  with increasing Fe doping. On each subplot in Figure 4.5, horizontal dashed and dotted lines mark the theoretical expected values for high-spin Fe<sup>3+</sup> and Fe<sup>4+</sup>, respectively. These ideal values are calculated using only the spin angular momentum number  $S$ , with the assumption that  $3d$  transition metal cations have orbital contributions ( $L$ ) to the total angular momentum number  $J$ . The  $\mu_{\text{eff}}/\text{Fe}$  values of all 1.2Fe samples correlate well with the EPR determination of the presence of high-spin Fe<sup>3+</sup>.  $M(H)$  curves with Brillouin fits for all samples sintered in air at 1300 °C are available in Supplemental Figure 4.12 as a representative example.

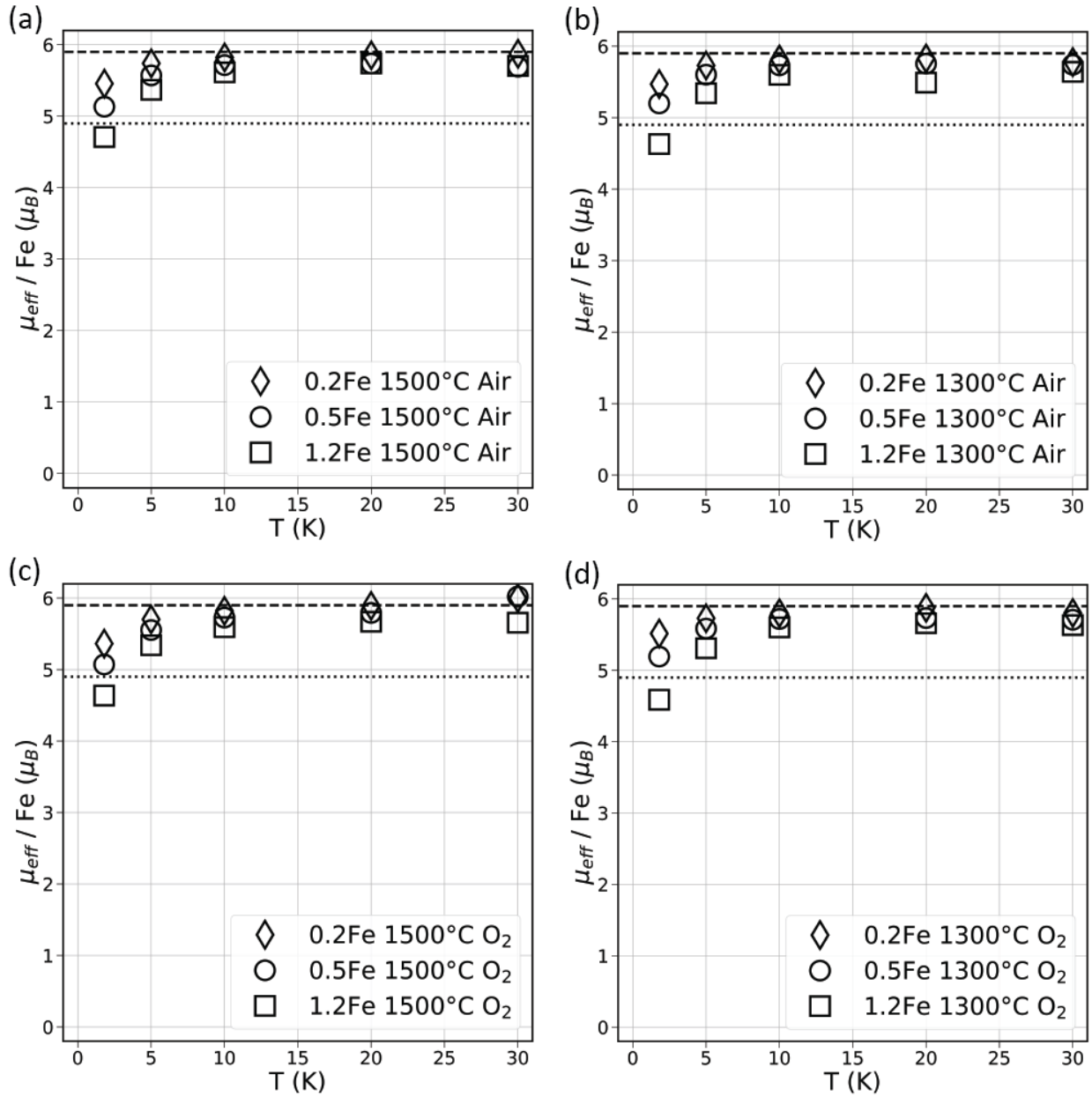


Figure 4.5  $\mu_{\text{eff}}/\text{Fe}$  values estimated from Brillouin fits of  $M(H)$  curves measured at 1.8 K, 5 K, 10 K, 20 K and 30 K for samples sintered at 1500 °C in air (a), sintered at 1300 °C in air (b), sintered at 1500 °C in O<sub>2</sub> (c), and sintered at 1300 °C in O<sub>2</sub> (d). Decreases at low-temperature may indicate the presence of negative exchange interactions. Horizontal dashed and dotted lines mark the expected spin-only moments for high-spin Fe<sup>3+</sup> and Fe<sup>4+</sup>, respectively. Additionally,  $\mu_{\text{eff}}/\text{Fe}$  decreases at all temperatures with increased Fe-doping, suggesting an Fe concentration dependent change in relative amounts of Fe<sup>3+</sup> and Fe<sup>4+</sup>.

Figure 4.6 (a) shows the estimated relative concentrations of  $\text{Fe}^{4+}$  and  $\text{Fe}^{3+}$  for all 1.2Fe samples. These estimations were made by fitting 30 K  $M(H)$  curves with two Brillouin functions for the number of magnetic species,  $N_{3+}$  and  $N_{4+}$ , with  $S$  fixed to 5/2 and 2 for high-spin  $\text{Fe}^{3+}$  and  $\text{Fe}^{4+}$ , respectively. This temperature was chosen for the analysis due to it being far from the decreasing  $\mu_{\text{eff}}/\text{Fe}$  values below 10 K, where complicated interactions between the Fe cations may affect the results. Only the 1.2Fe samples were analyzed by this method for comparison with EPR and Mössbauer results of the same samples. The individual fitted curves are shown in Supplemental Figure 4.13.

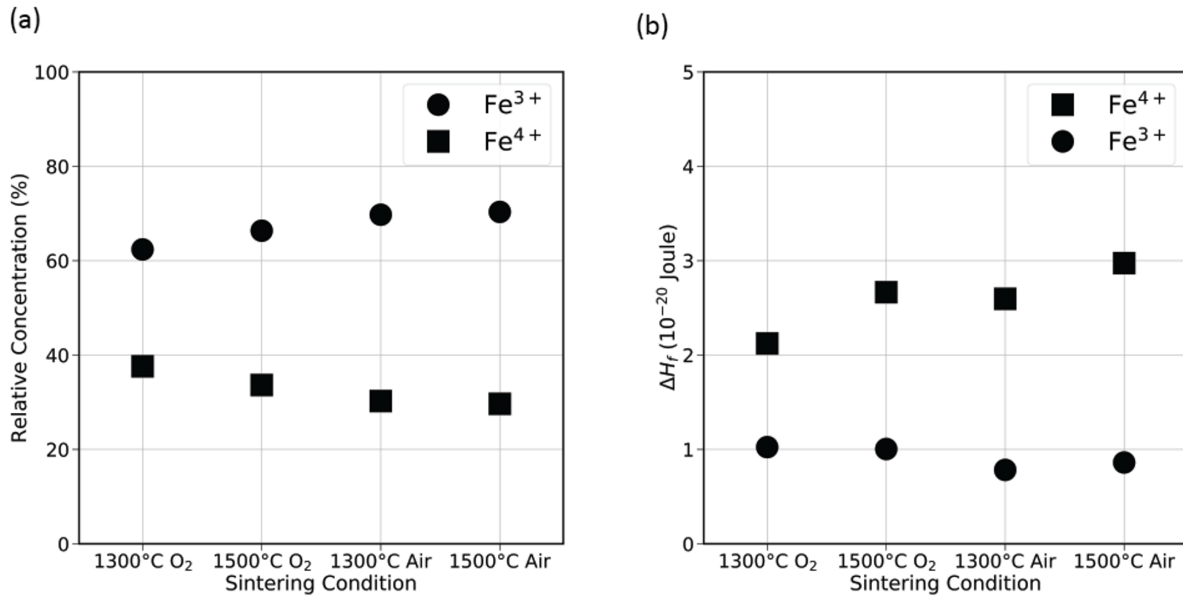


Figure 4.6 The estimated relative concentrations of  $\text{Fe}^{4+}$  and  $\text{Fe}^{3+}$  in all four 1.2 mol% Fe-doped samples is shown in (a). The estimated concentrations were used to estimate the  $\Delta H_f$  values of  $\text{Fe}^{4+}$  and  $\text{Fe}^{3+}$  shown in (b). Concentration estimations were determined by fitting 30 K  $M(H)$  curves with two Brillouin functions for the number of magnetic species,  $N_{5/2}$  ( $\text{Fe}^{3+}$ ) and  $N_2$  ( $\text{Fe}^{4+}$ ), with  $S$  values fixed at 5/2 and 2, respectively.

Sintering in pure O<sub>2</sub> resulted in more  $\text{Fe}^{4+}$  than sintering in air. Additionally, sintering at 1300 °C resulted in more  $\text{Fe}^{4+}$  than sintering at 1500 °C, where the largest relative concentration difference occurred when sintering in a pure O<sub>2</sub> atmosphere. Assuming theoretical density of STO (5.11 g/cm<sup>3</sup>), the total Fe concentration is estimated to be

around  $2 \times 10^{20} \text{Fe}/\text{cm}^3$  for doping concentrations of 1.2 mol%. Sums of the  $\text{Fe}^{4+}$  and  $\text{Fe}^{3+}$  fitted concentrations were close to the calculated value (between  $10^{19} \text{Fe}/\text{cm}^3$  and  $10^{20} \text{Fe}/\text{cm}^3$  for all four samples). The fitted concentrations were used to estimate enthalpy of formation,  $\Delta H_f$ , of each species for all four sintering conditions (Figure 4.6 (b)). The estimations of  $\Delta H_f$  were made by the following approximation:

$$n \approx \exp\left(-\frac{\Delta H_f}{k_B T}\right) \quad (4.1)$$

where  $n$  is the concentration of  $\text{Fe}^{4+}$  or  $\text{Fe}^{3+}$  relative to the total Fe concentration,  $k_B$  is Boltzmann's constant, and  $T$  is the sintering temperature. These results show higher  $\Delta H_f$  for  $\text{Fe}^{4+}$  in all samples, consistent with the fitted relative concentrations. These results are consistent with previous work by Baker et al., that showed increasing temperature, as well as, decreasing  $P_{\text{O}_2}$  results in less  $\text{Fe}^{4+}$  in STO.[82] Additionally, their results showed relative concentrations of  $\text{Fe}^{4+}$  and  $\text{Fe}^{3+}$  at similar orders of magnitude as the results shown here, although they only looked at temperatures up 900 °C.[82]

## 4.5 Discussion

As introduced earlier, the existence of excess  $\text{V}_{\text{O}}^{\bullet\bullet}$  at GB cores and subsequent accumulation of  $\text{Fe}'_{\text{Ti}}$  acceptors in the adjacent SC region is well understood theoretically, and is frequently correlated with conductivity measurements. However, observing this phenomenon directly is experimentally difficult when low Fe concentrations are present. The results presented here offer a unique approach to track the valence state and local environment of dilute Fe dopants in STO.

Except for the 1500 °C  $\text{O}_2$  samples, the lattice parameters of all samples containing Fe all slightly increased with Fe concentration (Table 4.1). The ionic radii of  $\text{Fe}^{4+}$  and  $\text{Fe}^{3+}$  are 0.585 Å and 0.645 Å, respectively.[190] Comparing these radii with that of  $\text{Ti}^{4+}$ , 0.605 Å, suggests  $\text{Fe}^{3+}$  is substituted for  $\text{Ti}^{4+}$ . An alternative explanation for the slight lattice expansion with increasing Fe concentration could be assumed to be caused by additional charge compensating  $\text{V}_{\text{O}}^{\bullet\bullet}$ . However, even for significant oxygen deficit of  $\delta = 0.5$ ,

the relative unit cell volume increase would be smaller than  $10^{-10}$ , and therefore oxygen deficiency is likely not the explanation for the lattice parameter change.[191]

Mössbauer spectroscopy results (Supplemental Figure 4.10) confirmed that Fe exists in mixed oxidation states for all 1.2Fe samples. The observation of very low-intensity signal with isomer shift of 1.35 mm/s in the 1500 °C air-sintered sample could indicate some  $\text{Fe}^{2+}$  is present, which may exist in a small amount of secondary  $\text{FeTiO}_3$  phase, or as a doubly-charged acceptor at the STO B-site. Alternatively, this third species could be another  $\text{Fe}^{3+}$  sitting in a dramatically different environment than the other  $\text{Fe}^{3+}$  species. Regardless, the signal of this third site is so low that it is impossible to make a conclusion and it may also exist in the other samples, but was indistinguishable from the background noise. The overall signal intensity for all samples is very low due to only having a natural abundance of the  $^{57}\text{Fe}$  isotope. Supplemental Table 4.2 shows the estimated fractions of each species (Relative Area), and the majority species in all cases is  $\text{Fe}^{3+}$ . EPR results confirmed significant presence of high-spin  $\text{Fe}^{3+}$  and revealed a small concentration of  $(\text{Fe}'_{\text{Ti}} - \text{V}^{\bullet\bullet}_{\text{O}})^{\bullet}$  defect associates exist in all 1.2Fe samples.

The  $\text{Fe}^{4+}$  species are expected to be randomly substituted for Ti in the STO lattice. Observation of a peak in the Raman spectra near  $690\text{ cm}^{-1}$  has been previously attributed to Jahn-Teller distortion of the oxygen octahedra around isovalent  $\text{Fe}^{\times}_{\text{Ti}}$ . [112] In the Raman spectra reported here, this  $690\text{ cm}^{-1}$  peak sharpens and shifts to higher frequency with increasing Fe concentration. This shift may indicate an average shortening of the Fe-O bonds, consistent with axial elongation of the oxygen octahedra around  $\text{Fe}^{4+}$ . This observation suggests isovalent  $\text{Fe}^{\times}_{\text{Ti}}$  are randomly distributed in the bulk lattice since the Raman spectra were collected from grain interior regions.

Additional evidence for mixed-valence Fe is drawn from the  $\mu_{\text{eff}}/\text{Fe}$  values shown in Figure 4.5. Above 10 K, the  $\mu_{\text{eff}}/\text{Fe}$  values for all samples are approximately constant with temperature, and the 0.2Fe samples are closest to matching the expected high-spin  $\text{Fe}^{3+}$  moment ( $5.9\mu_{\text{B}}$ ). As Fe doping increases,  $\mu_{\text{eff}}/\text{Fe}$  values slightly decrease. These decreases

in  $\mu_{\text{eff}}/\text{Fe}$  are proposed to be caused by some fraction of the Fe dopants existing as high-spin  $\text{Fe}^{4+}$ , which have an expected moment of  $4.9\mu_{\text{B}}$ . This assignment correlates with previous computational results by Evarestov et al. that showed the high-spin state for isolated  $\text{Fe}_{\text{Ti}}^{\times}$  defects in STO is preferred over the low-spin state.[110] This hypothesis is supported by the Mössbauer results, which revealed the presence of  $\text{Fe}^{4+}$  in all 1.2Fe samples. The relative concentrations and estimated  $\Delta H_f$  values of  $\text{Fe}^{4+}$  and  $\text{Fe}^{3+}$  shown in Figure 4.6 provide additional information on the effects of sintering atmosphere. As expected, sintering in pure  $\text{O}_2$  produced higher concentrations of  $\text{Fe}^{4+}$  compared to sintering in air.

For high concentrations of Fe, multiple exchange interactions between Fe cations can be present and produce different magnetic behaviors. Zhou proposed that the main interactions are: (1) antiferromagnetic  $\text{Fe}^{3+}\text{-O-Fe}^{3+}$ , (2) ferromagnetic  $\text{Fe}^{4+}\text{-O-Fe}^{3+}$ , and (3) ferromagnetic  $\text{Fe}^{4+}\text{-O-Fe}^{4+}$ . [103] In the presence of positively charged GB cores,  $\text{Fe}'_{\text{Ti}}$  acceptors accumulate in the SC region and could exist as next-nearest neighbors.[176, 192] In the present study, some  $\text{Fe}'_{\text{Ti}}$  acceptors are likely segregated near GBs and exist in configurations of  $180^\circ \text{Fe}^{3+}\text{-O-Fe}^{3+}$ , which leads to interaction (1). In this case, the  $\text{Fe}^{3+}$  have singly-occupied  $3d$  orbitals hybridized with oxygen  $2p$  orbitals and interact antiferromagnetically.[116] These interactions between  $\text{Fe}'_{\text{Ti}}$  acceptors are proposed to be connected to the decreasing  $\mu_{\text{eff}}/\text{Fe}$  values at low-temperature, where the extent of these interactions increases with increasing Fe concentration. This observation is consistent with the model of acceptor segregation in SC regions for positively charged GB cores in STO.

## 4.6 Conclusions

This work has shown that dilute Fe dopants in bulk polycrystalline STO exist in mixed-valence states, where some fraction of  $\text{Fe}^{3+}$  may be configured as next-nearest neighbors or in a defect complex with an oxygen vacancy. In this dilute limit, some might assume that the Fe-dopants can be treated as randomly distributed and non-interacting. However, magnetometry results suggest a concentration dependence on interaction between

Fe-dopants, as well as, how much of the Fe dopant exists as  $\text{Fe}^{4+}$ . Confirming  $\text{Fe}'_{\text{Ti}}$  segregation at these concentrations would be a difficult task, considering only some fraction of the Fe-dopants would be segregated, and are likely below the detection limits of common spectroscopy tools capable of spatial quantification. Estimating valences of Fe-dopants within the 0.2–1.2 mol% doping range is also difficult, however, magnetometry has been demonstrated as a highly sensitive tool to unify results from EPR and Mössbauer spectroscopy. To the authors best knowledge, this is the first report combining these three techniques to study the valence states of dilute Fe in bulk polycrystalline STO. Future work should prepare samples with  $^{57}\text{Fe}$  enriched precursor to significantly improve signal of Mössbauer spectra, as well as prepare samples with a variety of grain size distributions that have different SC volumes.

#### 4.7 Acknowledgments

The authors acknowledge Dr. Serena Eley (CSM) for access to the MPMS3, Dr. Don Williamson (CSM) for collecting the Mössbauer spectra, and Dr. Ron Goldfarb (NIST) for providing magnetometry advice. MK acknowledges support by the National Science Foundation Graduate Research Fellowship Program (NSFGRFP). MK and IR acknowledge support by the National Science Foundation award DMR-1563754. WR and JP acknowledge support by the German Research Foundation under grants no. HO 1165/20 and RH 146/1. The Tescan S8252G instrument used in this research was purchased through National Science Foundation MRI award DMR-1828454.

#### 4.8 Supplemental Information

This section contains supplemental figures referenced throughout the chapter. The SEM micrographs shown in this section were collected using only secondary electrons, while the micrographs in the main text were collected using a mix of secondary and backscattered electrons.

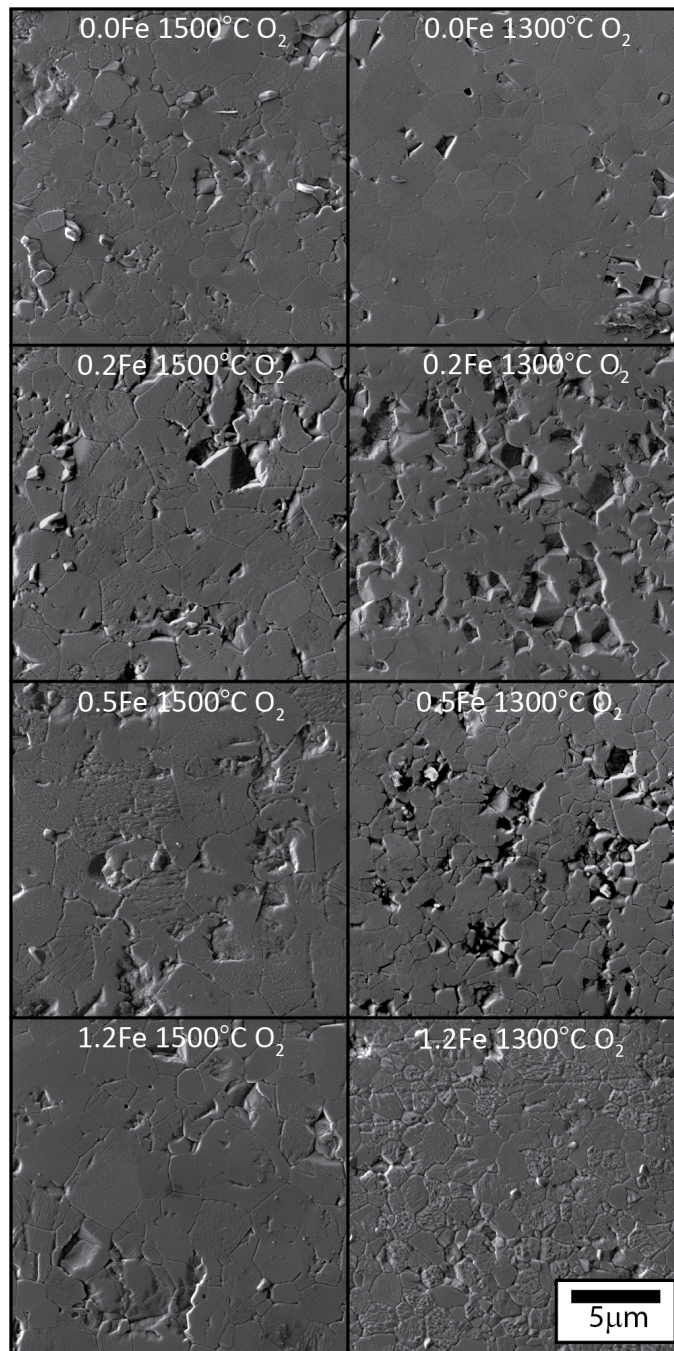


Figure 4.7 SEM micrographs (secondary electron imaging) of bulk 0 mol%, 0.2 mol%, 0.5 mol%, and 1.2 mol% Fe-doped STO samples sintered in flowing pure O<sub>2</sub> at either 1500 °C (left column) or 1300 °C (right column). Grain size distributions were not determined, however, the 1300 °C sintering temperature produced slightly smaller grain sizes than the 1500 °C sintering temperature, and residual porosity was observed in all samples.

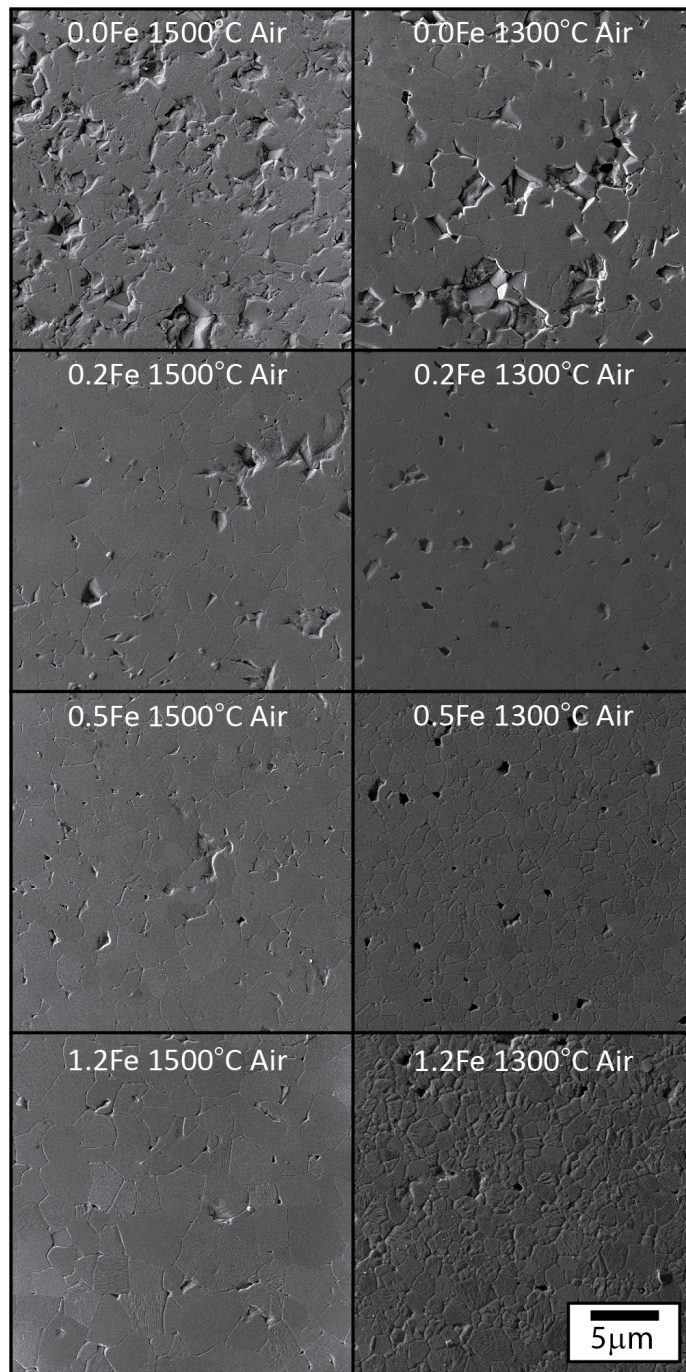


Figure 4.8 SEM micrographs (secondary electron imaging) of bulk 0 mol%, 0.2 mol%, 0.5 mol%, and 1.2 mol% Fe-doped STO samples sintered in air at either 1500 °C (left column) or 1300 °C (right column). Grain size distributions were not determined, however, the 1300 °C sintering temperature appears to have produced slightly smaller grain sizes than the 1500 °C sintering temperature. Less porosity was observed in these air-sintered samples compared to those sintered in pure O<sub>2</sub> (Figure 4.7).

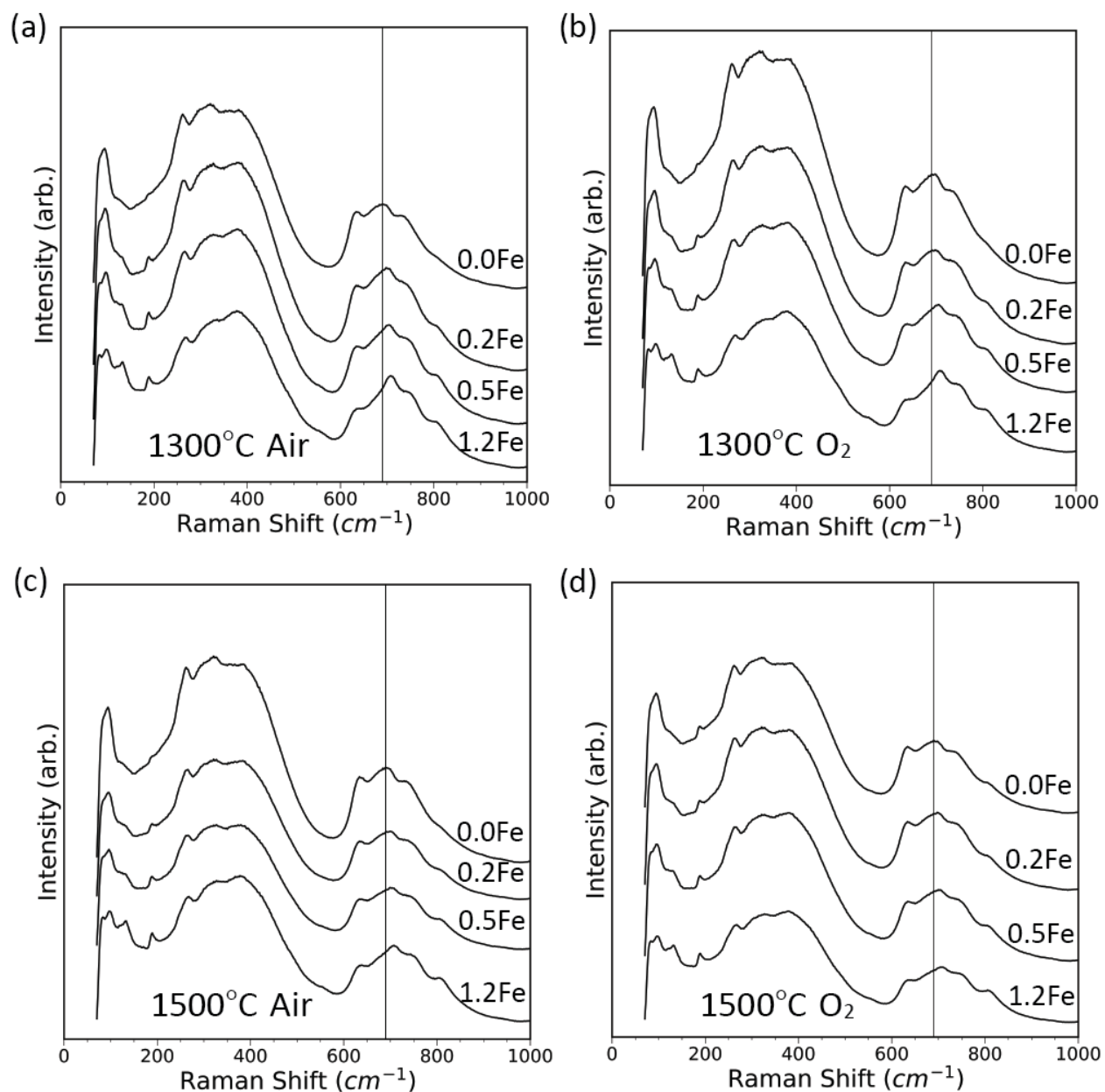


Figure 4.9 Raman spectra collected from grain interior regions of samples sintered in air at 1300 °C (a), pure oxygen at 1300 °C (b), air at 1500 °C (c), and pure oxygen at 1500 °C (d). The broad peaks are caused by second order (combination or difference phonon modes) scattering. As Fe-doping increases (top to bottom in each subplot), first order scattering (individual phonon modes) peaks appear and increase in resolution. The single vertical line at 690 $\text{cm}^{-1}$  indicates the frequency corresponding  $\text{Fe}^{4+}$  substituted for  $\text{Ti}^{4+}$  reported previously.[112] This peak shifts towards higher frequency with increased Fe-doping and the current authors propose this is caused by an average shortening of the Fe-O bond lengths.

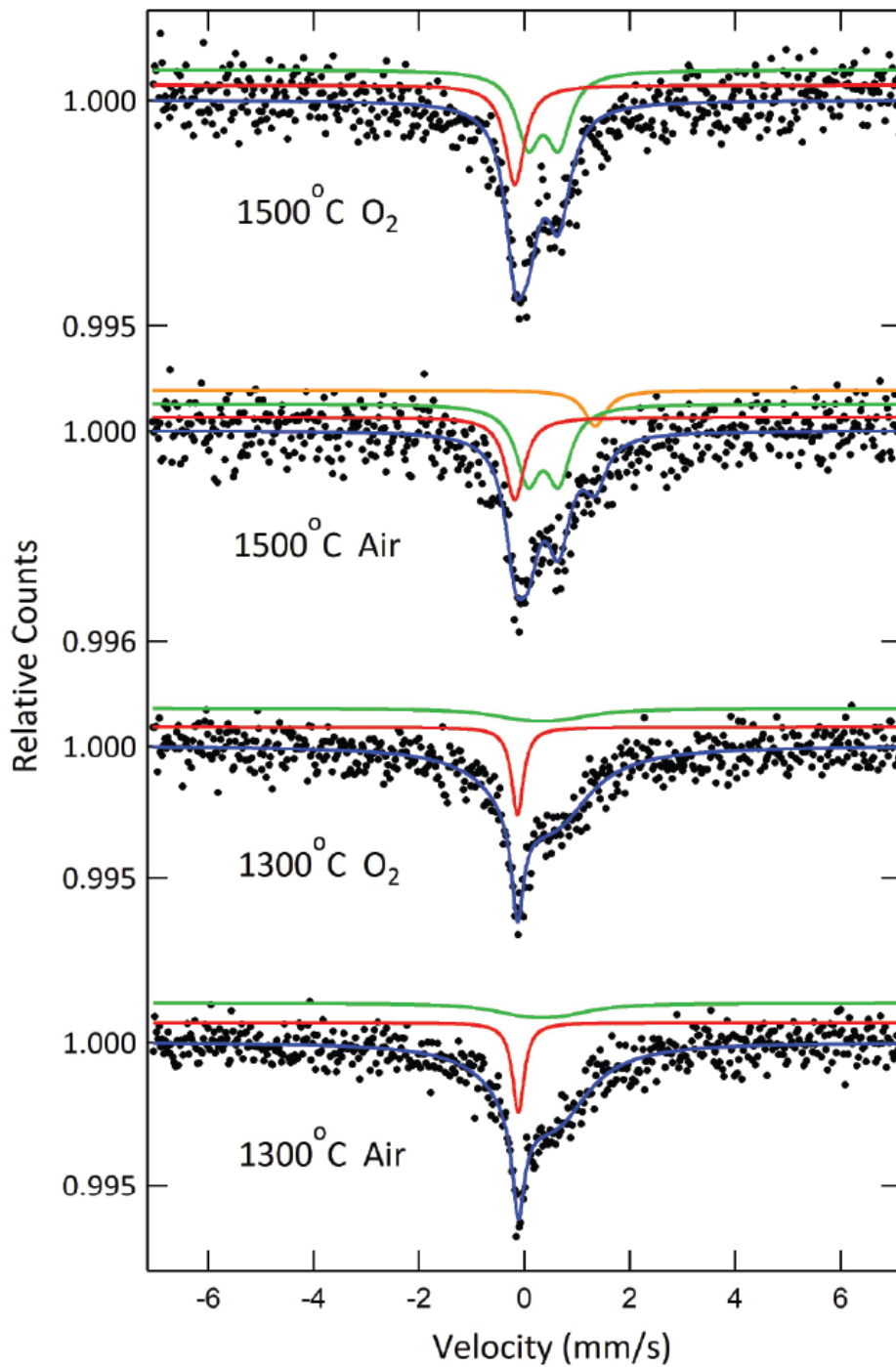


Figure 4.10 Mössbauer spectra of all four 1.2 mol% Fe-doped STO samples. The blue line is the least squares fit of the total spectra, while the green and red subspectrums were assigned to  $\text{Fe}^{3+}$  and  $\text{Fe}^{4+}$ , respectively. The third subspectrum (yellow) in the 1500 °C air-sintered sample may indicate a small concentration of  $\text{Fe}^{2+}$ , or  $\text{Fe}^{3+}$  in a dramatically different local environment, but this assignment is inconclusive.

Table 4.2 Fitted parameters from all four 1.2Fe Mössbauer spectra. Uncertainty in the last significant figure is in parentheses, where some values were fixed (f) in the sample having 3 Fe sites. Isomer shift is given relative to the center of the pure Fe calibration spectrum and minimum linewidth obtainable from the spectrometer is 0.23 mm/s.

Sample	Fe Site	Isomer Shift (mm/s)	Quadrupole Splitting (mm/s)	Linewidth (mm/s)	Relative Area (%)
1500 °C O <sub>2</sub>	Fe <sup>4+</sup> (red)	-0.18(2)	0	0.44(4)	32(6)
	Fe <sup>3+</sup> (green)	0.36(3)	0.58(6)	0.55(3)	68(6)
1500 °C Air	Fe <sup>4+</sup> (red)	-0.18(f)	0	0.44(f)	24(7)
	Fe <sup>3+</sup> (green)	0.36(f)	0.58(f)	0.55(f)	63(7)
	Site 3 (yellow)	1.35(10)	0	0.5(f)	13(7)
1300 °C O <sub>2</sub>	Fe <sup>4+</sup> (red)	-0.13(1)	0	0.27(5)	15(3)
	Fe <sup>3+</sup> (green)	0.33(4)	0.7(2)	1.6(2)	85(7)
1300 °C Air	Fe <sup>4+</sup> (red)	-0.12(1)	0	0.27(4)	15(3)
	Fe <sup>3+</sup> (green)	0.34(3)	0.7(2)	1.5(2)	85(6)

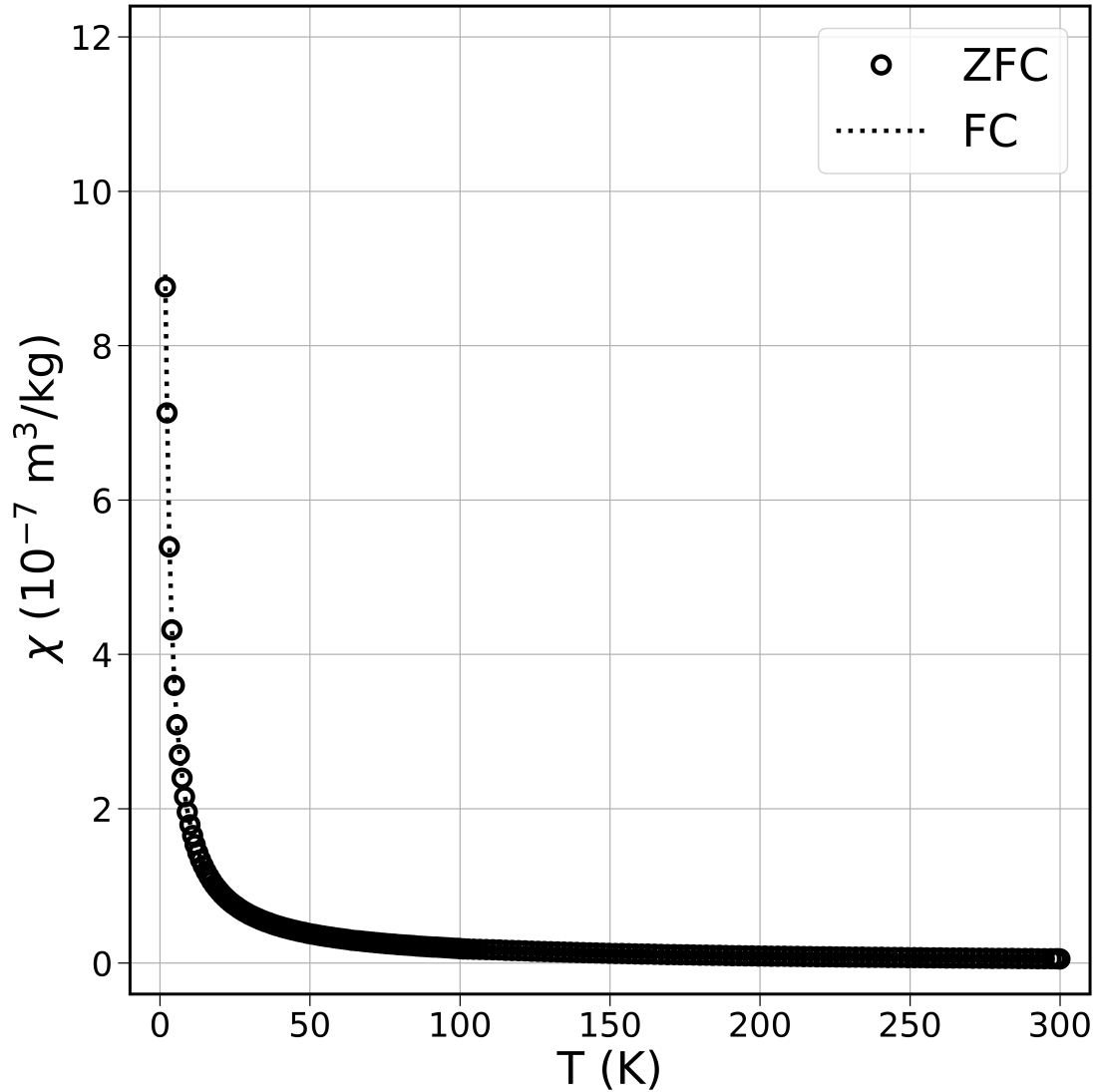


Figure 4.11 Zero-field-cooled and field-cooled magnetic susceptibility versus temperature of 1.2 mol% Fe-doped STO sample sintered in pure O<sub>2</sub>. This is a representative example for the dilute doping regime studied here, where no magnetic transitions indicate there is no long-range ordering of Fe cations. Transitions have been previously reported in this temperature range where long-range ordering of Fe occurs when higher Fe-doping concentrations are present.[103]

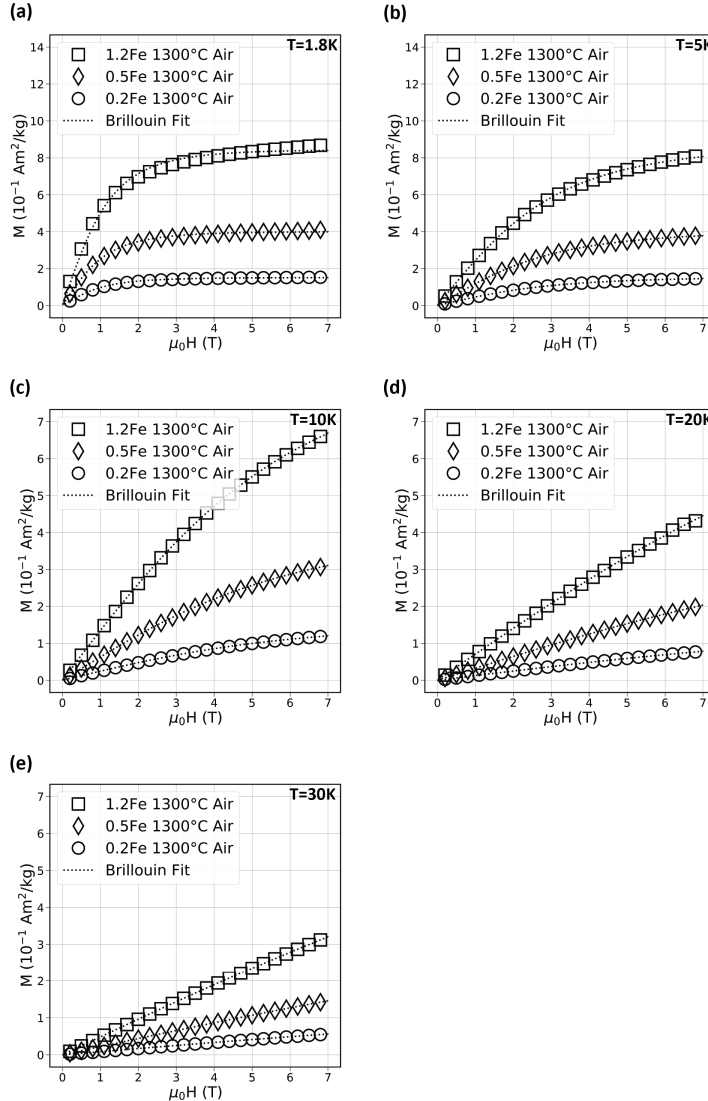


Figure 4.12 Fitted mass magnetization versus applied field curves collected at 1.8 K (a), 5 K (b), 10 K (c), 20 K (d), 30 K (e), for the three samples sintered at 1300 °C in air. Note the smaller y-axis scale in (c-e). The curves shown here for this sample set are representative of all sample sets. The quality of the fits are excellent (residual sum of squares  $< 10^{-7}$ ) for all temperatures except for the lowest temperature 1.8 K, where significant interactions between Fe are present and cause deviation from ideal paramagnetic response of dilute species in an applied magnetic field at low-temperature (saturation).

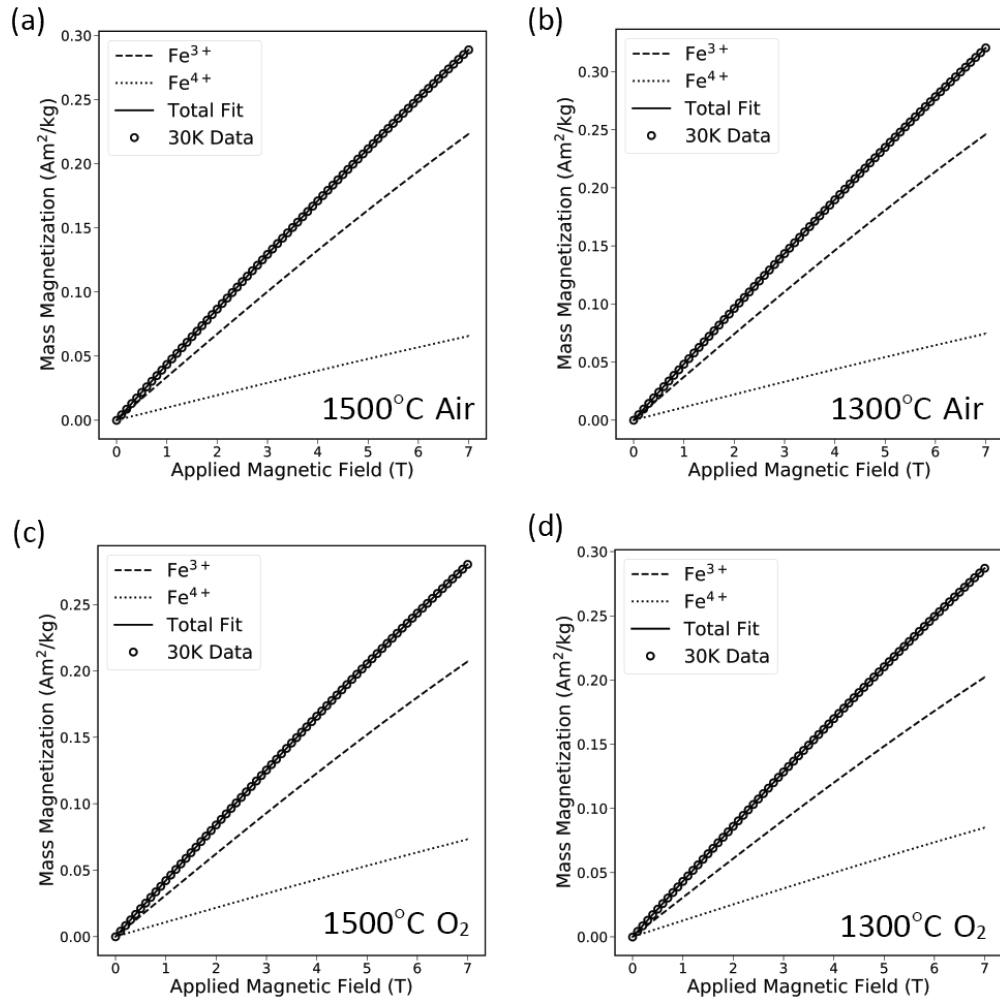


Figure 4.13 Mass magnetization curves for all 1.2 mol% Fe-doped STO samples fitted with two Brillouin functions. Each function was fitted for concentration of magnetic species with spin numbers fixed at  $S=5/2$  and  $S=2$  for  $\text{Fe}^{3+}$  and  $\text{Fe}^{4+}$  respectively.

CHAPTER 5  
ESTIMATING NICKEL VALENCE WITH MAGNETOMETRY  
IN SOLID-STATE REACTIVE SINTERED YTTRIUM  
DOPED BARIUM ZIRCONATE

This chapter is the reproduction of an article published in the Journal of the American Ceramic Society.<sup>6</sup> Michael Knight<sup>7</sup> prepared the manuscript and the samples, as well as, performed data analysis, scanning electron microscopy, X-ray diffraction, and magnetometry. Dylan Jennings<sup>7</sup> prepared lamella for, and performed, scanning transmission electron microscopy and energy dispersive X-ray spectroscopy. Sandrine Ricote<sup>8</sup> assisted in experimental design and manuscript editing. Ivar Reimanis<sup>7</sup> assisted in experimental design, manuscript editing, and provided funding for the project.

## 5.1 Abstract

Ni is known to have a significant impact on the sintering and microstructure evolution in yttrium-doped barium zirconate and yet details of its specific role remain unclear. The present study examined the valence state of Ni in solid-state reactive sintered yttrium-doped barium zirconate prepared with different amounts of Ni, formulated for deliberate substitution of Ni for Zr:  $\text{BaZr}_{0.8-x}\text{Y}_{0.2}\text{Ni}_x\text{O}_{3-\delta}$  with  $x = 0.005, 0.01, 0.02, 0.03, 0.04$  (approx. 0.1 wt%, 0.2 wt%, 0.4 wt%, 0.6 wt%, 0.8 wt%). Quenching from 1500 °C revealed that a transient  $\text{BaY}_2\text{NiO}_5$  phase was present in the microstructure for all concentrations of Ni studied here. Energy dispersive X-ray spectroscopy identified Ni-segregation in grain-boundary regions upon completion of the

---

<sup>6</sup> ©The American Ceramic Society. M. Knight, D. Jennings, S. Ricote, and I. Reimanis. Estimating nickel valence with magnetometry in solid-state reactive sintered yttrium-doped barium zirconate. *J Am Ceram Soc.* 2021; 105: 159–168

<sup>7</sup>Colorado Center for Advanced Ceramics, Metallurgical and Materials Engineering Department, Colorado School of Mines, Golden, Colorado

<sup>8</sup>Mechanical Engineering Department, Colorado School of Mines, Golden Colorado

solid-state reactive sintering process, and magnetometry is used to show that low-spin  $\text{Ni}^{3+}$  predominantly substitutes for  $\text{Zr}^{4+}$ .

## 5.2 Introduction

Yttrium-doped barium zirconate (BZY) is a promising proton conductor for applications in protonic ceramic fuel cells (PCFCs) operating on methane or other hydrocarbon fuels due to satisfactory conductivity and excellent chemical stability.[19, 45, 51, 117] A typical BZY based anode-supported cell assembly is made by co-sintering a NiO/BZY composite anode with a thin BZY electrolyte, but this can be problematic due to limited densification and grain growth of BZY at temperatures below  $1700\text{ }^\circ\text{C}$ .[54, 117] Babilo and Haile explored the use of different transition metal oxide sintering aides and observed that ZnO added during synthesis led to a significant reduction in sintering temperature.[57] Tong et al. demonstrated that adding NiO to BZY precursors before processing reduced sintering temperature.[58] This solid-state reactive sintering (SSRS) method combines the steps of solid-state reaction and powder sintering so that the desired phase is formed and densified in a single step, an attractive route for commercialization of BZY based devices.

The simple, one-step SSRS method with a sintering additive has demonstrated potential in high performance proton conducting fuel cells operating on various fuels.[61] The typical use consists of adding 1–2 wt% NiO to the BZY precursor powders before one or more mixing steps, followed by compacting the green body and one-step heating at between  $1400\text{ }^\circ\text{C}$  and  $1600\text{ }^\circ\text{C}$ .[61, 193] As low as 0.5 wt% NiO has also been confirmed to produce a dense electrolyte.[194] Previous work proposed the mechanism of enhanced sinterability involves the formation of an active intermediate phase with composition  $\text{BaY}_2\text{NiO}_5$  (BYN) that partially dissolves back into the BZY lattice.[59] Under typical proton conducting fuel cell anode operating conditions, the BYN phase decomposes into Ba-containing phases,  $\text{Y}_2\text{O}_3$ , and metallic Ni causing performance degradation.[63, 64] Additionally, formation of this Y-rich phase in the electrolyte implies decreased acceptor concentration in the BZY

phase, potentially reducing bulk proton conductivity. Therefore, it is critical to avoid forming excess BYN phase in the sintered electrolyte. A recent thermodynamic study describes regimes of phase equilibria in the BZY-NiO system, providing a guideline for useful compositions and sintering temperatures required to avoid the presence of BYN.[195]

Huang et al. suggest BYN phase formation is likely accompanied by BaNiO<sub>2</sub> (BN) phase formation in the presence of excess NiO.[65] The same authors employed a different process (not one-step reaction and sintering) to compare samples where NiO was added after calcination with those in which Ni was substituted for Zr (at 4 mol% and 8 mol%) before calcination (“Ni-substitution”). They found that proton uptake was improved by utilizing Ni-substitution compared with adding NiO after calcination. It has become clear recently that the role of Ni in the subsequent microstructure and phase evolution depends on whether it is added before or after calcination.[137] It is thus highly desirable to establish methods to track Ni in the microstructure.

Magnetometry may be used to help understand the role of Ni in the processing of BZY because Ni exhibits a variety of magnetic signatures, dependent on local bonding and valence state. Magnetometry involves the measurement of magnetization of a bulk, powder, or film sample within a range of applied magnetic fields and temperatures. This is readily applicable in the case of NiO-BZY processed in air because the only likely magnetic species present should be Ni<sup>2+</sup> and Ni<sup>3+</sup>. They can be distinguished via magnetic characterization by number of unpaired 3*d* electrons: Ni<sup>2+</sup> has two, and Ni<sup>3+</sup> has either one or three, for the low-spin or high-spin state respectively.[116] The utility of magnetometry is demonstrated here by estimating the effective valence of Ni, identifying the possible existence of a low-lying excited electronic state for Ni, and by detecting the existence of trace magnetic impurities in the absence of Ni-doping.

### 5.3 Experimental

Bulk polycrystalline samples of BaZr<sub>0.8-x</sub>Y<sub>0.2</sub>Ni<sub>x</sub>O<sub>3-δ</sub>, where  $x = 0.00, 0.005, 0.01, 0.02, 0.03, 0.04$ , were prepared similarly to the single step SSRS

process utilized in producing the PCFCs of Duan et al., as described below.[18] The compositions of precursors were chosen such that Ni replaced Zr (i.e., Ni-substitution). The highest concentration  $x = 0.04$  (0.8 wt%) is less than the 1 wt% concentration added in the SSRS method employed by Tong et al.[59] This upper limit was chosen in an attempt to maintain single phase BZY due to the BYN phase having been previously identified via X-ray diffraction when 1 wt% or more NiO was added.[163, 164] Shorthand notation for sample referencing of XNiBZY20 is used throughout the rest of the text, where X is Ni-doping expressed as mol%.

Stoichiometric quantities of the precursor powders BaCO<sub>3</sub> (Alfa Aesar, 99%), ZrO<sub>2</sub> (Alfa Aesar, 99.978%), Y<sub>2</sub>O<sub>3</sub> (CoorsTek, 99.999%), and NiO (Alfa Aesar, 99.998%) were massed and combined with 5mm ZrO<sub>2</sub> media (in a 2:1 media to powder mass ratio) and ethyl alcohol (in a 1:1 ml to g ratio), then ball-milled for 48 h in polyethylene bottles. The slurry was dried in an oven for 24 h at 130 °C. The dried precursor powders were ball-milled an additional 48 h without solvent to break up agglomerated particles. The final precursor powders were uniaxially pressed into 25 mm diameter cylindrical pellets at 375 MPa for 60 s. The pellets were buried in sacrificial precursor powders of each respective composition and heated at 1500 °C for 20 h in air using a covered high-purity alumina boat. The heating and cooling rate for the furnace was 5 °C/min. A second batch of xNiBZY20 pellets was prepared identically except the final 5 °C/min cooling step was replaced with air quenching to room temperature by removing the boat from a bottom loading box furnace after 20 h at 1500 °C. This was performed to verify the BYN phase also exists at 1500 °C when Ni is substituted for Zr, not just when NiO is added to stoichiometric BZY.

A focused ion beam (FIB) (FEI Helios Nanolab 600i) was used to prepare lift-outs for transmission electron microscopy (TEM) and scanning TEM (STEM) energy dispersive x-ray spectroscopy (EDS) (FEI Talos F200x) on 4NiBZY20 quenched and slow-cooled pellets. Regions of interest for the lift-out procedure had a protective layer of Pt deposited before etching with the Ga ion beam. Additionally, field emission scanning electron

microscopy (FESEM) (JEOL 7000) using a secondary electron detector was performed on internal surfaces of all pellets prepared in this study. All remaining pellet pieces were ground with an agate mortar and pestle for 20 min into fine powders for magnetometry and powder X-ray diffraction (XRD). Cu  $K_\alpha$  ( $\lambda = 1.540598 \text{ \AA}$ ) XRD patterns were collected (Malvern PANalytical Empyrean) at 25°C in Bragg-Brentano geometry from  $2\theta = 20^\circ$  to  $2\theta = 100^\circ$  with a step size of  $2\theta = 0.007^\circ$ . Lattice parameters were estimated using Rietveld refinement, as implemented in HighScore Plus XRD analysis software (Malvern PANalytical).

Magnetometry was performed on the powdered samples using a Magnetic Property Measurement System 3 (MPMS3) (Quantum Design Inc.). For each sample, approximately 0.5–1 g powder was loaded into a gelatin capsule and mounted inside a clear drinking straw, the typical method for powder measurements. Magnetization as a function of applied magnetic field was performed at 3 K and 100 K up to 7 T for Brillouin  $M(H)$  curve fits, which provides estimated total angular momentum quantum number and concentration of the magnetic cations.

For paramagnetic moments, the magnetization as a function of applied magnetic field,  $M(H)$  can be well described with the quantum theory of isolated, non-interacting moments.[116] The complete mass magnetization curve is modelled by:

$$M = M_0 \mathcal{B}(y) \quad (5.1)$$

where  $M_0 = Ng\mu_B J$  is the maximum magnitude of the moment and  $\mathcal{B}(y)$  is the Brillouin function:

$$\mathcal{B}(y) = \frac{2J+1}{2J} \coth \frac{2J+1}{2J} y - \frac{1}{2J} \coth \frac{y}{2J} \quad (5.2)$$

Here,  $y = J\mu_0 g\mu_B H/k_B T$ ,  $N$  is the number of magnetic cations per kg,  $g$  is the  $g$ -factor,  $\mu_B$  is the Bohr magneton,  $J$  is the total angular momentum quantum number,  $\mu_0$  is the permeability of vacuum,  $H$  is the applied magnetic field,  $k_B$  is Boltzmann's constant, and  $T$  is absolute temperature.

With minimal contribution from magnetic impurities, ideally  $J = 1.0$  for  $\text{Ni}^{2+}$ , and  $J = 0.5$  or  $J = 1.5$  for low-spin or high-spin  $\text{Ni}^{3+}$  respectively.[116] By fitting Equation 5.1 with the variables  $N$  and  $J$ , it is possible to estimate the effective valence and concentration of Ni in each sample. The  $g$ -factors implemented in the fitting routines of the samples were measured directly on the 4NiBZY20 powder at 3 K and 100 K with X-band electron paramagnetic resonance (EPR) (Bruker ELEXSYS E-500 CW EPR) measurements field swept from 0.25 T to 0.45 T. It was considered that the starting materials may have small concentrations of paramagnetic impurities and thus, a method of correction to the Ni total angular momentum quantum number  $J_{\text{Ni}}$  was proposed. After fitting the 0NiBZY20 sample  $M(H)$  data at for the total angular momentum,  $J_i$ , and concentration,  $N_i$ , of the paramagnetic impurities, a correction can be estimated with a simple mass fraction relationship:

$$J_{\text{tot}} = (1 - X_i)J_{\text{Ni}} + X_iJ_i \quad (5.3)$$

Where  $X_i$  is the mass fraction of impurity ions and  $J_i$  is the total angular momentum quantum number for the impurity ions.  $X_i$  for each sample was calculated using the ideal Ni-doping concentrations:  $X_i = N_i/N_{\text{doping}} = 1.0, 0.016, 0.008, 0.004, 0.003, 0.002$  (for Ni doping mol fractions of  $x = 0.0, 0.005, 0.01, 0.02, 0.03, 0.04$ ). It was determined the correction was not necessary after estimating the relative concentration of paramagnetic impurities to Ni cations was  $< 2\%$  for all samples.

Measurements of mass susceptibility as a function of temperature were performed from 1.8 K to 300 K under 0.2 T applied magnetic field for Curie-Weiss analysis. The effective magnetic moment per Ni,  $\mu_{\text{eff}}$ , can be estimated using the Curie-Weiss relation describing paramagnetic mass susceptibility, which is dependent on temperature:

$$\chi = \frac{C}{T - \theta} \quad (5.4)$$

where  $C = N\mu_0\mu_{\text{eff}}^2/3K_B$  and the Weiss constant  $\theta$  is a measure of the effective interaction between moments. When  $\theta > 0$ , there is an effective ferromagnetic (FM)

interaction (parallel alignment) and when  $\theta < 0$ , there is an effective antiferromagnetic (AF) interaction (antiparallel alignment).[116] The effective magnetic moment per magnetic ion can then be determined by linear fit to the reciprocal susceptibility data, where the slope is equal to  $1/C$  after correcting for the background diamagnetic susceptibility of the diamagnetic cations and sample holder. Additional details regarding analysis of magnetometry data are provided in Supplemental Section 5.8.1.

## 5.4 Results

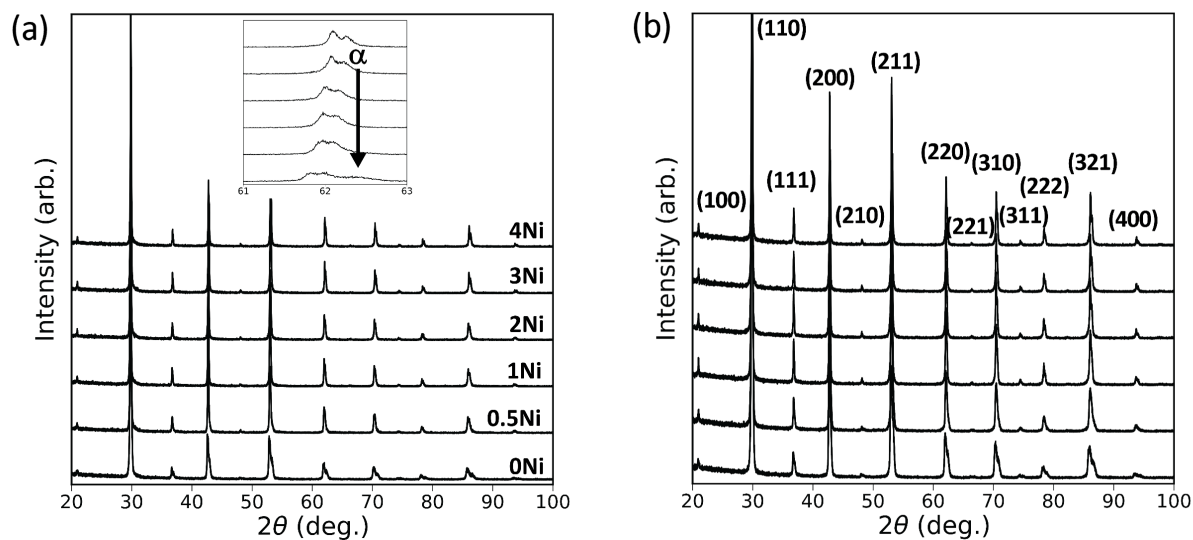


Figure 5.1 Powder X-ray diffraction for Ni-doped BZY20 samples prepared via solid-state reactive sintering (20h, 1500 °C) with 5 °C/min cooling (a) and air quenching (b). For 0mol% and 0.5 mol% Ni, two cubic perovskite ( $Pm\bar{3}m$ ) phases are present and Ni-doping above 0.5 mol% leads to formation of a single-phase material with decreasing lattice parameters. Inset in (a) is magnified region around  $2\theta = 62.4^\circ$  showing  $\alpha$ -phase peak, refined to  $BaZrO_3$ . Representative reflection indices of the phase pure 4 mol% Ni data are shown in (b).

XRD patterns for the two sets of  $xNiBZY20$  samples are shown in Figure 5.1. For both sample sets, the SSRS process at 1500 °C produced two cubic perovskite phases ( $Pm\bar{3}m$ ) with different lattice parameters for 0 mol% and 0.5 mol% Ni, where the phase with the smaller lattice parameter is referred to as  $\alpha$  and the one with larger lattice parameter is  $\beta$ . A decrease in the  $\alpha$ -phase intensity for increasing Ni is most clearly observed at the high  $2\theta$

angle peak shoulders (Figure 5.1(a) inset). Above 0.5 mol% Ni, all samples are comprised of pure  $\beta$ -phase.  $\beta$ -phase was refined to  $\text{BaZr}_{0.8}\text{Y}_{0.2}\text{O}_{2.9}$  and  $\alpha$ -phase was refined to  $\text{BaZrO}_3$ .

The lattice parameters of all samples decrease with increasing Ni-doping, as expected for smaller Ni cations substituted for Zr cations at the perovskite B-site. The lattice parameters of the slow cooled samples are larger than the quenched samples (Supplemental Figure 5.16). This lattice expansion may be in part due to partial hydration of the BZY20 material in ambient air upon slow cooling.[45] The observed XRD patterns are consistent with those of Han et al.[134] and Tong et al.,[58] where formation of BZY was promoted by NiO additions. The individual sample patterns are available in Appendix A. No extraneous peaks corresponding to BYN were observed in any of the patterns. The most intense peak would be located at  $2\theta = 32.4^\circ$  (Supplemental Figure 5.17). Similarly, no extraneous peaks corresponding to  $\text{Y}_2\text{O}_3$  were observed, however the most intense peak for this phase overlaps with the (110) cubic perovskite peak.

Scanning electron microscopy showed significant increase in densification and grain growth with increased Ni-doping, as expected in the SSRS process (Figure 5.2 and Figure 5.3). Unlike the quenched samples, discussed below, BYN was not observed in the slow-cooled samples. However, in the slow cooled 3NiBZY20 and 4NiBZY20 samples, a platelet shaped secondary phase was observed at some surfaces (Figure 5.2), and was determined by STEM-EDS mapping (Supplemental Figure 5.18) to likely be  $\text{Y}_2\text{O}_3$ ; it was not observed in the quenched samples. STEM-EDS mapping of grain interfaces in the 4NiBZY20 slow cooled sample (Figure 5.4) and a line scan across one of the interfaces (Supplemental Figure 5.19) revealed Ni mass percent was increased in the grain-boundary region, implying either that Ni cations segregate there or a thin Ni-containing phase is present. Only 4 mol% Ni-doping was examined by STEM-EDS because it provided the strongest signal of all the samples for Ni detection. Ni segregation was not observed in the quenched 4NiBZY20 sample (Supplemental Figure 5.20).

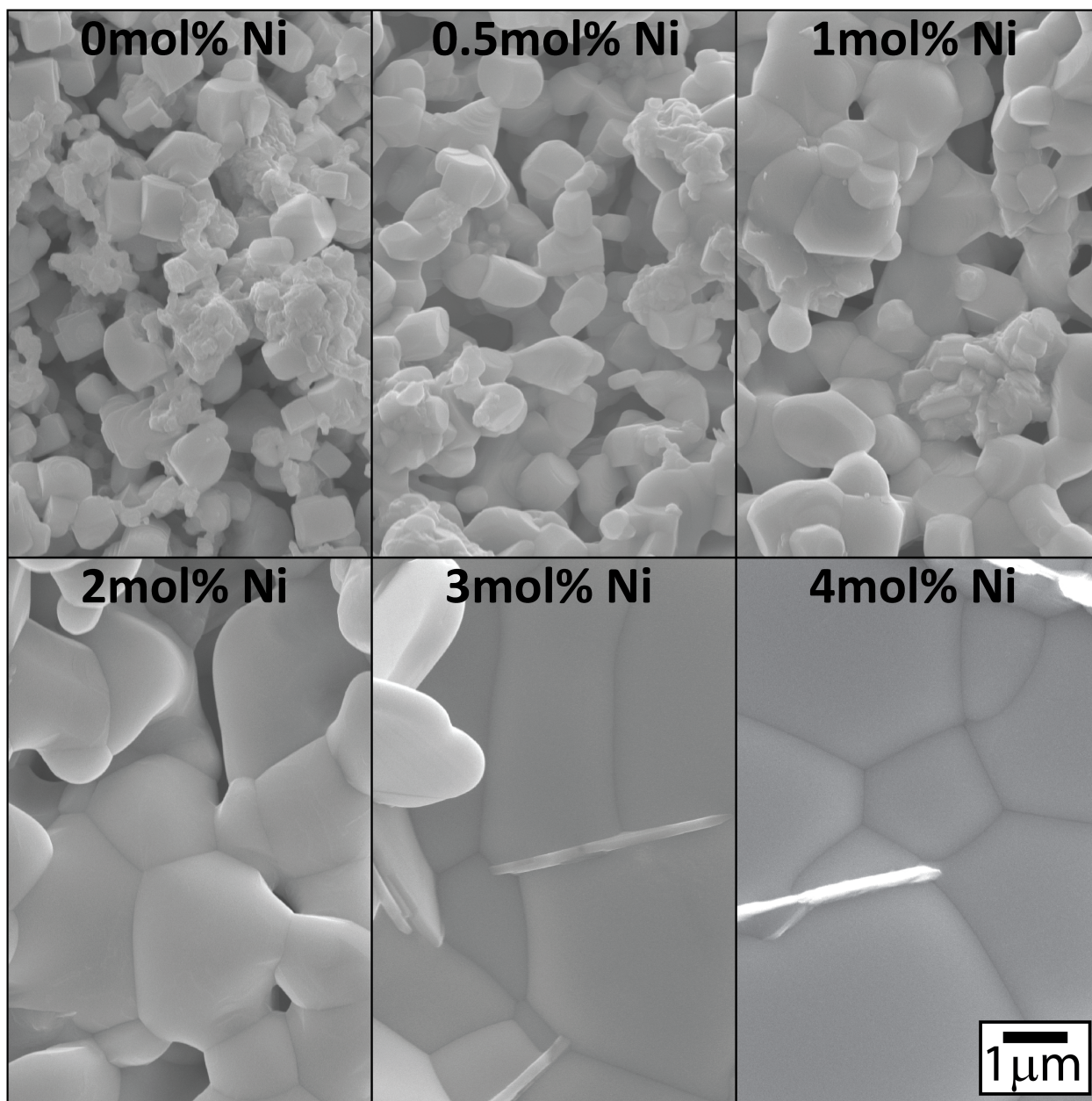


Figure 5.2 Scanning electron micrographs (secondary electron) of internal surfaces in Ni-doped BZY20 samples prepared via solid-state reactive sintering, cooled at 5 °C/min after 20 h at 1500 °C. As expected, grain growth significantly increased with increasing Ni-doping. The 3 mol% and 4 mol% Ni samples showed platelet-shaped precipitates in what are likely void surfaces and are not representative of the entire sample. STEM-EDS map in Supplemental Figure 5.18 revealed this phase is likely  $Y_2O_3$ .

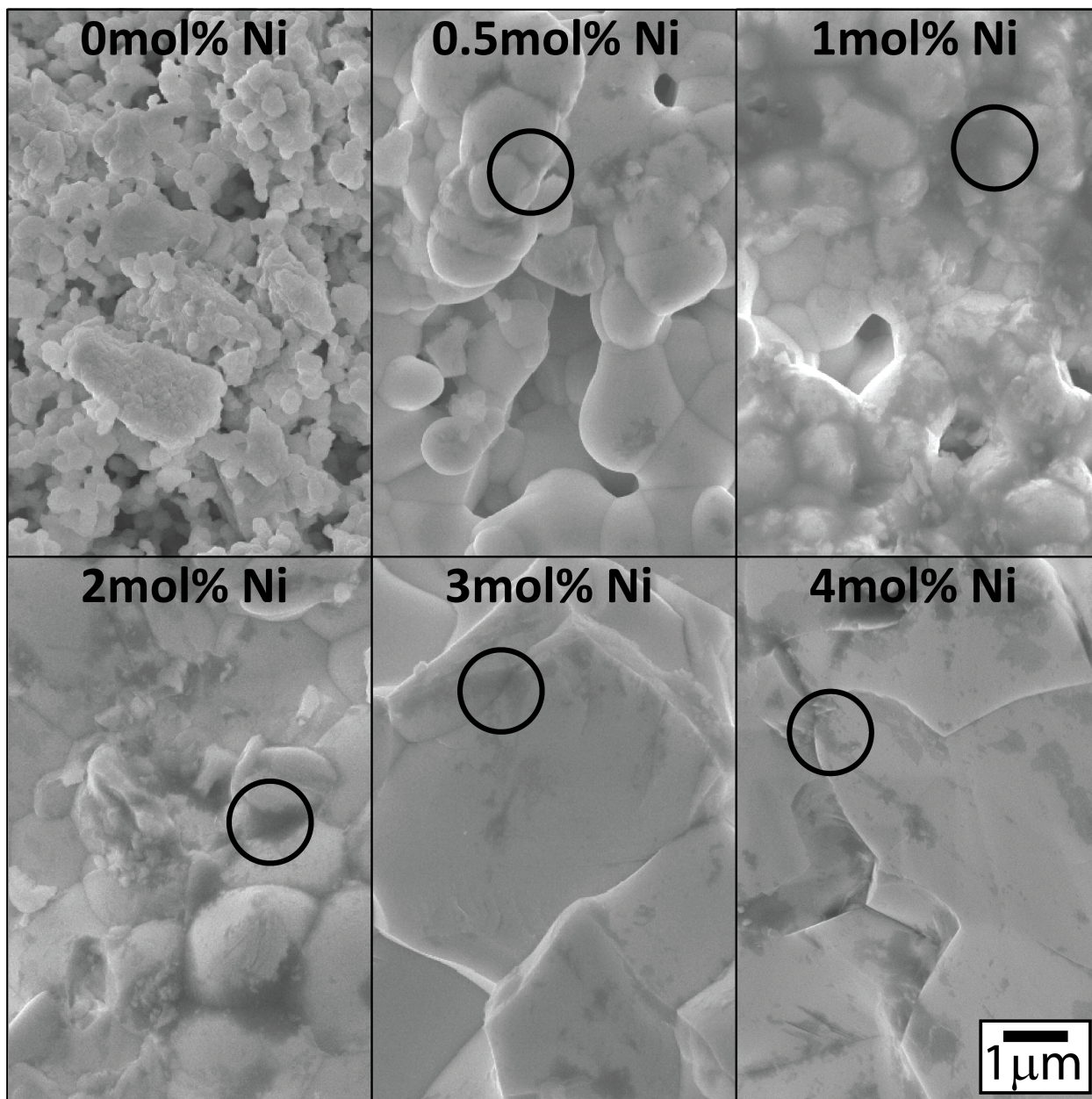


Figure 5.3 Scanning electron micrographs (secondary electron) of internal surfaces in Ni-doped BZY20 samples prepared via solid-state reactive sintering, air quenched after 20h at 1500 °C. In all quenched samples with Ni-doping, a secondary phase (highlighted by circles) that was not evident in XRD patterns is apparent as the darker contrast regions. STEM-EDS map in Figure 5.5 suggested this phase is  $\text{BaY}_2\text{NiO}_5$ .

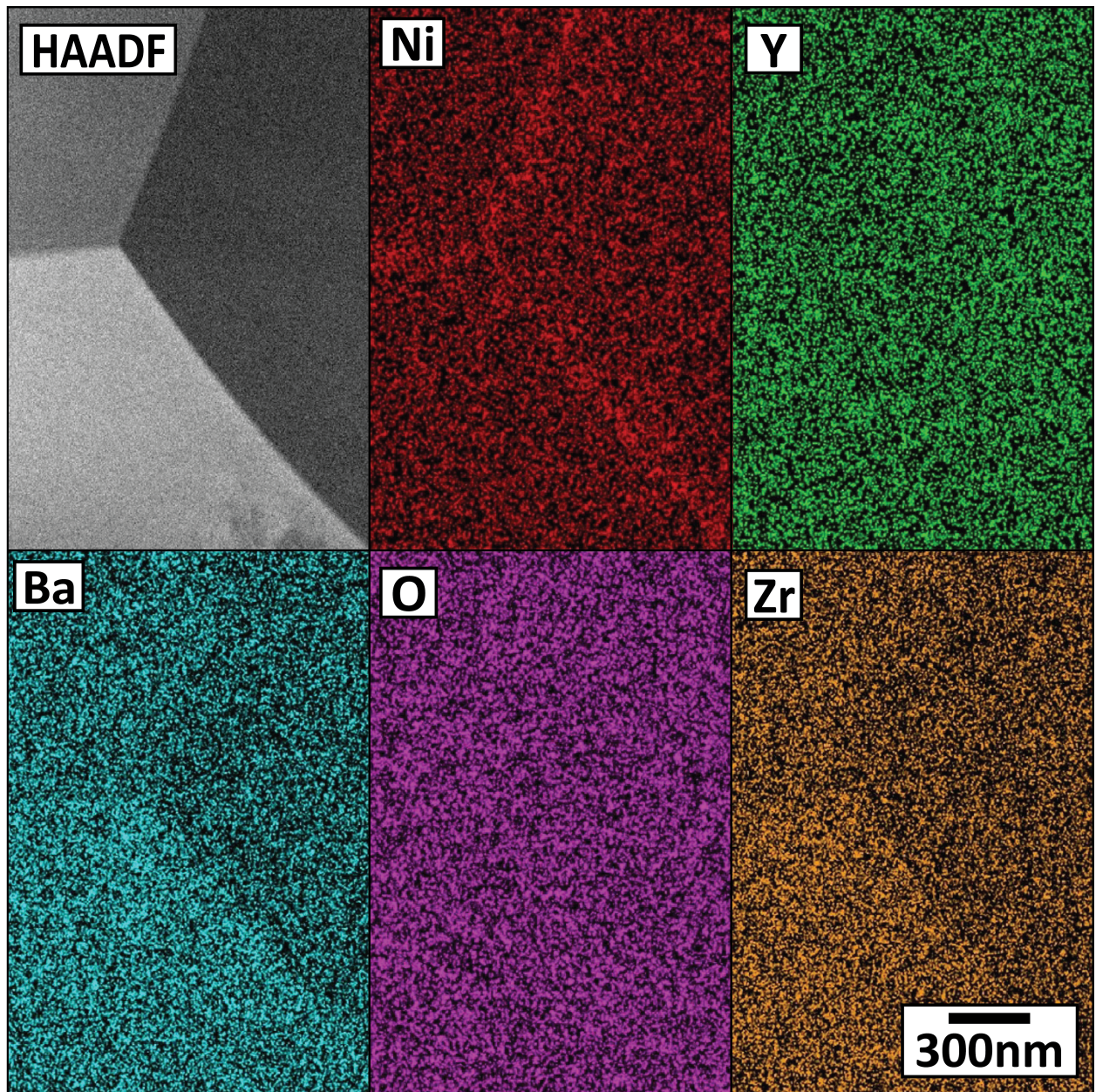


Figure 5.4 STEM-EDS mapping of FIB lift-out from 4 mol% Ni-doped BZY20 sample cooled at 5 °C/min after solid-state reactive sintering. Ni-segregation was identified in the grain-boundary regions. Line scan across one of the interfaces (Supplemental Figure 5.19) showed mass concentration of Ni increased in the grain boundary region.

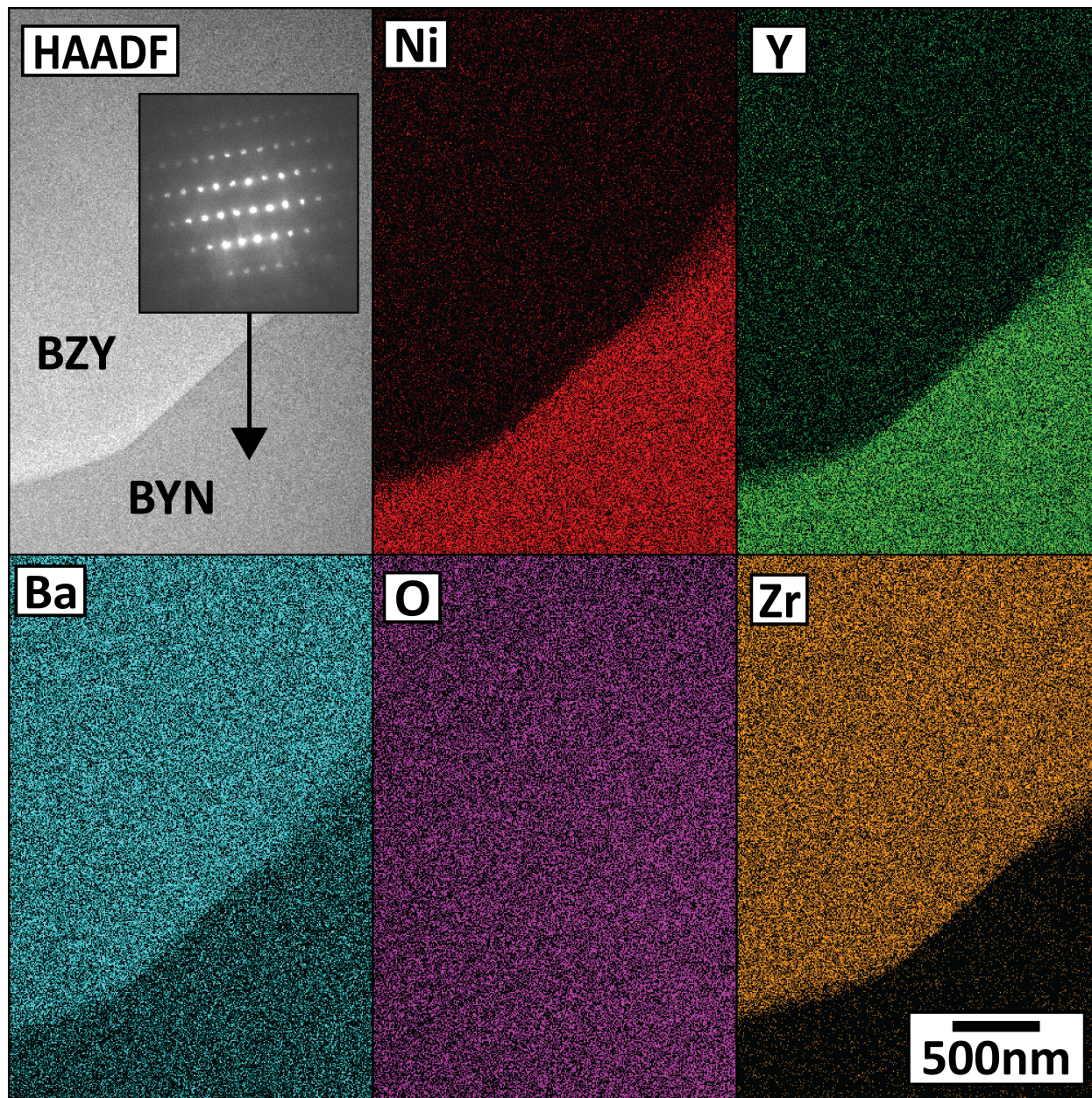


Figure 5.5 STEM-EDS mapping of adjacent BZY and BYN grains in SSRS quenched 4 mol% Ni-doped BZY20 sample. Inset shows electron diffraction pattern of BYN phase. Quantification estimates of phase compositions are available in Supplemental Figure 5.21

For all quenched Ni-doped samples, a darker contrast secondary phase was observed in micrographs of the internal surfaces (Figure 5.3). STEM-EDS of this darker contrast phase in the quenched 4NiBZY20 sample revealed significantly increased Y and Ni signal, slightly decreased Ba signal, and lack of Zr signal (Figure 5.5). Lower Ba signal was expected due to having a lower mass concentration with respect to the total stoichiometry of the BYN phase compared to the BZY phase. STEM-EDS estimated compositions of the 4NiBZY20 and BYN phases are available in Supplemental Figure 5.21. A TEM electron diffraction pattern of this darker-contrast phase was collected (inset in Figure 5.5) and used to estimate lattice parameters  $a \approx 3.1 \text{ \AA}$ ,  $b \approx 5.4 \text{ \AA}$ , and  $\gamma = 90^\circ$ , assuming the [001] zone axis of Orthorhombic BYN (*Immm*).<sup>[196]</sup> These estimated lattice parameters and STEM-EDS mapping results indicate the darker phase present in the quenched samples was BYN. In the slow-cooled samples BYN was not observed, consistent with previous work that proposed BYN is present at 1500 °C during sintering and decomposes upon cooling in the SSRS process.<sup>[58]</sup>

All slow-cooled samples were characterized with magnetometry. Because the quenched samples clearly contained a second phase having significant Ni, magnetometry results from those samples are not included here; essentially, the complexity in deconvoluting results from mixed magnetic phases provided a significant barrier in the analysis. Magnetic susceptibility *vs.* temperature,  $\chi(T)$ , measurements closely resembled Curie-Weiss paramagnetism (Supplemental Figure 5.9), indicating Curie-Weiss analysis can be used. However, as temperature increased to 300 K, the susceptibility remained increasingly positive, indicating temperature independent paramagnetism (TIP) may have contributed to the susceptibility increases with Ni-doping. TIP may occur when the magnetic cations have a low-lying excited electronic state and the applied field mixes some excited state character with the ground state.<sup>[116]</sup> Linear fits of the reciprocal susceptibilities and Weiss constants are shown in Figure 5.6, respectively.  $\theta$  became more negative with Ni-doping, suggesting AF interactions became stronger as Ni-doping increased.

The product function  $\chi T(T)$  (Figure 5.7) was plotted from 1.8 K to 300 K as a check for the presence of zero-field splitting (ZFS) due to magnetic anisotropy. A typical Curie paramagnet with non-interacting species in an isotropic ligand field would show a constant value of  $\chi T(T)$  across the entire temperature range.[189] Figure 5.7 shows a clear decrease in  $\chi T(T)$  at low temperature, where the magnitude increased dramatically with increased Ni-doping. Unfortunately, this observation cannot be solely attributed to ZFS, as negative exchange interaction between Ni-cations also contributes to this trend at low temperature.[189] Another utility of plotting  $\chi T(T)$  manifests upon inspection of the slope in the linear region (higher  $T$ ), where a small positive slope can indicate TIP.[189]

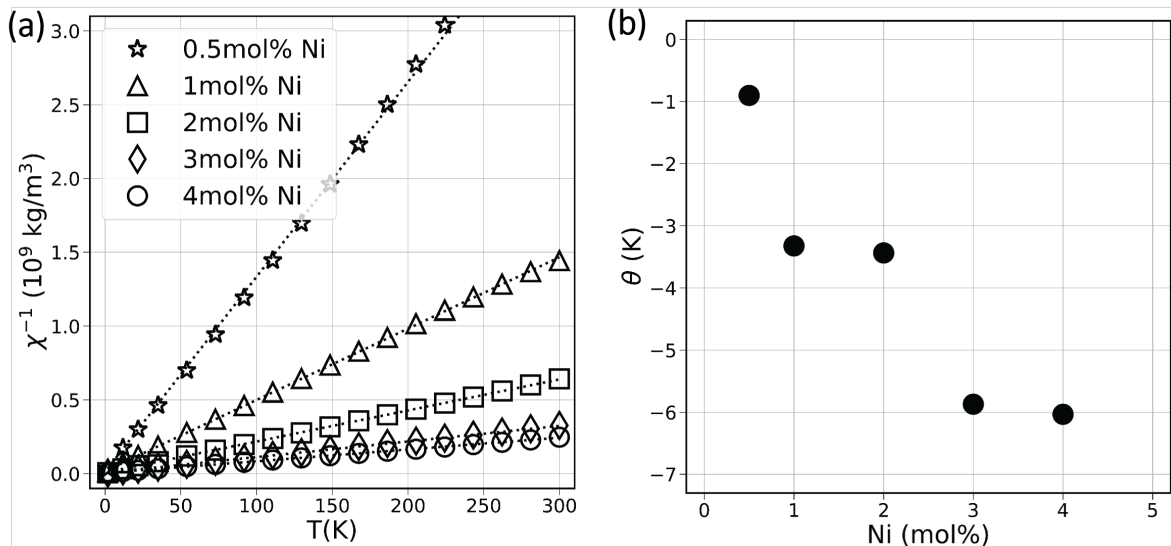


Figure 5.6 Reciprocal magnetic susceptibility of slow-cooled SSRS  $x\text{NiBZY}20$  samples. Linear fits for Curie-Weiss analysis provide estimated magnetic moments per Ni and Weiss exchange temperatures  $\theta$ . Errors in  $\theta$  were not estimated due to complexity in propagating error from the raw measurements through the background corrections and fitting analysis. Therefore, the trend towards more negative values with increasing Ni-doping is only qualitatively used to suggest negative exchange interactions between Ni, not for assigning quantitative values to the magnitude of the exchange.

EPR derivative spectra of the  $4\text{NiBZY}20$  sample at 3 K and 100 K (Supplemental Figure 5.10) resemble that of a nearly axial system, but show slight orthorhombic distortion. The most intense absorptions at  $g_2 \approx 2.24$ ,  $g_3 \approx 2.35$  were assigned to the

octahedron perpendicular axes ( $x, y$ ), and lower intensity absorption at  $g_1 \approx 2.03$  to the parallel axis ( $z$ ). The isotropic average is calculated to be  $g_{\text{avg}} = \frac{1}{3}(g_1 + g_2 + g_3) \approx 2.2$ , and overall anisotropy for the Ni-coordination environment was calculated to be  $\Delta g = g_{\parallel} - g_{\perp, \text{avg}} \approx -0.26$ . The presence of anisotropy verifies that the low-temperature decreases in  $\chi T(T)$  were not only caused by AF interactions, but ZFS as well.

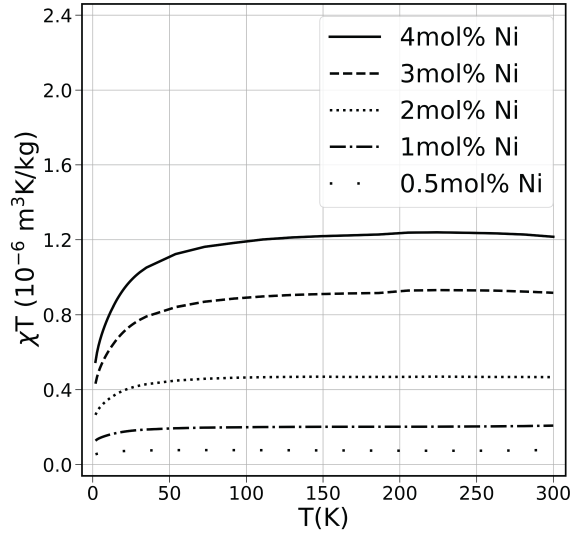


Figure 5.7 Product function  $\chi T(T)$  of SSRS  $x\text{NiBZY}20$  samples. Decreases at low temperature indicate the presence of negative exchange interactions (antiferromagnetic) and zero field splitting. Small positive slope in linear region suggests a small presence of temperature independent paramagnetism.[189]

Additionally, the relative size of  $g_{\parallel}$  versus  $g_{\perp}$  can provide useful information about the presence of defect complexes.[197] Here,  $g_{\parallel} < g_{\perp}$  indicates the defect complex  $(\text{Ni}_{\text{Zr}}' - \text{V}_{\text{O}}^{\bullet\bullet})^{\bullet}$  may be present.[198] Similar  $g$ -factors identifying this complex were reported for low-spin  $\text{Ni}^{3+}$  substituting  $\text{Ti}^{4+}$  in  $\text{SrTiO}_3$ , where negative  $g$ -factor anisotropy suggested the  $\text{Ni}^{3+}$  is displaced along the  $C_4$  axis by electrostatic repulsion of the  $\text{V}_{\text{O}}^{\bullet\bullet}$ , resulting in elongated octahedra.[199, 200] The  $4\text{NiBZY}20$  sample measured here contains a significant amount of  $\text{Ni}^{3+}$ , however, the presence of  $\text{Ni}^{2+}$  could not be determined, because  $\text{Ni}^{2+}$  is a non-Kramers ion requiring large magnetic fields/microwave frequencies to

detect resonance.[158] Regardless, these results show that acceptor  $\text{Ni}^{3+}$  substitutes for  $\text{Zr}^{4+}$ , it likely forms an oxygen vacancy defect complex, and EPR could be used in future work on this system.

The EPR determined average  $g$ -factor was used in Equation 5.1 to fit  $M(H)$  curves measured at 3 K and 100 K (Supplemental Figure 5.11) for the total angular momentum,  $J$ , and concentration,  $N$ , of the Ni-dopant. As the applied field approached 7 T, the 3 K magnetization saturated and the 100 K magnetization remained linear, as expected for a paramagnetic system.[116] The observation of TIP suggested low-field and high-field analysis of  $M(H)$  response could produce different results, so each  $M(H)$  data set was separately fit up to 0.5 T and 7 T. The fitted  $J$  values, combined with the measured  $g$ -factors, were used to calculate the effective magnetic moments per Ni in units of Bohr magnetons using the standard relationship:  $\mu_{\text{eff}} = g\sqrt{J(J+1)}$ . These results are compared with the Curie-Weiss fitting results for magnetic moment per Ni in Figure 5.8.

The 100 K low-field and high-field  $M(H)$  Brillouin fit  $\mu_{\text{eff}}$  values closely matched the Curie-Weiss  $\mu_{\text{eff}}$  values and the ideal Ni concentrations (Supplemental Figure 5.12). Assuming minimal orbital angular momentum contribution to the  $3d$  moments, the expected  $\mu_{\text{eff}}$  of low-spin state and high-spin state  $\text{Ni}^{3+}$  are  $\approx 1.8\mu_{\text{B}}$  and  $\approx 3.9\mu_{\text{B}}$ , respectively, while the expected magnetic moment of  $\text{Ni}^{2+}$  is  $\approx 2.8\mu_{\text{B}}$ . [116] The 100 K Brillouin and Curie-Weiss fits of the 0.5NiBZY20 sample have  $\mu_{\text{eff}}$  that closely matches the low-spin state  $\text{Ni}^{3+}$  value, and as Ni-doping increases,  $\mu_{\text{eff}}$  gradually increases. The 3 K Brillouin fitting results up to 7 T showed higher  $\mu_{\text{eff}}$ , that decreased with increasing Ni-doping, and produced fitted Ni concentrations lower than the ideal concentrations (Supplemental Figure 5.12).

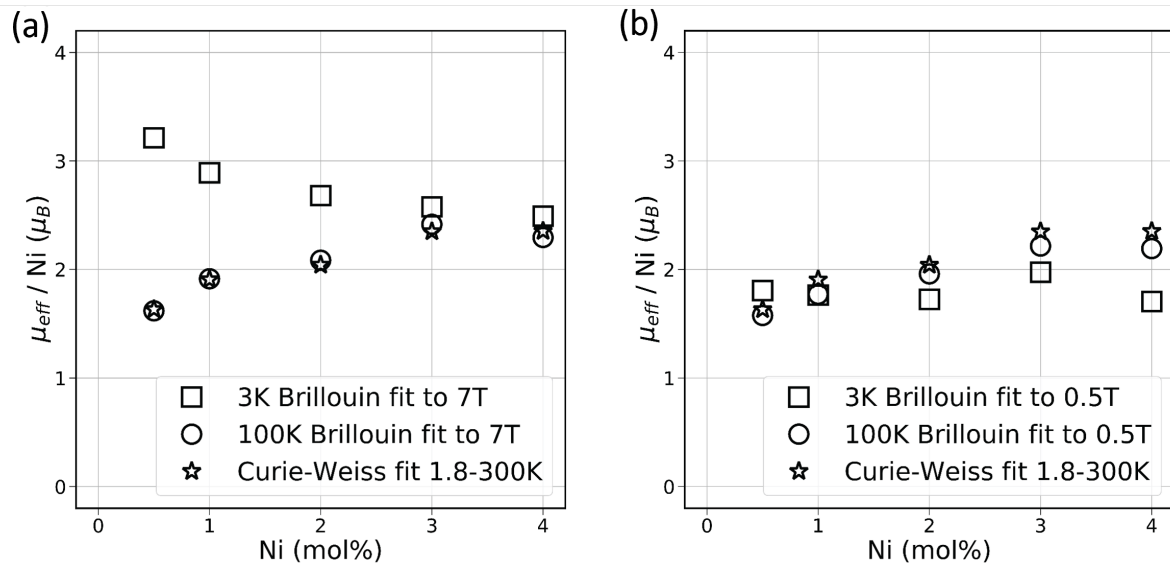


Figure 5.8 Effective magnetic moments per Ni determined by high-field (7 T) Brillouin fits of  $M(H)$  data (a) and low-field (0.5 T) Brillouin fits of  $M(H)$  (b) for SSRS  $x\text{NiBZY}20$  samples cooled at  $5^\circ\text{C}/\text{min}$ . Results for both cases are compared with effective magnetic moments per Ni determined by Curie-Weiss fits of reciprocal magnetic susceptibility data between 1.8 K and 300 K. Errors in this data were not estimated due to the complexity in propagating error from the raw data through fitting  $M(H)$  curves with the Brillouin function (5.2). Therefore, only qualitative information can be extracted from trends of the Ni moments.

## 5.5 Discussion

During high temperature formation of BYN, Ba and Y are presumed to be extracted from their respective A- and B-sites in the perovskite lattice of BZY. It is considered that the present samples may have an excess of insoluble Y, though it is unclear on what the maximum B-site substitution of Zr by Y is. When co-sintered with NiO at 1500 °C, a limit of Y substitution for Zr was experimentally estimated to be approximately 12 mol%, while EXAFS results estimated a limit of approximately 16 mol% without NiO.[195, 201] Yamazaki et al. determined BZY20 perovskite is tolerant to Ba deficiency up to 6 mol%, and recently, Huang et al. determined Ba deficiency increases with increasing NiO additions in SSRS BZY.[56, 65] The doping stoichiometries studied here (20 mol% Y, 0.5–4.0 mol% Ni) all displayed evidence of BYN phase formation during the 1500 °C SSRS process, consistent with BZY literature suggesting BZY cannot be in equilibrium at 1500 °C with NiO when Y-concentration is at 20 mol%.[195] This result is also consistent with computational results that calculated the exsolution of BYN from Ba-deficient BZY in the presence of NiO to be significantly exothermic ( $\Delta H = -4.43$  eV).[163]

The microscopy results presented here suggest the concentration of BYN phase formed increased with increasing Ni concentration (Figure 5.3). The observation that  $Y_2O_3$  was present in slow-cooled samples (Supplemental Figure 5.18) is consistent with the conclusion that BYN was a transient phase present at high temperatures, decomposed during slow cooling and left residual  $Y_2O_3$  in the microstructure (and likely a Ba containing phase that was not confirmed here). Ni segregation in the grain-boundary regions was observed in the slow-cooled 4NiBZY20 sample (Figure 5.4); however, in the quenched sample of the same composition, Ni segregation was not observed (Supplemental Figure 5.20). Therefore, it can be concluded that upon completion of the SSRS process, the observed Ni segregation in the grain-boundary regions likely resulted from decomposition of the secondary BYN phase.

The acceptor dopants  $Y^{3+}$  and  $Sc^{3+}$  have been previously observed to segregate in grain-boundary regions in BZY after sufficient time at high temperature.[119, 132] This

can be explained via a “space-charge” model: negatively charged defects compensate the positively charged grain-boundary core produced by excess oxygen vacancies. In the present work, the  $\text{Ni}^{3+}$  may behave similarly: upon decomposition of the transient BYN phase, acceptor  $\text{Ni}^{3+}$  remains in the grain-boundary space-charge regions to compensate the positively charged grain-boundary core. Conversely, as the SSRS samples cool down slowly from  $1500^\circ\text{C}$ , the BYN phase decomposes and the decreased temperature is not sufficient for mass transport of the Ni beyond the grain boundary regions into the bulk BZY lattice.

The magnetometry and EPR measurements presented here show unequivocally that significant concentration of Ni existed in a 3+ oxidation state in all Ni-doped samples. This Ni valence agrees with a study by Han et al. who concluded with XANES and EXAFS that  $\text{Ni}^{3+}$  sits on interstitial  $(1/2, 0, 0)$  sites in BZY mixed with excess NiO and sintered at  $1400^\circ\text{C}$  and  $1600^\circ\text{C}$  in air, then furnace cooled.[134] on the other hand, it contrasts with computational predictions that indicate  $\text{Ni}^{3+}$  is less energetically favorable than  $\text{Ni}^{2+}$  when NiO is added to BZY.[163] The following discussion offers the most likely explanation for the observations presented here.

Rapidly decaying  $\chi(T)$  from 1.8 K to 300 K (Supplemental Figure 5.9) and saturation of  $M(H)$  at 3 K (Supplemental Figure 5.11) clearly reveals that the predominant magnetism of the Ni-dopants is paramagnetic.[116] Observation of increasingly negative Weiss constants (Figure 5.6) suggests weakly antiferromagnetic (AF) interaction increases as Ni-doping increases. One explanation that connects this with Ni segregation, could be the presence of residual, AF  $\text{BaY}_2\text{NiO}_5$  or NiO phase at the GB. Alternatively, AF coupling between two next-nearest neighbor cations of the same valence through a nonmagnetic anion (superexchange) could also lead to the observation of negative  $\theta$  values.[116] Qualitatively, the splitting of  $3d$ -orbitals in octahedral oxygen coordination is treated as an electrostatic effect when the oxygen anion neighbors are treated as point charges. In reality, the nickel  $3d$ - and oxygen  $2p$ -orbitals overlap, where the overlap is greater for  $e_g$ - than  $t_{2g}$ -orbitals.[116] This overlap forms a partially covalent bond with

hybridized orbitals, and the oxygen 'bridge' enables superexchange interaction between the adjacent cations by virtual and simultaneous transfer of two  $e^-$ . [116] This interaction is AF when two identical cations have lobes of singly occupied  $3d$ -orbitals pointing towards each other, as expected here for  $180^\circ \text{Ni}^{3+}\text{-O-Ni}^{3+}$  configurations. Considering the dilute Ni concentrations studied here, these configurations are more probable where Ni is segregated *versus* inside the grains. Ni segregation in the samples having  $< 4 \text{ mol}\%$  Ni was not confirmed here, however, it is likely that the extent of segregation increases with Ni-doping.

The 100 K  $M(H)$  and  $\chi^{-1}(T)$  fitting results (Figure 5.8) showed a gradual increase in  $\mu_{\text{eff}}$  with increased Ni-doping. If decreasing  $\theta$  values were caused by increasing formation of minor AF phase(s) ( $\mu_{\text{eff}} = 0$ ), then  $\mu_{\text{eff}}$  would be expected to remain relatively constant as Ni-doping increases. The gradual increase in  $\mu_{\text{eff}}$  is most likely connected to the observed TIP (Supplemental Figure 5.9) contributions to magnetic susceptibility as Ni-doping increases. However, the alternative explanation that a thin grain boundary phase of  $\text{BaY}_2\text{NiO}_5$  or NiO (where Ni is in a 2+ state) having incomplete AF cancellation of moments cannot be ruled out.

The 3 K  $M(H)$  fitting results (Figure 5.8) revealed decreasing  $\mu_{\text{eff}}$  as Ni-doping increases. This is consistent with the proposed AF superexchange interaction having more pronounced effects at low-temperature (Figure 5.7). The least AF character was observed for the 0.5NiBZY20 sample, and the most for the 4NiBZY20 sample (Figure 5.6(b) and Figure 5.7). Therefore, as Ni-doping increases, the increasing presence of superexchange lowers  $\mu_{\text{eff}}$  accordingly. Additionally, the relatively larger  $\mu_{\text{eff}}$  values observed under high-field at 3 K for all samples, suggests the application of high-fields at 3 K enabled significant population of a low-lying excited electronic state. Examination of only the high-field  $M(H)$  at 3 K results (Figure 5.8(a)) revealed the highest value ( $\mu_{\text{eff}} \approx 3.2\mu_{\text{B}}$ ) for the 0.5NiBZY20 sample, which is smaller than the expected  $\text{Ni}^{3+}$  high-spin value ( $\approx 3.9\mu_{\text{B}}$ ). The crystal field is responsible for stabilizing ionic structures and determines occupation of the energy levels for the  $\text{Ni}^{3+}$  valence electrons. Strong octahedral crystal fields typically

drive the  $d^7$  cation ( $\text{Ni}^{3+}$ ) into a low-spin state (one unpaired  $e^-$ ).[116] When the low-spin state lies only slightly lower in energy than the high-spin state (3 unpaired  $e^-$  for  $\text{Ni}^{3+}$ ), a crossover may occur as a function of temperature due to magnetic entropy.[116] This likely explains why the high-field 3 K  $M(H)$   $\mu_{\text{eff}}$  values were relatively larger than those at 100 K.

The location of  $\text{Ni}^{3+}$  in the structure is important for performance of PCFCs utilizing SSRS preparation of BZY20. In the typical sintering additive approach, where NiO is added to stoichiometric BZY20, Ni was demonstrated experimentally and computationally to prefer the (1/2,0,0) interstitial site as a complex with adjacent Ba-site vacancy.[134, 163] Formation of Ba vacancies is known to be detrimental to proton conduction and therefore should be minimized.[56] The equilibrium conductivity of BZY20 with 1 wt% NiO additions is also lower than BZY20 without NiO additions.[202] Additionally, SSRS of BZY20 with NiO additions was shown to have lower proton uptake than BZY20 prepared with intentional Ni substitution for Zr.[65] It is reasonable to assume this improved proton uptake occurs when Ni is substituted at the Zr site, therefore minimizing the generation of Ba vacancies. Oikawa and Takamura reported oxygen vacancy associations with Sc-acceptors in  $\text{BaZrO}_3$  and suggested the net positive charge of such defects may inhibit proton trapping via electrostatic repulsion.[133] This would likely also be the case for acceptor  $\text{Ni}^{3+}$  here, resulting in a positive effect on the transport of protons through the lattice. With these considerations, SSRS preparation of BZY20 should incorporate Ni as a substitute for Zr, instead of adding excess NiO.

While this work was performed on dense BZY pellets, it is important to note that samples for fuel cell or electrolysis testing are prepared by depositing a thin BZY layer onto a BZY/NiO composite anode. The high temperatures required for co-sintering result in Ni diffusion into the electrolyte. Future work quantifying of the amount of Ni in the electrolyte as a function of sintering temperatures and compositions would provide useful information. The highest protonic conductivity in BZY is expected for well sintered large-grained samples, with no Ba under- or over-stoichiometry, and with clean

grain-boundaries. Because such a material is challenging to produce, compromise is needed. While this study focused on the decomposition of the BYN phase resultant from solid-state reactive sintering, conductivity measurements on samples slowly cooled and quenched could give more insight on the best preparation technique and optimal Ni content. Future work could focus on the impact of substituting Zr with Ce, or Y with Yb. Similar to the analysis of Ni-doping here, paramagnetic  $\text{Ce}^{3+}$  and  $\text{Yb}^{3+}$  could also be characterized with magnetometry having  $J = 2.5$  and  $J = 3.5$ , respectively.[116]

## 5.6 Conclusions

The SSRS process is certainly an attractive route to easily prepare dense BZY electrolytes. The results presented here reveal new information that correlates the oxidation state and microstructural distribution of the commonly used sintering additive Ni. This information could be used to improve understanding of PCFC performance when the SSRS process is implemented. Intentional Ni substitution for Zr was confirmed here to produce a secondary BYN phase at  $1500^\circ\text{C}$  that decomposed upon cooling (similar to NiO added to stoichiometric BZY precursor oxides) for all Ni concentrations studied. Based on the magnetic analysis presented here, a significant amount of  $\text{Ni}^{3+}$  was substituted for  $\text{Zr}^{4+}$ ; however, when NiO is added to stoichiometric BZY20 this substitution may be less favorable. EPR was utilized here to obtain accurate  $g$ -factors for fitting of magnetometry data, but in addition, the spectra also revealed useful information about local environment of the Ni-dopants and suggest further investigation with higher frequency resonance experiments would be worthwhile. Future work should include high-resolution TEM of the grain-boundary regions to confirm or rule-out a secondary  $\text{Ni}^{3+}$  containing phase and magnetometry of SSRS stoichiometric BZY20 with excess NiO.

## 5.7 Acknowledgements

The author acknowledges Dr. Serena Eley (CSM) for access to the MPMS3, Dr. Ron Goldfarb (NIST) for magnetometry advice, Abigail Meyer (CSM) for collecting the EPR

spectra, and Jake Huang (CSM) for useful discussions regarding the SSRS process. This research was supported by the National Science Foundation Graduate Research Fellowship Program (NSFGRFP) and National Science Foundation Division of Materials Research (DMR) award number 1563754.

## 5.8 Supplemental Information

This section contains supplemental figures and information supporting this work. It contains all of the same content as the supplemental file associated with the published article, with the exception of the individual XRD patterns.

### 5.8.1 Magnetic Characterization

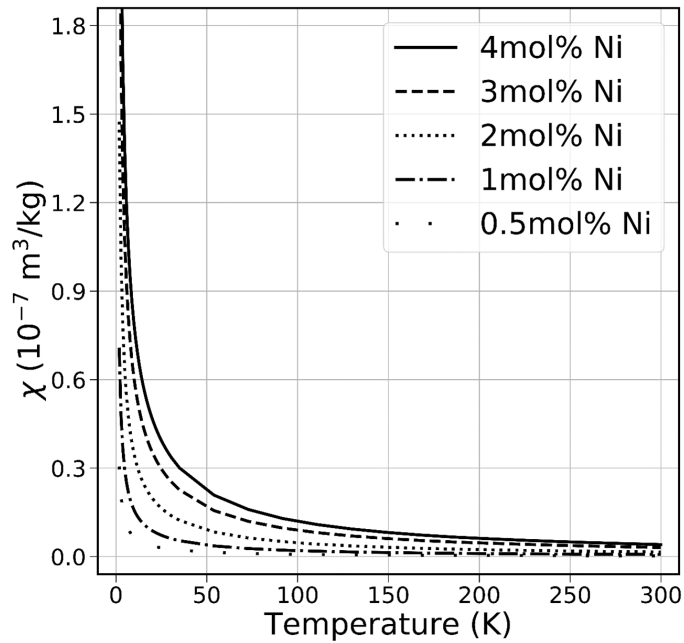


Figure 5.9 Mass magnetic susceptibility from 1.8 K to 300 K under 0.2 T applied field (below saturation at all  $T$ ) for slow-cooled SSRS  $x$ NiBZY20 samples. All data is corrected for diamagnetic background and displays paramagnetic behavior.

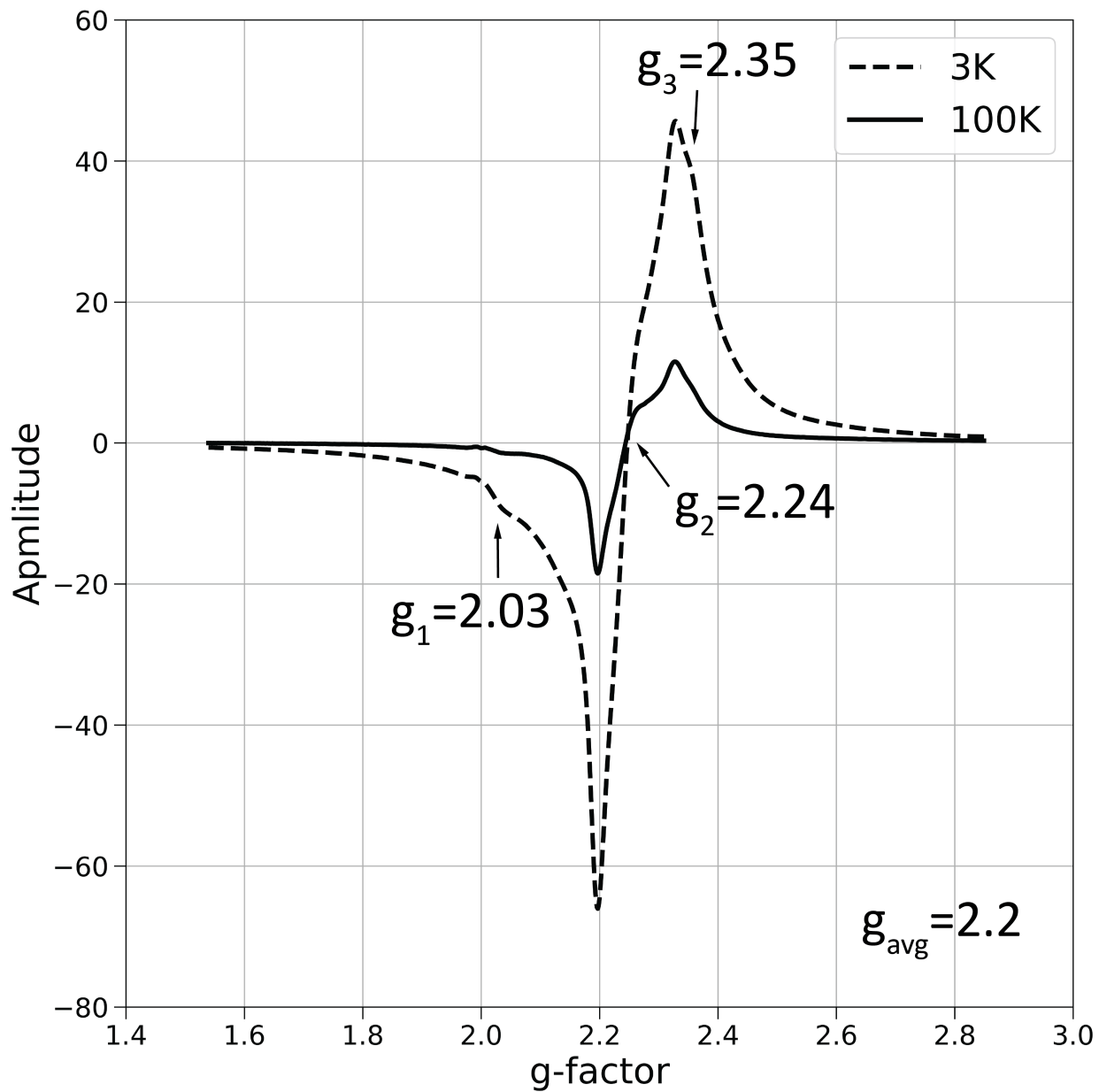


Figure 5.10 X-band EPR spectra of 4NiBZY20 sample collected at 3 K and 100 K. The spectra reveal slight orthorhombic distortion of the octahedra, suggesting the presence of zero field splitting and defect association with an adjacent oxygen vacancy.

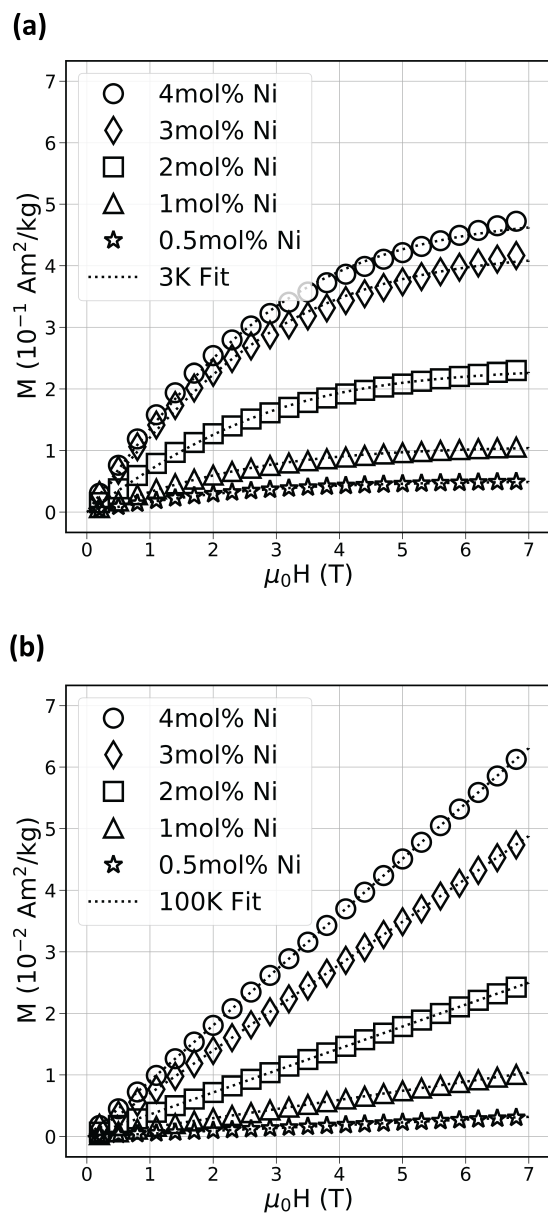


Figure 5.11 Mass magnetization *versus* applied magnetic field at 3 K (a) and 100 K (b) for slow-cooled SSRS  $x\text{NiBZY}_{20}$  samples. Note the  $10\times$  smaller values in (b), as expected at 100 K from the temperature dependence shown previously in Figure 5.9

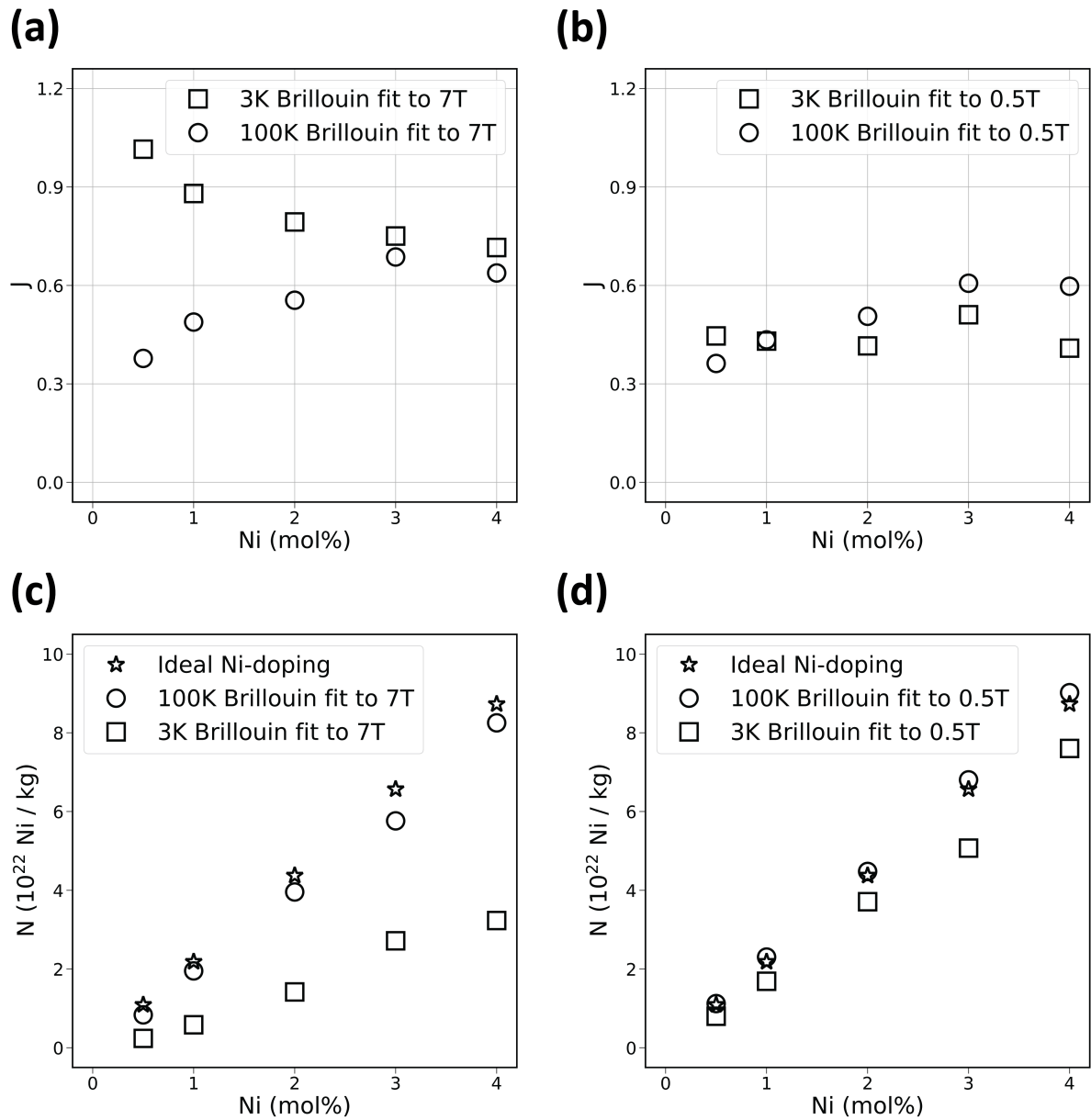


Figure 5.12 High-field (a and c) and low field (b and d) Brillouin fitting results for 3 K and 100 K  $M(H)$  data. The fitted concentrations,  $N$ , are compared against the ideal Ni-doping concentrations (c and d). Errors in this data were not estimated due to the complexity in propagating error from the raw data through fitting individual  $M(H)$  curves with the Brillouin function (5.2). Therefore, only qualitative information can be extracted from the absolute values and general trends of  $J$  and  $N$ .

The following discussion provides details for the analysis of magnetometry data with the 0NiBZY20 sample used as a representative example. This sample had no Ni-doping and provides a good approximation for the level of paramagnetic impurities present in the precursor powders as well as those potentially introduced during processing for all samples in this report. Great care was taken during all sample preparation and handling to avoid introduction of any magnetic impurities. During the processing of all samples, only new cleaned vessels and milling media were used. Additionally, no utensils made of stainless steel were ever used in any steps.

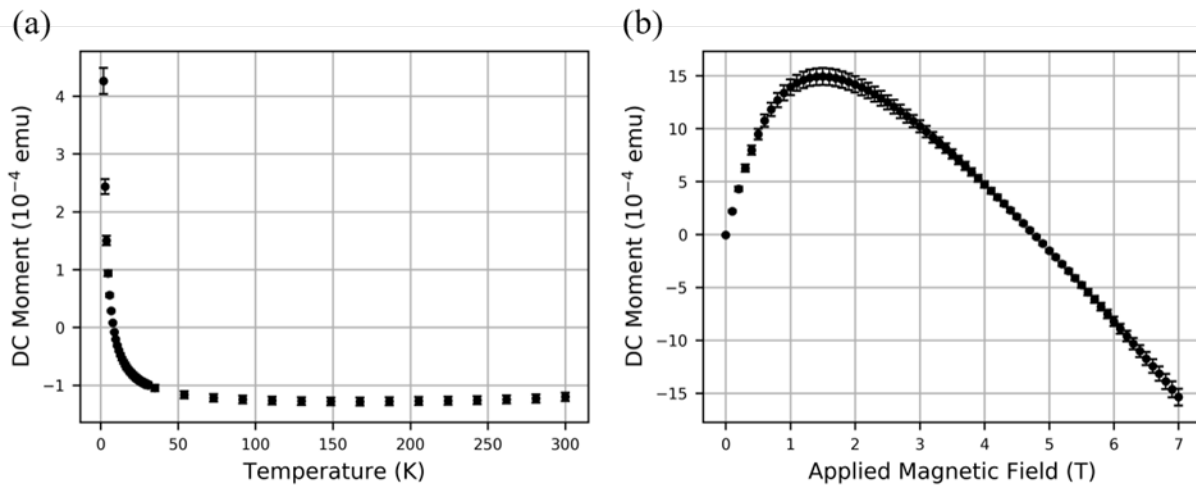


Figure 5.13 Raw magnetic moment versus temperature (a) and applied magnetic field (b) of 0NiBZY20 sample. The only magnetic species present in this sample are impurities introduced from the precursor powders and processing steps. This example is used to demonstrate the sensitivity of the DC SQUID magnetometer, which has low-field ( $< 0.25$  T) sensitivity of  $5 \times 10^{-8}$  emu, and high-field ( $> 0.25$  T) sensitivity of  $6 \times 10^{-7}$  emu.

The raw magnetic moments of pure BZY20 as a function of temperature and applied field are shown in Figure 5.13, respectively. This sample displays typical paramagnetic behavior. The moment rapidly decreases as temperature increases from 1.8 K and drops to the negative diamagnetic (T-independent) value. The paramagnetic impurity magnetization saturates around 1.5 T, and above 1.5 T just the diamagnetic background (negative  $\chi$ ) remains. The MPMS3 has reported sensitivity limits of:  $5 \times 10^{-8}$  emu for

low-field range ( $< 0.25$  T) and  $6 \times 10^{-7}$  emu for high field range ( $> 0.25$  T). The magnitude of the moment in this sample (having only magnetic impurities, no magnetic doping) is on the order of  $10^{-4}$  emu for almost all data points, 100 to 1000 times the sensitivity limit of the instrument.

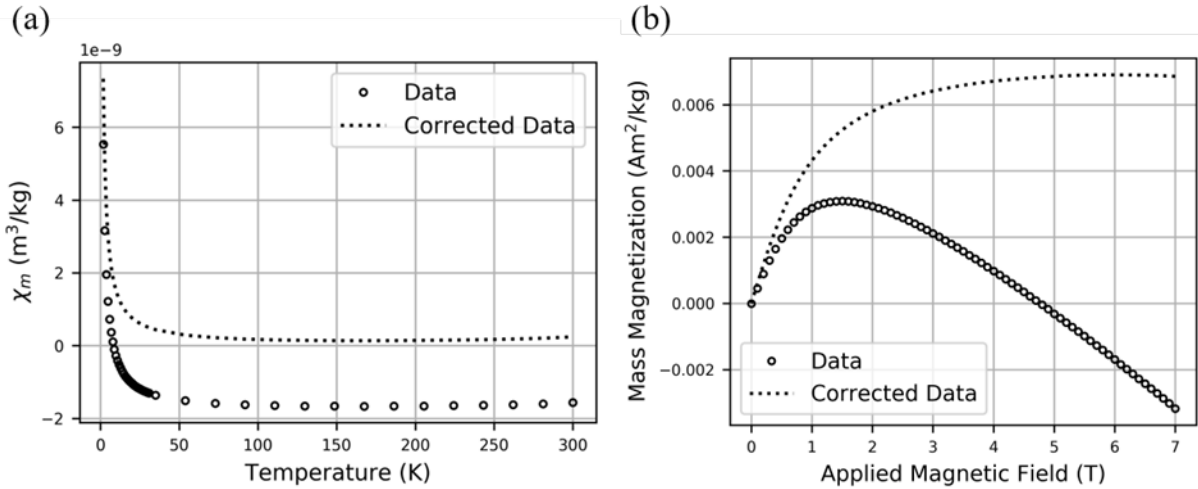


Figure 5.14 Magnetic mass susceptibility (a) and mass magnetization (b) curves normalized with powdered 0NiBZY20 sample mass in SI units. The data points are corrected for the diamagnetic background of the sample and sample holder components to isolate the magnetic impurities contribution to the signal.

To extract useful information from the temperature and field dependent datasets, the diamagnetic background needs to be removed. The diamagnetic background is due to multiple factors: nonmagnetic elements in the lattice (Ba, Zr, Y, O), gelatin capsule used to hold the powder, and the clear plastic drinking straw holding the capsule. This process is increasingly important with increasingly dilute magnetic species, as in this example (the most dilute of all samples). Figure 5.14 shows the corrected data sets after subtracting the diamagnetic component from the combined signal. The diamagnetic slope at high field (6-7 T) was used to estimate the diamagnetic mass susceptibility to be approximately  $-1.3 \times 10^{-9} \text{ m}^3/\text{kg}$ . This value was then used as a starting point to correct the data sets for all samples measured in this work.

After obtaining the mass magnetization versus applied field data, it can then be fit using Equation 5.1. The fitting routine utilized the scipy library implemented in Python 3 with the minimize function using a residual sum of squares and the Nelder-Mead algorithm. The initial values for the fit variables  $N$  and  $J$  were chosen based on the expected magnetic species for each sample:  $J_{\text{init}} = 1.5$  and  $N_{\text{init}} = 1E + 20$  for the pure BZY sample,  $J_{\text{init}} = 1$  and  $N_{\text{init}} = N_{\text{doping}}$  for the Ni-doped samples. The  $g$ -factor was set to 2 for the undoped sample, with the approximation that very dilute  $3d$ -cations in an ionic solid display only spin angular momentum. For the Ni-doped samples, the  $g$ -factor was measured directly by EPR, as mentioned in the main text.

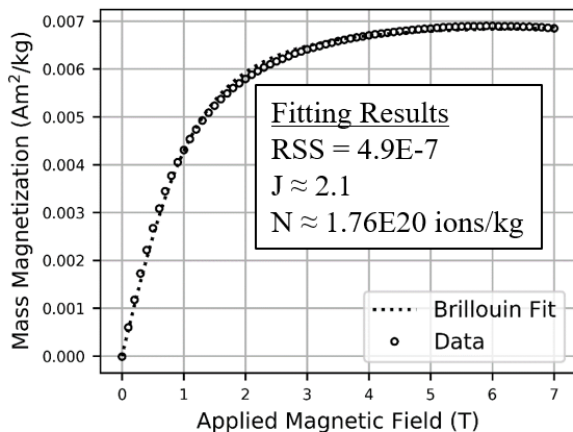


Figure 5.15 Fitting results for 0NiBZY20 mass magnetization curve using Equation 5.1.

The results of fitting the pure BZY sample mass magnetization data are shown in Figure 5.15. The fitted value of  $J \approx 2$  suggests the majority magnetic impurities are high-spin  $\text{Fe}^{4+}$  or  $\text{Fe}^{2+}$ , which both have 4 unpaired  $d$ -electrons in the high-spin state. The fitted concentration of magnetic species  $N \approx 1.76E20\text{ions/kg}$  corresponds to approximately 80ppm impurity concentration. Considering the sensitivity of the SQUID magnetometer, the level of Fe impurities in this sample could likely have been detected even if they were less than 1.

## 5.8.2 Powder X-ray Diffraction

This subsection contains Supplemental figures related to powder X-ray diffraction analysis of Ni-doped BZY20 samples. Figures of the individual XRD patterns for all samples are available in Appendix A.

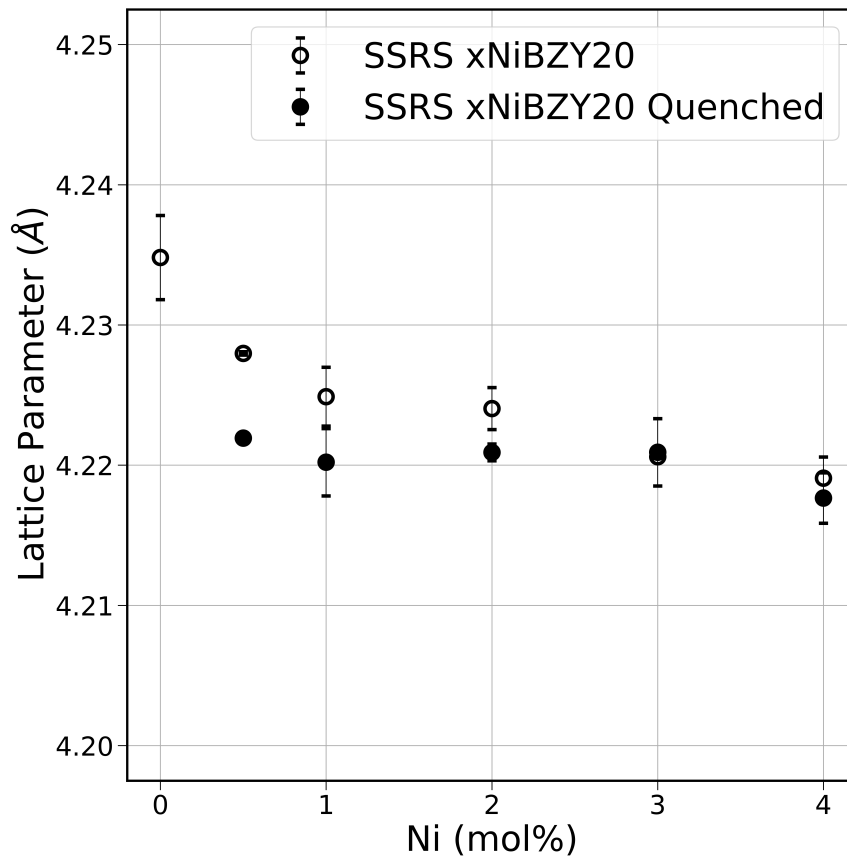


Figure 5.16 Lattice parameters of main BZY phase for solid-state reactive sintered (1500 °C, 20 h) in  $\text{BaZr}_{0.8-x}\text{Y}_{0.2}\text{Ni}_x\text{O}_{3-\delta}$  ( $x = 0.00, 0.005, 0.01, 0.02, 0.03, 0.04$ ) pellets cooled at 5 °C/min (empty circles) and air quenched (filled circles). Pellets were ground into powders for powder X-ray diffraction. The refined estimated standard deviation (ESD) values times a factor of three were used to estimate the errors.

Table 5.1 X-ray diffractometer instrument settings used for collecting powder X-ray diffraction patterns of Ni-doped BZY20 samples.

Parameter	Setting
Start Position ( $^{\circ}2\theta$ )	20
End Position ( $^{\circ}2\theta$ )	100
Step Size ( $^{\circ}2\theta$ )	0.0070
Scan Step Time (s)	25
Temperature ( $^{\circ}\text{C}$ )	25
Anode Material	Cu
K-Alpha1 ( $\text{\AA}$ )	1.54060
K-Alpha2 ( $\text{\AA}$ )	1.54443
K-A2 / K-A1 Ratio	0.50000
Generator	40 mA, 45

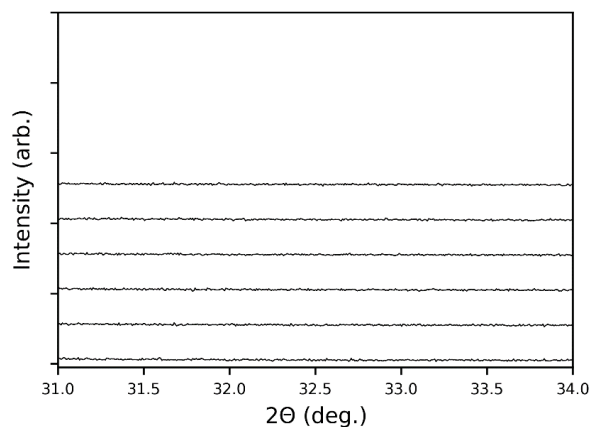


Figure 5.17 Powder X-ray diffraction pattern of quenched samples zoomed in at  $2\theta = 32.4^{\circ}$  where most intense peak of BYN would be located.

### 5.8.3 Electron Microscopy

This subsection contains additional scanning transmission electron microscopy (STEM) energy dispersive X-ray spectroscopy (EDS) figures supporting the results discussed in the main text. This supporting information was used to determine the composition of the secondary platlet-shaped phase found in slow-cooled 3NiBZY20 and 4NiBZY20 samples. Additionally, quantification results of Ni segregation in GB regions is shown for the slow-cooled 4NiBZY20 sample, and absence of Ni segregation in the quenched 4NiBZY20 sample.

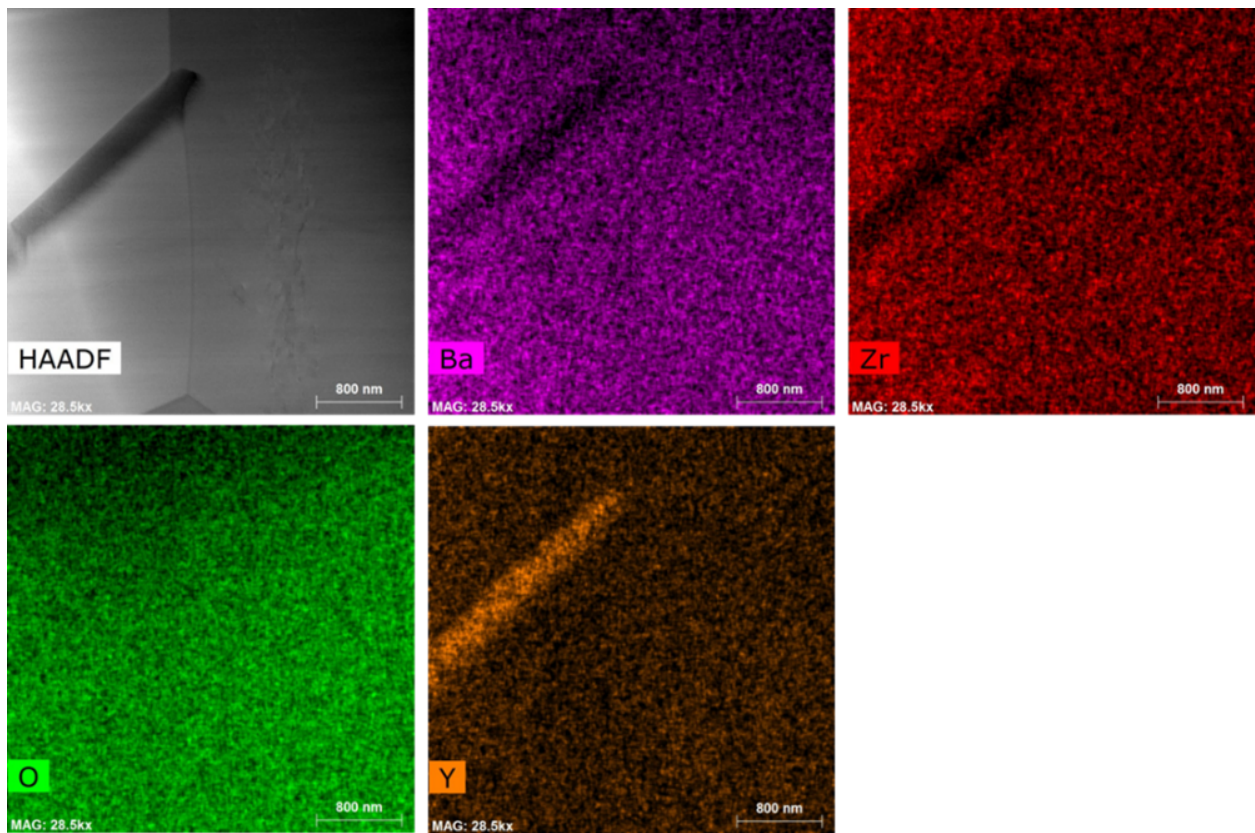


Figure 5.18 STEM-EDS map of platelet shaped precipitate discovered in 4 mol% Ni-doped BZY20 slow-cooled sample. The composition appears to be a secondary  $Y_2O_3$  phase that was left behind after completion of the SSRS process.

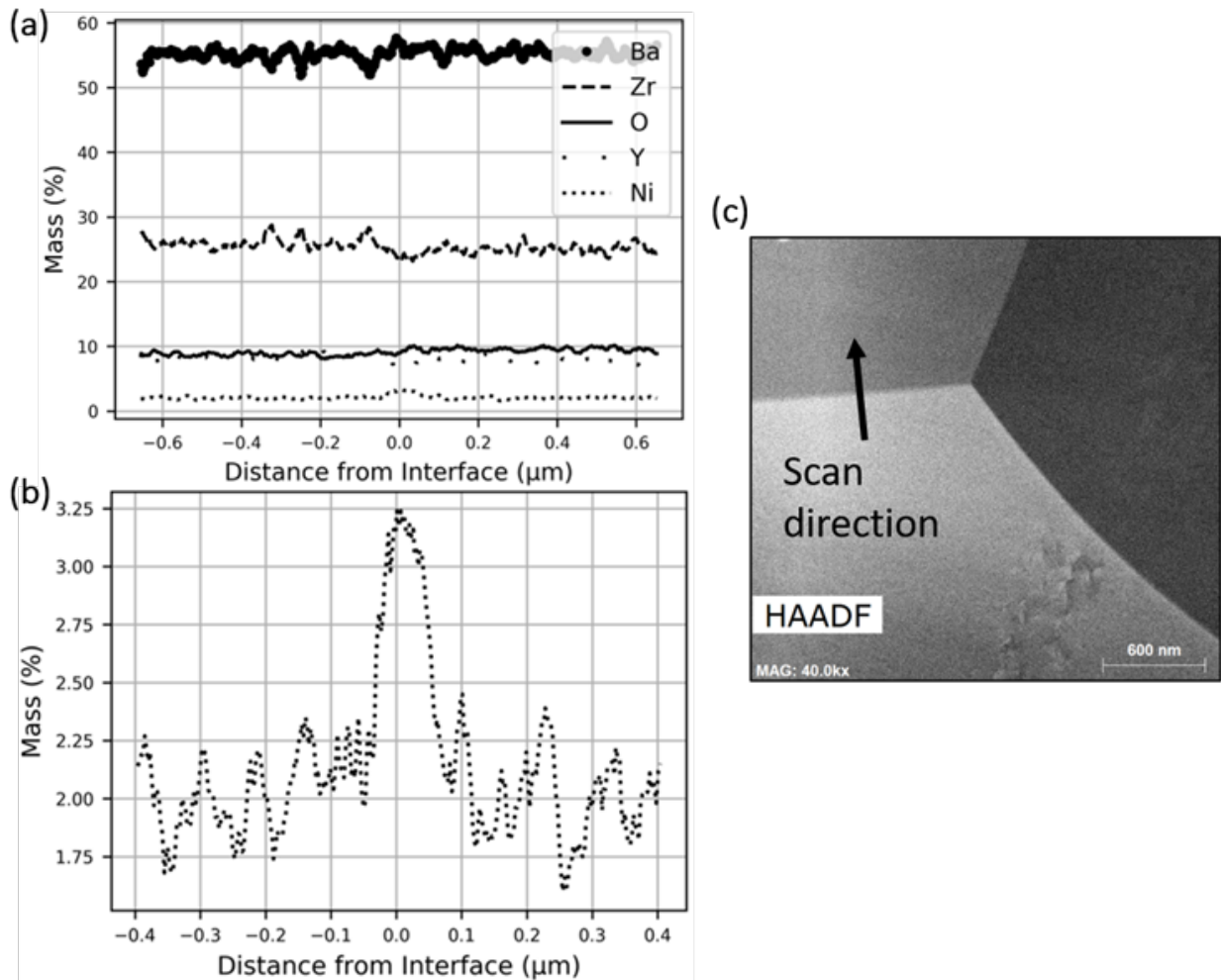


Figure 5.19 STEM-EDS line scan across grain boundary region of slow-cooled solid-state reactive sintered 4 mol% Ni-doped BZY20 sample lift-out. Quantification of all elements (a), magnified Ni concentration (b), and STEM HAADF image showing line scan direction across grain boundary region (c).

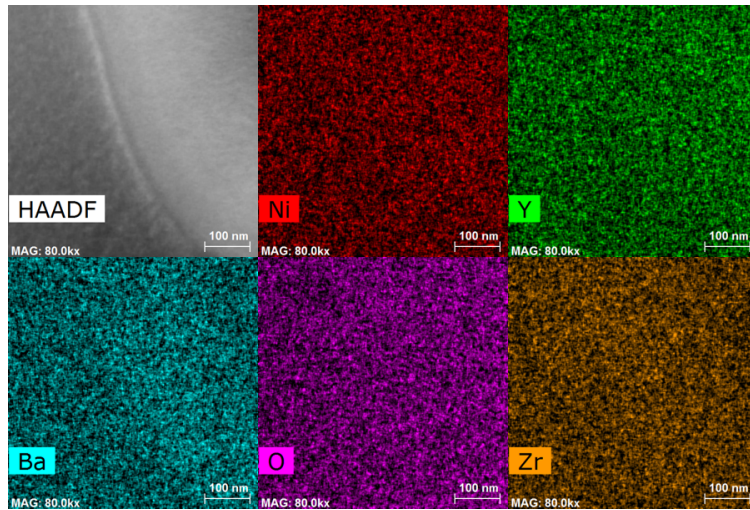
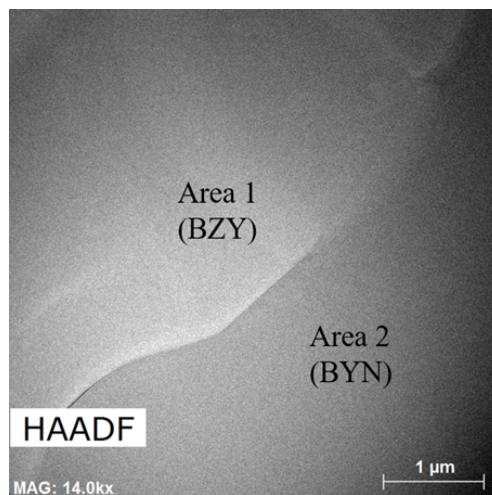


Figure 5.20 STEM-EDS mapping of adjacent BZY grains in quenched 4NiBZY20 sample lift-out. No obvious Ni segregation was observed in the grain boundary region.



Element	Area 1 (at%)	Area 2 (at%)
Ba	30.7 ± 9.3	14.8 ± 4.5
Zr	34.7 ± 3.2	0.7 ± 0.1
Y	5.6 ± 0.6	32.3 ± 3.0
Ni	1.5 ± 0.3	15.6 ± 2.0
O	27.4 ± 2.9	36.5 ± 3.6

Figure 5.21 STEM-EDS quantification of adjacent BZY/BYN grains in 4NiBZY20 quenched sample lift-out. Area 1 is BZY and area 2 is BYN. Errors are the  $3\sigma$  values obtained from the quantification routine.

CHAPTER 6  
MINIMIZING RESIDUAL BYN PHASE IN SSRS YTTRIUM  
DOPED BARIUM ZIRCONATE: NICKEL ADDITION  
VS. NICKEL SUBSTITUTION

This chapter contains additional experimental results for BZY with NiO additive and quenched BZY with Ni-doping. Experimental results from these two sample sets are compared with those in the previous chapter. Magnetometry results for the quenched SSRS Ni-doped BZY samples and the secondary BYN phase is demonstrated to bridge results from the two different Ni-incorporation methods. The results in this chapter are not currently published anywhere else.

### 6.1 Abstract

Solid-state reactive sintering (SSRS) of Yttrium-doped barium zirconate (BZY) typically involves addition of excess NiO to the BZY precursor powders before single-step heating. The SSRS preparation method has been previously shown to involve a transient secondary  $\text{BaY}_2\text{NiO}_5$  (BYN) phase that forms upon heating, then assists phase formation and sintering of the main BZY phase at high-temperatures. BZY samples prepared by SSRS at  $1500^\circ\text{C}$  with 0.5–4 mol% excess NiO are compared with samples prepared by SSRS with intentional 0.5–4 mol% Ni-doping (Zr substitution) that were quenched to room temperature from  $1500^\circ\text{C}$ . Quenching was previously shown to retain small amounts of the transient BYN phase in the BZY microstructure by avoiding its dissolution into the main BZY phase that occurs upon cooling slowly after SSRS at  $1500^\circ\text{C}$ . The presence of secondary BYN phase was confirmed to exist in both sample sets, so a pure BYN sample was also prepared to assist interpretation of magnetometry results. Powder X-ray diffraction (XRD) and magnetometry results reveal that SSRS preparation of BZY with

excess NiO additive leads to increased concentrations of residual BYN phase in the BZY microstructure, compared to doping with the same amount of Ni.

## 6.2 Characterization of SSRS BZY with NiO additive

The objective of this work is to compare the effective valence of Ni when NiO is added to stoichiometric BZY, with the results reported in the previous chapter for Ni-doped BZY. The comparisons in this section are based on data from powder X-ray diffraction and magnetometry. In the SSRS processing of BZY, the typical approach is to utilize NiO additions as a sintering aid, which has been shown to have lower proton uptake than BZY prepared with intentional Ni substitution for Zr.[65] Therefore, it is of interest to track the effective valence of Ni with this variation, and compare results with those of the previous chapter.

Samples of  $\text{BaZr}_{0.8}\text{Y}_{0.2}\text{O}_{3-\delta}$  with 0.5 mol%, 1 mol%, 2 mol%, 3 mol%, and 4 mol% superstoichiometric Ni were prepared similarly to the SSRS method used in the previous chapter. The precursor powders  $\text{BaCO}_3$  (Alfa Aesar, 99%),  $\text{ZrO}_2$  (Alfa Aesar, 99.978%),  $\text{Y}_2\text{O}_3$  (CoorsTek, 99.999%), and NiO (Alfa Aesar, 99.998%) were massed and combined with 5 mm  $\text{ZrO}_2$  media (in a 2:1 media to powder mass ratio) and ethyl alcohol (in a 1:1 ml to g ratio), then ball-milled for 48 h in polyethylene bottles. The slurry was dried in an oven for 24 h at 130 °C. The dried precursor powders were ball-milled an additional 48 h without solvent to break up agglomerated particles. The final precursor powders were uniaxially pressed into 13 mm diameter cylindrical pellets at 110 MPa for five minutes. The pellets were buried in sacrificial precursor powders of each respective composition and heated at 1500 °C for 20 h in air using a covered high-purity alumina boat. The heating and cooling rate for the furnace was 5 °C/min.

Powder samples were prepared by manual grinding with an agate mortar and pestle for 20 min each. Cu  $K\alpha$  ( $\lambda = 1.540598 \text{ \AA}$ ) XRD patterns were collected (Malvern PANalytical Empyrean) at 25 °C in Bragg-Brentano geometry from  $2\theta = 20^\circ$  to  $2\theta = 100^\circ$  with a step size of  $2\theta = 0.007^\circ$ . Lattice parameters and secondary phase quantification were estimated

using Rietveld refinement, as implemented in HighScore Plus XRD analysis software (Malvern PANalytical).

Magnetometry was performed on the powdered samples using a Magnetic Property Measurement System 3 (MPMS3) (Quantum Design Inc.). For each sample, approximately 0.5–1 g powder was loaded into a gelatin capsule and mounted inside a clear drinking straw. Magnetic susceptibility versus temperature under 0.2 T applied magnetic field from 1.8 K to 300 K was first performed after cooling in zero field, then repeated after cooling in a field of 0.2 T. Magnetization as a function of applied magnetic field was performed at 200 K up to 7 T for Brillouin  $M(H)$  curve fits, which provides estimated spin angular momentum quantum number and concentration of the magnetic cations. This temperature was chosen after analysis of the temperature dependence of the magnetic susceptibility showing decreased moments at low-temperature. All data was corrected for the diamagnetic background.

### 6.2.1 Powder X-ray Diffraction Results

Diffraction patterns of the 0.5–4 mol% Ni-added BZY samples are shown in Figure 6.1. The most noticeable difference between these samples and the Ni-doped samples is in the phase purity. Recall in the previous chapter that for 0.5–1 mol% Ni-doping, there was incomplete formation of the BZY phase and some residual  $\text{BaZrO}_3$  was present. For the same concentrations of Ni-added, the XRD patterns revealed only BZY phase. Additionally, diffraction patterns of the 3–4 mol% Ni-added samples revealed the presence of the secondary BYN phase, which was also observed by electron microscopy in the quenched SSRS Ni-substituted samples.

Rietveld refinement of the 3 mol% and 4 mol% Ni-added diffraction patterns estimated residual BYN concentrations of 3.8(3) wt% and 7.8(3) wt%, respectively. This phase was not detectable in the Ni-doped samples and suggests the BYN phase does not completely decompose and remains in the microstructure for these concentrations. The estimated lattice parameters of the Ni-added samples are plotted in Figure 6.2.

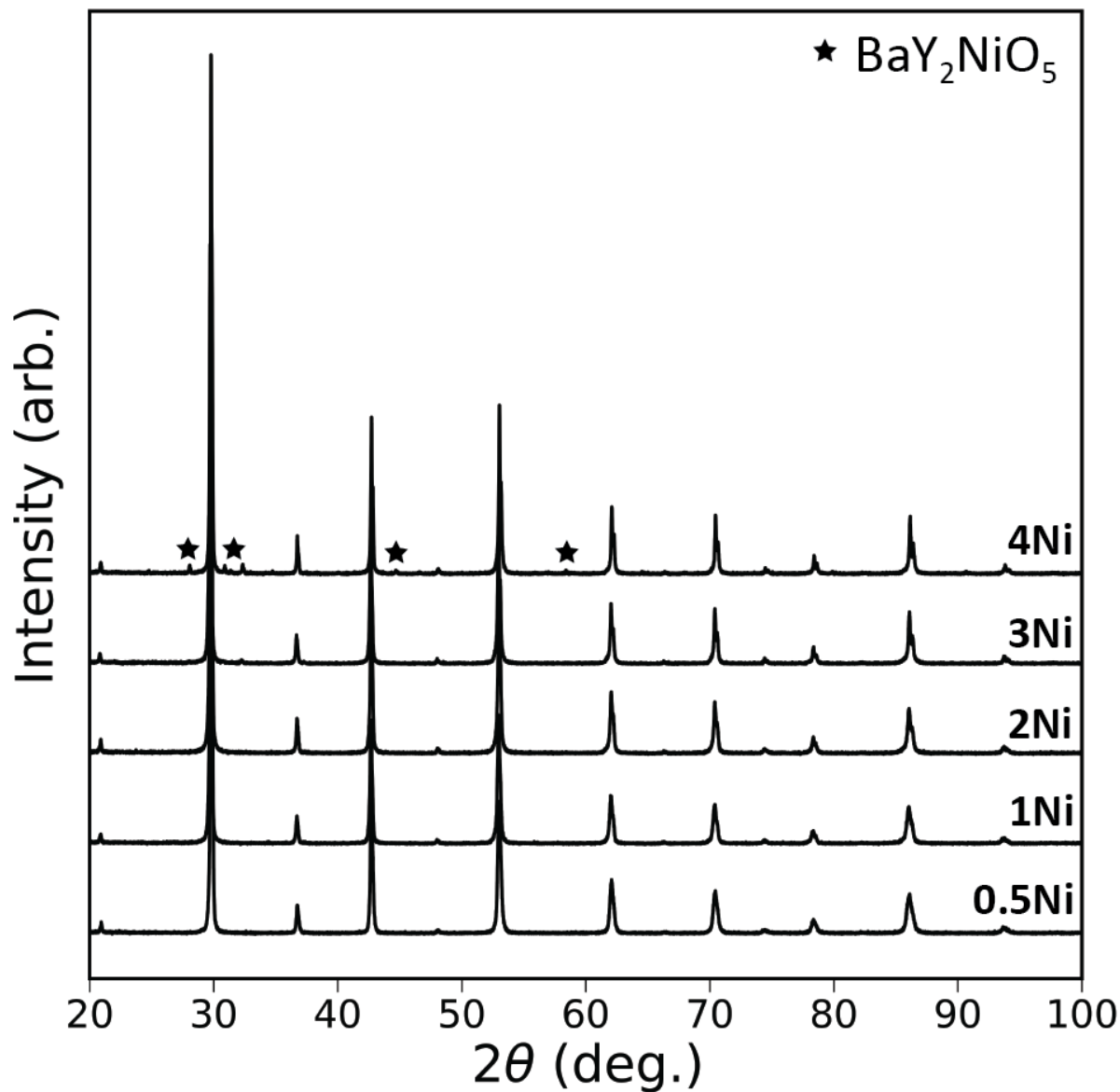


Figure 6.1 Powder XRD pattern of SSRS BZY with 0.5–4 mol% NiO additive. The main BZY phase was refined to the cubic perovskite space group  $Pm\bar{3}m$ . Stars indicate positions of peaks corresponding to secondary BYN phase, which was only detected in the 3 mol% and 4 mol% Ni-added samples. Reitveld refinement of the patterns estimated BYN concentrations of 3.8(3) wt% and 7.8(3) wt% in the 3 mol% and 4 mol% Ni-added samples, respectively.

No change in lattice parameter occurred between 0.5–1 mol% Ni-added, but going from 1–3 mol% Ni-added, the parameter decreases, then remains constant from 3–4 mol% Ni-added. This suggests the smaller Ni cation is substituting for Zr until 2–3 mol% Ni is added, then additional Ni is going into the secondary BYN phase that was observed in the diffraction patterns.

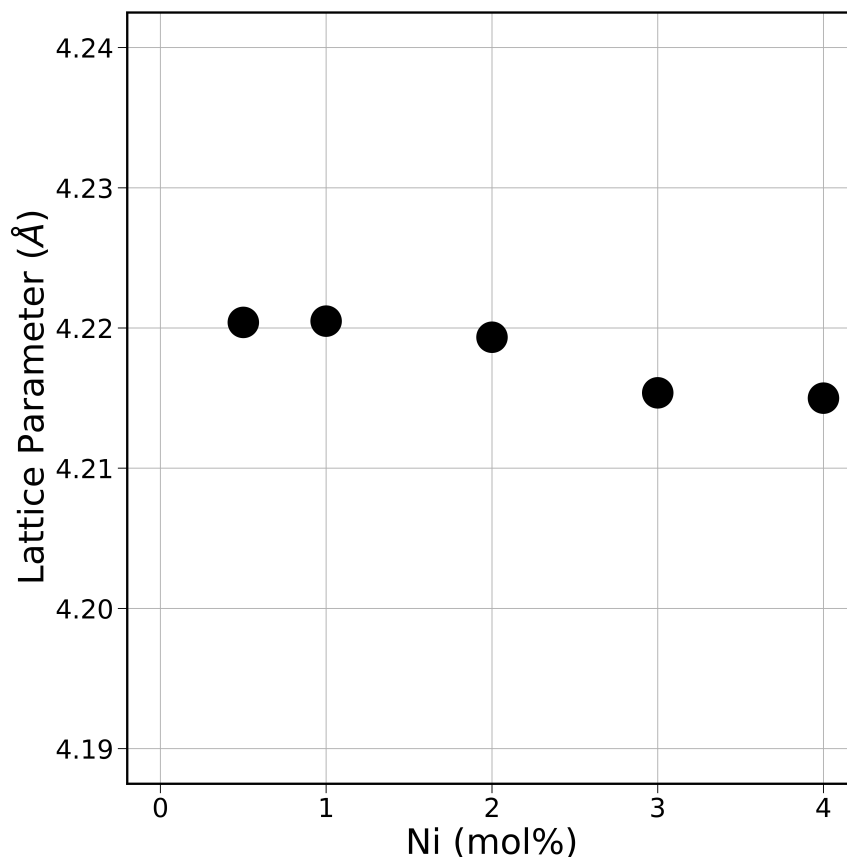


Figure 6.2 Estimated cubic lattice parameters of SSRS BZY with 0.5–4 mol% NiO additive. Decreasing values correlate with smaller Ni cations substituting for larger Zr cations. No change from 3 mol% to 4 mol% suggests solubility is reached, which correlates well with the observed secondary BYN phase formation at those concentrations.

### 6.2.2 Magnetometry Results

Temperature dependence of magnetic susceptibility for the 2–4 mol% Ni-added samples are shown in Figure 6.3 (a-c), respectively. The datasets were measured under an applied field of 0.2 T upon heating from 1.8–300 K. These measurements were performed after

cooling in zero applied field, then repeated after cooling in the 0.2 T applied field.

Figure 6.3 shows the ZFC-FC curves for each sample overlap and the temperature dependence resembles typical paramagnetic behavior. No magnetic transitions between 1.8–300 K were observed for any of the samples, however, the differences in magnitude between the samples reveals useful information.

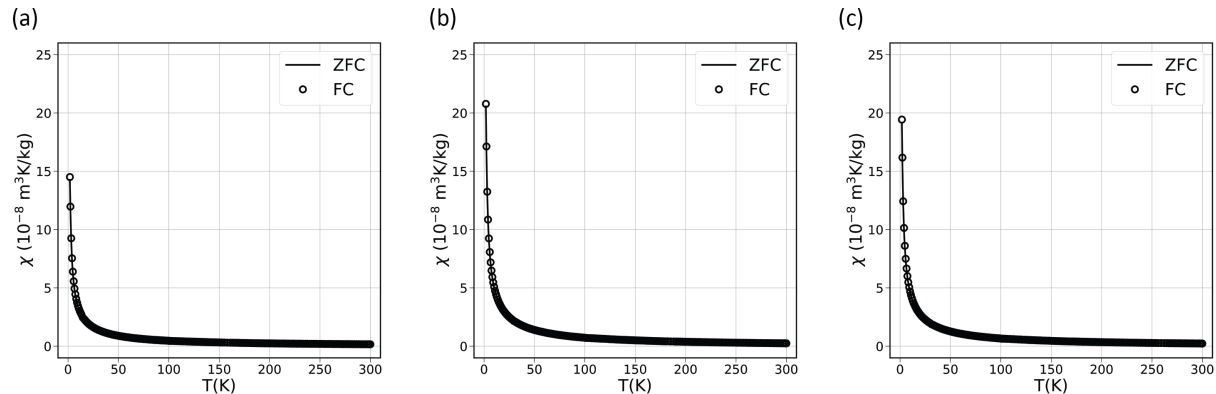


Figure 6.3 Superimposed zero-field-cooled (ZFC) and field-cooled (FC) mass susceptibility versus temperature curves for (a) 2 mol% Ni added, (b) 3 mol% Ni added, and (c) 4 mol% Ni added samples. These results show the majority of Ni is paramagnetic. The magnitude of the susceptibility of the 4 mol% Ni sample does not increase above the 3 mol% Ni sample, and actually decreases slightly.

Comparing the magnitudes of the magnetic susceptibility between the samples at 1.8 K correlates well with the formation of the weakly antiferromagnetic BYN phase observed by XRD in the 4 mol% Ni-added sample. The magnitude of the susceptibility increases with Ni content going from 2 mol% Ni-added (Figure 6.3 (a)) to 3 mol% Ni-added (Figure 6.3 (b)), as expected for increasing concentration of paramagnetic spins. The magnitude of the susceptibility decreases going from 3 mol% Ni-added to 4 mol% Ni-added. This decrease is likely due to antiferromagnetic compensation of the Ni moments in the BYN phase, since the magnitude of the susceptibility is directly related to the number of Ni moments aligned with the applied field.

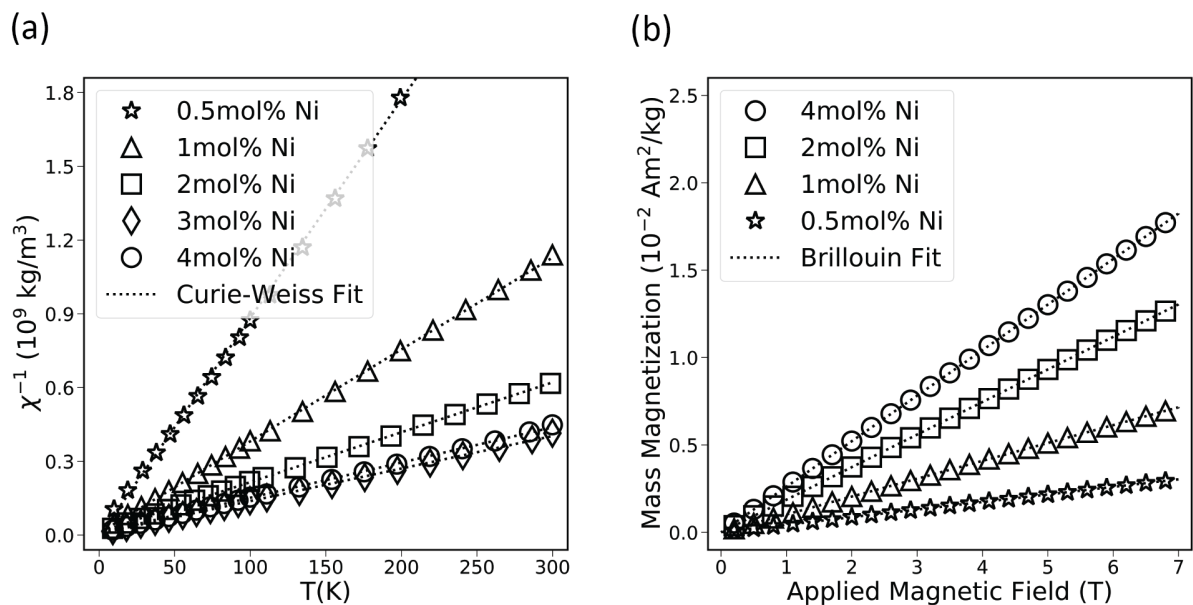


Figure 6.4 Reciprocal magnetic susceptibility (a) and magnetization versus applied magnetic field at 200 K (b) data for SSRS BZY with 0.5–4 mol% Ni additive. Note, in (b) the 3 mol% Ni sample was unable to be measured.

Figure 6.4 (a) shows the reciprocal magnetic susceptibility versus temperature,  $\chi^{-1}(T)$ , with linear fits for all samples. The linearity confirms the majority of Ni is paramagnetic, however, the slope of the 4 mol% Ni-added sample is very close to the 3 mol% Ni-added sample. This observation was expected due to the lack of increasing magnitude of susceptibility between these samples shown in Figure 6.3 and discussed in the previous paragraph. Figure 6.4 (b) shows the 200 K magnetization versus applied magnetic field,  $M(H)$ , with Brillouin fits for all but the 3 mol% Ni-added sample. This sample was unable to be measured, however, it is obvious the data would closely match the 4 mol% Ni-added sample based on the previous discussion about the concentration of paramagnetic Ni moments able to align with the applied field.

Additional useful information can be gleaned from plotting the product function  $\chi T(T)$  from 1.8–300 K. These results are shown in Figure 6.5 and are similar to the results reported in the previous chapter for Ni-doped BZY. Recall, these curves trend the same as the effective magnetic moment with temperature, and decreases at low temperature are

indicative of ZFS and superexchange interaction between moments.[189] This temperature dependence motivated the choice of  $M(H)$  measurements being performed at 200K, where the effective moments are not influenced by such effects.

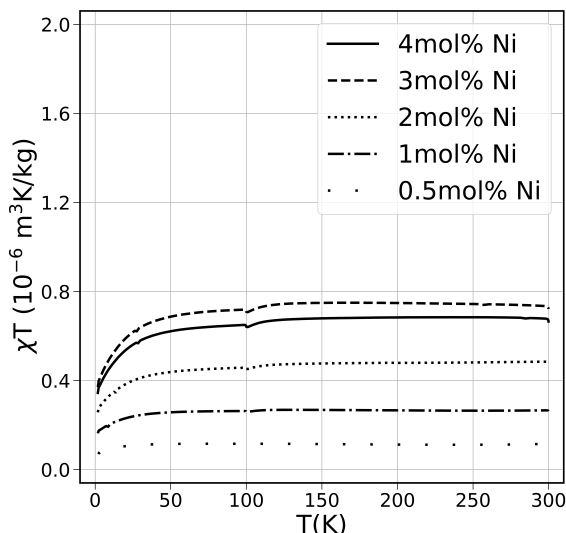


Figure 6.5 Product function  $\chi T(T)$  of SSRS BZY with 0.5–4 mol% Ni additive. The trends of these curves are equivalent with magnetic moment across the temperature range. Notice the magnitude of the 4 mol% Ni sample is actually less than the 3 mol% Ni sample. The cusp around 100 K is an artifact of the measurement process where the measurement sequence was parsed to collect closer spaced data points from 1.8–100K, and sample centering was performed upon starting the 100–300 K measurement.

The magnitude of the samples increase predictably from 0.5–3 mol% Ni-added, then only a slight increase occurs from 3–4 mol% Ni-added. This result was expected based on the results shown in Figure 6.3 and Figure 6.4, where additional Ni in the 4 mol% Ni-added sample experiences compensated magnetic moments in the BYN phase.

The  $\mu_{\text{eff}}/\text{Ni}$  results from fitting  $\chi^{-1}(T)$  and  $M(H)$  data are shown in Figure 6.6. The effective moments are around  $2\mu_B$  for Ni additions of 0.5–3 mol%, suggesting significant existence of low-spin  $\text{Ni}^{3+}$ , which has an estimated moment of  $1.9\mu_B$  due to the single unpaired valence electron.[116]  $\mu_{\text{eff}}/\text{Ni}$  in the 4 mol% Ni-added sample is lower than the rest, correlating well with the previous discussion about compensated Ni moments in this

sample. The Curie-Weiss fitting was determined using the ideal concentration of Ni, while the Brillouin fitting was determined by allowing both concentration and spin quantum number to vary. The fact that results from fitting both datasets are very similar provides greater confidence in the conclusions.

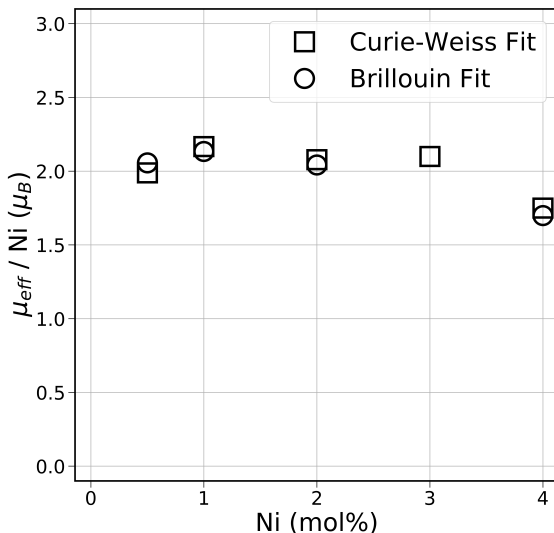


Figure 6.6  $\mu_{\text{eff}}/\text{Ni}$  of SSRS BZY with 0.5–4 mol% Ni additive from Curie-Weiss analysis of  $\chi^{-1}(T)$  data and Brillouin fitting of 200 K  $M(H)$  data. The expected moment for  $\text{Ni}^{2+}$  is  $2.8\mu_B$  and for  $\text{Ni}^{3+}$  is  $1.8\mu_B$ . This data shows the majority of Ni is most likely in a 3+ state. The moments begin to decrease above 1 mol% Ni content, which may correlate with the presence of the minority antiferromagnetic BYN phase observed by XRD in the 3 mol% and 4 mol% Ni samples. Note, the 3 mol% Ni sample was unable to be measured.

Comparing the results of Ni-doped BZY with the results reported here, suggests the Ni is mostly in a low-spin 3+ state for both preparation methods. However, residual undesirable BYN phase exists in the final microstructure in greater concentration when Ni is added compared to when Ni is intentionally substituted for Zr. Consequently, complete phase formation of BZY occurred with lower Ni concentrations when added versus intentionally substituted for Zr. The results reported here confirm the accepted knowledge that formation of the BYN phase during SSRS processing enables both formation and sintering of BZY. There must be a fine balance considered when deciding to dope or add Ni

in this system, because clearly the formation of excess BYN phase includes removal of the acceptor cation  $Y^{3+}$  from the BZY lattice, which would impact hydration and proton conductivity in PCFC applications.

### 6.3 Characterization of Ni-doped BZY Quenched after SSRS

This section provides further analysis of the same SSRS Ni-doped BZY samples quenched from 1500 °C in the previous chapter. First, powder XRD results are compared between all three sample sets, then magnetometry results are compared, and lastly analysis of pure BYN is performed to provide insight on the magnetic behavior in samples where it was confirmed to exist.

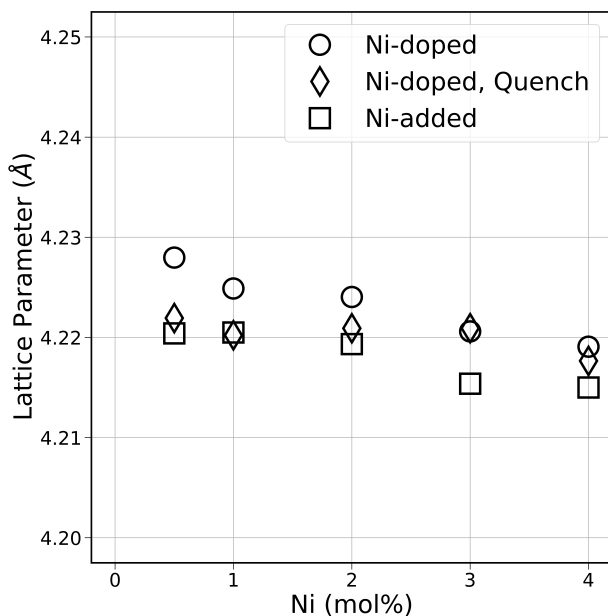


Figure 6.7 Comparison of cubic lattice parameters for all BZY sample sets prepared by SSRS with Ni-doping, Ni-doping with quench, and NiO additive. The most noticeable difference is that the quenched and additive sample sets have slightly smaller lattice parameters. This is likely due to higher amounts of Y removal from the lattice into the confirmed secondary BYN phase. Note, the data from both Ni-doped samples are taken from reference [203].

Figure 6.7 compares the lattice parameters between all three sample sets. The general trend of decreasing lattice parameters with increased Ni content is consistent with the

smaller Ni cations substituting for Zr in the BZY lattice. The lattice parameters are all noticeably larger in the Ni-doped samples cooled slowly than those observed in the quenched Ni-doped and Ni-added samples cooled slowly. Smaller lattice parameters in the latter two cases are consistent removal of an increased number of the larger  $Y^{3+}$  cations from the BZY lattice to form the BYN phase. The lattice parameters of the quenched samples and the Ni-added samples are quite similar, however, Ni additions appear to result in the most removal of Y from the lattice. Future use of the SSRS preparation method should consider intentional Ni doping, rather than adding excess NiO, to maintain maximum  $Y^{3+}$  acceptor and oxygen vacancy concentrations for optimal hydration and proton conduction.

### 6.3.1 Magnetometry Results

Figure 6.8 shows  $\chi^{-1}(T)$  from 1.8–300 K and 200 K  $M(H)$  curves with fits for the quenched Ni-doped samples. The results are nearly identical to the curves shown in the previous section for Ni-added BZY (Figure 6.4), however, the magnitudes of the curves are slightly different. The curves for 3–4 mol% Ni are nearly identical for both measurement conditions, consistent with the hypothesis that the increased Ni content from 3 mol% to 4 mol% goes almost entirely into the BYN phase having compensated Ni magnetic moments. Note that in Figure 6.8 (b) the 0.5 mol% Ni sample was not measured due to time constraints. All of the results so far have shown that this concentration is of little interest to understanding the overall picture of Ni effects in SSRS of BZY.

The magnetic susceptibility product functions,  $\chi T(T)$ , of the quenched Ni-doped SSRS BZY samples are shown in Figure 6.9. The curves are similar to those observed for Ni-added BZY, however, the magnitudes are all slightly larger. Recall, the BYN phase was only detectable by XRD in the Ni-added samples. Compared to the Ni-added samples, the larger magnitudes of  $\chi T(T)$  for these Ni-doped quenched samples is consistent with the formation of less BYN phase, which has compensated Ni moments.

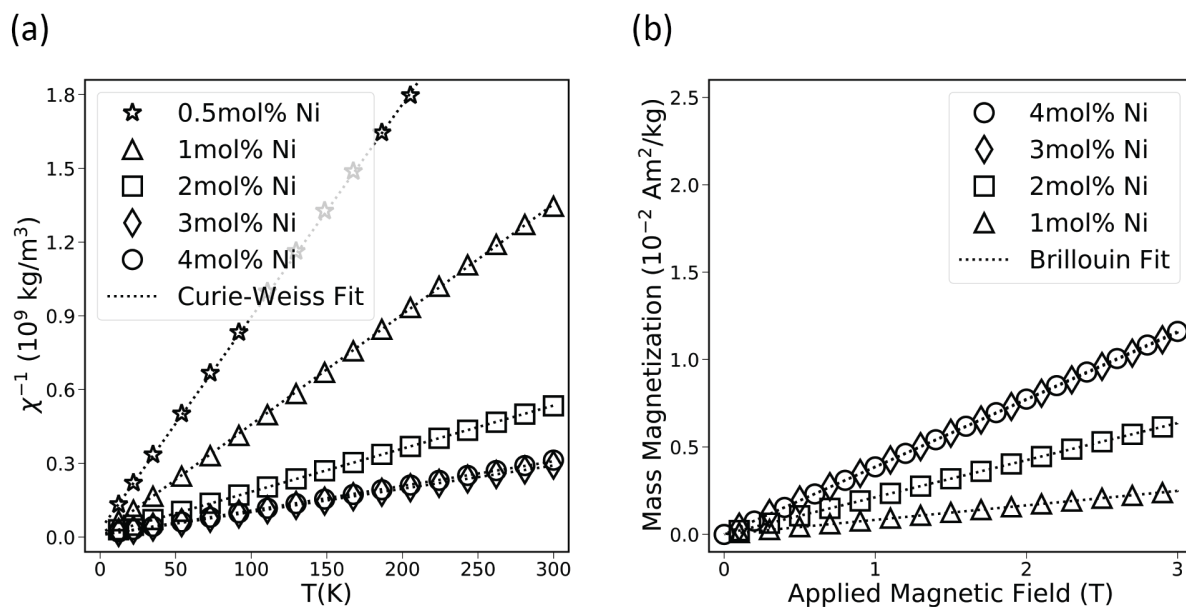


Figure 6.8 Reciprocal magnetic susceptibility versus temperature (a) and magnetization versus applied magnetic field at 200 K (b) data for quenched SSRS BZY with 0.5–4 mol% Ni doping. The 0.5 mol% Ni sample was not measured in (b).

The results shown up to this point suggest the formation of the undesirable yet necessary for processing BYN phase, occurs in largest concentration for SSRS with Ni additions, slightly lower concentration for SSRS-quenched Ni-doped, and in the least concentration for SSRS Ni-doped processing. The resulting  $\mu_{\text{eff}}/\text{Ni}$  values from fitting  $\chi^{-1}(T)$  and  $M(H)$  datasets are shown in Figure 6.10. The  $\mu_{\text{eff}}/\text{Ni}$  for Ni concentrations of 0.5–1 mol% is close to  $2\mu_{\text{B}}$ , consistent with previous the previous results showing Ni is mostly in a low-spin 3+ state. As doping increases from 1–3 mol%,  $\mu_{\text{eff}}/\text{Ni}$  increases, which could be due to increasing presence of  $\text{Ni}^{2+}$  in the very fine BYN crystallites observed by electron microscopy.  $\mu_{\text{eff}}/\text{Ni}$  drops back down in the 4 mol% sample, presumably from this additional Ni existing in the BYN phase.  $\text{Ni}^{2+}$  has a larger expected moment of  $2.8\mu_{\text{B}}$  from 2 unpaired valence electrons. Smaller BYN crystallites would lead to less of the Ni magnetic moments having antiferromagnetic compensation compared to larger crystallites. It is reasonable to assume the BYN phase in the Ni-added samples exists as larger crystallites because BYN was observable by XRD.

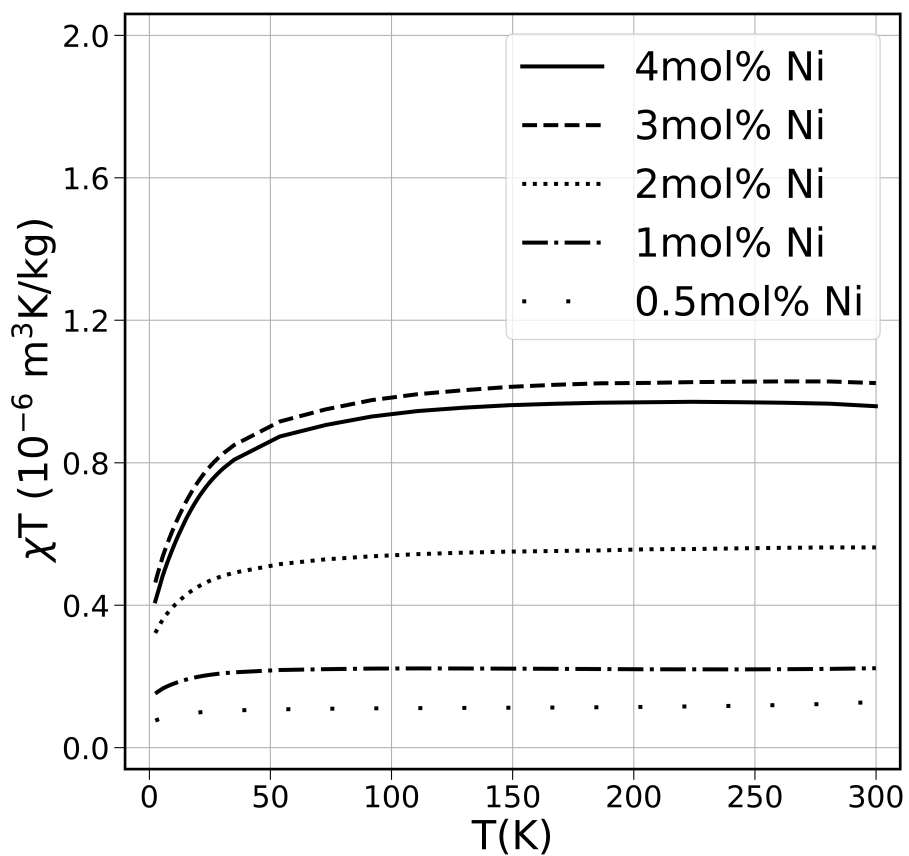


Figure 6.9 Product function  $\chi T (T)$  of quenched SSRS BZY with 0.5–4 mol% Ni doping. The trends of these curves are equivalent with magnetic moment across the temperature range. Notice the magnitude of the 4 mol% Ni sample is actually less than the 3 mol% Ni sample.

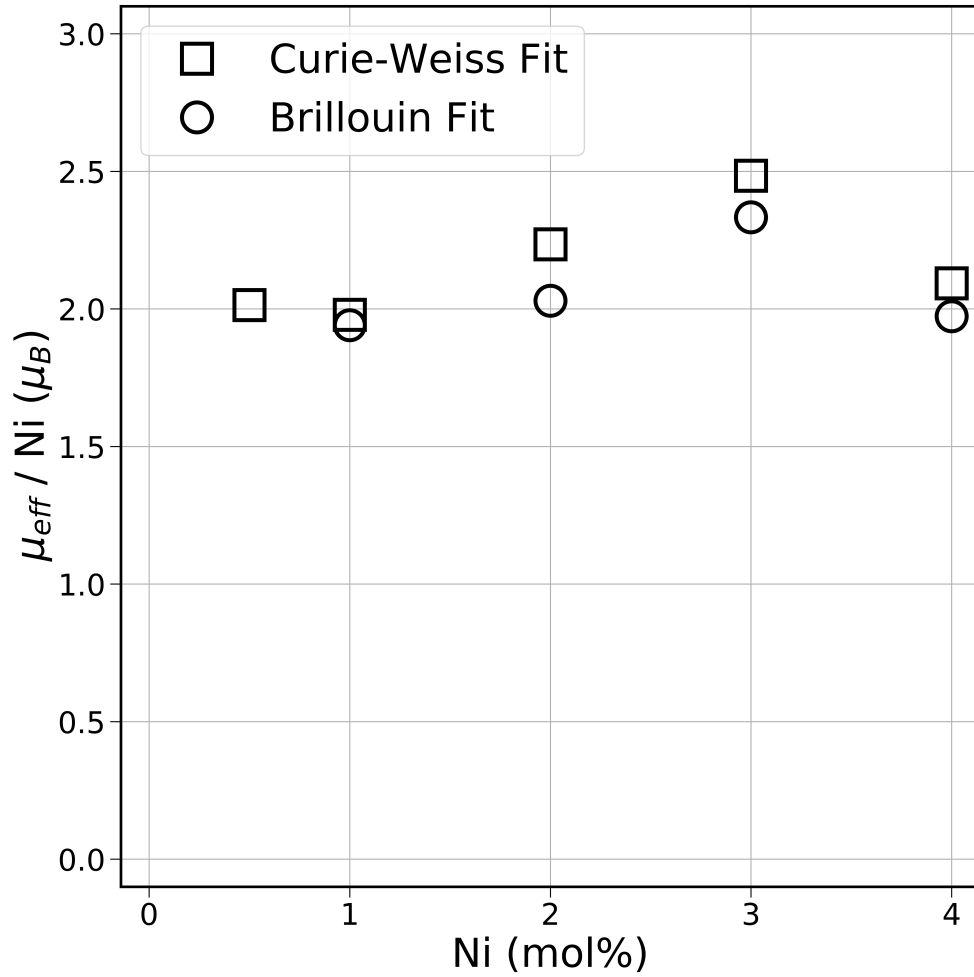


Figure 6.10  $\mu_{\text{eff}}/\text{Ni}$  of quenched SSRS BZY with 0.5–4 mol% Ni doping from Curie-Weiss analysis of  $\chi^{-1}(T)$  data and Brillouin fitting of 200 K  $M(H)$  data. The expected moment for  $\text{Ni}^{2+}$  is  $2.8\mu_{\text{B}}$  and for  $\text{Ni}^{3+}$  is  $1.8\mu_{\text{B}}$ . This data shows the majority of Ni is most likely in a 3+ state. The moments increase from 1 mol% Ni to 3 mol% Ni, suggesting the possible coexistence of  $\text{Ni}^{2+}$ . The 0.5 mol% Ni sample did not have  $M(H)$  measured at 200 K.

### 6.3.2 BYN Phase Analysis

A polycrystalline  $\text{BaY}_2\text{NiO}_5$  sample was prepared for analysis by solid-state reaction. Stoichiometric amounts of the precursor powders  $\text{BaCO}_3$  (Alfa Aesar, 99%),  $\text{Y}_2\text{O}_3$  (CoorsTek, 99.999%), and  $\text{NiO}$  (Alfa Aesar, 99.998%) were massed, and intimately mixed by grinding with an agate mortar and pestle. The precursor powder mixture was uniaxially pressed into a 13 mm diameter cylindrical pellet at 110 MPa for five minutes. The pellet was placed on a bed of sacrificial precursor powder in a covered alumina crucible and heated in a front-loading box furnace at 1200 °C for 10 h. The heating and cooling rate of the furnace was 5 °C/min. The pellet was ground into a powder by grinding with an agate mortar and pestle for 20 min to perform XRD and magnetometry.

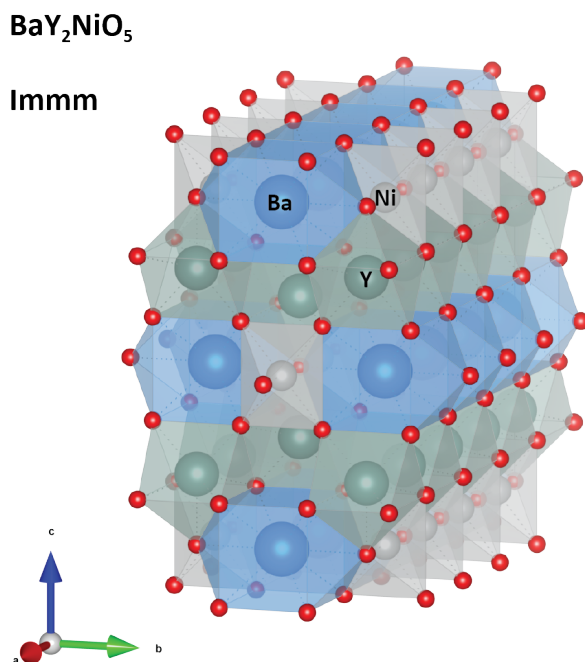


Figure 6.11 Crystal structure of  $\text{BaY}_2\text{NiO}_5$  phase. This orthorhombic structure is a member of the *Immm* space group, and the  $\text{Ni}^{2+}$  cations are ordered in one dimension along the a-axis and interact antiferromagnetically.[196]

The crystal structure of  $\text{BaY}_2\text{NiO}_5$  is shown graphically in Figure 6.11. It is orthorhombic and a member of the *Immm* space group. The  $\text{Ni}^{2+}$  cations in this structure

are octahedrally coordinated by oxygen and ordered in one dimension along the a-axis, interacting antiferromagnetically.[196] Aside from utility in (or side effect of) processing BZY, this material is very interesting because of the unique one-dimensional antiferromagnetic ordering of Ni.

The Cu  $K\alpha$  ( $\lambda = 1.540598$ ) XRD pattern of this sample was collected at 25 °C in Bragg-Brentano geometry from  $2\theta = 20^\circ$  to  $2\theta = 100^\circ$  with a step size of  $2\theta = 0.007^\circ$ . The resulting pattern is shown in Figure 6.12 and was confirmed to be phase pure  $\text{BaY}_2\text{NiO}_5$  by Reitveld refinement as implemented in HighScore Plus software.

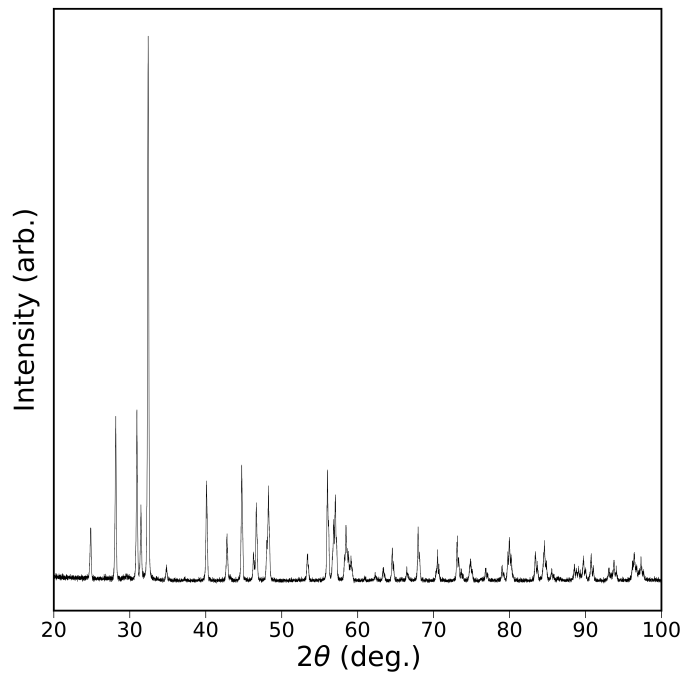


Figure 6.12 Powder XRD pattern of  $\text{BaY}_2\text{NiO}_5$  phase prepared by solid-state reaction at 1200 °C. The pattern was determined to be phase pure  $\text{BaY}_2\text{NiO}_5$  by Reitveld refinement.

Magnetometry was performed on this BYN sample to provide qualitative insight into the results shown in previous sections where the BYN phase was confirmed to exist. Magnetic susceptibility versus temperature under 0.2 T applied magnetic field from 1.8–300 K after cooling in zero magnetic field was performed first, then repeated under an applied magnetic field of 0.2 T. The superimposed ZFC-FC curves shown in Figure 6.13

revealed the absence of any magnetic transitions between 1.8–300 K, however, the curves revealed very interesting temperature dependence consistent with previous results.[196]

Upon initial heating from 1.8 K the  $\chi(T)$  curves resemble paramagnetism, however, the susceptibility does not continue trending towards zero like a pure paramagnet and actually rises slowly between 30 K and 300 K. Here,  $\chi(T)$  of BYN appears to behave in a manner consistent with a mixture of paramagnetism and antiferromagnetism, where  $T_N$  lies somewhere just above 300 K. Alternatively, Amador et al. suggested this rise in susceptibility at low-temperature may be caused by ferromagnetic interaction between the one dimensional Ni chains.[196]

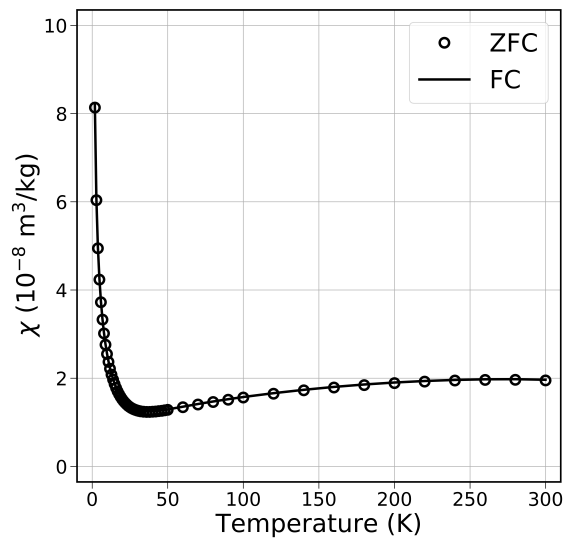


Figure 6.13 Superimposed zero-field-cooled (ZFC) and field-cooled (FC) mass susceptibility versus temperature curves for polycrystalline  $\text{BaY}_2\text{NiO}_5$  phase.

Magnetization versus applied magnetic field curves of the BYN sample at 1.8 K, 10 K, 20 K, 30 K, 40 K are shown in Figure 6.14. None of these curves revealed hysteresis, i.e., magnetization goes to zero at zero applied magnetic field. This suggests the rise in susceptibility at low temperature is not ferromagnetically induced. Clearly, this material cannot be classified as a pure antiferromagnet or paramagnet, which complicates analysis.

Because Ni in this material ideally exists as  $\text{Ni}^{2+}$ , the rise in  $\mu_{\text{eff}}/\text{Ni}$  from 1–3 mol% Ni in the quenched samples is likely caused by the presence of very fine grained BYN having uncompensated Ni moments. For the Ni-added samples, it may be considered that the larger (detectable by XRD) BYN crystallites contain a larger fraction of compensated Ni moments and the same increase in  $\mu_{\text{eff}}/\text{Ni}$  does not exist.

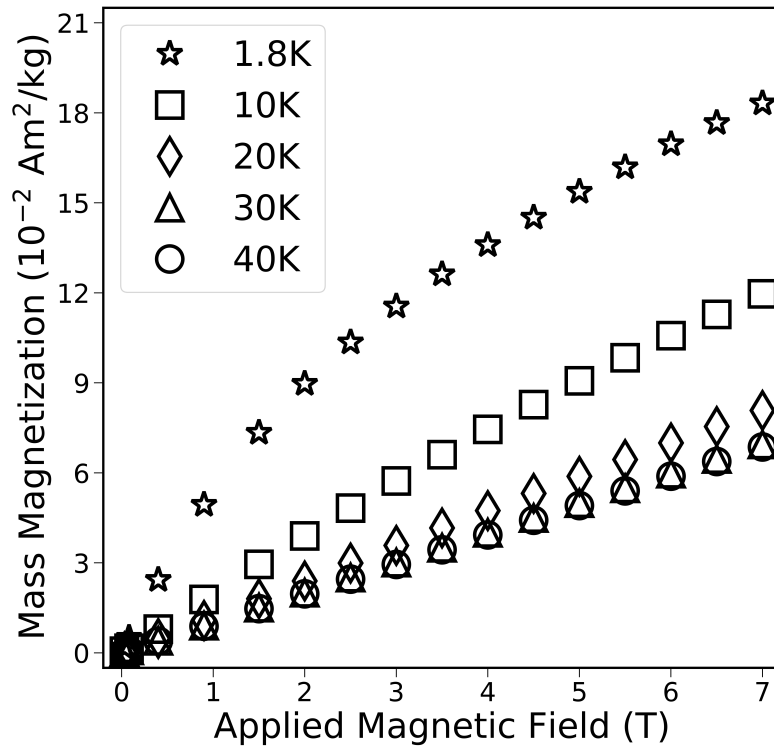


Figure 6.14 Magnetization versus applied magnetic field at 1.8 K, 10 K, 20 K, 30 K, 40 K of polycrystalline  $\text{BaY}_2\text{NiO}_5$  phase.

## 6.4 Conclusions

BZY samples prepared by SSRS at  $1500^\circ\text{C}$  with 0.5–4 mol% excess NiO were compared with samples prepared by SSRS with intentional 0.5–4 mol% Ni-doping (Zr substitution) that were quenched to room temperature after 20 h at  $1500^\circ\text{C}$ . The presence of secondary BYN phase was confirmed to exist in both sample sets, so a pure BYN sample was also

analyzed as a reference. Powder X-ray diffraction (XRD) and magnetometry results revealed that SSRS preparation of BZY with excess NiO additive leads to increased concentrations of residual BYN phase in the BZY microstructure, compared to doping with the same amount of Ni. Increasing Ni content in both cases, leads to increased amount of antiferromagnetic BYN phase, as evident from the corresponding decreasing magnetic moments. Future SSRS preparation of BZY with NiO should intentionally substitute Ni for Zr in the stoichiometry.

## CHAPTER 7

### CONCLUSIONS

Magnetometry has been shown here to be a useful tool for estimating valence states of dilute transition metal dopants in STO and BZY. Due to the small concentrations of interest, such estimations are typically difficult to make by many common spectroscopic techniques. The sensitivity of the SQUID magnetometer is unmatched in this regard. Furthermore, paramagnetism does not fundamentally impact performance of solid-state ion conducting oxides, however, many paramagnetic transition metal or rare-earth cations are used in these materials as acceptor dopants to improve processing or properties. The fact that these extrinsic cations are paramagnetic enables characterization of their valence states and local environment with magnetically selective measurements. The overarching goal of this work was to demonstrate the utility of magnetometry for characterizing transition metal dopants in solid-state ion conducting oxides. This was demonstrated by providing new information about the valence state and local interactions of dilute Fe and Ni in STO and BZY, respectively. This work also demonstrated synergy between EPR and magnetometry techniques. The individual results from each technique may necessitate certain assumptions, i.e.,  $g$ -values assumed to be isotropic, but the combined results connect and validate conclusions. Performing EPR spectroscopy was critical to confirming the presence of  $\text{Ni}^{3+}$  in Ni-doped BZY20, as well as confirming one of the Fe sites in the Mössbauer spectra was  $\text{Fe}^{3+}$  in Fe-doped STO.

#### 7.1 Strontium Titanate

This work revealed details about the mixed-valence character of dilute Fe dopants in polycrystalline STO. Figure 7.1 graphically summarizes the overall conclusions. The results presented in this work suggested that  $\text{Fe}^{3+}$  may interact with next-nearest neighbor  $\text{Fe}^{3+}$ , as well as oxygen vacancies. EPR spectroscopy results showed that some of the  $\text{Fe}^{3+}$

dopants effectively trap an  $V_{\text{O}}^{\bullet\bullet}$  and form the positively charged defect complex  $(\text{Fe}'_{\text{Ti}} - V_{\text{O}}^{\bullet\bullet})^{\bullet}$ . These defect complexes may then trap negatively charged carriers and repel positively charged carriers, e.g., trap  $e'$  and repel  $h^{\bullet}$  or  $V_{\text{O}}^{\bullet\bullet}$ . This phenomenon in Fe-doped STO would then affect ionic and mixed conductivity in practice.

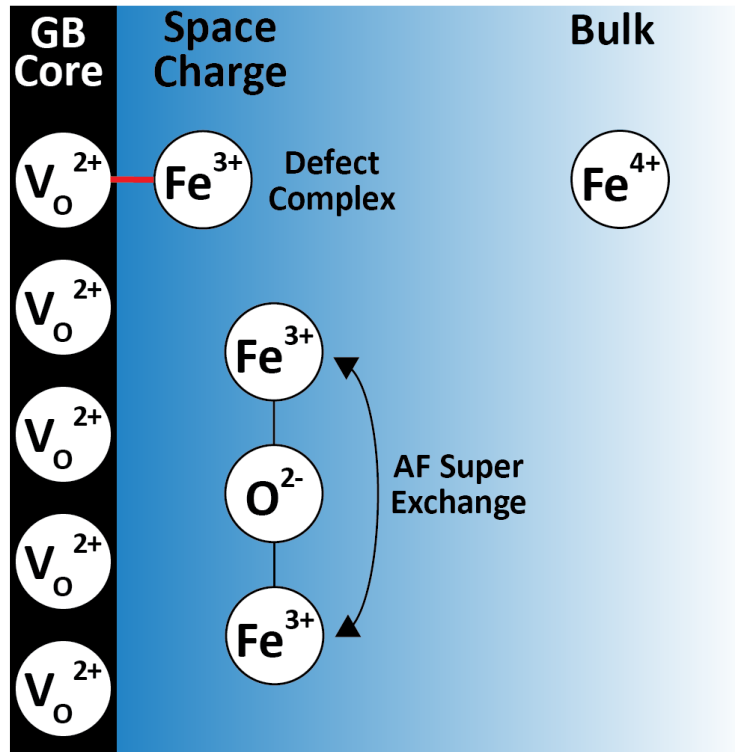


Figure 7.1 Diagram summarizing Fe-doped STO conclusions of this work. Evidence of the positively charged defect complex  $(\text{Fe}'_{\text{Ti}} - V_{\text{O}}^{\bullet\bullet})^{\bullet}$  was observed by EPR spectroscopy. Magnetometry results suggested additional interactions between next-nearest neighbor  $\text{Fe}^{3+}$  dopants, and Raman spectroscopy results suggested  $\text{Fe}^{4+}$  exists randomly distributed in the STO lattice.

Magnetometry results suggested the presence of interactions between  $\text{Fe}^{3+}$  dopants configured as next-nearest neighbors. These configurations would be expected to exist near GB regions where they experience electrostatic attraction to the positively charged GB cores. These acceptors would then be expected to repel negatively charged carriers and attract positively charged carriers in these regions. Therefore, careful consideration must be made when implementing dilute Fe-doped STO as a polycrystalline ionic or mixed

conductor. Additionally, Raman spectroscopy results of the grain interior regions suggested the presence of  $\text{Fe}^{4+}$  in the STO lattice. All these results are consistent with the overall defect chemistry and electroneutrality conditions in polycrystalline Fe-doped STO.

## 7.2 Yttrium-doped Barium Zirconate

The proton conductor BZY is arguably one of the most well studied materials in this category of materials. The most common preparation method for BZY in PCFC applications is the SSRS method with excess NiO as a sintering additive.[18, 46, 58, 59, 61] The typical approach is to add 1–2 wt% NiO to the BZY precursor powders before mixing and performing SSRS. The results shown in this work suggest Ni-doping, rather than NiO additions, leads to the same well densified microstructure, while minimizing formation of the secondary BYN phase. It is clear that the BYN phase is a critical contributor to, or byproduct of, the SSRS method for producing dense BZY at practical temperatures, however, there are potentially negative implications for the presence of unnecessary secondary phases in a BZY based electrolyte. Formation of more BYN phase in the Ni-added samples implies that less Y acceptors reside in the BZY lattice, leading to lower  $\text{V}_{\text{O}}^{\bullet\bullet}$  concentration that may negatively impact hydration and proton conductivity.

New information about Ni valence in BZY was determined here through a combination of magnetometry and EPR spectroscopy. Many reports on SSRS processed BZY with Ni have assumed Ni to exist in a 2+ state, however, the existence of  $\text{Ni}^{3+}$  in an anisotropic coordination environment was discovered here by EPR spectroscopy. Additionally, magnetometry revealed the possibility of superexchange interactions between Ni dopants. This situation would be expected to occur near GBs, where STEM-EDS results confirmed segregation of Ni. The proposed superexchange interaction between these dopants is shown graphically in Figure 7.2.

Anisotropy around  $\text{Ni}^{3+}$  could possibly indicate formation of a defect associate with an  $\text{V}_{\text{O}}^{\bullet\bullet}$ , which could have an effect on conductivity. Similar to the case for  $\text{Fe}^{3+}$  in STO, this net positively charged defect associate would act to repel protons and holes, or attract

electrons. This may be favorable considering electronic conduction through a BZY electrolyte is undesirable in a PCFC, and isolated acceptors can act as proton traps.

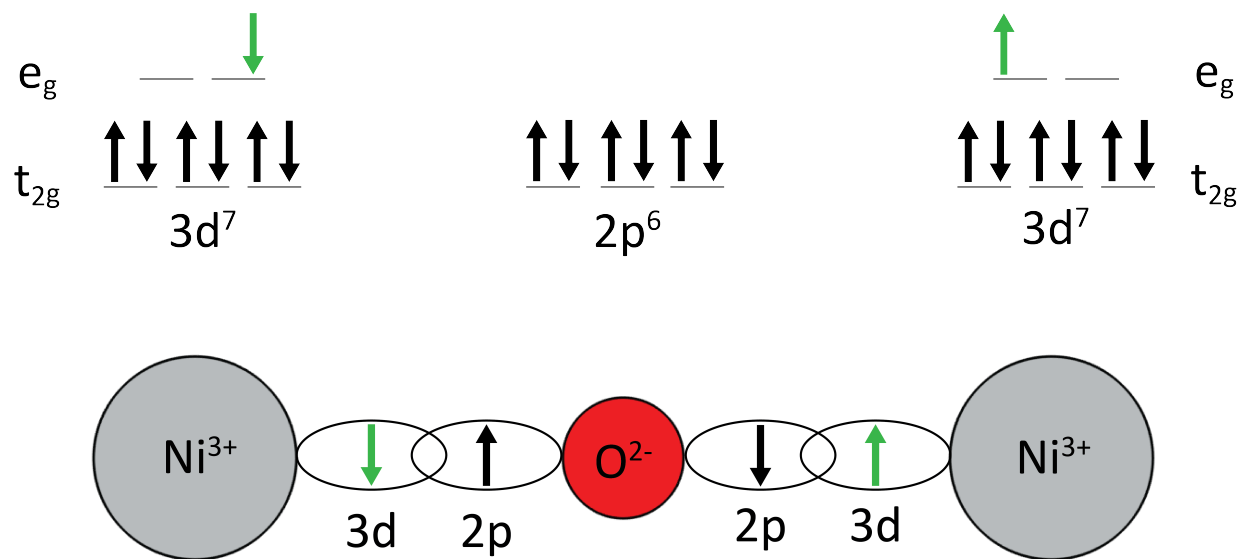


Figure 7.2 Proposed superexchange interaction between segregated Ni in SSRS xNiBZY20 samples. The Ni<sup>3+</sup> 3d and O<sup>2-</sup> 2p orbitals overlap and form hybridized orbitals, which leads to antiferromagnetic cancellation of Ni<sup>3+</sup> magnetic moments at low temperatures.

### 7.3 Recommendations for Future Work

For Fe-doped STO, future work could include preparation of samples with <sup>57</sup>Fe enriched precursor to significantly improve signal of Mössbauer spectra. This would improve spectral resolution between the different Fe sites. Systematically studying correlations between grain sizes and Fe valence changes may also be of interest. This could provide a connection between Fe valence changes and different space charge volumes, i.e., track relative concentration of Fe<sup>3+</sup> that may be more likely to exist near GBs. For both systems, higher frequency EPR experiments would provide greater resolution of the Fe<sup>3+</sup> and Ni<sup>3+</sup> resonance spectra. This information may improve the understanding of the local environment around these dopants.

For Ni-doped BZY, high-resolution TEM of the Ni segregation at GBs may also be of interest to rule out or confirm the presence of a separate Ni-containing phase. For Ni-added

BZY, electron micrographs comparing microstructural distribution of the BYN phase to that of the quenched Ni-doped samples may provide more insight to the different preparation methods. Additionally, conductivity measurements comparing slow-cooled and quenched BZY with Ni-doping may provide new information about the effects of Ni residing near GBs, versus in the BYN phase, on transport of protonic defects. Magnetometry should be applied to other BZY-based proton conducting oxides that contain paramagnetic rare-earth cations like Ce, Yb, Gd, etc. Magnetometry combined with EPR may provide new information about interactions between these dopants and with oxygen vacancies.

## REFERENCES

- [1] M.A. Pellow, C.J. Emmott, C.J. Barnhart, and S.M. Benson. Hydrogen or batteries for grid storage? A net energy analysis. *Energy and Environmental Science*, 8: 1938–1952, 2015.
- [2] A. Simpson and A. Lutz. Exergy analysis of hydrogen production via steam methane reforming. *International Journal of Hydrogen Energy*, 32:4811–4820, 2007.
- [3] J. Yang, D. Wang, H. Han, and C. Li. Roles of cocatalysts in photocatalysis and photoelectrocatalysis. *Accounts of Chemical Research*, 46:1900–1909, 2013.
- [4] C. Perkins and A. Weimer. Likely near-term solar-thermal water splitting technologies. *International Journal of Hydrogen Energy*, 29:1587–1599, 2004.
- [5] A. Steinfeld. Solar thermochemical production of hydrogen—a review. *Solar Energy*, 78:603–615, 2005.
- [6] C.L. Muhich, B.D. Ehrhart, I. Al-Shankiti, B.J. Ward, C.B. Musgrave, and A.W. Weimer. A review and perspective of efficient hydrogen generation via solar thermal water splitting. *Wiley Interdisciplinary Reviews: Energy and Environment*, 5: 261–287, 2015.
- [7] S. Chen, T. Takata, and K. Domen. Particulate photocatalysts for overall water splitting. *Nature Reviews Materials*, 2:1–17, 2017.
- [8] F. Zhang and C. Li. Solar to Chemical Energy Conversion: Theory and Application. In M. Sugiyama, K. Fujii, and S. Nakamura, editors, *Solar to Chemical Energy Conversion: Theory and Application*, pages 299–317. Springer, New York, USA, 2016.
- [9] W. Shockley and W. Read Jr. Statistics of the Recombinations of Holes and Electrons. *Physical Review*, 87(5):835–842, 1952.
- [10] Z. Luo and Q.H. Gao. Decrease in the photoactivity of TiO<sub>2</sub> pigment on doping with transition metals. *Journal of Photochemistry and Photobiology, A: Chemistry*, 63: 367–375, 1992.
- [11] N. Serpone, D. Lawless, J. Disdier, and J.M. Herrmann. Spectroscopic, Photoconductivity, and Photocatalytic Studies of TiO<sub>2</sub> Colloids: Naked and with the Lattice Doped with Cr<sup>3+</sup>, Fe<sup>3+</sup>, and V<sup>5+</sup> Cations. *Langmuir*, 10:643–652, 1994.

- [12] J. Lehn, J. Sauvage, and R. Ziessel. Photochemical Water Splitting Continuous Generation of Hydrogen and Oxygen by Irradiation of Aqueous Suspensions of Metal Loaded Strontium Titanate. *New Journal of Chemistry*, 4(11):624–627, 1980.
- [13] H. Kato and A. Kudo. Highly efficient decomposition of pure water into H<sub>2</sub> and O<sub>2</sub> over NaTaO<sub>3</sub> photocatalysts. *Catalysis Letters*, 58:153–155, 1999.
- [14] K. Domen, J.N. Kondo, M. Hara, and T. Takata. Photo- and mechano-catalytic overall water splitting reactions to form hydrogen and oxygen on heterogeneous catalysts. *Bulletin of the Chemical Society of Japan*, 73(6):1307–1331, 2000.
- [15] X. Zhou, J. Shi, and C. Li. Effect of metal doping on electronic structure and visible light absorption of SrTiO<sub>3</sub> and NaTaO<sub>3</sub> (Metal = Mn, Fe, and Co). *Journal of Physical Chemistry C*, 115:8305–8311, 2011.
- [16] G.W. Crabtree, M.S. Dresselhaus, and M.V. Buchanan. The hydrogen economy. *Physics Today*, 57(12):39–44, 2004.
- [17] S.A. Boudghene and E. Traversa. Fuel cells, an alternative to standard sources of energy. *Renewable and Sustainable Energy Reviews*, 6(3):295–304, 2002.
- [18] C. Duan, R.J. Kee, H. Zhu, C. Karakaya, Y. Chen, S. Ricote, A. Jarry, E.J. Crumlin, D. Hook, R. Braun, N.P. Sullivan, and R. O’Hayre. Highly durable, coking and sulfur tolerant, fuel-flexible protonic ceramic fuel cells. *Nature*, 557(7704):217–212, 2018.
- [19] S.M. Haile. Fuel cell materials and components. *Acta Materialia*, 51(19):5981–6000, 2003.
- [20] N. Mahato, A. Banerjee, A. Gupta, S. Omar, and K. Balani. Progress in material selection for solid oxide fuel cell technology: A review. *Progress in Materials Science*, 72:141–337, 2015.
- [21] H.L. Tuller. Defect engineering: Design tools for solid state electrochemical devices. *Electrochimica Acta*, 48:2879–2887, 2003.
- [22] J. Maier. Ionic conduction in space charge regions. *Progress in Solid State Chemistry*, 23:171–263, 1995.
- [23] M. Vollman and R. Waser. Grain Boundary Defect Chemistry of Acceptor-Doped Titanates: Space Charge Layer Width. *Journal of the American Ceramic Society*, 77: 235–243, 1994.

- [24] P.C McIntyre. Equilibrium Point Defect and Electronic Carrier Distributions near Interfaces in Acceptor-Doped Strontium Titanate. *Journal of the American Ceramic Society*, 83:1129–1136, 2000.
- [25] J. Claus, M. Leonhardt, and J. Maier. Tracer diffusion and chemical diffusion of oxygen in acceptor doped SrTiO<sub>3</sub>. *Journal of Physics and Chemistry of Solids*, 61: 1199–1207, 2000.
- [26] X. Guo, J. Fleig, and J. Maier. Separation of Electronic and Ionic Contributions to the Grain Boundary Conductivity in Acceptor-Doped SrTiO<sub>3</sub>. *Journal of The Electrochemical Society*, 148:J50, 2001.
- [27] R. Klie and N. Browning. Atomic scale characterization of oxygen vacancy segregation at SrTiO<sub>3</sub> grain boundaries. *Materials Research Society Symposium - Proceedings*, 654:1–4, 2001.
- [28] D. Fagg, V. Kharton, A. Kovalevsky, A. Viskup, E. Naumovich, and J. Frade. The stability and mixed conductivity in La and Fe doped SrTiO<sub>3</sub> in the search for potential SOFC anode materials. *Journal of the European Ceramic Society*, 21: 1831–1835, 2001.
- [29] R. Merkle and J. Maier. Oxygen incorporation into Fe-doped SrTiO<sub>3</sub>: Mechanistic interpretation of the surface reaction. *Physical Chemistry Chemical Physics*, 4: 4140–4148, 2002.
- [30] R.A. De Souza, J. Fleig, R. Merkle, and J. Maier. SrTiO<sub>3</sub>: A model electroceramic. *Zeitschrift fuer Metallkunde/Materials Research and Advanced Techniques*, 94: 218–225, 2003.
- [31] R. Merkle and J. Maier. Defect association in acceptor-doped SrTiO<sub>3</sub>: Case study for Fe'<sub>Ti</sub> - V<sup>••</sup><sub>O</sub> and Mn''<sub>Ti</sub> - V<sup>••</sup><sub>O</sub>. *Physical Chemistry Chemical Physics*, 5:2297–2303, 2003.
- [32] J.B. Goodenough. Oxide-ion electrolytes. *Annual Review of Materials Research*, 33: 91–128, 2003.
- [33] A. Rothschild, W. Menesklou, H.L. Tuller, and E. Ivers-Tiffée. Electronic structure, defect chemistry, and transport properties of SrTi<sub>1-x</sub>Fe<sub>x</sub>O<sub>3-y</sub> solid solutions. *Chemistry of Materials*, 18:3651–3659, 2006.
- [34] R. Merkle and J. Maier. How is oxygen incorporated into oxides? A comprehensive kinetic study of a simple solid-state reaction with SrTiO<sub>3</sub> as a model material. *Angewandte Chemie - International Edition*, 47:3874–3894, 2008.

- [35] W. Jung and H.L. Tuller. Impedance study of  $\text{SrTi}_{1-x}\text{Fe}_x\text{O}_{3-\delta}$  ( $x = 0.05$  to  $0.80$ ) mixed ionic electronic conducting model cathode. *Solid State Ionics*, 180:843–847, 2009.
- [36] S. Von Alfthan, N.A. Benedek, L. Chen, A. Chua, D. Cockayne, K.J. Dudeck, C. Elsässer, M.W. Finnis, C.T. Koch, B. Rahmati, M. Ruhle, S.J. Shih, and A.P. Sutton. The structure of grain boundaries in strontium titanate: Theory, simulation, and electron microscopy. *Annual Review of Materials Research*, 40:557–599, 2010.
- [37] H. Yang, P.G. Kotula, Y. Sato, M. Chi, Y. Ikuhara, and N.D. Browning. Segregation of  $\text{Mn}^{2+}$  Dopants as Interstitials in  $\text{SrTiO}_3$  Grain Boundaries. *Materials Research Letters*, 2(1):16–22, 2014.
- [38] G. Gregori, R. Merkle, and J. Maier. Ion conduction and redistribution at grain boundaries in oxide systems. *Progress in Materials Science*, 89:252–305, 2017.
- [39] H. Gu. Chemical structure of grain-boundary layer in  $\text{SrTiO}_3$  and its segregation-induced transition: A continuum interface approach. *Chinese Physics B*, 27(060503), 2018.
- [40] C.Y.S. Chang, I. Lubomirsky, and S. Kim. Applicability of a linear diffusion model to determination of the height of the potential barrier at the grain boundaries of Fe-doped  $\text{SrTiO}_3$ . *Physical Chemistry Chemical Physics*, 20:19250–19256, 2018.
- [41] R. De Souza and E. Dickey. The effect of space-charge formation on the grain-boundary energy of an ionic solid. *Philosophical Transactions of the Royal Society A: Mathematical, Physical and Engineering Sciences*, 377(20180430), 2019.
- [42] J. Szade, K. Szot, M. Kulpa, J. Kubacki, C. Lenser, R. Dittmann, and R. Waser. Electronic structure of epitaxial Fe-doped  $\text{SrTiO}_3$  thin films. *Phase Transitions*, 84:489–500, 2011.
- [43] A. Koehl, D. Kajewski, J. Kubacki, C. Lenser, R. Dittmann, P. Meuffels, K. Szot, R. Waser, and J. Szade. Detection of  $\text{Fe}^{2+}$  valence states in Fe doped  $\text{SrTiO}_3$  epitaxial thin films grown by pulsed laser deposition. *Physical Chemistry Chemical Physics*, 15:8311–8317, 2013.
- [44] J. He, X.X. Lu, W. Zhu, Y. Hou, R. Ti, F. Huang, X.X. Lu, T. Xu, J. Su, and J. Zhu. Induction and control of room-temperature ferromagnetism in dilute Fe-doped  $\text{SrTiO}_3$  ceramics. *Applied Physics Letters*, 107:0–5, 2015.
- [45] K.D. Kreuer. Proton-Conducting Oxides. *Annual Review of Materials Research*, 33:333–359, 2003.

- [46] C. Duan, J. Huang, N. Sullivan, and R. O’Hayre. Proton-conducting oxides for energy conversion and storage. *Applied Physics Reviews*, 7(011314), 2020.
- [47] W. Munch, G. Seifert, K.D. Kreuer, and J. Maier. A quantum molecular dynamics study of the cubic phase of BaTiO<sub>3</sub> and BaZrO<sub>3</sub>. *Solid State Ionics*, 97:39–44, 1997.
- [48] J. Roziere. Proton-Conducting Ceramics: From Fundamentals to Applied Research. In M. Marrony, editor, *Proton-Conducting Ceramics: From Fundamentals to Applied Research*, page 74. CRC Press, Taylor & Francis Group, Florida, USA, 2016.
- [49] H. Iwahara, T. Esaka, H. Uchida, and N. Maeda. Proton conduction in sintered oxides and its application to steam electrolysis for hydrogen production. *Solid State Ionics*, 3-4:359–363, 1981.
- [50] H. Iwahara, H. Uchida, K. Ono, and K. Ogaki. Proton Conduction in Sintered Oxides Based on BaCeO<sub>3</sub>. *Journal of The Electrochemical Society*, 135(2):529–533, 1988.
- [51] H. Iwahara, T. Yajima, T. Hibino, K. Ozaki, and H. Suzuki. Protonic conduction in calcium, strontium and barium zirconates. *Solid State Ionics*, 61:65–69, 1993.
- [52] K.H. Ryu and S.M. Haile. Chemical stability and proton conductivity of doped BaCeO<sub>3</sub>–BaZrO<sub>3</sub> solid solutions. *Solid State Ionics*, 125:355–367, 1999.
- [53] K. Kreuer, S. Adams, W. Munch, A. Fuchs, U. Klock, and J. Maier. Proton conducting alkaline earth zirconates and titanates for high drain electrochemical applications. *Solid State Ionics*, 145:295–306, 2001.
- [54] P. Babilo, T. Uda, and S.M. Haile. Processing of yttrium-doped barium zirconate for high proton conductivity. *Journal of Materials Research*, 22(5):1322–1330, 2007.
- [55] F. Iguchi, T. Yamada, N. Sata, T. Tsurui, and H. Yugami. The influence of grain structures on the electrical conductivity of a BaZr<sub>0.95</sub>Y<sub>0.05</sub>O<sub>3</sub> proton conductor. *Solid State Ionics*, 177:2381–2384, 2006.
- [56] Y. Yamazaki, R. Hernandez-Sanchez, and S.M. Haile. Cation non-stoichiometry in yttrium-doped barium zirconate: phase behavior, microstructure, and proton conductivity. *Journal of Materials Chemistry*, 20(37):8158–8166, 2010.
- [57] P. Babilo and S.M. Haile. Enhanced sintering of yttrium-doped barium zirconate by addition of ZnO. *Journal of the American Ceramic Society*, 88(9):2362–2368, 2005.
- [58] J. Tong, D. Clark, M. Hoban, and R. O’Hayre. Cost-effective solid-state reactive sintering method for high conductivity proton conducting yttrium-doped barium zirconium ceramics. *Solid State Ionics*, 181(11-12):496–503, 2010.

- [59] J. Tong, D. Clark, L. Bernau, M. Sanders, and R. O'Hayre. Solid-state reactive sintering mechanism for large-grained yttrium-doped barium zirconate proton conducting ceramics. *Journal of Materials Chemistry*, 20(30):6333–6341, 2010.
- [60] S. Ricote and N. Bonanos. Enhanced sintering and conductivity study of cobalt or nickel doped solid solution of barium cerate and zirconate. *Solid State Ionics*, 181: 694–700, 2010.
- [61] C. Duan, J. Tong, M. Shang, S. Nikodemski, M. Sanders, S. Ricote, A. Almansoori, and R. O'Hayre. Readily processed protonic ceramic fuel cells with high performance at low temperatures. *Science*, 349(6254):1321–1326, sep 2015.
- [62] S. Nikodemski, J. Tong, and R. O'Hayre. Solid-state reactive sintering mechanism for proton conducting ceramics. *Solid State Ionics*, 253:201–210, 2013.
- [63] S. Fang, S. Wang, K.S. Brinkman, Q. Su, H. Wang, and F. Chen. Relationship between fabrication method and chemical stability of Ni-BaZr<sub>0.8</sub>Y<sub>0.2</sub>O<sub>3- $\delta$</sub>  membrane. *Journal of Power Sources*, 278:614–622, 2015.
- [64] Y. Han, D. and Otani, Y. Noda, T. Onishi, M. Majima, and T. Uda. Strategy to improve phase compatibility between proton conductive BaZr<sub>0.8</sub>Y<sub>0.2</sub>O<sub>3- $\delta$</sub>  and nickel oxide. *RSC Advances*, 6(23):19288–19297, 2016.
- [65] Y. Huang, R. Merkle, and J. Maier. Effect of NiO addition on proton uptake of BaZr<sub>1-x</sub>Y<sub>x</sub>O<sub>3-x/2</sub> and BaZr<sub>1-x</sub>Sc<sub>x</sub>O<sub>3-x/2</sub> electrolytes. *Solid State Ionics*, 347:115256, apr 2020.
- [66] W.J. Yin, B. Weng, J. Ge, Q. Sun, Z. Li, and Y. Yan. Oxide perovskites, double perovskites and derivatives for electrocatalysis, photocatalysis, and photovoltaics. *Energy and Environmental Science*, 12(2):442–462, 2019.
- [67] P. Lupetin, G. Gregori, and J. Maier. Mesoscopic Charge Carriers Chemistry in Nanocrystalline SrTiO<sub>3</sub>. *Angewandte Chemie*, 122:10321–10324, 2010.
- [68] J. Luo. Interfacial engineering of solid electrolytes. *Journal of Materiomics*, 1:22–32, 2015.
- [69] S. Kim, J. Fleig, and J. Maier. Space charge conduction: Simple analytical solutions for ionic and mixed conductors and application to nanocrystalline ceria. *Physical Chemistry Chemical Physics*, 5:2268–2273, 2003.
- [70] J. Frenkel. *Kinetic Theory of Liquids*. Oxford University Press, New York, 1946.

- [71] K. Vikrant and R. Garcia. Charged grain boundary transitions in ionic ceramics for energy applications. *npj Computational Materials*, 24, 2019.
- [72] J. Luo. Stabilization of Nanoscale Quasi-Liquid Interfacial Films in Inorganic Materials: A Review and Critical Assessment. *Critical Reviews in Solid State and Materials Sciences*, 32:67–109, 2007.
- [73] J.H. Lee. Highly resistive intergranular phases in solid electrolytes: An overview. *Monatshefte fur Chemie*, 140:1081–1094, 2009.
- [74] K. Van Benthem, C. Elsasser, and R. French. Bulk electronic structure of SrTiO<sub>3</sub>: Experiment and theory. *Journal of Applied Physics*, 90(12):6156–6164, 2001.
- [75] G. Samara. Pressure and Temperature Dependences of the Dielectric Properties of the Perovskites BaTiO<sub>3</sub> and SrTiO<sub>3</sub>. *Physical Review*, 151:378–386, 1966.
- [76] I. Burn and D. Smyth. Energy Storage in Ceramic Dielectrics. *Journal of Materials Science*, 7:339–343, 1972.
- [77] D. Lowndes, D. Geohegan, A. Puretzky, D. Norton, and C. Rouleau. Synthesis of Novel Thin-Film Materials by Pulsed Laser Deposition. *Science*, 273(5277):898–903, 1996.
- [78] S. Tao and J. Irvine. A redox-stable efficient anode for solid-oxide fuel cells. *Nature Materials*, 2(5):320–323, 2003.
- [79] J. Fergus. Perovskite oxides for semiconductor-based gas sensors. *Sensors and Actuators B: Chemical*, 123(2):1169–1179, 2007.
- [80] R. Kubicek, M. and Schmitt, F. Messerschmitt, and J. Rupp. Uncovering Two Competing Switching Mechanisms for Epitaxial and Ultrathin Strontium Titanate-Based Resistive Switching Bits. *ACS Nano*, 9(11):10737–10748, 2015.
- [81] K. Fleck, N. Aslam, S. Hoffmann-Eifert, V. Longo, F. Roozeboom, W. Kessels, U. Bottger, R. Waser, and S. Menzel. The influence of non-stoichiometry on the switching kinetics of strontium-titanate ReRAM devices. *Journal of Applied Physics*, 120, 2016.
- [82] J.N. Baker, P.C. Bowes, D.M. Long, A. Moballeggh, J.S. Harris, E.C. Dickey, and D.L. Irving. Defect mechanisms of coloration in Fe-doped SrTiO<sub>3</sub> from first principles. *Applied Physics Letters*, 110(12), 2017.

- [83] P.C. Bowes, J.N. Baker, J.S. Harris, B.D. Behrhorst, and D.L. Irving. Influence of impurities on the high temperature conductivity of SrTiO<sub>3</sub>. *Applied Physics Letters*, 112(2), 2018.
- [84] J.N. Baker, P.C. Bowes, J.S. Harris, and D.L. Irving. Mechanisms governing metal vacancy formation in BaTiO<sub>3</sub> and SrTiO<sub>3</sub>. *Journal of Applied Physics*, 124(11), 2018.
- [85] J.N. Baker, P.C. Bowes, and D.L. Irving. Hydrogen solubility in donor-doped SrTiO<sub>3</sub> from first principles. *Applied Physics Letters*, 113(13), 2018.
- [86] P.C. Bowes, J.N. Baker, and D.L. Irving. Survey of acceptor dopants in SrTiO<sub>3</sub>: Factors limiting room temperature hole concentration. *Journal of the American Ceramic Society*, 103(2):1156–1173, 2020.
- [87] Y. Wu, P.C. Bowes, J.N. Baker, and D.L. Irving. Influence of space charge on the conductivity of nanocrystalline SrTiO<sub>3</sub>. *Journal of Applied Physics*, 128(1):014101, 2020.
- [88] M. McGibbon, N. Browning, M. Chisholm, A. McGibbon, S. Pennycook, V. Ravikumar, and V. Dravid. Direct determination of grain boundary atomic structure in SrTiO<sub>3</sub>. *Science*, 266(5182):102–104, 1994.
- [89] N. Browning and S. Pennycook. Direct experimental determination of the atomic structure at internal interfaces. *Journal of Physics D: Applied Physics*, 29(7):1779, 1996.
- [90] N. Browning, J. Buban, H. Moltaji, S. Pennycook, G. Duscher, K. Johnson, R. Rodrigues, and V. Dravid. The influence of atomic structure on the formation of electrical barriers at grain boundaries in SrTiO<sub>3</sub>. *Applied Physics Letters*, 74(18):2638–2640, 1999.
- [91] M. Kim, G. Duscher, N. Browning, K. Sohlberg, S. Pantelides, and S. Pennycook. Nonstoichiometry and the electrical activity of grain boundaries in SrTiO<sub>3</sub>. *Physical Review Letters*, 86(18):4056, 2001.
- [92] R. Moos and K.H. Hardtl. Defect chemistry of donor-doped and undoped strontium titanate ceramics between 1000°C and 1400°C. *Journal of the American Ceramic Society*, 80(10):2549–2562, 1997.
- [93] J. Crawford and P. Jacobs. Point defect energies for strontium titanate: A pair-potentials study. *Journal of Solid State Chemistry*, 144(2):423–429, 1999.
- [94] T. Bieger, J. Maier, and R. Waser. Optical investigation of oxygen incorporation in SrTiO<sub>3</sub>. *Solid State Ionics*, 53-56:578–582, 1992.

- [95] N. Chan, R. Sharma, and D. Smyth. Nonstoichiometry in SrTiO<sub>3</sub>. *Journal of the Electrochemical Society*, 128(8):1762, 1981.
- [96] R. Waser, T. Bieger, and J. Maier. Determination of acceptor concentrations and energy levels in oxides using an optoelectrochemical technique. *Solid State Communications*, 76(8):1077–1081, 1990.
- [97] I. Denk, W. Munch, and J. Maier. Partial Conductivities in SrTiO<sub>3</sub>: Bulk Polarization Experiments, Oxygen Concentration Cell Measurements, and Defect-Chemical Modeling. *Journal of the American Ceramic Society*, 78(12):3265–3272, 1995.
- [98] R.A. De Souza. The formation of equilibrium space-charge zones at grain boundaries in the perovskite oxide SrTiO<sub>3</sub>. *Physical Chemistry Chemical Physics*, 11:9939–9969, 2009.
- [99] R. Meyer, R. Waser, J. Helmbold, and G. Borchardt. Observation of vacancy defect migration in the cation sublattice of complex oxides by O18 tracer experiments. *Physical Review Letters*, 90(10):105901, 2003.
- [100] T.R. Clevenger. Effect of Fe<sup>4+</sup> in the System SrFeO<sub>3</sub>-SrTiO<sub>3</sub>. *Journal of the American Ceramic Society*, 46(5):207–210, 1963.
- [101] J. Rodriguez, J.A. Pereda, M. Vallet, J.G. Calbet, and J. Tejada. Mossbauer study of vacancy ordering in the system SrTi<sub>1-x</sub>Fe<sub>x</sub>O<sub>3-y</sub> (0.50 ≤ x ≤ 0.70). *Materials Research Bulletin*, 21(3):255–263, 1986.
- [102] P. Adler and S. Eriksson. Structural Properties, Mossbauer Spectra, and Magnetism of Perovskite-Type Oxides SrFe<sub>1-x</sub>Ti<sub>x</sub>O<sub>3-y</sub>. *Zeitschrift fur anorganische und allgemeine Chemie*, 626(1):118–124, 2000.
- [103] H. Zhou and J. Goodenough. Polaron morphologies in SrFe<sub>1-x</sub>Ti<sub>x</sub>O<sub>3-δ</sub>. *Journal of Solid State Chemistry*, 177:1952–1957, 2004.
- [104] H. Kim, L. Bi, G. Dionne, and C. Ross. Magnetic and magneto-optical properties of Fe-doped SrTiO<sub>3</sub> films. *Applied Physics Letters*, 93(9):4–7, 2008.
- [105] A. Sendil Kumar, P. Suresh, M. Mahesh Kumar, H. Srikanth, M. Post, K. Sahner, R. Moos, and S. Srinath. Magnetic and ferroelectric properties of Fe doped SrTiO<sub>3-δ</sub> films. *Journal of Physics: Conference Series*, 200:092010, 2010.
- [106] M. Drahus, P. Jakes, E. Erdem, and R. Eichel. Defect structure of the mixed ionic-electronic conducting Sr(Ti,Fe)O<sub>x</sub> solid-solution system - Change in iron oxidation states and defect complexation. *Solid State Ionics*, 184:47–51, 2011.

- [107] C. Lenser, A. Kalinko, A. Kuzmin, D. Berzins, J. Purans, K. Szot, R. Waser, and R. Dittmann. Spectroscopic study of the electric field induced valence change of Fe-defect centers in SrTiO<sub>3</sub>. *Physical Chemistry Chemical Physics*, 13(46):20779–20786, 2011.
- [108] X. Wang, Z. Wang, Q. Hu, C. Zhang, D. Wang, and L. Li. Room temperature multiferroic properties of Fe-doped nonstoichiometric SrTiO<sub>3</sub> ceramics at both A and B sites. *Solid State Communications*, 289:22–26, 2019.
- [109] M. Abdullah, R.J. Nelson, and K.R. Kittilstved. Tunable Redox Activity at Fe<sup>3+</sup> Centers in Colloidal ATiO<sub>3</sub> (A = Sr and Ba) Nanocrystals. *Chemistry of Materials*, 33(11):4196–4203, 2021.
- [110] R. Evarestov, S. Piskunov, E. Kotomin, G. Borstel, E. Kotomin, and E. Kotomin. Single impurities in insulators: Ab initio study of Fe-doped SrTiO<sub>3</sub>. *Physical Review B - Condensed Matter and Materials Physics*, 67:064101, 2003.
- [111] V. Alexandrov, J. Maier, and R. Evarestov. Ab initio study of SrFe<sub>x</sub>Ti<sub>1-x</sub>O<sub>3</sub>: Jahn-Teller distortion and electronic structure. *Physical Review B - Condensed Matter and Materials Physics*, 77(7):1–9, 2008.
- [112] M. Vracar, A. Kuzmin, R. Merkle, J. Purans, E. Kotomin, J. Maier, and O. Mathon. How is oxygen incorporated into oxides? A comprehensive kinetic study of a simple solid-state reaction with SrTiO<sub>3</sub> as a model material. *Physical Review B - Condensed Matter and Materials Physics*, 76(17):1–12, 2007.
- [113] L.F. da Silva, J.C. M’Peko, J. Andres, A. Beltran, L. Gracia, M.I. Bernardi, A. Mesquita, E. Antonelli, M.L. Moreira, and V.R. Mastelaro. Insight into the Effects of Fe Addition on the Local Structure and Electronic Properties of SrTiO<sub>3</sub>. *The Journal of Physical Chemistry C*, 118(9):4930–4940, 2014.
- [114] E. Sediva, T. Defferriere, N.H. Perry, H.L. Tuller, and J.L. Rupp. In Situ Method Correlating Raman Vibrational Characteristics to Chemical Expansion via Oxygen Nonstoichiometry of Perovskite Thin Films. *Advanced Materials*, 31(33):1–9, 2019.
- [115] A. Hadj Youssef, J. Zhang, A. Ehteshami, G. Kolhatkar, C. Dab, D. Berthomieu, A. Merlen, F. Legare, and A. Ruediger. Symmetry-Forbidden-Mode Detection in SrTiO<sub>3</sub> Nanoislands with Tip-Enhanced Raman Spectroscopy. *Journal of Physical Chemistry C*, 125(11):6200–6208, 2021.
- [116] J.M.D. Coey. *Magnetism and Magnetic Materials*. Cambridge University Press, Cambridge, first edition, 2009.

- [117] T. Schober and H.G. Bohn. Water vapor solubility and electrochemical characterization of the high temperature proton conductor  $\text{BaZr}_{0.9}\text{Y}_{0.1}\text{O}_{2.95}$ . *Solid State Ionics*, 127:351–360, 2000.
- [118] A. Azad and J. Irvine. Synthesis, chemical stability and proton conductivity of the perovskites  $\text{Ba}(\text{Ce,Zr})_{1-x}\text{Sc}_x\text{O}_{3-\delta}$ . *Solid State Ionics*, 178(7-10):635–640, 2007.
- [119] M. Shirpour, B. Rahmati, W. Sigle, P.A. Van Aken, R. Merkle, and J. Maier. Dopant segregation and space charge effects in proton-conducting  $\text{BaZrO}_3$  perovskites. *Journal of Physical Chemistry C*, 116(3):2453–2461, 2012.
- [120] J. Jamnik, J. Maier, and S. Pejovnik. Interfaces in solid ionic conductors: Equilibrium and small signal picture. *Solid State Ionics*, 75:51–58, 1995.
- [121] F. Iguchi, N. Sata, T. Tsurui, and H. Yugami. Microstructures and grain boundary conductivity of  $\text{BaZr}_{1-x}\text{Y}_x\text{O}_3$  ( $x = 0.05, 0.10, 0.15$ ) ceramics. *Solid State Ionics*, 178(7):691–695, 2007.
- [122] F. Iguchi, T. Tsurui, N. Sata, Y. Nagao, and H. Yugami. The relationship between chemical composition distributions and specific grain boundary conductivity in Y-doped  $\text{BaZrO}_3$  proton conductors. *Solid State Ionics*, 180(6-8):563–568, 2009.
- [123] C. Kjølseth, H. Fjeld, O. Prytz, P. Inge Dahl, C. Estournes, R. Haugrud, and T. Norby. Space-charge theory applied to the grain boundary impedance of proton conducting  $\text{BaZr}_{0.9}\text{Y}_{0.1}\text{O}_{3-\delta}$ . *Solid State Ionics*, 181(5):268–275, 2010.
- [124] C. Chen, C. Danel, and S. Kim. On the origin of the blocking effect of grain-boundaries on proton transport in yttrium-doped barium zirconates. *Journal of Materials Chemistry*, 21:5435–5442, 2011.
- [125] F. Iguchi, N. Sata, and H. Yugami. Proton transport properties at the grain boundary of barium zirconate based proton conductors for intermediate temperature operating SOFC. *Journal of Materials Chemistry*, 20:6265–6270, 2010.
- [126] F. Iguchi, C. Chen, H. Yugami, and S. Kim. Direct evidence of potential barriers at grain boundaries in Y-doped  $\text{BaZrO}_3$  from dc-bias dependence measurements. *Journal of Materials Chemistry*, 21:16517–16523, 2011.
- [127] M. Shirpour, R. Merkle, C. Lin, and J. Maier. Nonlinear electrical grain boundary properties in proton conducting Y– $\text{BaZrO}_3$  supporting the space charge depletion model. *Phys. Chem. Chem. Phys.*, 14(2):730–740, 2012.

- [128] A. Lindman, T. Bjorheim, and G. Wahnstrom. Defect segregation to grain boundaries in BaZrO<sub>3</sub> from first-principles free energy calculations. *Journal of Materials Chemistry A*, 5(26):13421–13429, 2017.
- [129] A. Lindman, E. Helgee, and G. Wahnstrom. Comparison of Space-Charge Formation at Grain Boundaries in Proton-Conducting BaZrO<sub>3</sub> and BaCeO<sub>3</sub>. *Chemistry of Materials*, 29(18):7931–7941, 2017.
- [130] T. Tauer, R. O’Hayre, and J. Medlin. Computational investigation of defect segregation at the (001) surface of BaCeO<sub>3</sub> and BaZrO<sub>3</sub>: the role of metal–oxygen bond strength in controlling vacancy segregation. *Journal of Materials Chemistry A*, 1:2840–2846, 2013.
- [131] M. Shirpour, G. Gregori, L. Houben, R. Merkle, and J. Maier. High spatially resolved cation concentration profile at the grain boundaries of Sc-doped BaZrO<sub>3</sub>. *Solid State Ionics*, 262:860–864, 2014.
- [132] D.R. Clark, H. Zhu, D.R. Diercks, S. Ricote, R.J. Kee, A. Almansoori, B.P. Gorman, and R.P. O’Hayre. Probing Grain-Boundary Chemistry and Electronic Structure in Proton-Conducting Oxides by Atom Probe Tomography. *ACS Nano Letters*, 16(11):6924–6930, 2016.
- [133] I. Oikawa and H. Takamura. Correlation among Oxygen Vacancies, Protonic Defects, and the Acceptor Dopant in Sc-Doped BaZrO<sub>3</sub> Studied by <sup>45</sup>Sc Nuclear Magnetic Resonance. *Chemistry of Materials*, 27(19):6660–6667, 2015.
- [134] D. Han, K. Shinoda, S. Tsukimoto, H. Takeuchi, C. Hiraiwa, M. Majima, and T. Uda. Origins of structural and electrochemical influence on Y-doped BaZrO<sub>3</sub> heat-treated with NiO additive. *Journal of Materials Chemistry A*, 2(31):12552, 2014.
- [135] B. Singh, S. Ghosh, S. Aich, and B. Roy. Low temperature solid oxide electrolytes (LT-SOE): A review. *Journal of Power Sources*, 339:103–135, 2017.
- [136] H. Dai, H. Kou, H. Wang, and L. Bi. Electrochemical performance of protonic ceramic fuel cells with stable BaZrO<sub>3</sub>-based electrolyte: A mini-review. *Electrochemistry Communications*, 96(11-15), 2018.
- [137] F.J.A. Loureiro, N. Nasani, G.S. Reddy, N.R. Munirathnam, and D.P. Fagg. A review on sintering technology of proton conducting BaCeO<sub>3</sub>-BaZrO<sub>3</sub> perovskite oxide materials for Protonic Ceramic Fuel Cells. *Journal of Power Sources*, 438 (226991):1–18, 2019.

- [138] J. Kim, S. Sengodan, S. Kim, O. Kwon, Y. Bu, and G. Kim. Proton conducting oxides: A review of materials and applications for renewable energy conversion and storage. *Renewable and Sustainable Energy Reviews*, 109:606–618, 2019.
- [139] J. Li, C. Wang, X. Wang, and L. Bi. Sintering aids for proton-conducting oxides – A double-edged sword? A mini review. *Electrochemistry Communications*, 112(106672), 2020.
- [140] J. Van Vleck. Spin, the great indicator of valence behaviour. *Pure and Applied Chemistry*, 24(1):235–256, 1970.
- [141] R. Voorhoeve. Experimental Relationships between Catalysis and Magnetism. *MAGNETISM AND MAGNETIC MATERIALS — 1973: Nineteenth Annual Conference*, 19(1974):19–32, 1974.
- [142] T. Schlesinger, R. Cammarata, A. Gavrin, J. Xiao, C. Chien, M. Ferber, and C. Hayzelden. Enhanced mechanical and magnetic properties of granular metal thin films. *Journal of Applied Physics*, 70(6):3275–3280, 1991.
- [143] T. Sekino, T. Nakajima, S. Ueda, and K. Niihara. Reduction and Sintering of a Nickel-Dispersed-Alumina Composite and Its Properties. *Journal of the American Ceramic Society*, 80(5):1139–1148, 1997.
- [144] P. Selwood, S. Adler, and T. Phillips. Thermomagnetic Analysis of Supported Nickel Catalysts. *Journal of the American Chemical Society*, 77(6):1462–1468, 1955.
- [145] L. Moore and P. Selwood. The Influence of Chemisorbed Gases on the Magnetization of Catalytically Active Nickel. *Journal of the American Chemical Society*, 78(4): 697–701, 1956.
- [146] G. Rymer, J. Bridges, and J. Tomlinson. Kinetic and magnetic studies on supported nickel oxide catalysts. *Journal of Physical Chemistry*, 65(12):2152–2157, 1961.
- [147] J. Carter, J. Cusumano, and J. Sinfelt. Catalysis over supported metals. V. The effect of crystallite size on the catalytic activity of nickel. *Journal of Physical Chemistry*, 70(7):2257–2263, 1966.
- [148] J. Richardson. Magnetism and catalysis. *Journal of Applied Physics*, 49(3): 1781–1786, 1978.
- [149] A. Banerjee and S. Sen. Some Aspects of Magneto-Chemistry in NiO-Al<sub>2</sub>O<sub>3</sub> Catalysts. *IEEE Transactions on Magnetics*, 18(6):1825–1828, 1982.

- [150] P. Dutta, A. Manivannan, M. Seehra, P. Adekkanattu, and J. Guin. Determination of the electronic state and concentration of nickel in NiSAPO catalysts by magnetic measurements. *Catalysis Letters*, 94(3-4):181–185, 2004.
- [151] M. Senaris-Rodriguez, S. Castro-Garcia, A. Castro-Couceiro, C. Julien, L. Hueso, and J. Rivas. Magnetic clusters in  $\text{LiNi}_{1-y}\text{Co}_y\text{O}_2$  nanomaterials used as cathodes in lithium-ion batteries. *Nanotechnology*, 14:277–282, 2003.
- [152] D. Schaniel, T. Woike, G. Weckwerth, J. Schefer, M. Imlau, M. Wohlecke, and R. Pankrath. Determination of  $\text{Ce}^{3+}$  concentration in doped  $\text{Sr}_{0.61}\text{Ba}_{0.39}\text{Nb}_2\text{O}_6$  from magnetization measurements. *Photorefractive Effects, Materials, and Devices*, pages 256–261, 2005.
- [153] J. Abiade, G. Miao, A. Gupta, A. Gapud, and D. Kumar. Structural and magnetic properties of self-assembled nickel nanoparticles in a yttria stabilized zirconia matrix. *Thin Solid Films*, 516:2082–2086, 2008.
- [154] J.T. White, I.E. Reimanis, J. Tong, J.R. O'Brien, and A. Morrissey. Internal reduction of  $\text{Ni}^{2+}$  in  $\text{ZrO}_2$  stabilized with 10 mol%  $\text{Y}_2\text{O}_3$  examined with VSM and SQUID magnetometry. *Journal of the American Ceramic Society*, 95(12):4008–4014, 2012.
- [155] A. Morrissey, J. Tong, B.P. Gorman, and I.E. Reimanis. Characterization of nickel ions in nickel-doped yttria-stabilized zirconia. *Journal of the American Ceramic Society*, 97(4):1041–1047, 2014.
- [156] A. Bose, R. Ramamoorthy, and S. Ramasamy. Formability of metastable tetragonal solid solution in nanocrystalline nio-zro<sub>2</sub> powders. *Materials letters*, 44(3-4):203–207, 2000.
- [157] A. Morrissey, J.R. O'Brien, and I.E. Reimanis. Microstructure evolution during internal reduction of polycrystalline nickel-doped yttria-stabilized zirconia. *Acta Materialia*, 105:84–93, 2016.
- [158] A. Abragam and B. Bleaney. *EPR of Transition Metal Ions*. Oxford University Press, Oxford, 1st ed. edition, 1970. ISBN 9780199651528.
- [159] J.H. Lunsford. Electron spin resonance in catalysis. In *Advances in Catalysis*, volume 22, pages 265–344. Elsevier, 1972.
- [160] R.F. Howe. EPR spectroscopy in surface chemistry: recent developments. *Advances in Colloid and Interface Science*, 18(1-2):1–55, 1982.

- [161] K. Dyrek and M. Che. EPR as a tool to investigate the transition metal chemistry on oxide surfaces. *Chemical Reviews*, 97(1):305–332, 1997.
- [162] Z. Sojka and M. Che. EPR techniques applied to the study of chemistry and catalysis on oxide surfaces. *Applied Magnetic Resonance*, 20(3):433–456, 2001.
- [163] J.M. Polfus, M.L. Fontaine, A. Thogersen, M. Riktor, T. Norby, and R. Bredesen. Solubility of transition metal interstitials in proton conducting BaZrO<sub>3</sub> and similar perovskite oxides. *Journal of Materials Chemistry A*, 4(21):8105–8112, 2016.
- [164] Z. Liu, X. Wang, M. Liu, and J. Liu. Enhancing sinterability and electrochemical properties of Ba(Zr<sub>0.1</sub>Ce<sub>0.7</sub>Y<sub>0.2</sub>)O<sub>3-δ</sub> proton conducting electrolyte for solid oxide fuel cells by addition of NiO. *International Journal of Hydrogen Energy*, 43(29):13501–13511, 2018.
- [165] R. Fagaly. Superconducting quantum interference device instruments and applications. *Review of Scientific Instruments*, 77(101101), 2006.
- [166] R.B. Goldfarb. Electromagnetic Units, the Giorgi System, and the Revised International System of Units. *IEEE Magnetism Letters*, 9:1–5, 2018.
- [167] D.M. Murphy. EPR (Electron Paramagnetic Resonance) Spectroscopy of Polycrystalline Oxide Systems. In *Metal Oxide Catalysis*, volume 1, pages 1–50. Wiley-vch, 2009. ISBN 9783527318155.
- [168] K. Szot, W. Speier, G. Bihlmayer, and R. Waser. Switching the electrical resistance of individual dislocations in single-crystalline SrTiO<sub>3</sub>. *Nature Materials*, 5:312–320, 2006.
- [169] D. Gryaznov, J. Fleig, and J. Maier. Numerical study of grain boundary diffusion in nanocrystalline ionic materials including blocking space charges. *Solid State Ionics*, 177:1583–1586, 2006.
- [170] H. Ohta, S. Kim, Y. Mune, T. Mizoguchi, K. Nomura, S. Ohta, T. Nomura, Y. Nakanishi, Y. Ikuhara, M. Hirano, H. Hosono, and K. Koumoto. Giant thermoelectric Seebeck coefficient of a two-dimensional electron gas in SrTiO<sub>3</sub>. *Nature Materials*, 6:129–134, 2007.
- [171] N. Reyren, S. Thiel, A. Cavaglia, L. Fitting-Kourkoutis, G. Hammerl, C. Richter, C. Schneider, T. Kopp, A. Ruetschi, D. Jaccard, M. Gabay, D. Muller, J. Trisconne, and J. Mannhart. Superconducting Interfaces Between Insulating Oxides. *Science*, 317:1196–1200, 2007.

- [172] B. Phoon, C. Lai, J. Juan, P. Show, and G. Pan. Recent developments of strontium titanate for photocatalytic water splitting application. *International Journal of Hydrogen Energy*, 44:14316–14340, 2019.
- [173] A. Tang, J. Pellicciari, Q. Song, Q. Song, S. Ning, J. Freeland, R. Comin, and C. Ross. XMCD study of magnetism and valence state in iron-substituted strontium titanate. *Physical Review Materials*, 3:054408, 2019.
- [174] U. Knauer. Distribution of the Iron Dopant in Barium Titanate Ceramic, Determined by the Scanning Transmission Electron Microscope. *Physica Status Solidi (a)*, 53:207–210, 1979.
- [175] S. Desu and D. Payne. Interfacial Segregation in Perovskites: II, Experimental Evidence. *Journal of the American Ceramic Society*, 73:3398–3406, 1990.
- [176] Y. Chiang and T. Takagi. Grain-Boundary Chemistry of Barium Titanate and Strontium Titanate: I, High-Temperature Equilibrium Space Charge. *Journal of the American Ceramic Society*, 73:3278–3285, 1990.
- [177] W. Rheinheimer and M.J. Hoffmann. Non-Arrhenius behavior of grain growth in strontium titanate: New evidence for a structural transition of grain boundaries. *Scripta Materialia*, 101:68–71, 2015.
- [178] K.S.N. Vikrant, W. Rheinheimer, H. Sternlicht, M. Bäurer, and R.E. García. Electrochemically-driven abnormal grain growth in ionic ceramics. *Acta Materialia*, 200:727–734, 2020.
- [179] W. Nilsen and J. Skinner. Raman spectrum of strontium titanate. *The Journal of Chemical Physics*, 48(5):2240–2248, 1968.
- [180] S. Fuentes, P. Munoz, N. Barraza, E. Chavez-Angel, and C. Sotomayor-Torres. Structural characterisation of slightly Fe-doped SrTiO<sub>3</sub> grown via a sol-gel hydrothermal synthesis. *Journal of Sol-Gel Science and Technology*, 75(3):593–601, 2015.
- [181] U. Balachandran and N. Eror. Raman Spectra of Strontium Titanate. *Communications of the American Ceramic Society*, 65:54–56, 1982.
- [182] V. Bhide and H. Bhasin. Mossbauer Studies of the SrTiO<sub>3</sub>:Fe<sup>57</sup> System. *Physical Review*, 172(2):290–294, 1968.
- [183] C. Luiskutty and P. Ouseph. Valence states of iron in photochromic strontium titanate by Mossbauer effect. *Solid State Communications*, 13(3):405–409, 1973.

- [184] M. Multani. Ultra-Stable High-Precision Mossbauer Spectroscopy of Photochromic Centers in Fe:SrTiO<sub>3</sub>. *Materials Research Bulletin*, 19:25–34, 1984.
- [185] E. Dulov, N. Ivoilov, O. Strebkov, L. Tagirov, V. Nuzhdin, R. Khaibullin, S. Kazan, and F. Mikailzade. Magnetic phase composition of strontium titanate implanted with iron ions. *Materials Research Bulletin*, 46:2304–2307, 2011.
- [186] T. Goto, D.H. Kim, X. Sun, M.C. Onbasli, J.M. Florez, S.P. Ong, P. Vargas, K. Ackland, P. Stamenov, N.M. Aimon, M. Inoue, H.L. Tuller, G.F. Dionne, J.M.D. Coey, and C.A. Ross. Magnetism and Faraday Rotation in Oxygen-Deficient Polycrystalline and Single-Crystal Iron-Substituted Strontium Titanate. *Physical Review Applied*, 7(2):26–28, 2017.
- [187] A.T. Raghavender, N. Hoa Hong, K. Joon Lee, M.H. Jung, Z. Skoko, M. Vasilevskiy, M.F. Cerqueira, and A.P. Samantilleke. Nano-ilmenite FeTiO<sub>3</sub>: Synthesis and characterization. *Journal of Magnetism and Magnetic Materials*, 331:129–132, 2013.
- [188] T. Takeda, Y. Yamaguchi, and H. Watanabe. Magnetic Structure of SrFeO<sub>3</sub>. *Journal of the Physical Society of Japan*, 33(4):967–969, 1972.
- [189] R. Boca and J. Titis. Magnetostructural D-correlation for Zero-Field Splitting in Nickel(II) Complexes. In T. Cartere and K. Verley, editors, *Coordination Chemistry Research Progress*, pages 247–304. Nova Science Publishers, New York, USA, 2008.
- [190] R. Shannon. Revised Effective Ionic Radii and Systematic Studies of Interatomic Distances in Halides and Chalcogenides. *Acta Crystallographica*, A32:751–767, 1976.
- [191] D.A. Freedman, D. Roundy, and T. Arias. Elastic effects of vacancies in strontium titanate: Short- and long-range strain fields, elastic dipole tensors, and chemical strain. *Physical Review B - Condensed Matter and Materials Physics*, 80(6):1–13, 2009.
- [192] R. Klie and N. Browning. Atomic scale characterization of oxygen vacancy segregation at SrTiO<sub>3</sub> grain boundaries. *MRS Online Proceedings Library (OPL)*, 654, 2000.
- [193] T. Onishi, D. Han, Y. Noda, N. Hatada, M. Majima, and T. Uda. Evaluation of performance and durability of Ni-BZY cermet electrodes with BZY electrolyte. *Solid State Ionics*, 317(January):127–135, 2018.
- [194] S. Ricote, B.L. Kee, and W.G. Coors. Channelized substrates made from BaZr<sub>0.75</sub>Ce<sub>0.05</sub>Y<sub>0.2</sub>O<sub>3-δ</sub> proton-conducting ceramic polymer clay. *Membranes*, 9(130):1–12, 2019.

- [195] K. Ueno, N. Hatada, D. Han, and T. Uda. Thermodynamic maximum of Y doping level in barium zirconate in co-sintering with NiO. *Journal of Materials Chemistry A*, 7(12):7232–7241, 2019.
- [196] J. Amador, E. Gutierrez-Puebla, M.A. Monge, I. Rasines, C. Ruiz-Valero, F. Fernandez, R. Saez-Puche, and J. Campa. Evidence of low-dimensional antiferromagnetic ordering and crystal structure in the  $R_2\text{BaNiO}_{4/3}$  ( $R=\text{Y,Er}$ ) oxides. *Physical Review B - Condensed Matter*, 42(13):7918–7924, 1990.
- [197] R. Eichel, E. Erunal, P. Jakes, S. Korbel, C. Elsasser, H. Kungl, J. Acker, and M. Hoffmann. Interactions of defect complexes and domain walls in CuO-doped ferroelectric (K,Na)NbO<sub>3</sub>. *Applied Physics Letters*, 102:1–5, 2013.
- [198] R. Eichel. Structural and dynamic properties of oxygen vacancies in perovskite oxides - Analysis of defect chemistry by modern multi-frequency and pulsed EPR techniques. *Physical Chemistry Chemical Physics*, 13:368–384, 2011.
- [199] S. Wu, J. Lin, Q. Fu, and H. Zhang. Investigations on the impurity displacements and the  $g$  factors of the two tetragonal  $\text{Ni}^{3+}$  centres in SrTiO<sub>3</sub>. *Physica Scripta*, 75(2):147–151, 2007.
- [200] K. Muller, W. Berlinger, and R. Rubins. Observation of two charged states of a nickel-oxygen vacancy pair in SrTiO<sub>3</sub> by paramagnetic resonance. *Physical Review*, 186(2):361–371, 1969.
- [201] F. Giannici, M. Shirpour, A. Longo, A. Martorana, R. Merkle, and J. Maier. Long-range and short-range structure of proton-conducting Y:BaZrO<sub>3</sub>. *Chemistry of Materials*, 23(11):2994–3002, 2011.
- [202] E. Kim, Y. Yamazaki, S. Haile, and H. Yoo. Effect of NiO sintering-aid on hydration kinetics and defect-chemical parameters of BaZr<sub>0.8</sub>Y<sub>0.2</sub>O<sub>3- $\delta$</sub> . *Solid State Ionics*, 275: 23–28, 2015.
- [203] M. Knight, D. Jennings, S. Ricote, and I. Reimanis. Estimating nickel valence with magnetometry in yttrium-doped barium zirconate. *Journal of the American Ceramic Society*, 105:159–168, 2021.

## APPENDIX A

### ADDITIONAL RESULTS AND FIGURES

This appendix contains additional results characterizing Cu dopants in BZY15 prepared by wet-chemical methods, as well as, additional figures that were not necessary to include in the main chapters.

#### A.1 Cu-doped BZY15 Prepared by Wet Chemical Methods

Samples of  $\text{BaZr}_{0.85-x}\text{Y}_{0.15}\text{Cu}_x\text{O}_{3-\delta}$  ( $x = 0.005, 0.01, 0.015$ ) were prepared via solution chemistry. Stoichiometric amounts of barium acetate, zirconium acetate, yttrium acetate, and nickel acetate in solution were measured and combined in a beaker. The mixture was heated at  $80^\circ\text{C}$  while stirring. Chelating agents, citric acid and ethylenediaminetetraacetic acid (EDTA), were added to the mixture and dissolved with ammonium hydroxide. The solution was heated until all  $\text{H}_2\text{O}$  was evaporated and a viscous gel remained. The gel was then dried in an oven at  $150^\circ\text{C}$  for 24 h into a char. The char was then loaded into a high-purity alumina crucible and calcined at  $900^\circ\text{C}$  for 20 h.

The calcined powders were ground with an agate mortar and pestle for 20 min to break apart agglomerates and promote homogeneity of particle sizes. Cu  $K\alpha$  ( $\lambda = 1.540598 \text{ \AA}$ ) XRD patterns were collected at  $25^\circ\text{C}$  in Bragg-Brentano geometry from  $2\theta = 20^\circ$  to  $2\theta = 100^\circ$  with a step size of  $2\theta = 0.007^\circ$ . Lattice parameters and secondary phase quantification were estimated using Rietveld refinement. The XRD patterns shown in Figure A.1 consist of the main BZY15 phase with a Rietveld estimated 2wt%  $\text{BaCO}_3$  phase. The diffraction peaks are much broader than those typically observed in solid-state reaction prepared BZY, consistent with very fine crystallites that could prove to be beneficial when sintering.

Magnetometry was performed on the powders using a Magnetic Property Measurement System (MPMS) located at the National Institute of Standards and Technology (NIST) in

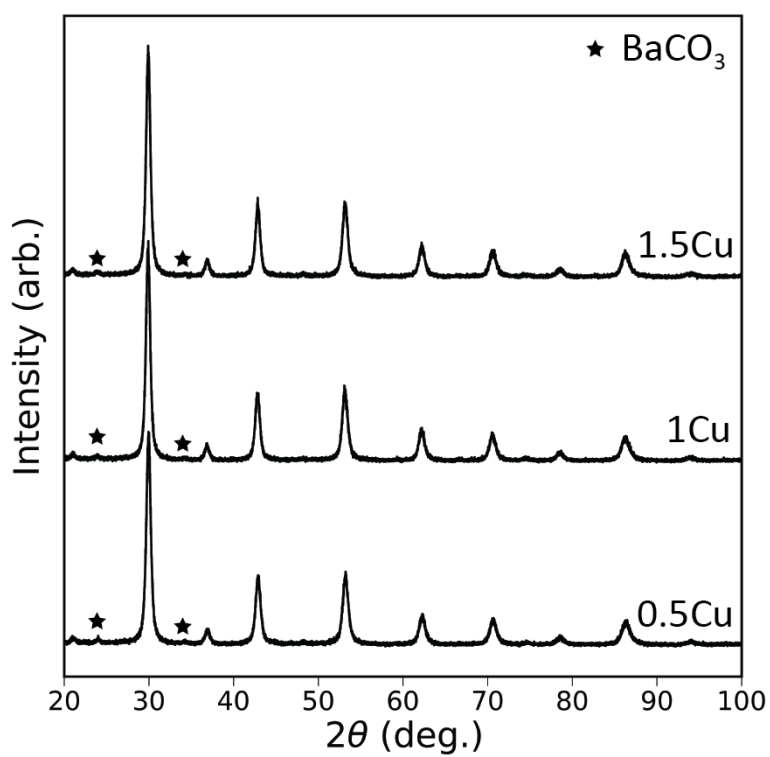


Figure A.1 XRD patterns of  $\text{BaZr}_{0.85-x}\text{Y}_{0.15}\text{Cu}_x\text{O}_{3-\delta}$  ( $x = 0.005, 0.01, 0.015$ ) prepared by sol-gel method. Reitveld refinement estimated approximately 2 wt%  $\text{BaCO}_3$  (stars) residual phase remained in the samples after calcination at  $900^\circ\text{C}$ .

Boulder, CO. Magnetic susceptibility versus temperature under 1 T applied magnetic field was performed upon heating from 1.8 K to 300 K. The 1 T field was chosen to provide significant magnetization of the samples for more accurate measurements when dealing with a very weakly magnetic system. The reciprocal susceptibilities with Curie-Weiss fits are shown in Figure A.2 (a), and the resulting  $\mu_{\text{eff}}/\text{Cu}$  values are shown in Figure A.2 (b).

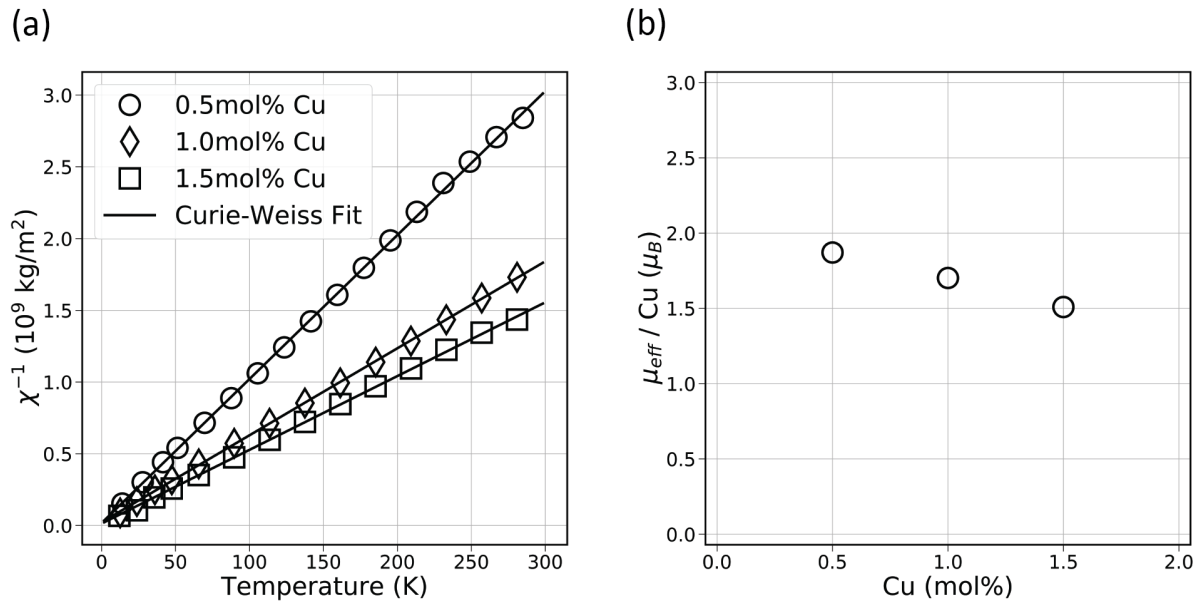


Figure A.2 Reciprocal magnetic susceptibilities with Curie-Weiss fits (a) and resulting  $\mu_{\text{eff}}/\text{Cu}$  values (b) for sol-gel prepared BZY15. The linear fits of  $\chi^{-1}(T)$  in (a) were used to estimate the  $\mu_{\text{eff}}/\text{Cu}$  values in (b).

As Cu-doping increased from 0.5 mol% to 1.5 mol%,  $\mu_{\text{eff}}/\text{Cu}$  decreased from the ideal  $\text{Cu}^{2+}$  of  $1.8\mu_B$  to  $1.5\mu_B$ . This decrease could be due to inhomogeneous distribution of the Cu in the crystallites. If the Cu was preferentially located at, or near, surfaces or crystallite interfaces in particles they could exist as next-nearest neighbors on the perovskite B-sites. Similar to the explanations in the main chapters for Fe-doped STO and Ni-doped BZY20, this situation could lead to antiferromagnetic interaction between the dopants, reducing the effective moments. Because Cu was identified here to exist in a 2+ state, which has one unpaired valence electron, further analysis with EPR is suggested.

## A.2 Additional Figures

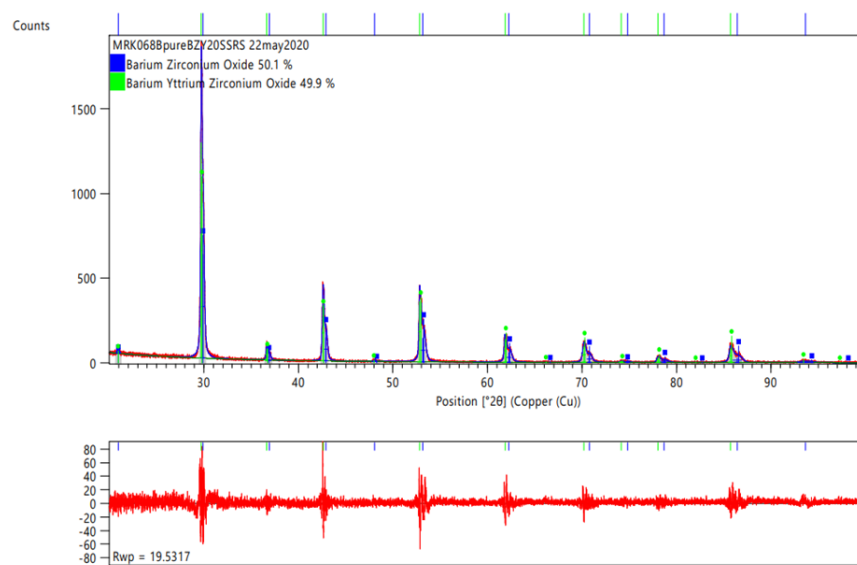


Figure A.3 Powder X-ray diffraction of slow-cooled  $\text{BaZr}_{0.8}\text{Y}_{0.2}\text{O}_{3-\delta}$

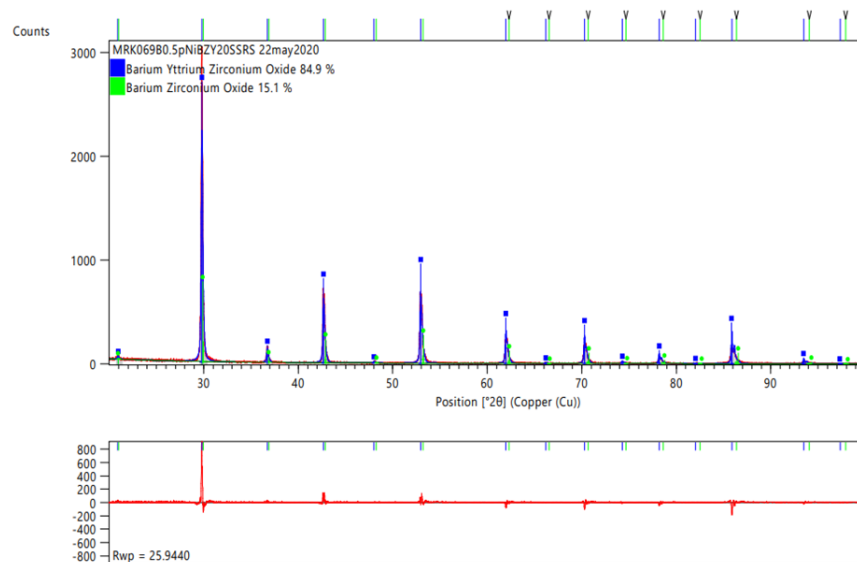


Figure A.4 Powder X-ray diffraction of slow-cooled  $\text{BaZr}_{0.795}\text{Y}_{0.2}\text{Ni}_{0.005}\text{O}_{3-\delta}$

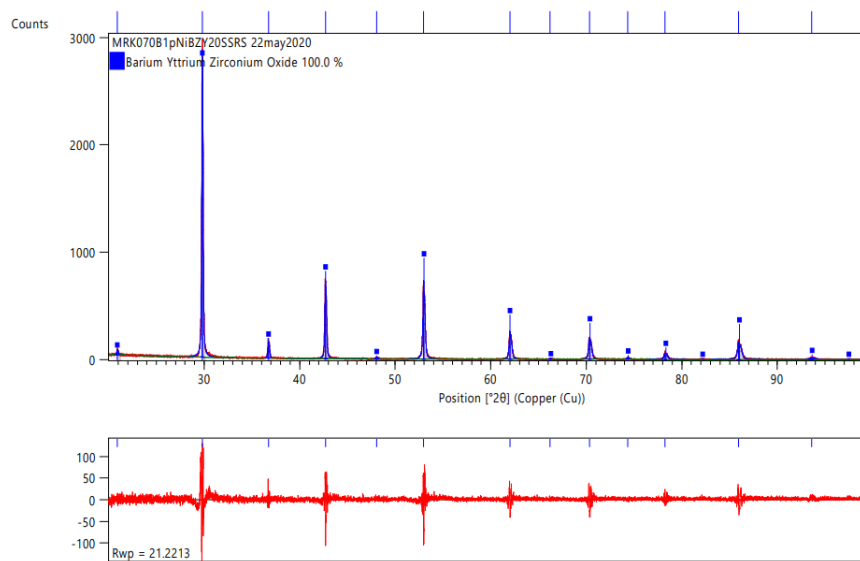


Figure A.5 Powder X-ray diffraction of slow-cooled  $\text{BaZr}_{0.79}\text{Y}_{0.2}\text{Ni}_{0.01}\text{O}_{3-\delta}$

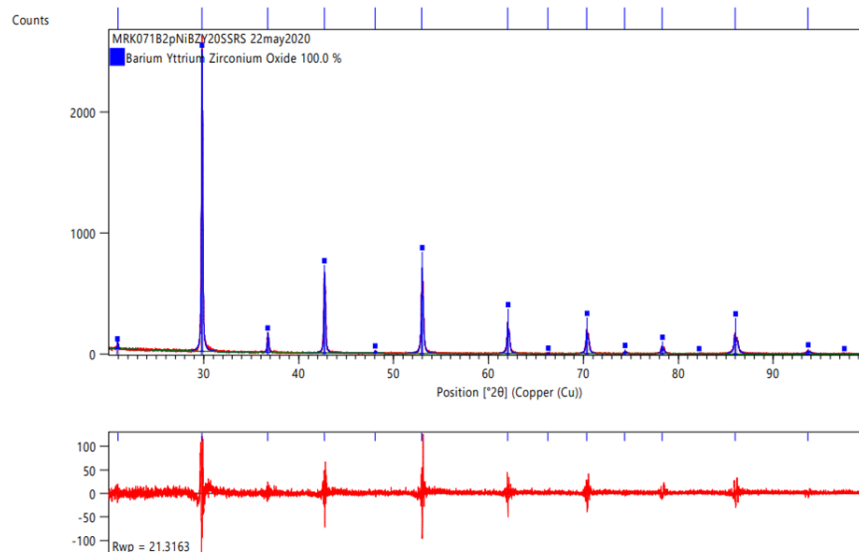


Figure A.6 Powder X-ray diffraction of slow-cooled  $\text{BaZr}_{0.78}\text{Y}_{0.2}\text{Ni}_{0.02}\text{O}_{3-\delta}$

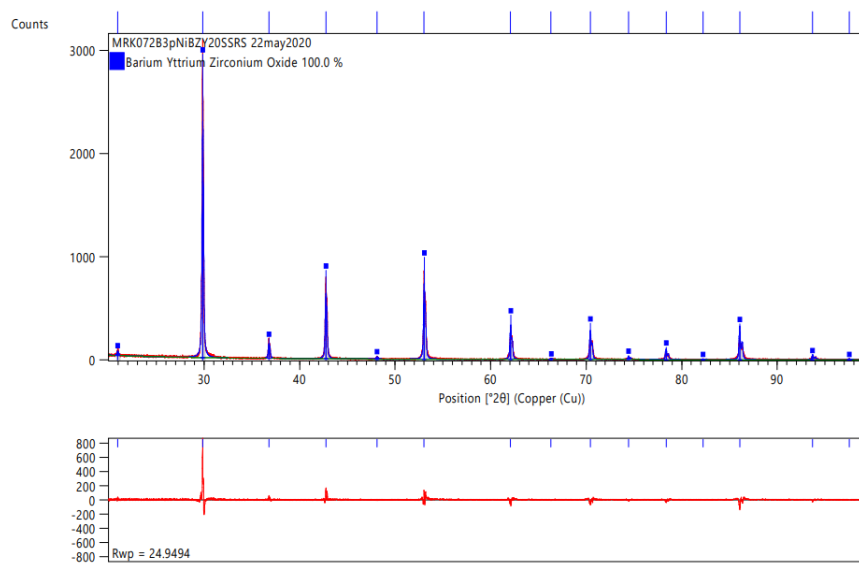


Figure A.7 Powder X-ray diffraction of slow-cooled  $\text{BaZr}_{0.77}\text{Y}_{0.2}\text{Ni}_{0.03}\text{O}_{3-\delta}$

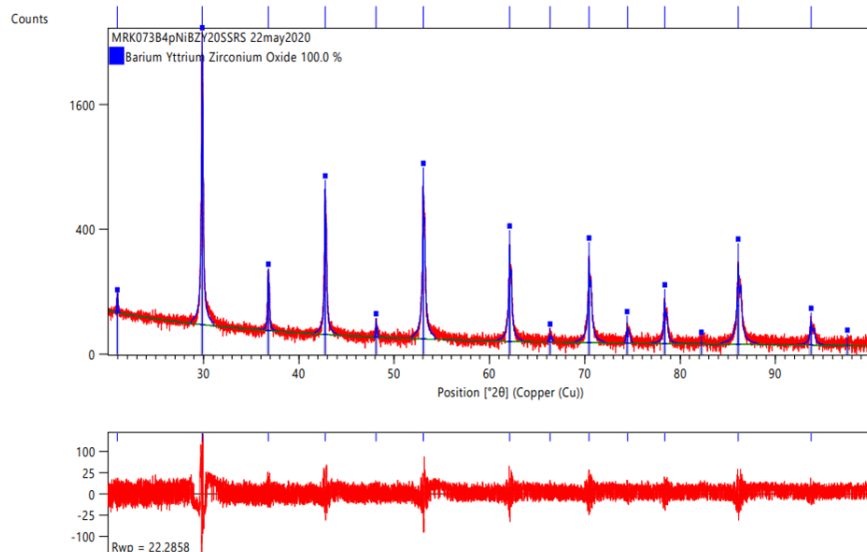


Figure A.8 Powder X-ray diffraction of slow-cooled  $\text{BaZr}_{0.76}\text{Y}_{0.2}\text{Ni}_{0.04}\text{O}_{3-\delta}$

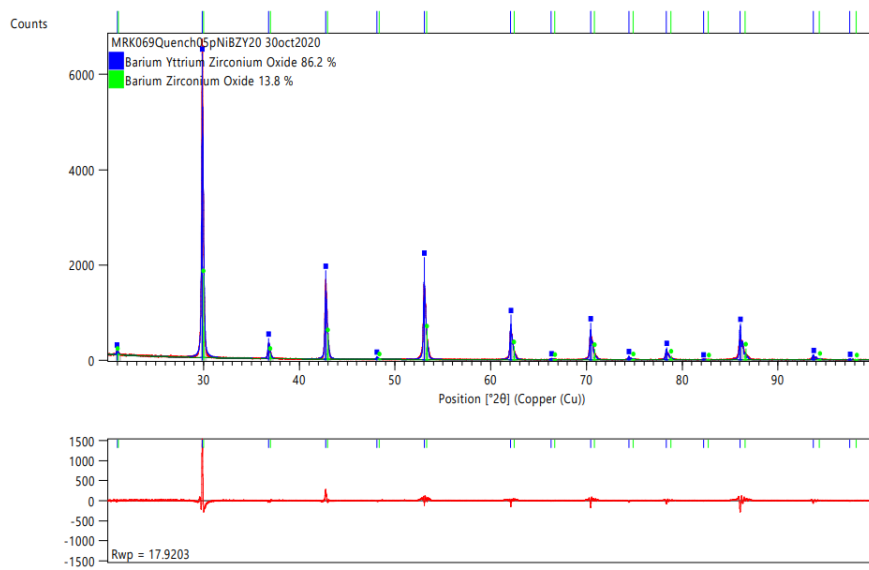


Figure A.9 Powder X-ray diffraction of quenched  $\text{BaZr}_{0.795}\text{Y}_{0.2}\text{Ni}_{0.005}\text{O}_{3-\delta}$

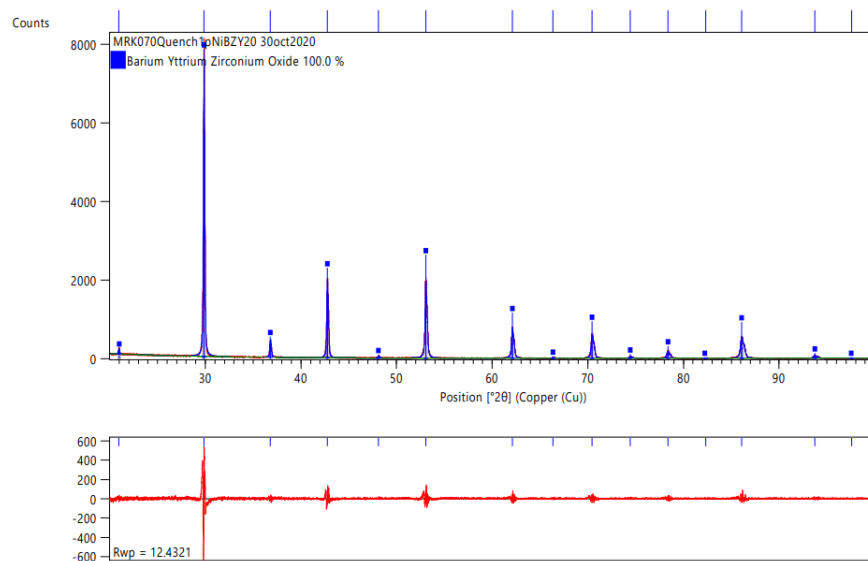


Figure A.10 Powder X-ray diffraction of quenched  $\text{BaZr}_{0.79}\text{Y}_{0.2}\text{Ni}_{0.01}\text{O}_{3-\delta}$

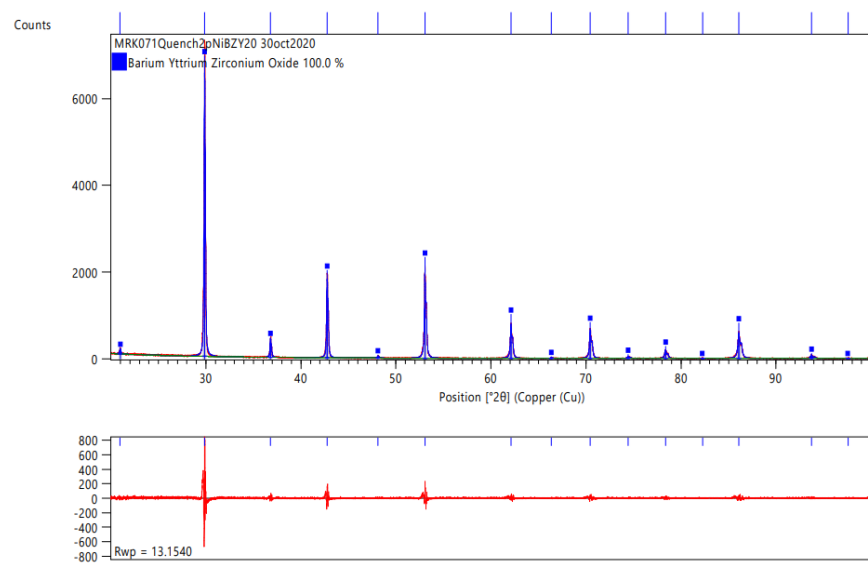


Figure A.11 Powder X-ray diffraction of quenched  $\text{BaZr}_{0.78}\text{Y}_{0.2}\text{Ni}_{0.02}\text{O}_{3-\delta}$

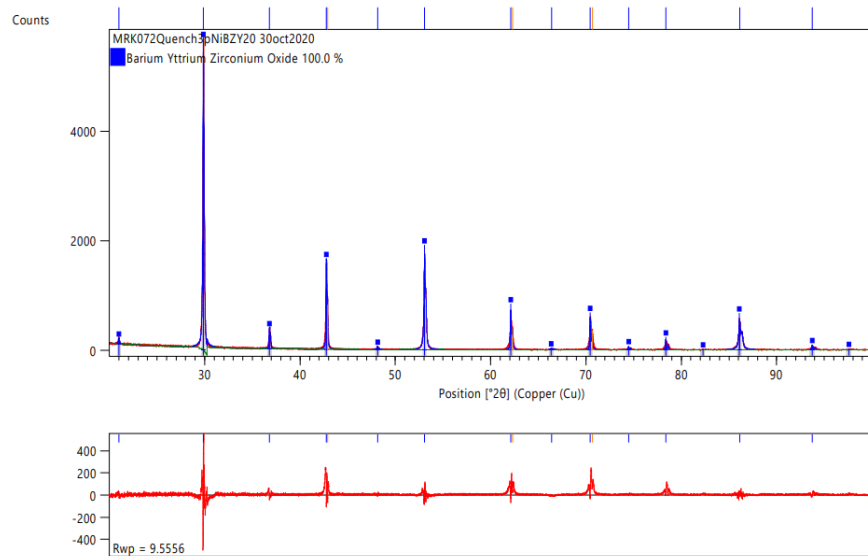


Figure A.12 Powder X-ray diffraction of quenched  $\text{BaZr}_{0.77}\text{Y}_{0.2}\text{Ni}_{0.03}\text{O}_{3-\delta}$

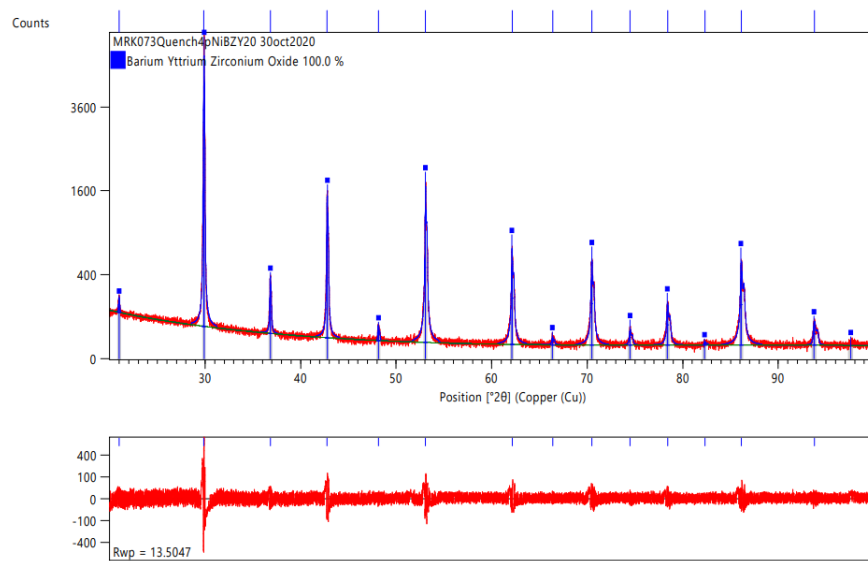


Figure A.13 Powder X-ray diffraction of quenched  $\text{BaZr}_{0.76}\text{Y}_{0.2}\text{Ni}_{0.04}\text{O}_{3-\delta}$

## APPENDIX B

### MAGNETOMETRY SEQUENCES AND DATA FITTING SCRIPTS

This appendix contains examples of MultiVu sequences used to operate the MPMS3 SQUID magnetometer, and Python scripts used to analyze magnetometry data. These examples are not comprehensive, but provide a starting point for the interested reader to explore.

#### B.1 Example ZFC-FC M(T) MultiVu Sequence

```
New Datafile "C:\QdSquidVsm\Data\ZFC.dat"
Set Temperature 10K at 50K/min. Fast Settle
Wait For Temperature, Delay 120 secs (2.0 mins), No Action
Set Temperature 1.8K at 12K/min. No O'Shoot
Wait For Temperature, Delay 120 secs (2.0 mins), No Action
Set Magnetic Field 2000.00e at 100.000e/sec, No O'Shoot, Stable
Wait For Field, Delay 60 secs (1.0 mins), No Action
MPMS3 Locate by DC Scan
MPMS3 Moment (DC) vs Temperature 1.8K to 100K Sweep Continuous Auto-Tracking
MPMS3 Moment (DC) vs Temperature 101K to 300K Sweep Continuous Auto-Tracking
Set Temperature 300K at 12K/min. Fast Settle
Wait For Temperature, Delay 10 secs, No Action
New Datafile "C:\QdSquidVsm\Data\FC.dat"
Set Temperature 10K at 50K/min. Fast Settle
Wait For Temperature, Delay 120 secs (2.0 mins), No Action
Set Temperature 1.8K at 12K/min. No O'Shoot
Wait For Temperature, Delay 120 secs (2.0 mins), No Action
MPMS3 Locate by DC Scan
```

```
MPMS3 Moment (DC) vs Temperature 1.8K to 100K Sweep Continuous
MPMS3 Moment (DC) vs Temperature 101K to 300K Sweep Continuous
Set Temperature 300K at 12K/min. Fast Settle
Wait For Temperature, Delay 10 secs, No Action
Set Magnetic Field 0.00e at 700.000e/sec, Oscillate, Stable
Wait For Field, Delay 1 secs, No Action
```

## B.2 Example M(H) MultiVu Sequence

```
New Datafile "C:\QdSquidVsm\Data\MH 10K.dat"
Set Temperature 10K at 50K/min. Fast Settle
Wait For Temperature, Delay 120 secs (2.0 mins), No Action
Set Temperature 1.8K at 12K/min. No O'Shoot
Wait For Temperature, Delay 120 secs (2.0 mins), No Action
Set Magnetic Field 70000.00e at 700.000e/sec, Linear, Stable
Wait For Field, Delay 120 secs (2.0 mins), No Action
MPMS3 Locate by DC Scan
MPMS3 Moment (DC) vs Field 1 Quadrant (70000 0e->0 0e) Step Linear
Set Magnetic Field 0.00e at 700.000e/sec, Linear, Stable
Wait For Field, Delay 10 secs, No Action
```

## B.3 Example Code for Magnetometry Data Analysis

All data analysis and plotting was performed with Python scripts based on the following examples.

### B.3.1 Importing and Converting Data to SI Units

```
#import necessary libraries
import pandas as pd
import os
```

```

import glob
import matplotlib.pyplot as plt
import numpy as np
from scipy.optimize import minimize
from scipy import stats

#automatically show plots
\%matplotlib inline

#set directory for folders containing data
datadir="C:\\Users\\Human\\Data"
os.listdir(datadir)

#choose a consistent label for output of processed data
filelabel="Sample Set ID"

#choose folder in directory for .dat files of interest and import them
#skiprows may need to be adjusted based on MultiVu version changing header
#usecols can be chosen based on what data you need
files=glob.glob(os.path.join(datadir,"folder","*.dat"))
filedict={}
for file in files:
    filename=os.path.basename(file)
    df=pd.read_csv(file, skiprows=26, usecols=["Temperature (K)",
        "Magnetic Field (Oe)", "DC Moment Fixed Ctr (emu)", "DC Fixed Fit"])
    with open(file) as f:
        txt=f.read()

```

```

txt.split("\n")
txtsplit=txt.split("\n")
mass=float(txtsplit[10].split(",")[1])/1000 #convert mass to kg

#do some useful conversions to SI units
df["Magnetic Field (A/m)"]=df["Magnetic Field (Oe)"]*1000/(4*np.pi)
df["Mass Magnetization (Am2/kg)"]=df["DC Moment Fixed Ctr (emu)"]/mass
df["Magnetic Field (T)"]=df["Magnetic Field (Oe)"]/10000
df["Mass Susceptibility (m3/kg)"]=df["Mass Magnetization (Am2/kg)"/
df["Magnetic Field (A/m)"]

#plot and save M(H) data if needed
#identifies M(H) and M(T) data by naming convention used: data MH.dat,
if filename.split(" ")[1]=="MH":

fig = plt.figure()
ax = fig.add_subplot(1, 1, 1)
ax.plot(df["Magnetic Field (T)"],df["Mass Magnetization (Am2/kg)"],
color='k', ls='none',marker='.')
ax.set_xlabel("Applied Magnetic Field (T)")
ax.set_ylabel("Mass Magnetization (Am2/kg)")
ax.grid()

fig.savefig(filelabel + " M(H)"+".png",dpi=600)
df.to_csv(filelabel + " M(H)" + " processed data"+".csv")

#plot and save M(T) data

```

```

elif filename.split(" ")[1]=="MT":

    fig = plt.figure()
    ax = fig.add_subplot(1, 1, 1)
    ax.plot(df["Temperature (K)"], df["Mass Susceptibility (m3/kg)"],
            color='k', ls='none', marker='.')
    ax.set_xlabel("Temperature (K)")
    ax.set_ylabel("Mass Susceptibility (m3/kg)")
    ax.grid()

    fig.savefig(filelabel+" M(T)".png",dpi=600)
    df.to_csv(filelabel+" M(T)" +" processed data".csv)

filedict[filename]=df

```

### B.3.2 Correcting Data for Diamagnetic Background

```

#assign variables to the data frames you want to correct
df0 = filedict['Data MT.dat']
df1 = filedict['Data MH.dat']

#negative diamagnetic susceptibility value in m3/kg for correction
chiDM = -1.6e-9

#create diamagnetic M(H) curve
Mdm = chiDM*df1["Magnetic Field (A/m)"]

#create new entries in the data frames for corrected data
df0["Corrected Mass Susceptibility (m3/kg)"] =

```

```
df0["Mass Susceptibility (m3/kg)"] - chiDM
```

```
df1["Corrected Mass Magnetization (Am2/kg)"] =
```

```
df1["Mass Magnetization (Am2/kg)"] - Mdm
```

### B.3.3 Curie-Weiss Analysis of Paramagnetic M(T) Data

```
#define necessary constants
```

```
muB=9.274E-24      #Bohr Magneton (Joule/Tesla)
```

```
kB=1.3806E-23     #Boltzmann's (Joule/Kelvin)
```

```
mu0=4*np.pi*10**-7 #permeability of vac (Tesla-meter/Ampere)
```

```
#assign variable to data frame you want to use
```

```
dfcw=filedict['Data MT.dat']
```

```
#set concentration of magnetic cations per kg if known,
```

```
#or use ideal concentration
```

```
N=1.9E22
```

```
#assign variables corresponding to bounds of fitting
```

```
Tmax=50 #indice for max temperature
```

```
Tmin=1 #indice for min temperature
```

```
#assign variables to temperature and susceptibility data
```

```
Tcw=dfcw["Temperature (K)"]
```

```
chi=dfcw["Corrected Mass Susceptibility (m3/kg)"]
```

```
#create variable for reciprocal susceptibility and save it to the
```

```
#data frame to output later
```

```

ichi=1/chi
dfcw["Reciprocal Mass Susceptibility (kg/m^3)"]=ichi

#perform linear fitting
slope, intercept, rvalue, pvalue, stderr =
stats.linregress(Tcw[Tmin:Tmax],ichi[Tmin:Tmax])

#use slope to calculate Curie constant, then effective magnetic moment
#from Curie-Weiss relation
C=1/slope #Curie constant per kg
mu=((C*3*kB/(mu0*N))**0.5)/muB #moment per magnetic cation
theta=-intercept/slope #weiss constant in K

#save fitted curve to data frame to output later
dfcw["Linear Fit (kg/m^3)"]=intercept+slope*Tcw[Tmin:Tmax]

#plot reciprocal susceptibility versus temperature with fit
fig = plt.figure()
ax = fig.add_subplot(1, 1, 1)
ax.plot(Tcw[Tmin:Tmax],intercept+slope*Tcw[Tmin:Tmax],ls=':',color='k')
ax.plot(Tcw[Tmin:Tmax],ichi[Tmin:Tmax],ls='none', marker='.',
fillstyle='none', color='k')
ax.set_xlabel("Temperature (K)")
ax.set_ylabel("$\chi^{-1}$ (kg/m$^3$)")
ax.legend(['Linear Fit', 'Data'],loc='best')
ax.grid()

```

```

#save figure and data frame
fig.savefig(filelabel + " inverse Chi(T) with fit" + ".png",dpi=600)
dfcw.to_csv(filelabel + " inverse Chi(T) with fit"+ ".csv")

#Export simple .txt file with the Curie-Weiss fitting results
with open(filelabel+" inverse Chi(T) with fit.txt", "w") as file:
    file.write("slope:"+str(slope))
    file.write("\n")
    file.write("intercept:"+str(intercept))
    file.write("\n")
    file.write("R-squared:"+str(rvalue**2))
    file.write("\n")
    file.write("moment:"+str(mu))
    file.write("\n")
    file.write("theta:"+str(theta))

print("slope: %f    intercept: %f    R-squared: %f    moment per ion: %f BM
theta: %f" % (slope, intercept,rvalue**2,mu,theta))

```

### B.3.4 Brillouin Analysis of Paramagnetic M(H) Data

```

#create useful variables to easily choose A/m fields in Tesla units
H1T=800000    #1Tesla
H2T=1600000   #2Tesla
H3T=2400000   #etc..
H4T=3200000
H5T=4000000
H6T=4800000
H7T=5600000

```

```

#set user Parameters for fitting and data output
Temp = "30K"      #choose which temperture data you want to fit
                  #see naming convention below
maxfield = "7T"   #set convenient label of max fitting field for file output
Hmax = H7T        #chose max field to fit up to

#choose the data frame for your M(H) data
#naming convention used here: SampleID MH Temp FieldRange.data
df=filedict['Data MH ' + Temp + ' 0-7T.dat']

Jinit = 2.5       #choose initial J from expected unpaired electrons
Ninit = 3.94E22   #choose initial N from ideal concentration
#ginit = 2        #choose initial g if not 2

#known variables, can be used instead of initial values above
g=2               #g-factor (unitless), comment if using ginit
#N=3.94E22        #number of magnetic atoms/kg if not using Ninit
#J=1              #total spin if not using Jinit

#assign variables to data for fitting
T=df["Temperature (K)"]
H=df["Magnetic Field (A/m)"]

#define Brillouin function
def Brillouin(T,H,g,J):
    x=(mu0*g*muB*H*J)/(kB*T)

```

```

    return ((2*J+1)/(2*J))*1/(np.tanh(((2*J+1)*x)/(2*J)))-(1/(2*J))*
    1/(np.tanh(x/(2*J)))

#define paramagnetic magnetization function
def Magnetization(T,H,g,N,J):
    B=Brillouin(T,H,g,J)
    return N*g*muB*J*B

#define residual sum of squares function for fit quality
def RSS(x,data):
    J,N = x
    M = data["Corrected Mass Magnetization (Am^2/kg)"]
    M_hat = Magnetization(T,data["Magnetic Field (A/m)"],g,N,J)
    return np.sum((M-M_hat)**2)

#assign temporary data frame to enable selection of maximum fitting field
tdf = df[df["Magnetic Field (A/m)"]<=Hmax]

# set initial values for fitting
x0 = np.array([Jinit,Ninit])

#use minimize function from scipy.optimize, can change method
result = minimize(RSS,x0,args=(tdf),method="Nelder-Mead")

#assign fitting results to variables for plotting and export
Jopt,Nopt = result["x"]

```

```

#calculate fitted effective moment using theory
meff=float(g*(np.sqrt(Jopt*(Jopt+1))))

#save fit curve to the data frame
df["Brillouin Fit"]=Magnetization(tdf["Temperature (K)"],
tdf["Magnetic Field (A/m)"],g,Nopt,Jopt)

#plot fitting results
fig = plt.figure()
ax = fig.add_subplot(1, 1, 1)
ax.plot(tdf["Magnetic Field (T)"],Magnetization(tdf["Temperature (K)"],
tdf["Magnetic Field (A/m)"],g,Nopt,Jopt),ls=':', color='k')

ax.plot(tdf["Magnetic Field (T)"],tdf["Corrected Mass Magnetization
(Am2/kg)"],ls='none', marker='.', fillstyle='none', color='k')

ax.set_xlabel("Applied Magnetic Field (T)")
ax.set_ylabel("Mass Magnetization (Am2/kg)")
ax.legend(['Brillouin Fit',Temp +' Data'],loc='best')
ax.grid()

#save figure and data as .csv file
fig.savefig(filelabel + " " + Temp + " M(H) fit to " +
maxfield + ".png",dpi=600)
df.to_csv(filelabel + " " + Temp + " M(H) fit to " +
maxfield + ".csv")

```

```

#create variables from fitting results
RSS = result['fun']
J = result['x'][0]
N = result['x'][1]

#export plain .txt file with fitting results
with open(filelabel + " " + Temp + " M(H) fit to " +
maxfield + ".txt", "w") as file:
    file.write("RSS:"+str(RSS))
    file.write("\n")
    file.write("Nions:"+str(N))
    file.write("\n")
    file.write("J:"+str(J))
    file.write("\n")
    file.write("Moment:" + str(meff))

print("RSS:"+str(RSS))
print("J:"+str(J))
print("Number Magnetic Ions per kg:"+str(N))
print("Effective Moment:" + str(meff))

```